Technische Universität München
Lehrstuhl für Elektrische Energiespeichertechnik
Prof. Dr.-Ing. Andreas Jossen

Influence of Cell Size on Performance and Lifetime of Lithium-Ion Batteries

Raghavendra Arunachala

Vollständiger Abdruck der von der Fakultät für Elektrotechnik und Informationstechnik der Technischen Universität München zur Erlangung des akademischen Grades eines

Doktor-Ingenieurs

genehmigten Dissertation.

Vorsitzender:	Prof. Dr.-Ing. Kindersberger
Prüfer der Dissertation:	
	1. Prof. Dr.-Ing. Andreas Jossen
	2. Prof. Dr.-Ing. Markus Lienkamp

Die Dissertation wurde am 23.11.2017 bei der Technischen Universität München eingereicht und durch die Fakultät für Elektrotechnik und Informationstechnik am 07.05.2018 angenommen.

Declaration of Authorship

I hereby declare that the thesis submitted is my own unaided work. All direct or indirect sources used are acknowledged as references.

I am aware that the thesis in digital form can be examined for the use of unauthorized aid and in order to determine whether the thesis as a whole or parts incorporated in it may be deemed as plagiarism. For the comparison of my work with existing sources I agree that it shall be entered in a database where it shall also remain after examination, to enable comparison with future theses submitted. Further rights of reproduction and usage, however, are not granted here.

This paper was not previously presented to another examination board and has not been published.

Raghavendra Arunachala

Berlin, November 16, 2017

Abstract

The lithium-ion battery is the most preferred choice for energy storage in electric vehicles and hybrid electric vehicle application, as it exhibits superior energy density, power density, low self-discharge, and excellent cycle life. The performance of this battery is influenced by temperature, current rate, cycling regime, aging process, and cell chemistry. The aging mechanism has been studied extensively to predict and to increase the lifetime of the battery, by identifying the stress factors and by focusing on specific aging tests. However, there has been little focus on the influence of cell size on performance and lifetime at a time when large-format cells are becoming increasingly popular over short-format cells because of several advantages. The main advantages is fewer connections between the cells and wiring for the battery pack, fewer individual cells to monitor for the battery management system, more options for delivering high energy and scale-up as the energy demand increases. However, despite these advantages, a few challenges have to be addressed as the cell sizes increase.

An increase in cell size introduces spatial inhomogeneity in the cell, such as non-uniform temperature, current density, and state of charge distribution. These inhomogeneities cause non-uniform utilization of the cell's active material and, in the long term, may lead to localized aging and the premature end of life of the cell. This thesis is aimed at studying the inhomogeneity occurring in the cell due to an increase in its size. Commercial cylindrical and pouch cells were selected for the sizing investigation. The cells were chosen from the same chemistry and same manufacturer. They were subjected to calendar and cycle aging tests to evaluate the evolution of the aging process with respect to different cell sizes. The cycle aging results showed that the largest cell size aged faster than cells of smaller sizes, and the smallest cell size experienced the least aging. The calendar aging results showed no influence of cell sizing; there was no current flow leading to different current or temperature distribution, and all the cells aged at a similar rate. Additional measurements were performed to evaluate spatial temperature and spatial volume expansion during cycle aging. The maximum temperature gradient was recorded in the largest cell size under all operating conditions. The volume expansion measurement showed non-uniform expansion on the cell surface; it is a function of cell voltage or state of charge. The cycle aging tests revealed that the cell thickness accumulated during the aging process, which is an indication of a deteriorating state of health.

A pseudo-two-dimensional electrochemical and three-dimensional thermal model was developed with a COMSOL Multiphysics FEM tool to simulate temperature, current density, and SOC distribution in the cell. The voltage and temperature measurements were validated with this model for different pouch cells with reasonable accuracy. The aging inhomogeneity was evaluated by developing a spatially resolved equivalent circuit model on a Matlab/Simulink® platform. The model simulated current and SOC distribution in fresh and aged cells. The results illustrated that aging increases cell inhomogeneity and causes premature end of life, especially in large-format cells.

“Karmanye vadhikaraste Ma Phaleshu Kadachana |
Ma Karmaphalaheturbhurma Te Sangostvakarmani ||”

— Bhagawad Gita

“ You have the right to perform your prescribed duties, but you are not entitled to the fruits of your actions.
Never consider yourself to be the cause of results of your actions, and never be attached to not doing your duties.”

Acknowledgement

First and foremost I would like to thank my supervisor Prof. Andreas Jossen at Technical University of Munich and my mentor Prof. Juergen Garche who made this research work possible. Without your support and guidance, I would have lost myself in countless ways in the quest for solving my research problem.

Throughout my PhD journey, I have had close co operations with my fellow colleagues Kamyar Makinejad, Sabine Arnold, Jan Geder and Eliud Cabrera Castillo. Our numerous discussions on battery testing, aging mechanism, Multiphysics based modelling, deeper understanding to the chemistry side of the battery, and safety topics has helped me to bring a proper order and structure in my work. In addition, I have been ably assisted by Lemuel Moraleja in building up test rigs, performing cell characterization and aging tests. Without his support it would be difficult to achieve the desired results.

I would like to thank my family and my wife Bhavya Nandodi Venkatagiri for the emotional support during my difficult times and encouraging me work with great enthusiasm.

This work was financially supported by the Singapore National Research Foundation (NRF) under TUM CREATE Ltd., and it is greatly appreciated. Finally I would like to thank the Institute of Electrical Energy Storage Technology (TUM) and working staff, for supporting my research activities in Germany and Singapore.

Raghavendra Arunachala
Berlin, Germany
November 16, 2017

List of Publications

Raghavendra Arunachala, Chethan Parthasarathy, Andreas Jossen, and Juergen Garche. "Inhomogeneities in Large Format Lithium Ion Cells: A Study by Battery Modelling Approach." ECS Transactions 73, no. 1 (2016): 201-212.

Raghavendra Arunachala, Lemuel Moraleja, Andreas Jossen, Juergen Garche (2015) " Aging Inhomogeneity influenced by Cell Size in Commercial Pouch Cells." In: European Battery, Hybrid and Fuel Cell Electric Vehicle Congress EEVC European Electric Vehicle Congress Brussels, Belgium, December 1-4, 2015

Raghavendra Arunachala, Sabine Arnold, Lemuel Moraleja, Tim Pixis, Andreas Jossen, Juergen Garche (2015) "Influence of Cell Size on Performance of Lithium Ion Battery." In: Kraftwerk Batterie 2015 [Poster], Aachen, Germany, April 27-29, 2015

Jan Geder, Raghavendra Arunachala, Shishir Jairam, Andreas Jossen (2015) "Thermal Behavior of Aged Lithium-Ion Batteries: Calorimetric Observations." In: IEEE Green Energy Systems Conference CSU Long Beach, USA, November 9, 2015

Sabine Arnold, Raghavendra Arunachala, Lemuel Moraleja, Andreas Jossen (2015) "Study of Inhomogeneity in Large Format Li-Ion Cells with different Multiphysics Models." In: COMSOL conference 2015 COMSOL Kuala Lumpur

Kamyar Makinejad, Raghavendra Arunachala, Sabine Arnold, Hassen Ennifar, Han Zhou, Andreas Jossen, Wen Changyun (2015) "A Lumped Electro-Thermal Model for Li-Ion Cells in Electric Vehicle Application." In: EVS28 14 KINTEX, Korea

Peter Keil, Simon F Schuster, Christian von Lueders, Holger Hesse, Raghavendra Arunachala, Jossen (2015) "Lifetime Analyses of Lithium-Ion EV Batteries." In: 3rd Electromobility Challenging Issues conference (ECI), Singapore, 1st - 4th December 2015 Electromobility Challenging Issues Conference

Annette E Trippe, Raghavendra Arunachala, Tobias Massier, Thomas Hamacher, Andreas Jossen (2014) "Charging Optimization of Battery Electric Vehicles including Cycle Battery Aging." In:

5th IEEE PES Innovative Smart Grid Technologies (ISGT) European 2014 Conference

Raghavendra Arunachala, Kamyar Makinejad, Satyajit Athlekar, Andreas Jossen, Juergen Garche (2013) "Cycle Life Characterisation of Large Format Lithium-ion Cells." In: EVS 27, Barcelona

J Geder, S Arnold, N Martiny, K Makinejad, R Arunachala (2013) "Battery cell research between a molecule and an electric vehicle Asia Smart Grid/Electromobility.", 2013, Singapore [Poster]

Thanagasundram Suguna, Arunachala Raghavendra, Makinejad Kamyar, Teutsch Tanja, Jossen Andreas (2012) "A Cell Level Model for Battery Simulation." In: European Electric Vehicle Conference 2012

Contents

List of Abbreviations

0D ..... 0 Dimensional
2D ..... Two Dimensional
3D ..... Three Dimensional
AEKF ..... Adaptive Extended Kalman Filter
ANN ..... Artificial Neural Networks
ARC ..... Accelerating Rate Calorimeter
BMS ..... Battery Management System
BOL ..... Beginning of life
C-rate ..... Current Rate
CC ..... Constant Current
CCCV ..... Constant Current Constant Voltage
CID ..... Current Interrupting Device
CT ..... Counter Tab Design
CV ..... Constant Voltage
DEC ..... Diethyl Carbonate
DMC ..... Dimethyl Carbonate
DSC ..... Differential Rate Calorimeter
EC ..... Ethylene Carbonate
ECM ..... Equivalent Circuit Model
EIS ..... Electrochemical Impedance Spectroscopy
EKF ..... Extended Kalman Filter
ELM ..... Extreme Learning Machine
EMC ..... Ethyl Methyl Carbonate
EOCV ..... End of Charge Voltage
EOD ..... End of Discharge
EOL ..... End of Life
EV ..... Electric Vehicle
FEM ..... Finite Element Method
HEV ..... Hybrid Electric Vehicle
HF ..... Hydrofluoric Acid
HiL ..... Hardware in Loop
HPPC ..... Hybrid Pulse Power Characterization
ICE ..... Internal Combustion Engine
LCO ..... Lithium Cobalt Oxide ($LiCoO_2$)
LFP ..... Lithium Iron Phosphate ($LiFePO_4$)
LMO ..... Lithium Manganese Oxide ($LiMn_2O_4$)

LS ..... Long Stack Design
LTO ..... Lithium Titanate (Li_2TiO_3)
MSMD ..... Multi Scale Multi Domain
MUMPS ..... Multifrontal Massively Parallel Solver
NCA ..... Lithium Cobalt Nickel Aluminium Oxide ($LiNi_xCo_yAl_zO_2$)
NiMH ..... Nickel Metal Hydride
NMC ..... Lithium Nickel Manganese Cobalt Oxide ($LiNi_xMn_yCo_zO_2$)
NT ..... Normal Tab Design
OCV ..... Open Circuit Voltage
P2D ..... Pseudo Two Dimensional
PARADISO .. Parallel Direct Solver
PC ..... Propylene Carbonate
PF ..... Particle Filter
PTC ..... Positive Temperature Coefficient
RC ..... Resistor in parallel with Capacitor
RPT ..... Reference Performance Test
RTD ..... Resistance Temperature Detectors
RUL ..... Remaining Useful Life
RVM ..... Relevance Vector Machine
SEI ..... Solid Electrolyte Interface
SMO ..... Sliding Mode Observer
SOC ..... State of Charge
SOF ..... State of Function
SOH ..... State of Health
SRECM ..... Spatially Resolved Equivalent Circuit Model
ST ..... Short Tab Design
SVM ..... Support Vector Machine
WCT ..... Wide Counter Tab Design
WS ..... Wide Stack Design
WT ..... Wide Tab Design

List of Symbols

α ..... Charge transfer coefficient
ΔV ..... Over potential / V
$\delta_{cc,j}$ ..... Thickness of current collector / m
ϵ_e ..... Electrolyte phase volume fraction
ϵ_s ..... Porous electrode volume fraction
$\hat{u}$ ..... Unit vector indicting direction of J
κ ..... Li^+ conductivity of electrolyte / S m^{-1}
κ^{eff} ..... Effective Li^+ conductivity of electrolyte / S m^{-1}
κ_D^{eff} ..... Effective Li^+ diffusional conductivity of electrolyte / A m^{-1}
λ ..... Thermal conductivity / W m^{-1} K^{-1}
ρ ..... Density / kg m^{-3}
σ ..... Electrical conductivity / S m^{-1}
C_p ..... Specific heat capacity / J kg^{-1} K^{-1}
E_a ..... Activation energy / kJ mol^{-1}
k_0, k_1, k_2 ..... Coefficients of Q_{loss}
N ..... No. of cycles
R_C ..... Constriction resistance / Ω
R_S ..... Spreading resistance / Ω
$\phi_{cc,j}$ ..... Voltage distribution in current collector / V
ϕ_s ..... Potential in the solid phase / V
ρ_{foil} ..... Resistivity of the foil / Ω m
σ^{eff} ..... Reference conductivity of active material / S m^{-1}
$\sigma_{p,n}^{eff}$ ..... Effective conductivity of positive and negative active material respectively / S m^{-1}
$\sigma_{cc,j}$ ..... Electrical conductivity of the current collector / S m^{-1}
τ_e^p ..... Tortuosity correction factor
A ..... Area of the electrode plate / m^2
a_s ..... Specific interfacial surface area per unit volume / m^2 m^{-3}
c_e ..... Lithium concentration in electrolyte phase / mol m^{-3}
c_r ..... Radial position / m
$c_{s,e}$ ..... Lithium concentration in electrode/electrolyte interphase / mol m^{-3}
c_s ..... Lithium concentration in solid phase / mol m^{-3}
D_e^{eff} ..... Effective diffusion coefficient in electrolyte phase / m^2 s^{-1}
D_e ..... Relative diffusion coefficient in electrolyte phase / m^2 s^{-1}
D_s ..... Solid phase diffusion coefficient / m^2 s^{-1}
$f_\pm$ ..... Activity coefficient
i_0 ..... Exchange current density / A m^{-2}

j^{Li} ..... Electrode current density / A m^{-2}
J_s^{Li} ..... Current density of side reaction / A m^{-2}
$P_{loss,foil}$ ..... Power loss in current collector foil / W
Q_{loss} ..... Capacity loss / A s
S_n ..... Active surface area of negative electrode / m^2
t_+^0 ..... Transference number of Li^+
t_0 ..... Initial time / s
t_s ..... Final time / s
C ..... Battery Capacity / A h
e ..... Mathematical Constant = 2.71828
F ..... Faraday constant = 96485.33 / C mol^{-1}
I ..... Current / A
k ..... Rate of chemical reaction / s^{-1}
n ..... Number of electrons involved in the electrode reaction
p ..... Peukert constant
R ..... Universal gas constant = 8.314 J K^{-1} mol^{-1}
T ..... Absolute Temperature / K
t ..... Time / s

List of Figures

List of Tables

Chapter 1

Introduction

1.1 Background

The success story of lithium-ion batteries started during the 1990s, when Sony Corporation first developed carbon-negative intercalation electrodes. This led to its successful introduction into the sector of consumer electronics, such as cell phones, laptops, electronics, music devices and so on. The chemistry quickly gained popularity, as it exhibited superior energy density, power density, low self-discharge, and an excellent cycle life. These characteristics are the preferred choice for electric vehicle (EV) and hybrid electric vehicle (HEV) applications [1]. Existing battery technologies, such as lead-acid and nickel metal hydride batteries, fell out of favour because of their heavy weight and size compared to lithium-ion batteries.

The versatile chemistry composition of lithium-ion batteries has provided several options for high energy cells, high power cells, safer chemistry, and good lifetime performance for EV application. The most prominent cell chemistries for automotive applications use lithium nickel cobalt aluminium oxide (NCA), lithium nickel manganese cobalt oxide (NMC), lithium iron phosphate (LFP), lithium manganese oxide (LMO), and lithium cobalt oxide (LCO) for the cathode. Graphite or lithium titanate (LTO) is used for the anode. Not all the above-mentioned characteristics can be fulfilled by one cell chemistry. LFP chemistry is considered to be safer, but it compromises energy density and power density. Whereas NMC and NCA suffer from poor safety, they excel in specific energy, specific power, and cycle life. Another class of anode material that provides excellent safety is LTO. However, this chemistry has a higher operating voltage compared to metallic lithium and graphite, which results in low specific energy [2]. The listed cell chemistries are already being used by several manufacturers to produce batteries for EV and HEV application.

EVs have a long history that dates back to 19^{th} century and remained as a preferred mode of transportation until the advent of the gasoline-powered internal combustion engine (ICE) in the 1920s. It created revolution in the transportation sector and nearly wiped out the existence of EVs until the end of 20^{th} century. Despite several advantages of EVs, they were considered to be too bulky, and they could only store a little energy compared to gasoline-driven vehicles. It was only during the late 1970s that the massive energy crisis and volatility in the oil market triggered the idea of efficient transportation through an alternative energy source. This led to the development of HEVs powered by gasoline and lead-acid batteries.

In the 1990s, numerous efforts by car manufacturers with support from governments persuaded them to develop EVs. Chrysler introduced TEVan, a battery-powered EV in United States that used nickel cadmium batteries. The Ford Ranger EV was produced by Ford Motor Company between 1998 and 2002 and used lead-acid batteries, but it is no longer in production. The REVAi, produced by REVA Electric Car Company, was introduced into the market in 2001. This EV was also powered by lead-acid batteries. General Motor Corporation produced the EV1 from 1996 to 1999, which also used lead-acid batteries. They also introduced the Chevrolet S10 Electric around the same time, powered by nickel metal hydride (NiMH). Both models were later discontinued. Honda EV Plus and Toyota RAV4 EV were introduced in 1997, powered by NiMH. By the early 2000s most of these models were discontinued, and the focus was shifted towards HEVs.

After the introduction of HEVs, many car manufacturers adopted lithium-ion batteries due to their inherent advantage over lead-acid and NiMH batteries. By late 2000s, interest in EVs was renewed by the introduction of the Tesla Roadster, a battery-powered sports cars from Tesla Motors. Lithium-ion cells produced by Panasonic were used in this battery pack. The cell type is 18650 cylindrical based on NCA chemistry, a cell form commonly used in laptops. The production was discontinued by 2012. Although they announced an optional upgrade to the Roadster 3.0 in December 2014, this will have a new battery from LG Chem[1]. The Tesla Model S is a full-size EV, introduced in 2012, and is much heavier compared to the Roadster but costs only half of the price. It has different options for a battery pack, 70, 85, and 90 kWh, which provide a driving range between 390 km and 480 km. Telsa is now producing Model X, an SUV variant with an additional motor driving the front wheels. Nissan LEAF, a full range EV, was introduced in Japan and the US market. It is a compact, five-door hatch-back EV, powered by lithium-ion pouch cells with manganese-based spinel chemistry, with a driving range of 135 km. The new 2018 Nissan LEAF offers a driving range of 400 km, nearly triple that of the first-generation LEAF. It is now the world's leading producer of EVs, and is available in 46 countries with global sales of over 300,000 vehicles by January 2018.

The BMW i3 was introduced into the European market at the end of 2013. It is a five-door urban EV, powered by a 22 kWh battery pack with a driving range of 160 km. In May 2012, Toyota announced production of its new EV version of the RAV4, a mini SUV. This was produced in joint venture with Tesla, which provided the power train. It had a 42 kWh lithium-ion battery pack, with a driving range of 160 km. Another leading manufacturer, Mitsubishi Motors, produced Mitsubishi i-MiEV which uses lithium-ion cells for the battery pack. The popularity of lithium-ion batteries has been growing ever since, and it has become the primary choice for EVs and HEVs. Fig. 1.1 shows the global forecasts for light-duty HEVs and EVs between the years 2013 and 2020 [3]. Many EV producers such as BYD E6, Chevrolet Spark, and Mahindra e20, and demonstration fleets such as Mini E, BMW ActiveE, Tata Indica Vista EV, Toyota eQ/Scion iQ EV, and Volkswagen Golf Blue-e-Motion have embraced lithium-ion batteries to power vehicles [4]. The latest addition to the demonstration e-Fleet is EVA, the first EV specifically designed as a taxi for tropical megacities. This EV was built in collaboration between Nanyang Technological University (NTU) and Technische Universität München (TUM), funded by Singapore's National Research Foundation (NRF). It has a 50 kWh lithium-ion battery pack made of pouch cells, and it has a driving range of 300 km [5].

As the market has evolved, lithium-ion batteries have undergone several changes in chemistry, cell form, and design since its inception to meet the specific demands of EVs and HEVs. In the initial stages, battery cells were produced in cylindrical form. This cell form is still popular and the most

[1] The facts and figures of EVs and HEVs are based on November 2017. As this is a developing field, the numbers can change, in a short span of time. However, these numbers do not affect the results of this thesis.

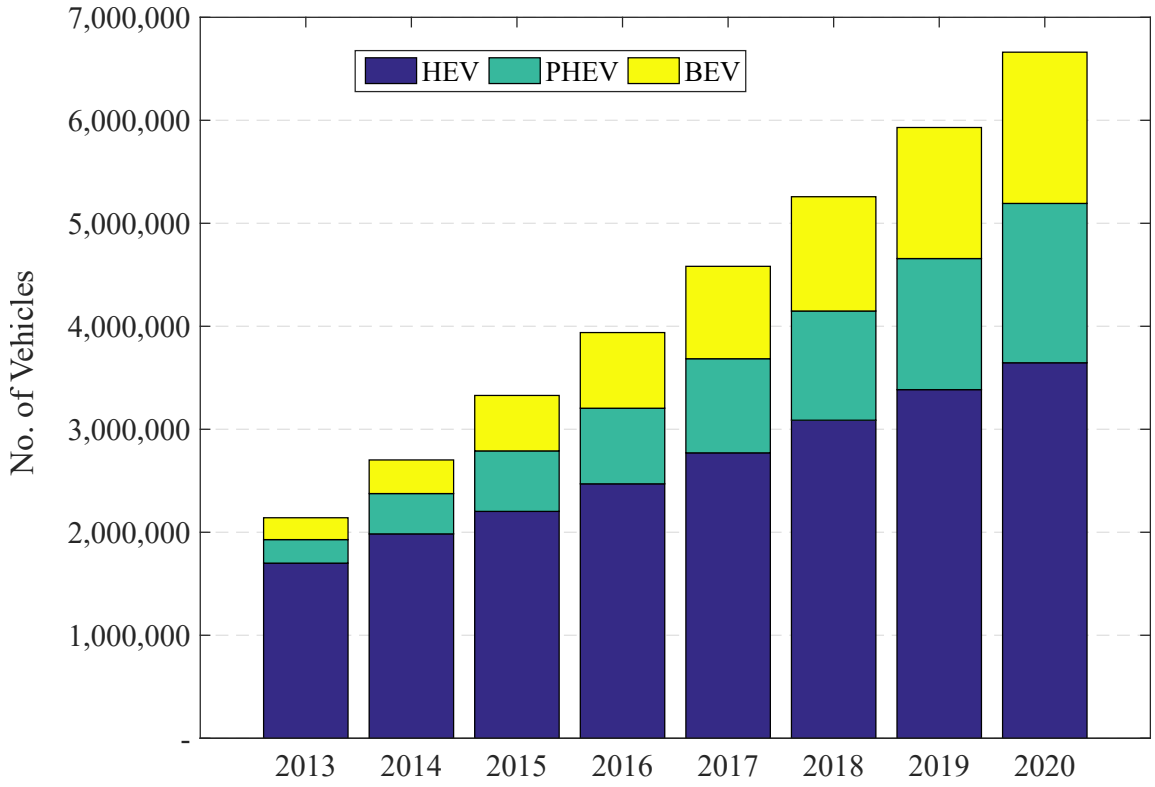

Figure 1.1: Annual electric vehicle sales by drivetrain, World Markets: 2013-2020 [3]

widely used design for rechargeable lithium-ion batteries. They are easy to manufacture, are low-cost, provide good mechanical stability, and have excellent safety features. Cylindrical cells are designed for robustness, with the ability to withstand vibration, shock, and high internal pressure. These cells come in a standardized format. The most commonly available cell format is 18650. This format cell is 18 mm in diameter and 65 mm in length. Other variants of cylindrical cells are 26650 and 32113, designed for high-power applications, commonly used in HEVs. Some cell manufacturers, such as Saft, Gaia, EIG, and so on, have developed even bigger cylindrical cells with up to 200 Ah capacity for high-energy and high-power applications. But due to their geometry, they make for inefficient usage of space, and for this reason, the volumetric packing efficiency is low compared to other cell forms. The heat transfer to ambient is not optimal, because of the lower surface-area-to-volume ratio. For this reason, cell designers are moving towards flat battery cells. Despite these limitations, cylindrical cells have high energy density and compensate for the low packing efficiency.

To improve the volumetric packing efficiency, prismatic design was introduced. The prismatic cells are contained in a metallic or plastic can, with electrodes either stacked or in the form of a flattened spiral. This arrangement has greatly improved the space utilization, but it comes at a higher cost of manufacturing, lower energy density, and more vulnerability to swelling. The dimensions of these cells are not standardized, hence each manufacturer can have their own flexible design. These cells are mainly used in mobile applications, but they are gaining popularity in HEV and EV applications.

The pouch cell offers a simple, flexible, and light-weight solution for battery design. It makes for efficient usage of space and provides about 90–95% packing efficiency, which is the highest among all battery designs. It has a polymer laminate enclosure instead of a metallic enclosure, which significantly reduces the dead weight of the cells. Because of these advantages, they are extensively used in HEV

and EV applications [6]. However, this design comes with a compromise, as the pouch cells are most vulnerable to safety issues, and the mechanical stability is affected by the soft pouch casing. Additional packing materials should be included in the pouch cells to handle shock, vibration, impact and so on and this reduces the energy density of the cell. Fig. 1.2 shows the price comparison of different cell forms between the years 2005 and 2014. Though the costs of flat prismatic design and pouch design were high in the initial years, but they have been decreasing ever since and getting more competitive in price [7]. This design should equal or better the performance of cylindrical cells.

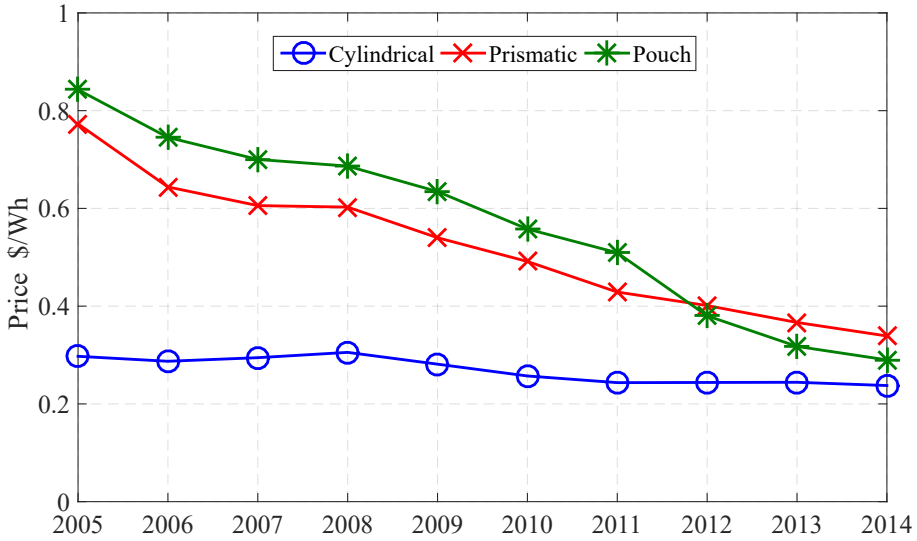

Figure 1.2: Average lithium-ion battery-cell price comparison among different cell forms [7]

Another important ongoing development in lithium-ion battery technology is with respect to the size and capacity of the individual cell. The cell size and capacity terminology can be used interchangeably, as the increase in cell size enhances the cell capacity. The new terms such as short-format and large-format cells were coined to describe cells of different sizes. In any energy storage system, several cells should be connected in a series and/or parallel combination to obtain required voltage and energy values, because the existing battery technology can only provide around 3.7 V of nominal voltage, and it is limited by energy content (about 400 Wh with the newest cells) at a single cell level. The integration of the energy storage system is particularly challenging when the system voltage and energy capacity is higher, especially for short-format cells, as they are limited by energy. Therefore, the question arises for the energy-storage-system integration as to which combination is better, either the combination of many small cells (short format) or the combination of a few large cells (large-format). To make a proper comparison, several factors, such as cost/kWh, safety, assembly and integration cost, reliability, battery monitoring, thermal management, and so on, should be considered.

Short-format cells have many advantages in comparison to large-format cells. Some of them can be listed as having lower cell cost, improved safety due to lower energy, simple thermal management, and so on. However, these cells also have certain disadvantages, which include many interconnections, higher integration and assembly costs, lower weight and volume efficiency, low reliability due to the presence of many components. The nominal voltage of the cells does not change by varying cell size, but large-format cells do have certain advantages when the cell capacity needs to be upscaled. Many blocks of short-format cells have to be connected in parallel to scale up the capacity. If the cell blocks are not built with narrow distribution of internal resistance, this will have an impact on the lifetime of the battery pack, due to high currents in individual cells at different stages of battery operation [8].

The performance and lifetime of the individual cells, such as cell-to-cell internal resistance, discharge capacity, aging, and so on, should be similar for the longevity of the battery pack. Otherwise, it leads to over-utilization and under-utilization of individual cells at different stages in their lifetime. Therefore, the choice of cell size for the battery pack design should take all these factors into account, with several trade-offs in design, to build the battery packs of EVs.

1.2 Research Problem and Hypotheses

The performance of lithium-ion battery cells is influenced by many parameters; some of them are microscopic in nature, and others are macroscopic. The parameters with microscopic influence in cell performance are chemistry, particle size, diffusion coefficient, equilibrium potential, reaction rate, thermodynamic parameters, thermal and electrical conductivity, heat capacity of active materials and different components of a cell, and many more. These parameters are by and large responsible for the electrochemical, thermal, safety, and lifetime performance of a battery. Besides the microscopic effects, there are certain macroscopic effects that influence the overall performance of a battery. These parameters are cell form, aspect ratio, overall cell thickness, number of layers, tab size and location, thicknesses of active materials, separator, and current collectors. They are primarily used in the cell design process. They might prove to be insignificant for short-format cells or smaller cell sizes, but, if the geometry is scaled up to attain a larger cell size with a higher Ah capacity, it will have a substantial effect on the performance, lifetime, and safety of a battery.

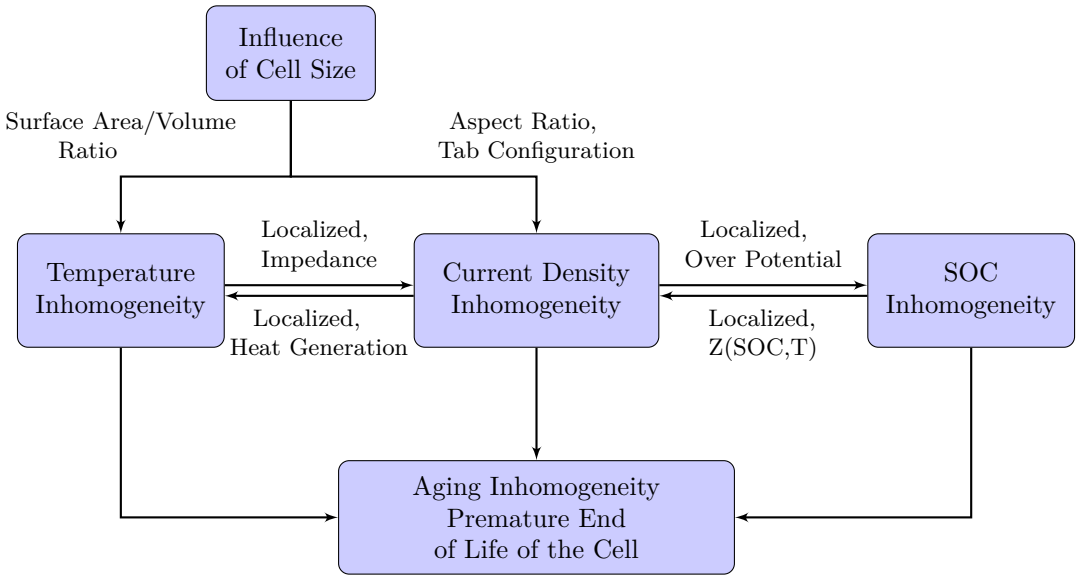

Figure 1.3: Schematic of aging inhomogeneity and its influencing factors

Increase in the cell size has certain inherent disadvantages, such as inhomogeneous temperature, current, and state of charge (SOC) distribution. The current distribution in the cell is affected by cell size, that is, tab size, tab location, current-collector thickness, and the aspect ratio of the cell. An increase in current-collector thickness improves its electrical conductivity and contributes to low cell internal resistance, and vice versa. It influences the flow of current in the current collector and into the electrodes of the cell. A uniform current flow due to an increase in current-collector thickness reduces the current density distribution, but contributes to the excess weight of the cell, resulting in lower energy

density. Despite optimizing the design, the current flow near the tabs is constricted, and the locations near cell tabs experience higher current density compared to surfaces far away from the tabs. The current distribution under this scenario has a direct influence on the SOC distribution. The SOC of a cell can affect many parameters, such as cell impedance, open circuit voltage (OCV) and so on. The current distribution influences the local heat generation and introduces temperature inhomogeneity. Increase in the cell size reduces the effective surface-area-to-volume-ratio, which means reducing the heating dissipation on the cell surface with respect to its volumetric heat generation. A low ratio leads to larger temperature inhomogeneity, and vice versa. These inhomogeneities are interrelated and will have a cascading effect on the overall cell performance. A long-term exposure to these inhomogeneities could lead to localized aging in the cell, as shown in the schematic of Fig. 1.3. A localized aging is the flash point that leads the cell to enter a premature end of life (EOL). In some regions of the cell where localized aging is severe, those parts of the cell hold less capacity and are more quickly discharged than the stronger regions of the cell, and in some cases, they might go into a deep discharge phase. Upon charge, the weaker regions are already charged while the stronger regions are still being charged. In both cases, the weaker regions are at a disadvantage, deteriorating them further and affecting the overall cell performance. This is similar to battery packs where unmatched cells perform worse than those groups of cells that exhibit similar characteristics. Therefore, aging inhomogeneity leads to an early EOL of a given cell.

The aging process in lithium-ion batteries is a well explained topic that is characterized by loss of cell capacity and an increase in impedance over time and usage. Many literature has described several aging processes, such as formation and growth of solid electrolyte interface (SEI) layers, loss of cyclable lithium-ions (Li^+), and electrolyte decomposition [9–11]. Secondary losses, such as degradation of active materials, decomposition of binders, and loss of contact between the current collector and active material due to volume changes during cycling, are also taken into account during the aging processes. There are several stress factors, such as temperature, current rate (C-rate), operating voltage, SOC range, depth of cycling, and so on, that influence these aging processes. There are extensive studies that describe how certain stress factors accelerate the aging processes, but there has been limited focus on the effect of cell size as an influencing factor for aging processes. Much of the focuses have been limited to the short-term performance of the cell, as this topic is still in the early stage of its evolution. Therefore, through this thesis, an additional stress factor is introduced in the form of cell inhomogeneity caused by the cell sizing effect. This stress factor needs to be considered in the aging evaluation of the cells, especially for large-format cells. This type of study could be further extended to other scopes, such as cell-to-cell variation in performance and aging for a large-scale battery-pack system.

Research on cell inhomogeneity shows that it occurs during different cycling conditions, such as ambient temperature and C-rate [12–15]. A decrease in ambient temperature and an increase in the C-rate together increase cell inhomogeneity caused by variation in the internal resistance and heat generation within the cell. Together with inhomogeneity introduced by cell sizing and different operating conditions of the cells [16], this has led to the following hypotheses:

- Cell sizing influences cycle aging, i.e., when the cells are charged and discharged regularly.
- Cell sizing should not influence calendar aging, as the inhomogeneities do not occur when the cells are stored in an OCV relaxation state.
- From a theoretical point of view, cell inhomogeneities are dependent on the electrode size, which could influence the calendar aging (at fixed OCV storage).

To prove the first hypothesis, cells have to be chosen from the same commercial manufacturer with the criteria of superior manufacturing process and reproducibility of the results. Aside from these conditions, the cell-chemistry should be the same in order to have only sizing as the influencing parameter for the studies. The proposed hypotheses need to be proved by conducting storage and cycle aging tests on the cells. The reason for the third hypothesis could be due to different local SEI formation rates caused by slightly different electrolyte distribution in the anode based on different local porosity. These differences in local porosity, however, are not primarily influenced by the cell size. Hence, evaluation of the third hypothesis is beyond the scope of this thesis.

1.3 Dissertation Outline

- In chapter 2, a comprehensive literature review on cell sizing and its influence is provided. The review includes (i) inhomogeneity caused by increase in cell size, geometry, macroscopic parameters, and so on, (ii) different forms of cell inhomogeneity and influence of operating conditions, and (iii) modelling techniques to study cell inhomogeneity. It also provides deep insight into the aging mechanism and factors influencing cell aging. The influence of cell aging on battery safety is also discussed.

- Chapter 3 reviews the existing measurement techniques and new measurements employed in this thesis to evaluate cell inhomogeneity. The reason for the choice of cells for sizing investigation is described. It also provides details about the experimental investigation performed on the cells, including the short-term and long-term aging tests.

- Chapter 4 describes different battery modelling approaches that are widely used. An objective comparison of three widely used battery modelling methods with varied accuracy and complexity is provided. The development of models, including their parameterization in Equivalent Circuit Models and Electrochemical Thermal Models, is explained in detail.

- In chapter 5, important results are discussed. The results are classified based on the type of experimentation and duration of the tests. Section 5.1 of the results focuses on the findings of calendar and cycle aging tests. The aging results prove the hypotheses proposed in chapter 2. Section 5.2 evaluates the findings of the experimental results, such as temperature inhomogeneity in different cell sizes at different operating condition. It also evaluates non-uniform volume expansion, especially in pouch cells, and how it is affected by cell size and aging process. Section 5.3 validates voltage and temperature measurements performed on different cell sizes, with the modelling results simulated in COMSOL. The models also simulate non-measureable parameters such as current and SOC gradients in the cells. Section 5.4 describes a new modelling approach to studying aging inhomogeneity through Matlab/Simulink® models. The model only describes electrical characteristics of the cell.

- Chapter 6 explains the benefits of the cell sizing investigation. The first part describes the necessity of selecting the right cell type for a given vehicle application. It compares the technical details of five battery packs from car manufacturers, such as total energy content, cell form, type of cooling, battery pack topology and so on. It explains the challenges in the design and development of a battery pack from large-format cells. It also proposes improvement in the cell design to reduce inhomogeneity.

- Finally, in chapter 7, the thesis work is summarized with concluding remarks, and avenues for future work are presented.

Chapter 2

Lithium-Ion Battery Aging and the Influence of Cell Size

2.1 Literature Review

Large-format cells are becoming popular in EV applications due to several advantages over the short-format cells. The main advantages are, fewer connections and wiring for the battery pack, lower integration and assembly costs, a higher weight-to-volume-ratio. Each individual cell can be monitored easily, which makes the battery management system more efficient. Large-format cells provide more options to deliver high energy and scale-up as the energy demand increases [17].

Cell manufacturers are working in the area of scale-up process by incorporating the manufacturing method for the shorter version. LG Chem [18] adopted this approach to produce large-format cells. Some distinguishing features of this approach are using stack and fold assembly, spinel based chemistry, and laminate packing to reduce the cost of manufacturing. The modelling approach is the most commonly used method to scale-up the cell size to study the performance of the battery. Mathematical modelling plays an important role in scaling up small-format to large-format cells, as endless options for design parameters can be used to simulate the cell performance. Kim et al. [19] used scale-up modelling approach on 10 Ah lithium-ion cells to simulate the performance of 26 Ah cells and verified this model with experimental discharge curves. The results showed that voltage and current density distribution are functions of discharge time and tab configuration.

NREL developed multi-scale multi-domain (MSMD) models to simulate large-format cylindrical, stacked prismatic, and pouch cells. The microscopic design parameters, such as material composition, porosity, and electrode thickness, were kept constant during the development of the model. The objective was to study the impact of large-format cell design by varying tab size, tab position, electrode area of the unit stack, and so on. The models were simulated to study current and potential distribution, and temperature distribution within the cell [20]. Taheri et al. [21] used a two-dimensional (2D) model to describe the effects of cell-tab design on inhomogeneous voltage drop in a 75 Ah lithium-ion pouch cell. An analytical model was developed to determine the bulk resistance and constriction/spreading resistance of a current collector. The results have confirmed that domain aspect ratio, tab width, tab eccentricity, and electronic conductivity contribute to constriction/spreading resistance, which causes inhomogeneous voltage and current density distribution.

Grevel et al. [13] used a coupled thermal and electrochemical model to simulate the performance of large-format cells. It described the influence of different cooling strategies on current density and temperature distribution inside the cell and within the cells in a stack. The main findings of this work were that, by employing a better cooling strategy, inhomogeneity in temperature and current density distribution can be reduced. These parameters have a significant impact on cell performance and lifetime, depending on the features, such as thermal/electrical path, cell form factor, and cell dimensions. In small-format cells, those features can be neglected, but the impact becomes more significant in large-format cells [22]. The significance of tab configuration was explained by Du et al. [23], where the effect of single-sided and cross-tab distribution was presented. The cross tab configuration improved the temperature distribution in the cell, and widening of the tabs greatly reduced the maximum temperature of the cell. These results were substantiated by Samba et al. [24], using a coupled 3D electrochemical and thermal modelling approach for large-format LFP cells. This model showed that cross tab configuration leads to more uniform distribution of temperature, SOC, and current density.

The interdependence between current density, SOC, and temperature distribution has been described by many authors. Zhang et al. [25] showed that current density distribution is already non-uniform at the beginning of discharge and evolves as the discharge continues. In the beginning, current-collector tabs attribute to higher ohmic drop due to higher local currents. The current distribution pattern reverses at the end of discharge (EOD), caused by localized SOC non-uniformity. A new in-situ method to measure the local potential of the cell was proposed by Osswald et al. [26]. This method utilizes the existing multi-tab configuration of commercial A123 cells to measure the voltage gradient between the multi-tabs at different discharge rates. The data measured were validated with multi-dimensional modelling, which evaluates internal cell variables such current density and SOC distribution. The simulation results show that the electrode areas near the terminals carry high current density compared to the areas farthest away, but the pattern reverses near the EOD [27]. Li et al. [28] studied inhomogeneous temperature distribution in 25 Ah large-format cells and devised a different cooling strategy to reduce it. Thermocouples were housed inside the cell as well as on the surface at the same location. Results showed that, in the through-plane direction, temperature variation was as high as 1.1°C in spite of the smaller thickness of the cell. The in-plane direction temperature variation was even higher, above 10°C under the adiabatic conditions during discharge. In another approach, the thermal behaviour of large-format cells was modelled using the finite element method [29]. At first, potential and current density distribution were modelled from the experimental results. Later, these parameters were used to calculate the heat generation rate to predict the temperature distribution in the cell. However, Fleckenstein et al. [14] described that variation in current density and SOC distribution is mainly caused by inhomogeneous temperature distribution inside $LiFePO_4$-based cylindrical cells. The inhomogeneous current density distribution is a result of varying electrochemical impedance, which is dependent on temperature. Furthermore, SOC inhomogeneity is caused by non-uniform current distribution and open circuit voltage that is influenced by temperature.

Liu et al. [30] described a method to determine and visualize SOC in a composite electrode of a lithium-ion battery. The results showed evidence of different in-plane SOC profiles while charging at a high C-rate. A higher SOC was recorded at the region closer to the current-collector tab and decreased towards the unconnected end of the electrodes. Gerschler et al. [15] discussed the effect of inhomogeneous temperature distribution on the lifetime of single cells and battery packs through a spatially distributed heuristic modelling approach. The influence of inhomogeneous temperature distribution has a direct impact on internal resistance, which results in inhomogeneous current distribution. Simulation results

showed that, by employing different cooling strategies, the resulting temperature distribution can become homogeneous, which will increase the safety and lifetime of the cells. A three-dimensional (3D) electric thermal modelling approach was presented by Veth et al. [31] to evaluate the internal states of large-format cells and their inhomogeneities. This model predicted internal temperature, voltage, current, and SOC distribution within the cell. It makes it possible to assess cooling and operation strategies concerning the internal state values of the cell and their influence on cell performance and lifetime. Zhang et al. [32] presented a multi-dimensional electric thermal model to evaluate the spatial temperature inhomogeneity in large format-cells. The main cause of temperature inhomogeneity was linked to high heat flux near the cell tabs and not due to non-uniform heat generation in the cell core. Thermal parameters such as specific heat capacity and thermal conductivity, influence the maximum cell temperature and temperature gradient along the in-plane direction, respectively.

Awarke [33] developed a pseudo 3D electrochemical model to study aging caused by inhomogeneous current distribution on large-format 40 Ah Kokam cells. The model was simulated with a high C-rate to increase the degree of inhomogeneity. The results showed that non-homogeneous growth of SEI layers during the first half of cycling would be destroyed in the second half of cycling, ensuring homogeneous-aging in one complete cycle. However, SEI growth is strongly dependent on temperature, and this dependency was not considered in this work. Veth [34] performed thermal characterization of 50 Ah large-format cells and showed strong temperature inhomogeneity in differently aged cells. The results indicate different temperature distribution strongly exhibiting the presence of local aging effects, which results in non-uniform utilization of the cell capacity. Cai et al. [35] presented a non-destructive approach for studying inhomogeneous degradation in large format-pouch cells. In-situ neutron diffraction patterns were analyzed on fresh and aged cells. SOC distribution in fresh cells was largely homogeneous, but, as the cells aged, inhomogeneous degradation was observed near the edges of the electrodes, which resulted in capacity fade. Contradicting this result, another study with spatially resolved neutron-diffraction patterns on fresh cells and aged cells showed no spatial inhomogeneity in SOC distribution. These studies were performed on commercially available short-format 18650 cells [36]. This indicates that spatial inhomogeneity is strongly influenced by cell size.

Kim et al. [37] developed a 3D thermal abuse model to study the thermal behaviour of large-format lithium-ion cells used in automotive applications. The model results showed that small cells had better heat rejection compared to larger cells, which prevented them from going into a thermal runaway state under identical operating conditions. The model results also showed that small cells heated rapidly and stayed at higher-than-ambient temperature. Whereas larger cells heated continuously, this resulted in continuous heat accumulation and increase in temperature. These results were supported by another research group, which developed a 3D thermal abuse model on large-format $LiFePO_4$ cells [38]. The results indicated that LFP active materials are more thermally stable and are attractive for large-format cells to prevent the cells from going into thermal runaway. Kim et al. [39] described that the difficulty of detecting faults in large-format cells at an early stage of internal short circuit or thermal runaway, as the effects are confined to a localized area, and a larger part of the cell is not affected. The existing safety features do not function properly if they are incorporated into large-format cells.

Stress generation inside a battery plays a significant role in determining its performance and lifetime. It can come from different sources, such as volume changes during the intercalation and deintercalation process, particle size, diffusion coefficient, ion concentration, and so on. Some authors [10, 40] described the main stress as coming from volume expansion, which causes fracturing of active material. The stress generated in anode material is higher compared to cathode material due to different material properties. Different anode materials have a different magnitude of volume expansion. During the

charging process, the anode volume increases and cathode volume decreases simultaneously, with some exceptions, depending on the cathode material, that is, LCO also increases volume while the cell is being charged. This process is reversed during the discharge process. As the magnitude of anode volume expansion is much higher compared to the cathode material, cell volume expands during charge and contracts in the reverse process [41]. The high ion concentration gradient as a result of a high C-rate is another source of stress generation. Large particle size is susceptible to volume expansion, which causes particle fracture. A low diffusion coefficient leads to a higher ion concentration gradient and causes pressure-induced stress volume expansion [42, 43]. Oh et al. [44] showed that, at high C-rates, residual expansion can be observed due to thermal expansion and internal SOC, which contributes to volume expansion. Spatial expansion was different on the cell surface, indicating inhomogeneous cell characteristics. Bitzer [45] proposed cell volume expansion as a method of lithium plating. The experimental conditions favouring lithium plating showed an increase in the cell thickness during cycling, which indicates irreversible volume expansion. However, this literature does not explain the influence of cell size on stress generation. Therefore, these microscopic parameters, such as material properties, particle size, and diffusion coefficient, are assumed not to have significant influence at the macroscopic level, such as cell size, cell type (cylindrical, prismatic, and pouch configuration) in determining stress generated within the battery.

The literature study can be summarized in the following:

- Inhomogeneity exists in all cell formats, but it has a huge impact on the performance and lifetime of large-format cells bacause of increase in cell size.
- The cell inhomogeneity is mainly caused by the evolution of non-uniform distribution of electrical and thermal paths during the cycling operation, originated from cell design, material properties, and different cooling strategies employed for the cells.
- Multi-scale multi-physics models can be used as tools to simulate internal states of the battery, such as current density, SOC, voltage, and temperature distribution.
- The non-uniform distribution of these internal states causes cell inhomogeneity, and they are interdependent on one another.
- Low ambient temperature and high C-rate increase cell inhomogeneity, and vice versa.
- Cell inhomogeneity leads to non-uniform utilization of the active electrode material and causes localized aging.
- Short-format cells are inherently safer than large-format cells because of lower energy.
- Several in-situ and ex-situ methods are being employed to evaluate cell inhomogeneity.

2.2 Aging Mechanism

The aging mechanism is a structural and chemical change in the components of the battery or the materials used in the battery. It is characterized by modification of battery properties with time and usage, and it ultimately results in the failure of the battery. Essential properties of a battery are the available energy and power throughput during its lifetime [1, 46, 47]. By definition, the EOL of the battery is reached if its nominal capacity is reduced to $\leq$80%. The failure of the battery occurs due

to a long process of degradation or due to short catastrophic events. The cell degradation is a result of a slow process of deterioration and gradual loss of its performance, until these suddenly lead to cell death. The short-term catastrophic events occur due to a short circuit or thermal runaway or due to abusive operation of the battery [48–52]. In lithium-ion batteries, the aging mechanism can be explained by active material degradation, formation and growth of a solid electrolyte interface (SEI) layer, electrolyte degradation, lithium plating, and so on. Aging mechanisms occurring in an anode and cathode are different, due to the different chemical and structural constituents of the materials [9, 46]. When the battery ages, it does not necessarily mean all the components age at the same rate, but, more often, the components age at different rates. Therefore, it is important to study the aging behaviour of the main components and characterize which component has a dominant aging mechanism.

Graphite material is the most commonly used anode electrode in commercially available lithium-ion cells. However, there are different anode materials used in lithium-ion batteries with the combination of different cell chemistries. It is difficult to analyze every combination of cell chemistries and to understand the aging behaviour. Aging of an anode leads to modification of the electrode properties with time and cycling. The aging process during storage will affect the calendar life of the battery, which is mainly because of irreversible self-discharge by forming SEI layer. During cycle life, this irreversible self-discharge is superimposed by mechanical degradation, lithium plating, and so on, as a result of frequent charging and discharging of cells [10]. Both calendar and cycle aging will change the performance characteristics of the cell, such as remaining capacity, cell impedance, OCV, charge/discharge curve, SOC, and state of health (SOH). Fig. 2.2 shows the chart of aging effects, causes, and effects.

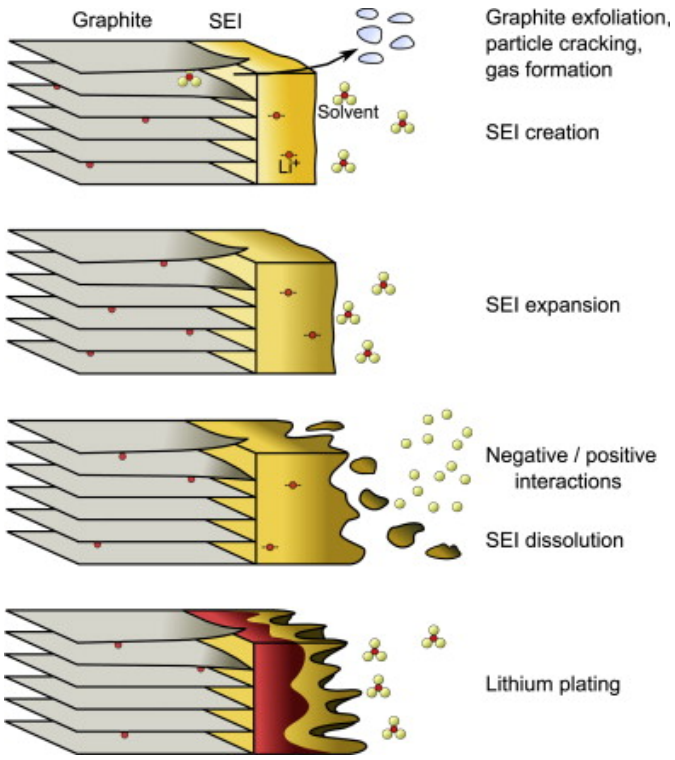

Figure 2.1: Aging mechanism in a lithium-ion battery negative graphite electrode [10]

Lithium-ion battery anode material operates at a voltage outside the electrochemical stability window,

and it is detrimental to the stability of electrolyte materials. Fig. 2.1 shows the illustration of an aging mechanism in the anode. The electrolyte reduction occurs at the anode electrolyte interface layer, and it reacts with free Li^+ to form an interfacial layer on the surface of the anode. This process happens at the beginning of the formation of the anode and continues later during cycling as well as during storage. The interfacial layer reduces the rate of further SEI formation under the decomposition of electrolyte. It acts as a protective layer by allowing only Li^+ intercalation and deintercalation; this semi-permeable membrane is called the SEI layer. It continues to grow from the very first cycle, but the growth gradually fades over a few hundred cycles. In the long-term cycling, the SEI layer can penetrate into the pores of the electrode materials and separators. This may result in reduced accessibility of the active surface area. This phenomenon can be attributed to the impedance rise of the cell, which reduces its power capability. A stable SEI layer is therefore essential for low irreversible capacity loss, low self-discharge, and high safety of the cell. Elevated temperature enhances the kinetics of the Li^+ intercalation and deintercalation, but it has a severe impact on the stability of the SEI layer due to changes in its morphology and composition. The negative impact of high temperatures can be attributed to increased degradation of SEI, which eventually leads to the break-down and dissolution of the layer at a temperature of $> 100°C$. This may result in reformation of the SEI layer, leading to consumption of cyclable Li^+. In the worst case, it is the first step towards thermal runaway, which could lead to fire or even an explosion of the cell. Low temperatures have different effects; the slow diffusion of Li^+ into anode, compounded with operating voltage close to lithium metal, leads to metallic lithium plating on the anode surface. The process continues and forms lithium dendrites during charging. Lithium dendrites subsequently react with electrolyte to accelerate the aging process or in the worst case, an internal short circuit [11]. Fig. 2.2 shows a chart of the aging mechanism in anode materials.

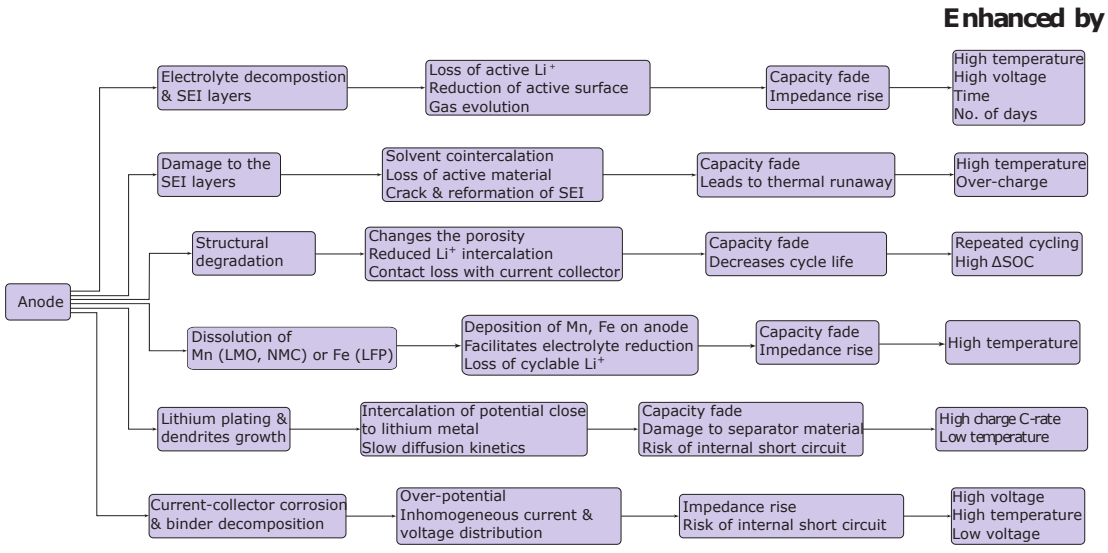

Figure 2.2: Aging mechanisms of the anode materials; causes, effects, and results [10]

Aging mechanisms in cathode materials can originate from structural changes, phase transition in the active material, electrolyte decomposition, dissolution of metal oxide, and secondary reactions such as current-collector corrosion and binder decomposition. Fig. 2.3 shows the schematic of the aging mechanism in cathode materials. These reactions vary depending upon the choice of cell chemistry, which will be discussed in detail in section 2.3.2. The intercalation and deintercalation of Li^+ cause changes in the molar volume fraction, which may induce mechanical stress and strain in the active material. It also causes phase transition, leading to distortion of the lattice structure, and the entire

process is not 100% reversible. In some cell chemistry, this process leads to dissolution of transition metal oxides in the electrolyte and triggers further side reactions. Besides this, there is also layer formation at the cathode electrolyte interface [53, 54].

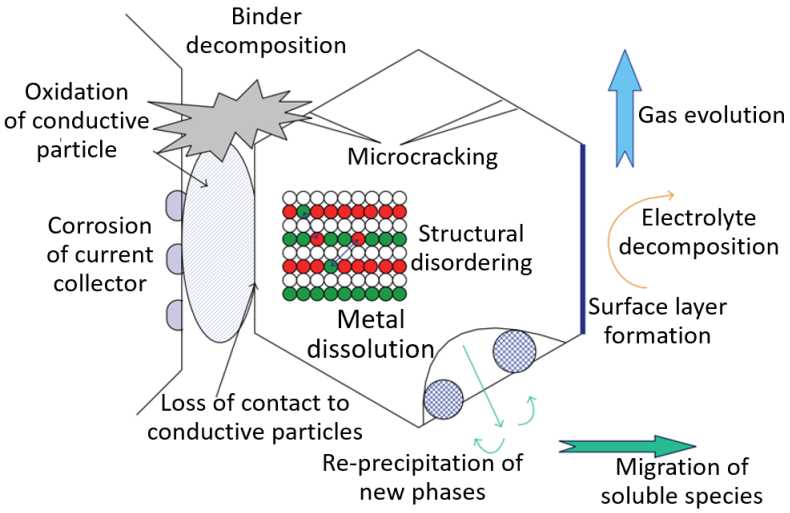

Figure 2.3: Schematic diagram of the aging mechanisms of cathode materials [10]

2.3 Factors Influencing Battery Aging

The lifetime of the battery can be predicted with the knowledge of complex aging processes and many factors that determine the nature of battery aging. These factors can be classified as stress factors, which are derived from different operating conditions of the battery, such as temperature, operating voltage, applied current, duration of operation, and so on. In addition to these stress factor, several microscopic parameters, such as material structure, equilibrium potential, reaction rates, and so on, and some macroscopic parameters, such as cell size and cell design also influence battery aging. This section describes these factors and their effects on the lifetime of the battery.

2.3.1 Operational Factors

Temperature

The temperature has both, positive and negative effects on the cell performance. Temperature accelerates the rate of chemical reaction in the cell, which results in increased cell capacity and decreased cell impedance. But, as the rate of chemical reaction increases, the parasitic/side-reaction rate also increases exposure to temperature for a long time has an adverse effect on the cell performance. The cell ages at a faster rate when subjected to a high temperature and long exposure time due to increase in the internal resistance and reduction in cell capacity. The temperature dependency of a chemical reaction can be described by the Arrhenius equation Eqn. (2.1).

$$Q_{loss} = k_0 \cdot exp\left(\frac{-E_a}{RT}\right) \tag{2.1}$$

As a rule of thumb, every 10°C increase in temperature nearly doubles the rate of reactions, including side reactions and hence aging [55]. The cells stored at elevated temperatures, show increased internal impedance and capacity fade. These characteristics can be observed by conducting a discharge capacity test of the cell. The test results show a decrease in the discharge time and high voltage polarization, (Fig. 5.34) which corresponds with loss of cell capacity and increase in its impedance. Electrochemical impedance spectroscopy (EIS) of a 75 Ah cell during the same aging interval is shown in Fig. 2.4. The impedance spectroscopy consists of several impedances, such as high frequency ohmic resistance, semi-circular high-frequency SEI film resistance, semi-circular low-frequency charge transfer resistance, and a semi-infinite diffusion Warburg impedance. During high temperature storage, changes in the anode resistance are smaller compared to the cathode. In the anode, the resistance largely changes due to surface film and charge transfer. Partial decomposition of electrolyte thickens the SEI layer and impedes the movement of Li^+ during intercalation and deintercalation process. The growth of the film layer is accelerated at high temperatures [10, 11, 46]. In the cathode, the resistance change patterns are different compared to the anode. The increase in film resistance is contributed by the formation of the SEI layer; unlike the anode, the major contribution to cathode impedance is charge transfer resistance, which increases significantly as the temperature increases. Charge transfer resistance is strongly dependent on the surface properties of the cathode [9, 56, 57]. Therefore, increase in the charge transfer resistance means structural deterioration of the cathode, which leads to the blocking of the intercalation and deintercalation of Li^+. Since the cathode impedance primarily contributes to cell impedance, the change in the diffusion impedance also has an impact on high temperature storage, because it reduces the diffusion path in the cathode surface. High temperature cycling also has a similar effect compared to storage aging. It has been found that cycling at an elevated temperature increases the impedance of the anode at a faster rate compared to the cathode. Under normal conditions, cycling at room temperature increases the SEI layer thickness at a constant rate, and thus the increase in impedance of the anode is lower compared to the cathode. Elevated temperature increases the rate of growth of SEI thickness, and hence increases the anode resistance [58–60]. Therefore, an increase in the anode electrode impedance, compounded with loss of primary and secondary active material, explains the high capacity fade for the cells cycled at an elevated temperature. Aging rates increase with decrease in temperature during cycling below 25°C. The predominant aging mechanism is plating of lithium metal on the anode surface and formation of dendrites [61]. Subsequently, a part of the deposited lithium reacts with the electrolyte, leading to the loss of cyclable Li^+. Hence, the optimal operating temperature during cycling is between 25°C and 35°C.

Time

Time determines the length of calendar life of the cell. The reaction kinetics in the cell are assumed to be limited by the rate at which SEI layer conductivity occurs during storage and cycling conditions. The layer conductivity of the SEI depends on its thickness, that is, smaller thickness results in larger ionic conductivity, and vice versa. The consumption of Li^+ during the formation of the SEI is higher, and it gradually reduces as the layer stabilizes because it acts as a protective film to prevent further side reactions at the interface. The consumption of Li^+ over time has a square root of time ($\sqrt{t}$) relationship [62–64]. It is directly related to impedance rise and capacity fade, hence these parameters can be modelled with a $\sqrt{t}$ function.

Voltage

An increase or decrease in the cell voltage also has effects on the rate of capacity fade and impedance rise. These parameters increase with high voltage or high SOC. The side reactions are at their peak at

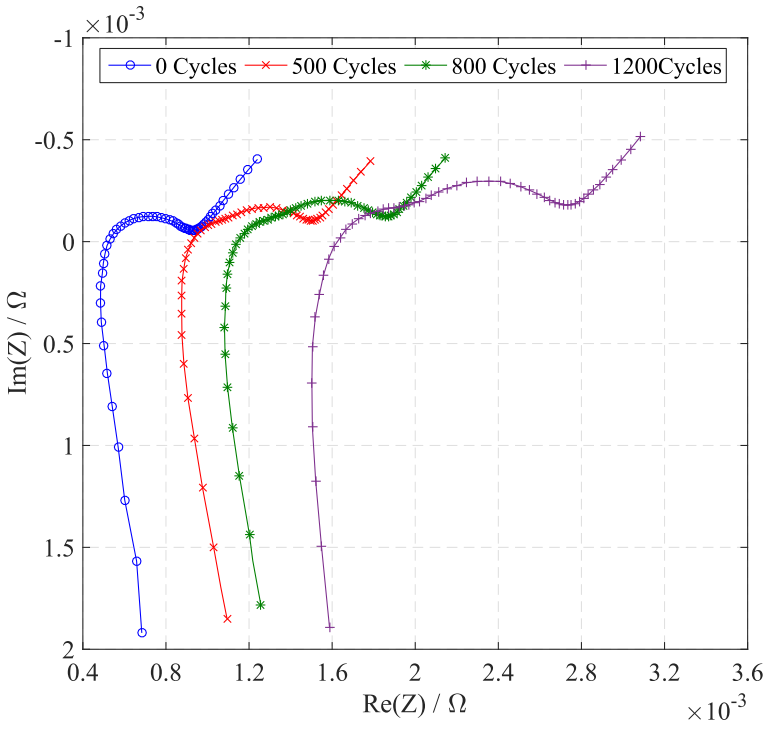

Figure 2.4: Nyquist plot of a 75 Ah cell at different aging intervals

high SOC, thus, the loss of active Li^+ has a direct relation with the over-potential of the side reactions on the anode surface. This phenomenon can be observed in cells stored at the same temperature but at different SOC levels. The cells stored at 100% SOC have maximum self-discharge compared to lower SOC levels. The cells cycled at the same partial SOC (ΔSOC), but at different end-of-charge voltage (EOCV), have effects similar to calendar aging, that is, cells operating at higher voltage will have faster capacity fade and impedance rise [65–67]. The side reaction rate at the anode surface is given by Tafel's relation as show in Eqn. (2.2). It indicates that an increase in over potential increases the exchange current density of the side reaction, which contribute to capacity fade and impedance rise. It can also be noted that this equation also has a temperature dependency, therefore over potential has increased effect at high temperature.

$$J_s^{Li} = nFk \cdot exp\left(\frac{\pm\alpha nF}{RT} \cdot \Delta V\right) \tag{2.2}$$

Where J_s^{Li} is the current density of side reaction, F is the Faraday constant, α is the charge transfer coefficient, ΔV is the over potential, R is the universal gas constant, T is the absolute temperature.

Cycles

The number of charge and discharge cycles influences capacity and impedance of the cell. When the cycle number increases, the electrode material undergoes structural changes due to volume expansion and contraction, and also undergoes phase transition during this process. Due to repeated cycling, the electrode material experiences variable stress and leads to material degradation. Besides these activities the side reactions in the cell increase and lead to formation and growth of SEI layer, which increases the cell impedance and capacity fade. The evolution of capacity fade over cycle number

shows para linear behaviour ($\sqrt{\mathrm{N}}$ dependency) in the initial cycles, followed by a gradual change to linear behaviour (N dependency) at the latter cycles.

$$Q_{loss} = k_0\sqrt{N} + k_1 N + k_2 \tag{2.3}$$

Δ SOC

ΔSOC, also known as partial SOC cycling, also has an influence on the cycle life of the cell. ΔSOC means the battery is not fully charged nor fully discharged, but the SOC is maintained at a certain level [68]. This cycling regime is practiced in off-grid energy storage or HEV application. For the same ΔSOC value, the average SOC can vary, that is, a change in SOC from 10% to 30% has the same ΔSOC as a change of SOC from 50% to 70%, but at different SOC levels. This factor has a significant impact on the long-term cycle life of the battery. Several experimental results show a decrease in battery life if the Δ SOC is higher, that is, 40% ΔSOC will have an extended battery life compared to 60% ΔSOC for the same cycle number. The half-cell study explains that cells cycled with higher ΔSOC show a sharp increase in the anode potential near the end of discharge state, that is, it mainly results in more mechanical stress on the anode surface and causes SEI cracking. It leads to damage of the SEI layers, and additional active Li^+ are consumed by the reformation and the growth of SEI film [63, 69, 70]. A higher ΔSOC value increases the duration of the side reaction, as shown in Eqn. (2.4), where the time interval of the integral function indicates the duration of exposure to side reactions, $\mathrm{J_s^{Li}}$ indicates the current density of the side reaction, and $\mathrm{S_n}$ is the active surface area.

$$Q_{loss} = \int_{t=t_0}^{t=t_s} J_s^{Li} S_n \, dt \tag{2.4}$$

C-rate

Long-term exposure to high discharge rates accelerates the cell aging process. It is typically characterized by an increase in the cell impedance, which shortens the time for it to reach the cut-off voltage. Hence, the performance of the battery at high discharge rates is hampered by the increase in the cell over-potential thereby causing capacity fade. The anode degrades at a faster rate compared to the cathode because of intercalation and thermal stresses. During cycling at high discharge rates, the heat generation rate increases due to the Joule heating effect. Additionally, the internal pressure increases due to the release of gases during cycling at a high discharge current. The heat generated cannot be easily dissipated out of the cell. As a result of this, the reduction rate at the anode surface will proceed at a faster rate, and more gaseous products will form to increase the internal pressure. The build-up of pressure and evaporation of electrolyte at a high temperature might easily stretch and damage the parts of the surface film. In the process, active Li^+ and electrolyte reacts with lithiated carbon particles, causing damage to the anode electrode. The product of these side reactions forms new SEI layers, and the layer grows and becomes thicker over many cycles. This increases the surface film resistance and the resistance of the anode material. The side reactions continue to protect the SEI layer from cracks due to the high temperature as a result of the high discharge current. The overall process leads to faster degradation of the cell at high discharge rates.

Table 2.1: Stress factors and their influence of the lithium-ion battery aging mechanism

Stress Factor	Aging Mechanism	Causes and Effects	Mathematical Fomulation	Ref.
Temperature	Cathode degardation	Structural degradation during storage	Eqn. (2.1)	[57]
		Dissolution of transition metal oxide		[58]
		Increase in charge transfer resistance		[46]
	SEI layer	Formation and growth of SEI layer		[71]
		Change in morphology and chemical composition		[10]
		Dissolution, reformation of SEI, increase in over-potential		[62]
	Anode degradation	Unstable SEI exposes anode to side reaction		[59]
		Surface area reduction due to SEI penetration into pores		[11]
		Decomposition and reaction with Li^+ to form SEI		[72]
	Electrolyte decomposition	Increase in cell impedance		[63]
		Electrolyte evaporation at a high temperature		
	Surface reaction at anode	High SOC increases side reactions at the anode surface		[65, 66]
	Active Li^+ loss	Accelerates the rate of SEI growth		[66, 72, 73]
Voltage/SOC	Electrolyte decomposition	Accelerates the rate of SEI growth	Eqn. (2.2)	[10, 62]
		Unstable electrolytes when operated at high voltage		[74]
		Over-potential increases loss of Li^+		[71, 75]
	Loss of active Li^+,	Formed SEI layer restricts ionic conductivity		[46, 56]
Time	SEI formation	SEI continuous to grow over time, reduces side reaction	$\sqrt{t}$	[10, 62]
	Electrolyte decomposition	Capacity fade and impedance rise are proportional to Li^+ loss		[64, 71, 72]
	Loss of active Li^+	Increases side reaction due to over-potential for longer duration		[60, 75]
ΔSOC	Side reactions	Loss of active Li^+ is directly proportional to exposure time	Eqn. (2.4)	[63, 69, 70]
	Structural change due to volume expansion	Volume expansion induces mechanical stress and causes structural damage to the anode		[10] [40]
Cycles	Side reactions	Anode degradation can also occur because of side reactions	Eqn. (2.3)	[47]
	Phase transition and metal oxide dissolution	Destabilization of the cathode structure initiates further side reactions		[64] [1, 62]
		Internal impedance increases due to limitation of diffusion		[76]
Discharge Rate	Anode degradation	SEI breakdown and reformation due to a high temperature		[64]
	Electrolyte decomposition	Anode stability is affected by side reactions and high pressure		[69, 74]
	Interfacial resistance	Internal resistance increases by slow diffusion limited by reaction kinetics		[76, 77]
Charge Rate	Side reactions	High charge rate causes lithium plating and dendrites growth		[78, 79]

During the charge phase, the over-potential of the cell is higher at a high C-rate. This leads to a shortened time in the constant current (CC) and a longer time in the constant voltage (CV) phases. The entire process accelerates electrolyte decomposition supported by a high temperature as a result of a high current. At a high C-rate, the reaction kinetics are limited by slow diffusion of Li^+. Instead of intercalating into the anode electrode, the migrated Li^+ are reduced to lithium metal, and the process is called lithium plating. Besides a high-charge C-rate, low temperature also supports lithium plating. As the process of lithium plating continues, the deposited lithium metal grows and form dendrites, hence accelerating the aging process.

2.3.2 Cell Chemistry

The choice of the cell chemistry plays a major role in determining the cell performance, lifetime, and safety of the battery. The electrolyte material used in lithium-ion batteries are Li-salts and organic solvents, the most common Li-salt being $LiPF_6$, which has low electrical resistance, and the solvents are polycarbonates. They are ionic-conductive and electronic-non-conductive liquid solutions, which act as a medium to transport the Li^+ between the cathode and anode. Another electrolyte material is a solid electrolyte, and it finds application in solid-state batteries. The choice of anode material is fairly simple, as the commercially available lithium-ion cells use graphite as anode materials. Besides

LTO anodes, more recently, silicon-based anode materials are also being synthesized, which exhibits a theoretical capacity of up to 4200 mAh g^{-1} in comparison to 372 mAh g^{-1} for graphite-based anode materials [80]. However, pure silicon-based material cannot be applied to commercially available cells due to structural weakness and dramatic volume changes during cycling. Consumer 18650 cells with C-Si composite anodes are, however, already commercially available from Panasonic, LG, and Samsung.

The cathode materials for lithium-ion batteries can be classified based on their compound structure as layered oxide, spinel, and olivine structure, as shown in Fig. 2.5. The blue colour indicates the structure of the host lattice, and the red dots indicate the occupation of Li^+ in the host lattice. In the layered oxide structure, the most commonly used materials are LCO, NMC, and NCA. While LCO is not as stable compared to other layered-based cathodes, it undergoes performance degradation at high voltage. The increase in charge voltage increases the cell capacity, but it leads to rapid capacity loss after subsequent recharges. The main reason for this performance loss is due to the dissolution of cobalt in the electrolyte, which results in less Li^+ reintercalation in the discharge phase. Structural modification due to less lithium content and the CoO_2 layer formed after the delithiation cut into the electrode surface, which can lead to stress and micro-cracking of the cathode particles [81]. In the NCA structure, during the charge phase, the delithiated layers lead to migration of nickel cations into the lithium planes and hamper the process of lithiation and delithiation. Another approach to the mixing of $LiNiO_2$ and $LiMn_2O_4$ leads to good cycle life performance and stability at high temperatures. The dissolution of the metal oxide is reported to be quite low. However, a large amount of non-removable Ni in the Li layers blocks the diffusion of Li^+, hence reducing its rate capability [82]. An addition of Co ions to the existing structure reduces the occupation of Ni in the Li layers, and hence NMC composition is regarded as a stable structure during the lithiation and delithiation process. It improves the cycle life performance of the cell, especially with low Co content [2]. In summary, layered oxide chemistries deliver a high capacity due to their high operating voltage, hence they have good energy density. However, in practical applications, the reversible capacity is limited by structural instability at low concentrations and high voltage. The rate capability is still low due to the slow diffusion process.

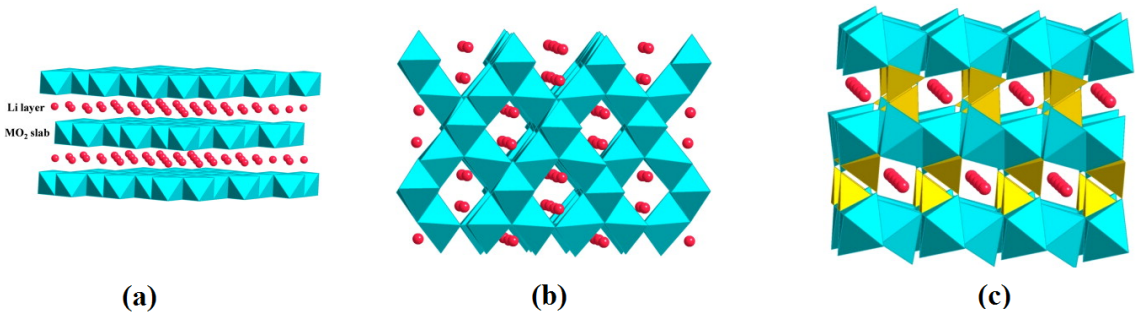

Figure 2.5: Crystaline Structures of different cathode materials (a) Layered Oxide, (b) Spinel, and (c) Olivine [83]

The spinel structure in LMO is another promising cathode material, in which Mn occupies the octahedral sites, while Li^+ occupies the tetrahedral sites. This structure is based on a 3D network where the intercalation and deintercalation of Li^+ are faster compared to the layered oxide materials, while the latter permits only 2D transport of ions. However, this material is found to encounter severe capacity fade, which occurs both at low and high SOC. At low potentials, LMO can insert additional Li, and a Mn^{3+} Jahn-Teller distorted tetragonal phase is formed. Low potentials also lead to a decomposition

reaction and dissolution of Mn^{2+} in the electrolyte. At higher potentials, Mn dissolution is evolved by a chemical delithiated reaction with hydrofluoric acid (HF). Mn dissolution leads to loss of cyclable Li^+, and dissolved manganese ions migrate to the negative electrode and incorporate into the SEI. This leads to electrolyte decomposition and increases self-discharge of the lithiated anode. Partial substitution of manganese ions by trivalent or divalent cations like Cr, Co, Al, and Mg and partial substitution of manganese by excess lithium can improve capacity retention. Acid dissolution can be minimized by HF free-conducting salts [83].

The LFP chemistry has an olivine structure, and it is considered a promising battery material for HEVs. Despite low material cost and abundance compared to other cathode materials, the drawbacks mainly come from low operating voltage, poor electronic conductivity, and low ionic diffusivity. Several improvements have been made to conductivity and diffusivity by carbon coating and reducing particle size, respectively. For LFP cathodes, long cycle lives have been achieved through various laboratory tests. The possible aging mechanism of LFP/Graphite cells that contributes to capacity fade are loss of cyclable Li^+ or Li inventory, active material degradation due to cracking and dissolution, impedance rise due to SEI layer formation, and physical degradation of electrodes [40, 47]. Iron precipitates are observed on the surface of the anode and separator. The dissolution of iron has multiple effects, such as catalyzing the formation of the SEI layer and thereby reducing the Li inventory and impedance rise. The dissolution rate of iron depends on many factors, such as high temperature, cut-off voltage, impurities, and so on. The capacity retention can also be improved by coating the graphite anode or LFP particles with polymer or oxide films to retard the iron dissolution and deposition [84].

2.3.3 Cell Size and Design

Lithium-ion batteries have undergone several changes in cell design since their inception, to meet the demands of the EVs and HEVs. Different geometries have been designed to meet higher gravimetric and volumetric energy density, minimize packing space, reduce manufacturing cost, and so on. There are various geometries in lithium-ion batteries, of which planner, spirally wound, and prismatic wound designs are being used. Fig. 2.6 illustrates the designs of commonly used geometries. The spirally wound design is used in cylindrical cells, which consists of a positive current collector, a negative current collector, a separator, a positive and negative active materials stacked together and rolled in the form of a jelly roll. These colours indicate the positive electrode, separator, negative electrode, and separator. The planar design looks like sheets of paper stacked upon one another, where each sheet can be viewed as an electrochemical cell. This design is used in pouch cells. The prismatic design is a hybrid version of the spiral and planar designs, which is wound around a rectangular centre. It has both flat and spiral portions [85]. Spiral designs are easier to assemble, and their manufacturing cost is quite low. But they offer poor volumetric space, which is a major drawback for the construction of battery packs for EVs and HEVs. The planar design offers very good volumetric space, but it is time-consuming and costly to assemble. The prismatic design provides a trade-off between better volumetric space utilization and low cost of assembly, similarly to the spiral design.

Upscaling to large-format cells does not have an influence at the microscopic level. However, at the macroscopic level, it has a significant influence on the performance and lifetime of the cell. As described in section 1.2, a large-format cell reduces the total surface-area-to-volume ratio, which results in lower heat dissipation than the amount of heat generated in the cell. This causes significant internal heating of the cell, which is strongly influenced by the ambient temperature and C-rate. As a result,

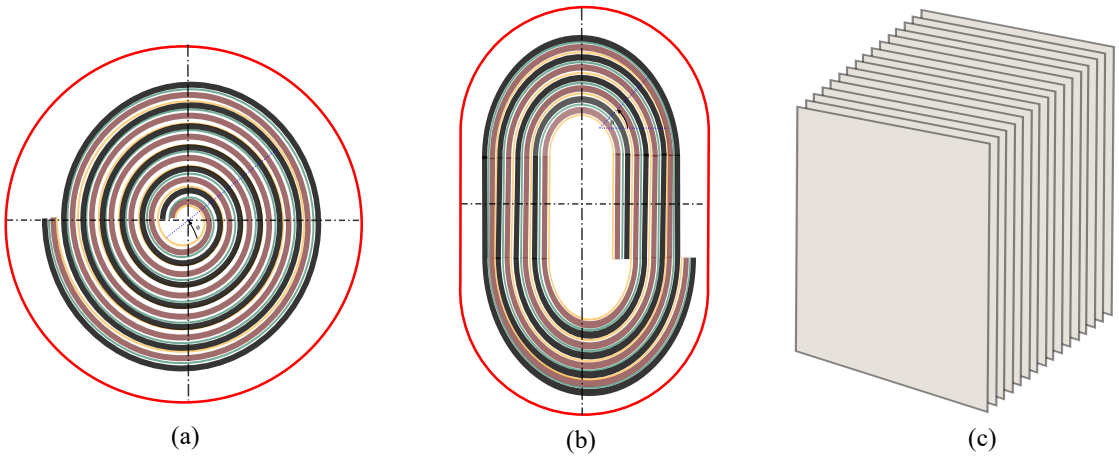

Figure 2.6: Different cell geometric designs; (a) Spirally wound (b) Prismatic wound (c) Planar [85]

inhomogeneous distribution of temperature occurs and leads to internal current and SOC imbalance, causing localized degradation. Certain design parameters have greater influence on heat generation and distribution in the cell, such as temperature and current inhomogeneity. These design parameters listed below have been known to influence the microscopic electrochemical processes and degradation mechanism, which affect the performance and lifetime of the cell:

- Cell aspect ratio
- Tab size and location
- Current-collector thickness
- Multi-tab configuration
- External heat transfer

The aspect ratio in a cylindrical cell is the ratio of diameter to its height. By changing the aspect ratio, different cylindrical geometry can be designed, as shown in Fig. 2.7. Tall height or large diameter increases the path of current flow[1] in the cell. Eqn. (2.5) shows, that an increase in the length of the current flow (l) in the foil can increase the power loss, thereby reducing the battery power capability. This can be overcome by adding multiple tabs to the current-collector foil to effectively reduce the length of current flow path. However, the most critical disadvantage of a thicker cell is the bad heat transport in the radial direction, especially if the height of the cell is not low. Kim et al. [86] showed that cylindrical cells with a tall height have low power capability compared to a normal height and large diameter. Tall height has the greatest temperature rise due to lower heat rejection, as most of the heat is trapped in the cell core.

$$P_{loss,foil} = \frac{\rho_{foil} \cdot l \cdot I^2}{\delta \cdot W} \tag{2.5}$$

[1] assuming only part of the foil is in contact with the terminal

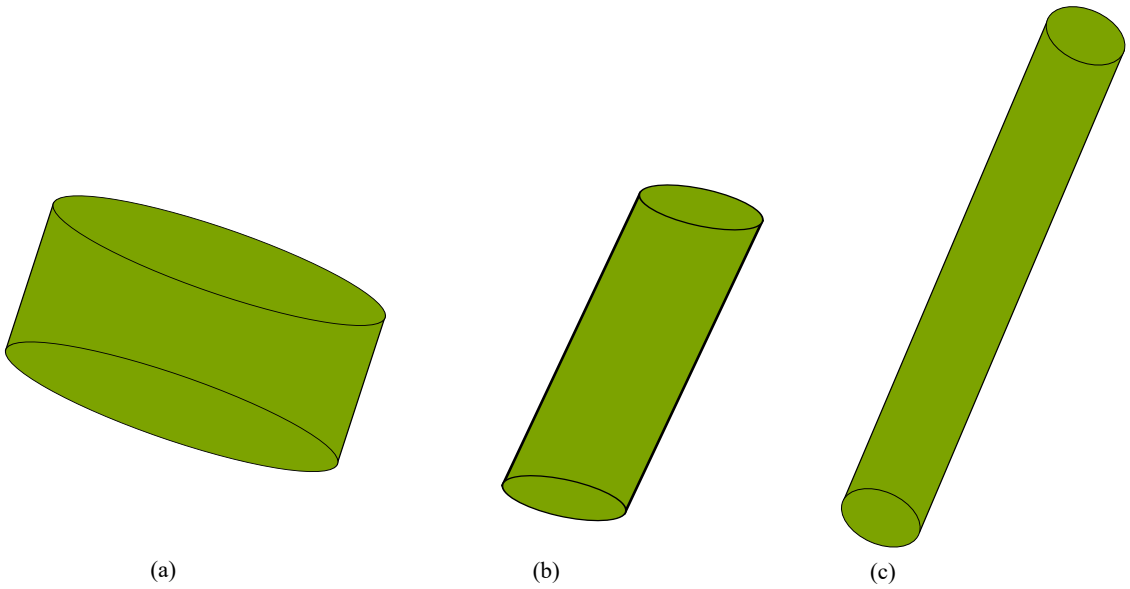

Figure 2.7: Cylindrical cells with different aspect ratio; (a) Large diameter , (b) Nominal, (c) Tall height [86]

In pouch cells, different designs can be achieved by varying the aspect ratio, changing tab location, using a different tab size, and so on. Aspect ratio is defined as the ratio of length to width. The cell stack area can be effectively increased by increasing the width or length. In normal tab design (NT), the tabs are located adjacently, whereas, in counter tab design (CT), they are located on the opposite faces of geometry. Tab size can be made smaller, and these designs are called small tab design (ST); in addition to these, the aspect ratio of the electrode can be changed to obtain wide stack design (WS) and long stack design (LS). The performance of the cell varies for each design, depending on the current flow path, heat generation rate, and heat dissipation rate. Tab. 2.2 shows the comparison of different cell design on the performance of pouch cells.

Electric current in current-collect foil converges and diverges near the cell tabs during the charge and discharge process. The convergence and divergence of current flow in a current-collector foil represents electrical constriction (R_C) and spreading resistance (R_S) respectively. The bulk resistance (R_B) is the resistance of the current-collector. The sum of this resistance together with electrochemical resistance contributes to the internal resistance of the cell [21], as shown in Fig. 2.8. The resistances R_C and R_S contribute more to potential drop compared to R_B, which causes larger local deviation of electrochemical and thermal equilibrium near the tabs, as described in section 1.2. As a result, active material near the tab vicinity charges and discharges at a faster rate. A high resistance value contributes to heat generation in the cell and increases localized electrochemical reaction. Additionally, a high C-rate enhances local transfer reaction. All these factors contribute to non-uniform charge/discharge reaction, temperature, and current density distribution along the in-plane direction.

Increasing tab size and reducing tab eccentricity also decreases the in-plane temperature inhomogeneity. Tab eccentricity can be reduced by placing tabs at the centre along the length direction. Positioning the tab on either side of the centre increases eccentricity, and, as a result, constriction and spreading resistance increases. This is the main reason why ND, ST, and WS introduce greater inhomogeneity, as there is no option in design to use the centric tab position, because both positive and negative tabs are positioned along the same side. Therefore, CT design, with its inherent low tab eccentricity, offers

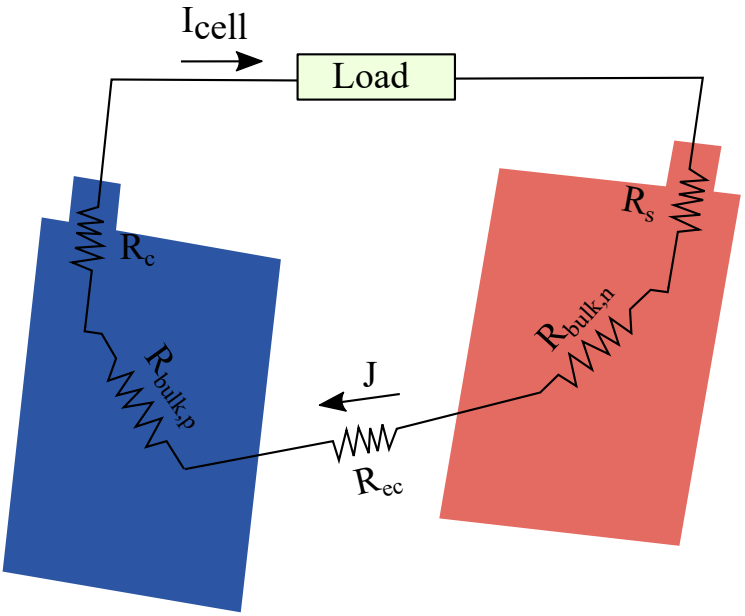

Figure 2.8: Schematic representation of constriction, spreading, and bulb resistances in the cell [21]

a better in-plane temperature, current density, and potential distribution in the cell [88].

Cylindrical cells do not have the benefit of positioning tabs to reduce inhomogeneity. This limitation can be overcome by introducing multiple tabs in parallel, which results in better distribution of incoming/outgoing current. In a normal cylindrical cell design, a pair of long and continuous current collectors is attached to the electrode layers, which delivers an electrical current to the external circuit through an extension of a small portion of the current collector (discrete tab). As the electric current converges, there is a large potential change near the tabs compared to other locations. The ideal way to minimize this potential change is to extend the entire current collectors (continuous tab), where every single point acts as a tab. However, this is difficult to achieve; instead, multiple discrete tabs can help to reduce the inhomogeneity. Fig. 2.9 shows the temperature contour simulation of wound cylindrical cell and its unwound section during a 5 min discharge at 4C current for a 20 Ah cell of different tab designs. It is apparent that increasing the number of tabs greatly reduces temperature inhomogeneity. It is also revealed that poor electrical and thermal conduction in a large-format cell could lead to non-uniform utilization of the cell. It also shows the significance of these macroscopic parameters and how the inhomogeneity is influenced by the cell design [89].

The electric and thermal properties of the current collector pairs are critical to temperature and current density distribution in the cell. Since copper material has higher electrical and thermal conductivity compared to aluminium, temperature and current density distribution can be more uniform in these materials inside the cell. To negate this imbalance, the aluminium current collector foils are thicker than copper foils, in order to have similar heat generation and heat transport in both foils. Increasing the thickness of the copper and aluminium foils decreases ohmic resistance, which is primarily dominated by constriction/spreading resistance and bulk resistance of the current collector [21].

Table 2.2: Different cell designs in pouch cells and how it affects the cell performance [22, 87]

Cell Design	Causes and Effects	Inhomomgeneity
NT	Potential drop near cell tabs due to concentrated electric and thermal paths near the tabs. Average temperature is similar to CT and ST.	Current density, SOC, and temperature inhomogeneities are similar to ST but greater than CT.
CT	Uniform potential drop due to better distribution of electric and thermal paths. Average temperature is similar to NT and ST.	Better temperature, current density, and SOC distribution among all designs. Performance and lifetime can be improved by this design.
ST	Potential drop due to small tabs, as electric and thermal paths are highly concentrated near the tabs. Average temperature is similar to CT and ST.	Current density, SOC, and temperature inhomogeneities are similar to NT but greater than CT.
WS	Highest potential gradient due to wider stack area non-uniform potential drop across the in plane. Average temperature is lower due to a better heat rejection rate.	Current density, SOC, and temperature inhomogeneities are worse than CT, NT, and ST.

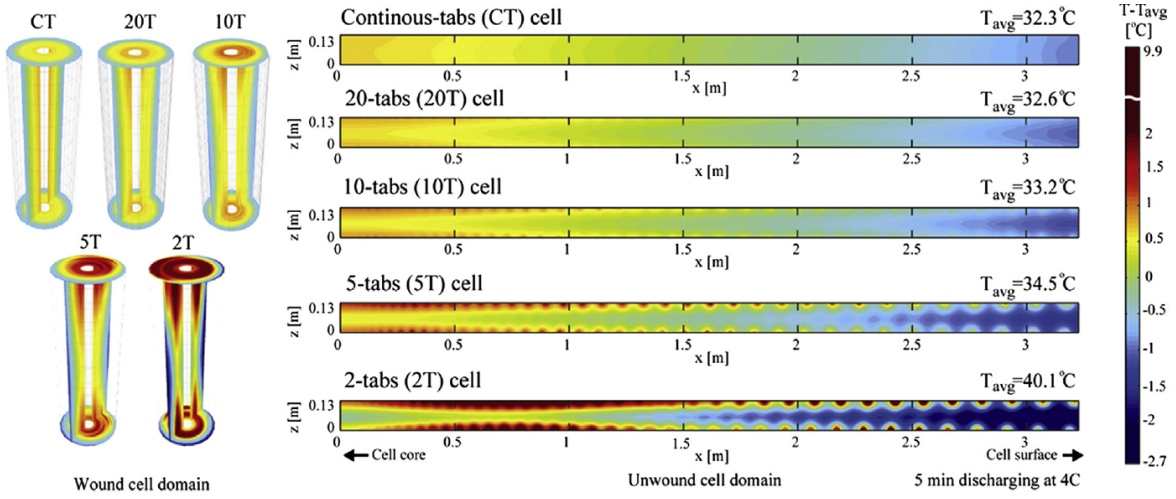

Figure 2.9: Temperature contours in the wound view (left) and unwound view (right) of the five different cell designs investigated at 5 min after the start of 80 A (4C) constant current discharge [89]

2.4 Inhomogeneities in Large-format Cells

2.4.1 Current Density Distribution

Current density is one of the main parameters that needs to be considered in the macroscopic design of large-format cells. It is the measure of electric current flowing per unit area of the cross section. There have been several methods for evaluating current density distribution through unique measurement techniques. These methods are described in section 3.1. This parameter is important for the electrical and thermal design of a cell. The cell performance strongly depends on distribution of current density during a charge/discharge process. Uneven current density distribution has an adverse effect on the performance and lifetime of the cell. The regions with higher current density experience a higher magnitude of current flow, which leads to a loss of power in the form of heat. This increases the local temperature of active material and creates interdependent effect between temperature and current density. At the first instance, the increase in local temperature reduces the local internal impedance of the cell, which further causes the current density to increase. This process continues as local current density and temperature increase as a function of time. As a consequence of these effects, the active

materials are either over-utilized or under-utilized at localized spots, depending on the active material's temperature and current density distribution. Therefore, local SOC distribution also changes. It is difficult to come to a conclusion about what the cause (temperature/current) is and what its effects (temperature/current/SOC distribution) are.

Cell macroscopic design has a critical impact on current density distribution, which has already been described in section 2.3.3, especially the electric current paths in the vicinity of the cell tabs. There is a concentration of current flux at the beginning of discharge, mainly caused by cell design, which creates uneven current density distribution along the in-plane of the electrode. This results in high heat generation and over-utilization of the active material. As the discharge process continues, the current density redistributes due to non-uniform utilization of active materials across the plane. The currents follow the the path of least resistance[2], because the transverse current density caused by Li^+ transport is normal to the plane of the electrode. This finally leads to reversal of the current distribution pattern towards the EOD [25].

The C-rate also influences the current density distribution in the cell. At a low C-rate, the discharge current is low; therefore, power loss due to heat dissipation is also low. This leads to lower deviation of cell temperature from ambient conditions. As cell impedance is sensitive to temperature, the spatial distribution of impedance is more uniform, hence the current density distribution is homogeneous at low C-rates. In contrast, high C-rates have significant Joule heating loss due to higher over-potential, and the temperature distribution is highly heterogeneous, which again leads to non-uniform spatial distribution of impedance. Therefore, it can be concluded that low C-rates have more uniform current distribution compared to high C-rates.

2.4.2 Temperature Distribution

The temperature distribution in a cell is contributed by several factors, including cell design parameters (described in section 2.3.3) and the source of heat generation, and heat dissipation. Additionally, cooling strategies employed on a cell also determine the temperature distribution during a charge/discharge process. The amount of heat generation in a cell depends on its total volume, and heat dissipation is influenced by the total surface area of the cell. As the cell size increases, the surface-area-to-volume ratio decreases, thereby increasing the overall cell temperature [86]. Therefore, the thermal management becomes challenging, and additional cooling methods should be employed to remove excess heat generated in the cell. Hence, different strategies should be used to meet the cooling requirements, as the amount of heat generated to heat dissipation ratio determines the overall temperature of the cell. Fig. 2.10 shows the graphical representation of inhomogeneity as a function of cell size.

Heat generation in the cell has two sources: Joule heating and entropic heating. A cell internal resistance is the main contributor to Joule heat or irreversible heat. It is called irreversible heat because, irrespective of the direction of current flow in the cell, the process is always exothermic, whereas the entropic heat, a thermodynamic phenomenon that is related to the temperature coefficient of the OCV, also accounts for the heat generation in the cell. However, the entropic heat is reversible and depends on the direction of the current flow; hence, it is also called reversible heat. The contribution of entropic heat is dominantly endothermic during charge and exothermic during discharge [90] for most lithium-ion chemistries. Therefore, the amount of heat generated in the lithium-ion cells during the discharge process is always greater than in the charge process in case of identical currents. The contribution

[2]Current in a parallel network always follows path of least resistance

of entropic heat and Joule heat to the total heat generation is different at different C-rates and at different SOCs. At low C-rates, entropic heat generation is more dominant, and, at a high C-rate, it can be neglected. Heat generation towards the EOD is mainly contributed by an entropic coefficient, and it is higher at low SOCs.

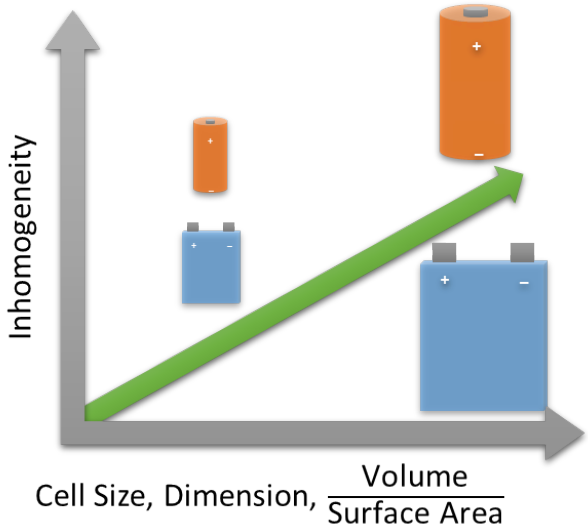

Figure 2.10: Graphical representation of inhomogeneity as a function of cell size [86]

The thermal properties of the battery material determine the temperature evolution and its distribution throughout the volume. Some thermal parameters, such as specific heat capacity (C_p), thermal conductivity (λ), material density (ρ), and electrical conductivity (σ), influence the temperature profile, along with the macroscopic cell design. The C_p and λ values affect the maximum temperature and temperature distribution in the cell, which are largely determined by the battery material composition. The temperature at the positive tab increases faster compared to other locations in the battery, which is due to larger electrical resistivity and the contact resistance to the external circuit. However, the negative tab's temperature is lower compared to the positive tab, as the electrical conductivity of copper is better than that of aluminium. In general, the area near the tabs remains at a higher temperature compared to other locations, due to higher current density, which generates more heat in this region. However, other locations far way from the tabs also experience a higher temperature due to the redistribution of current density [32].

Ambient temperature also influences the temperature distribution in the cell. The cell internal resistance is very sensitive to temperature, especially at low temperatures. A small change in the temperature can increase or decrease the internal resistance, which determines the heat generation in the cell. However, at a high ambient temperature, the internal resistance is very low and not so sensitive to the temperature changes. Therefore, at a low temperature, the combination of heat generation and temperature change creates a large temperature variation in the cell and increases the temperature inhomogeneity, and the effects are reversed at a high ambient temperature. The cell tab size and positions have effects on temperature distribution similar to that of current distribution. The primary effect of the tab configuration is on the current distribution, and the temperature distribution is the result of the current distribution, and not the other way around.

On the other hand, optimizing the cooling strategy for battery modules/packs used in EV for different charging currents will help to reduce the operating temperature and decrease inhomogeneity, and thus

improve the performance and lifetime of the battery [13, 15]. Different cooling strategies, such as free convection [13], contact heat sink, forced air circulation, and terminal cooling (on the tab surface), are being employed to study the effectiveness of these cooling strategies. The terminal cooling also depends on tab positioning, and whether it is ND or CT configuration. The cell temperature distribution is more uniform in natural convection because no cooling methods are employed. This is good for homogeneous temperature distribution, but the main disadvantage is a higher average temperature, which reduces the lifetime of cell. The cooling with contact heat sinks helps to reduce the average temperature of the cell significantly, but temperature inhomogeneity is very high. This has a long-term effect in the form of inhomogeneous aging within the cell, which effectively reduces the lifetime of the cell. Using adiabatic conditions (no heat exchange with the outside) as a cooling method leads to operating the cells in dangerous conditions, and the cell is more likely to go into a thermal runaway condition if the temperature rises at an uncontrollable rate. Air cooling with forced air convection is another cooling strategy that is being used in some battery-pack thermal management. It is cheaper than contact heat sinks, the principle being that cool air is made to flow from left and right on the larger surface of the pouch cell, where cool air absorbs heat from the cell surface and relatively hot air comes out of the outlet. This is not an effective solution, as the left half of the cell is relatively cooler than the right half, and it is also not effective for the cell, with cross tab configuration where hot spots are generated on both sides of the surface. The efficient means of cooling is via terminal cooling, where terminals can be connected to the cooling plates or any other passive heat sinks. This cooling strategy also depends on the configuration of cell tabs.

2.4.3 Voltage/SOC Distribution

The current distribution in the cell has a direct influence on the SOC or voltage distribution. The SOC is the integration of current over time, and non-uniform distribution of current can cause SOC inhomogeneity. The drop in SOC percentage is also an indication of reduction in OCV, terminal voltage, and the energy content of the cell, and vice versa when the SOC percentage increases. The SOC level indicates whether the local active material is over-utilized or under-utilized. Due to the cell design, the locations closer to the cell tab experience higher current density compared to the farthest location. As a result, there is lower SOC closer to the tabs during discharge. The non-uniform SOC distribution also changes the local impedance of the cell and influences the redistribution of current and heat generation at the later stage of discharge process. The redistribution of current occurs when there is a change in local impedance due to a change in SOC. This helps to slightly reduce the SOC imbalance within the cell, but not that much, as the over-utilized active material could enter into an over-discharge state or, in the least case, could reach the cut-off voltage sooner when a large part of the active material is still in an under-discharge state. This leads to non-uniform utilization of active materials, reducing the total energy throughput of the cell, and it is also likely to cause localized degradation and earlier EOL of the cell.

The non-uniform SOC distribution can be improved by using CT or multi-tab configuration [25, 87]. Increasing the number of tabs can definitely improve the current and SOC distribution, but having many tabs does not make any significant improvement in current distribution beyond a certain threshold. An increase in the C-rate also increases the SOC inhomogeneity, as described in section 2.4.1.

2.4.4 Aging Inhomogeneity

Many of the aging inhomogeneity studies have focused on battery modules and packs, as a lot of emphasis has been place on the cell-to-cell variation in battery systems. The causes of aging inhomogeneity in a battery-pack, due to the cell-to-cell variation, are nevertheless similar to what happens in a single cell, by taking into account of inhomogeneous distribution of temperature, current, and SOC, within the cell. At the module and pack level, in addition to the existing inhomogeneities, variation in cell-to-cell initial resistance and capacity, contact resistance between the cells in a module and the module-to-module connection in the battery pack at the beginning of life (BOL) of the cells also influence the variation in aging between many cells in a battery pack [8, 91].

As shown in Tab. 2.1, temperature, current, and SOC have major influence on battery lifetime. It is imperative to assume that cell inhomogeneity leads to aging inhomogeneity with long-term usage. On the one hand, a large ΔT accelerates the aging process at locations that experience high temperatures. On the other hand, a large SOC gradient caused by current density distribution leads to under-utilization or over-utilization of the cell's active material, depending on the location in the cell. Over-utilization of the active material on a certain location could lead to deep-discharge or over-charge if the cut-off voltage is not reached. If this process continues for many cycles, the regions of over-utilized active material undergo accelerated aging, and overall cell performance is determined by the regions of over-utilized active material [16].

It has been reported in some literature that inhomogeneous current density distribution on the anode surface results in the formation of small lithium deposits and dendrites, especially at a high C-rate supported by low temperature. This process is well known as lithium plating. During a high C-rate operation, the high current density induces stress and creates cracks in the SEI layer and exposes the anode surface to lithium plating, which will further increase the localized current distribution that accelerates the growth of dendrites. Hence, the detection of lithium plating is an indication of inhomogeneous aging in the cell [92, 93]. The occurrence of aging-induced lithium plating is also described as a source of nonlinear aging in the cell, because the plated lithium further restricts the ionic movement by reducing its conductivity to graphite. This further promotes SEI layer growth and lithium plating in a vicious cycle, thus accelerating the aging process [94]. Another method used to detect inhomogeneous aging includes in-situ neutron diffraction patterns of aged cells and thermal characterization to evaluate localized aging, which are discussed in section 2.1.

2.5 Influence of Aging on Safety

Safety is critical, especially for automotive applications, keeping in the mind that batteries should store more energy, deliver high power, and have a wide temperature range of operation. The electrochemical energy stored in a battery must not be released in an uncontrolled way under any operating or external conditions. Practically, it is impossible to achieve these criteria, and hence several safety tests, such as over-charge and over-discharge tests, short-circuit tests, thermal-abuse tests, and other mechanical abuse and environmental tests, are performed to ensure the safe operation limits of the battery. There are several factors that determine the safety of lithium-ion batteries.

- Cell chemistry: The choice of cell chemistry is vital to the safety and stability of a battery (section 2.3.2).

- Cell size and design: Safety is directly related to the size of the cell. Small-format cells contain less active material and, therefore, less energy, and they are safer than large-format cells of the same design and chemistry. Additionally, small cells have a higher surface area per unit volume, which results in more relative cooling in the case of overheating.
- External casing: This aspect should be considered, as the cells should be able to meet the mechanical and environmental conditions to which they will be exposed. High shock and vibration, temperature extremities, or other adverse conditions may be encountered during use and handling, and the cell and its mechanical integrity must be maintained. Cells should be hermetically sealed to contain the materials inside and to prevent them from leaking.
- Safety features: The safety features should be incorporated into the cell, taking into account accidental or unexpected handling procedures. Some examples of these features are pressure vents to prevent excessive internal cell pressure build-up, a current interrupting device (CID), a positive temperature coefficient (PTC) device, external protection circuitry, and so on, as shown in Fig. 2.11
- Heat exchange with surroundings: Adequate thermal management should be implemented such that there is a good rate of heat exchange between the cells and the external environment. The worst case scenario would be adiabatic conditions between the battery system and the surroundings, which increase the self-heating rate in the battery and lead to thermal runaway.
- BMS: External battery monitoring units that ensure the operation of the battery is well within the safety limits and prevent operation whenever the safety limits are about to be breached.

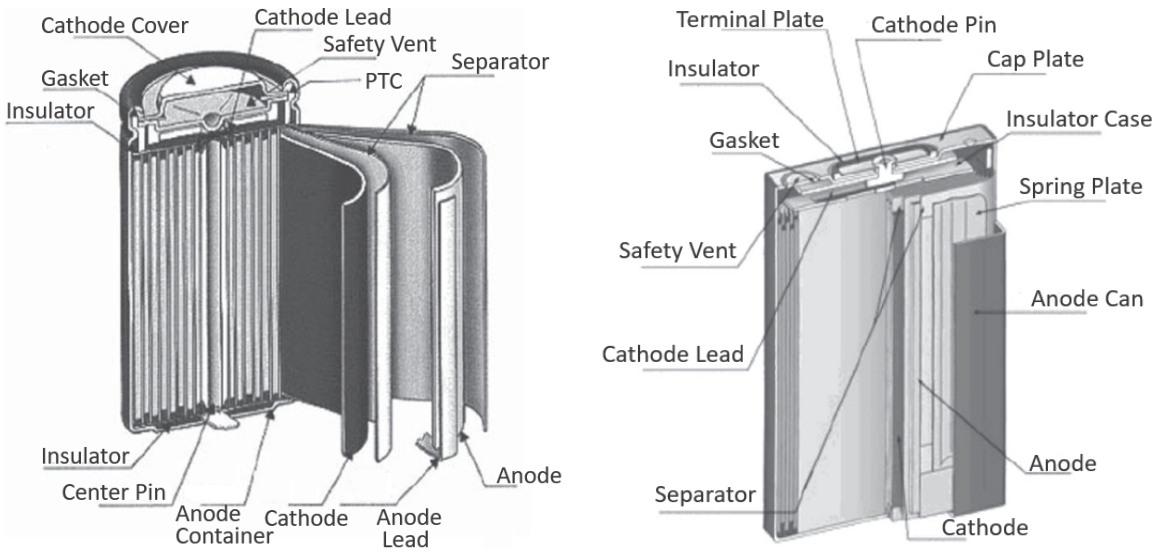

(a) Cylindrical cell

(b) Prismatic cell

Figure 2.11: A schematic of cell forms with safety features [95]

Internal short circuits leading to thermal runaway are the most catastrophic failures of lithium-ion batteries, and they are treated as safety hazards because of the large amount of energy released in a short period of time. Thermal runaway is related to the thermal stability of the components of the battery material, primarily dominated by choice of electrode material, in particular, cathode material composition. It is also influenced by the nature of the SEI layer, solvents, electrolyte, and so on. The

source of heat generation, exothermic reactions gradually increase the cell temperature. Above 80°C, the SEI layers become unstable and start its decomposition process between 90°C–120°C. Until this point is the first onset of thermal runaway; after this event, a chain of reaction proceeds: At first, an exothermic reaction occurs between intercalated lithium and electrolyte at temperatures above 120°C. The positive active material in the oxidized state decomposes at temperatures above 200°C, releasing oxygen and reacting with electrolyte in a highly exothermic reaction, which leads to the thermal runaway event with fire and may be even explosions (see Fig. 2.12).

As the chemical and thermal characteristics of the electrode material, separator, and electrolyte changes during the aging of the battery, aging process can also influence the thermal runaway profile at various stages of heat generation. There is a good literature database to describe the thermal stability of new cells, but it is equally important to ensure the safety of the battery during its entire lifetime. However, there has been evidence to suggest that the aging process improves the thermal stability of the cell based on the accelerating rate calorimeter (ARC) and differential rate calorimeter (DSC) measurements. The improved thermal stability of the cell can be ascribed to the following changes.

- Aged cells show a higher onset temperature and a reduced heating rate, which means thermal runaway is triggered at a higher temperature in comparison to fresh cells [96, 97].
- In high-temperature aging, pronounced SEI layer growth reduces the onset temperature, but it also significantly reduces the exothermic heat released because the aged anode contains less intercalated lithium, which could react with the electrolyte during the thermal runaway [98].
- In aged cells, less active material is left, as some portion of it is consumed during the side reaction. Therefore, impact of thermal runaway is not as severe as in new cells, where the abundance of active material can release more heat at the trigger point [99, 100].

However, on the other hand, aged cells pose more of a risk than a safety hazard due to excess self-heat generation during the normal operation. At high discharge and charge C-rates, the temperature rise is more in aged cells in comparison to fresh cells under similar operating conditions due to higher internal resistance developed during the aging process [102, 103]. Therefore, adequate safety thresholds must be adapted aside from improving the cooling medium for heat exchange between the cell and the surroundings, which could limit the rise in cell temperature. In the research of Wu et al. [104], it is reported that the thermal stability of electrode materials decreases with aging, in contrast to what has been explained by other sources. It also mentions that the breakdown of the SEI layer increases the exothermic heat generation as the cells age. Therefore, the safety mechanism, such as a separator shutdown, may not be useful for the aged cells due to reduced thermal stability. Even though the results are contrary to various sources, it is clear that improving the thermal stability of the battery materials can improve a battery's safety.

Moreover, all aging conditions do not improve the safety of the battery. Safety depends on the conditions in which the cells are handled, such as storage, cycling, temperature, and charge and discharge C-rate, that is their aging history. The cells cycled at low temperatures when subjected to ARC measurements show that the self-heating rate started at a lower temperature. This thermal behaviour is significantly different from that of the fresh cells. Around ∼180°C the self-heating rate in the cell increased to an uncontrollable level and resulted in thermal runaway. This shows the worsening in safety behaviour as the thermal runaway shifted to a lower temperature than usual in comparison to fresh cells. However, cycling at a high C-rate showed only marginal changes in the safety behaviour, an

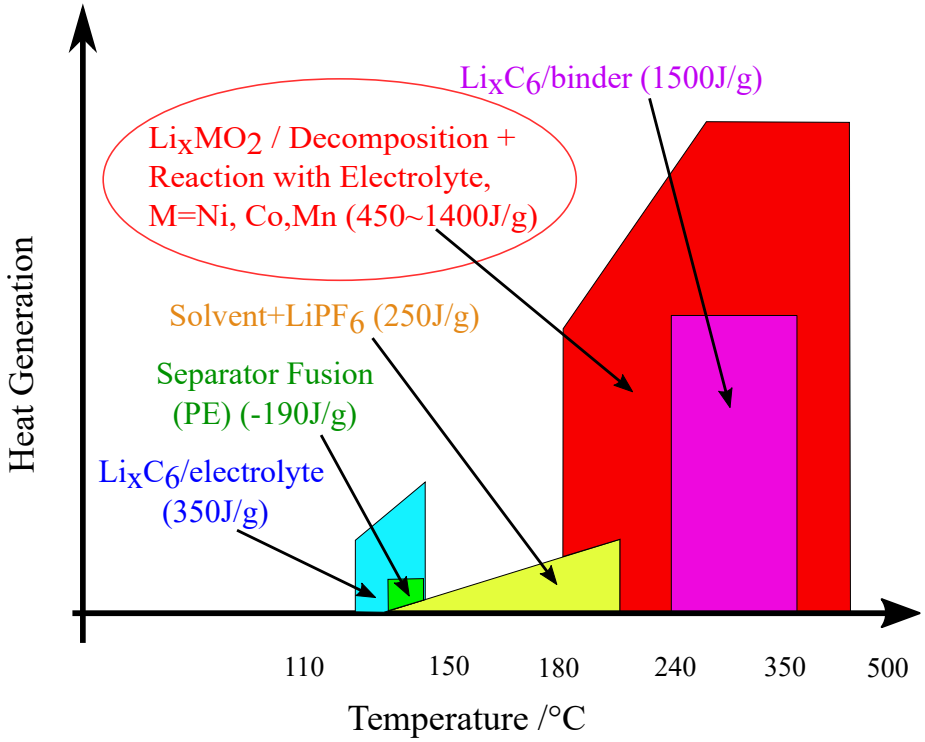

Figure 2.12: Source of heat generation and temperature evolution in lithium-ion cells [101]

indication that thermal stability was not disturbed by this cycling regime. As low temperature cycling enhances lithium plating, this could have possibly increased the self-heating rate of the cell. Lithium plating supports the growth of dendrites, along the anode surface and could lead to puncturing of the separator and connecting both electrodes of the cells, to cause internal short circuit [105]. In addition to this, cell safety with respect to cell size is critical to the commercial success of large-format cells. These aspects are summarized in section 2.1.

Chapter 3

Methodology and Experiments

3.1 Review of Existing Measurement Techniques

This section compares different measurement techniques to evaluate inhomogeneous temperature, current, and SOC distribution. Most of the methods described have been developed very recently, as most of the cell measurements are primarily focused on cell characterization and aging, thermal management, safety, and so on, rather than on cell inhomogeneities and its effects. With the enhancement of cell capacity by increasing size and design, the topic of cell inhomogeneity has become more relevant. Although electrochemical model-based simulations have existed for long time, it is still being used to measure complex parameters such as internal temperature, current, and SOC distribution within the cell and at the battery pack level. This model-based approach is now being used to develop accelerated battery designs, which provide endless combinations of size, geometry, and chemistries to improve the performance and lifetime of lithium-ion batteries. At present, this is the only method that provides detailed analysis of temperature, current, and SOC distribution in the cell with reasonably good accuracy, depending on the complexity of the model.

A more practical approach uses a direct measurement technique, which can be validated with the simulation results. However, this is a very tedious, time-consuming, expensive approach, and it takes a lot of effort to develop such a method, while it also has its own challenges and limitations. Nonetheless, several attempts made at direct measurements have been met with reasonable success, just at a smaller cell size. Indirect methods have also been proposed in some works that do not require lot of effort, and they are also less expensive. The summary of direct and indirect measurement techniques for the evaluation of cell inhomogeneities are shown here:

Surface temperature measurements with temperature sensors

- A relatively old and easy approach, now it has been improved with spatial temperature measurements at several locations on the cell surface, as shown in Fig. 3.1.
- Thermocouples or resistance temperature detector (RTD) sensors can be used to record temperature values.
- It is easier and less expensive to setup the measurement devices.

- The volume of the data measurements depends on the measurement sampling rate, cell size. For example, the data volume is higher if the sampling rate is high and the cell size is bigger, which makes it difficult to handle data if the experiments run for a long time, especially in aging tests.
- The method may not be suitable for cylindrical cell forms, as internal and surface temperature differences are quite high even at a low C-rate and high temperature.
- This method is more suitable for pouch cells considering its form, and it is applicable for all cell size.
- Cell characteristics are not affected and it is easier to reproduce the results.

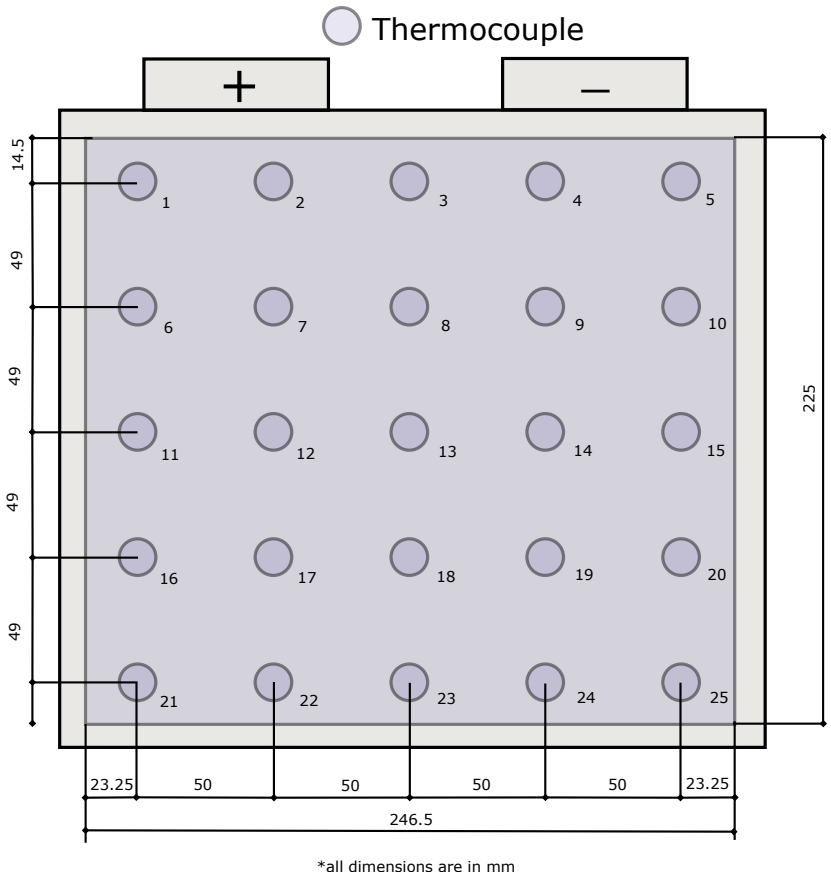

Figure 3.1: Schematic of temperature sensors distributed spatially along the surface of a 75 Ah cell [12, 28]

Surface temperature measurement with a thermal camera

- A relatively old and easy approach to capturing the surface temperature with a high-resolution thermal camera, as shown in Fig. 3.2.
- It is easier, but expensive cameras are required to set up the measurement device.
- It is not suitable for capturing data for a long period, but can be used to capture measurements at different stages of aging. Measurement accuracy and the sampling rate are determined by camera settings (e.g., image resolution to distinguish temperature contour).

- For a cylindrical cell, it requires multiple cameras to capture the temperature along the cell contour.
- This method is being used practically.
- Cell characteristics are not affected, and it is easier to reproduce the results.

Figure 3.2: Picture of a thermal camera setup to measure the surface temperature of a pouch cell [106]

Internal temperature measurement

- A newer and difficult approach, it can capture internal temperature, as shown in Fig. 3.3.
- Specially designed thermocouples are required to be placed inside the cell.
- It is expensive, know-how expertise is required for the measurement setup, and complexity increases with an increase in cell size.
- Suitable for capturing measurements for a long time, provided the sensors do not fail. The volume of the data measurements depends on the measurement sampling rate and cell size.
- This method is suitable for all cell forms, but there are many complexities and challenges in placing sensors for a large cell size.
- It is used very rarely, because of the complexities of placing sensors inside a cell and sealing them, and they should be non-reactive to the cell components.

- Cell characteristics might be affected, and the reproducibility of the results depends on the quality of the cell, as most of these cells are produced in laboratories without advanced equipment for cell construction.

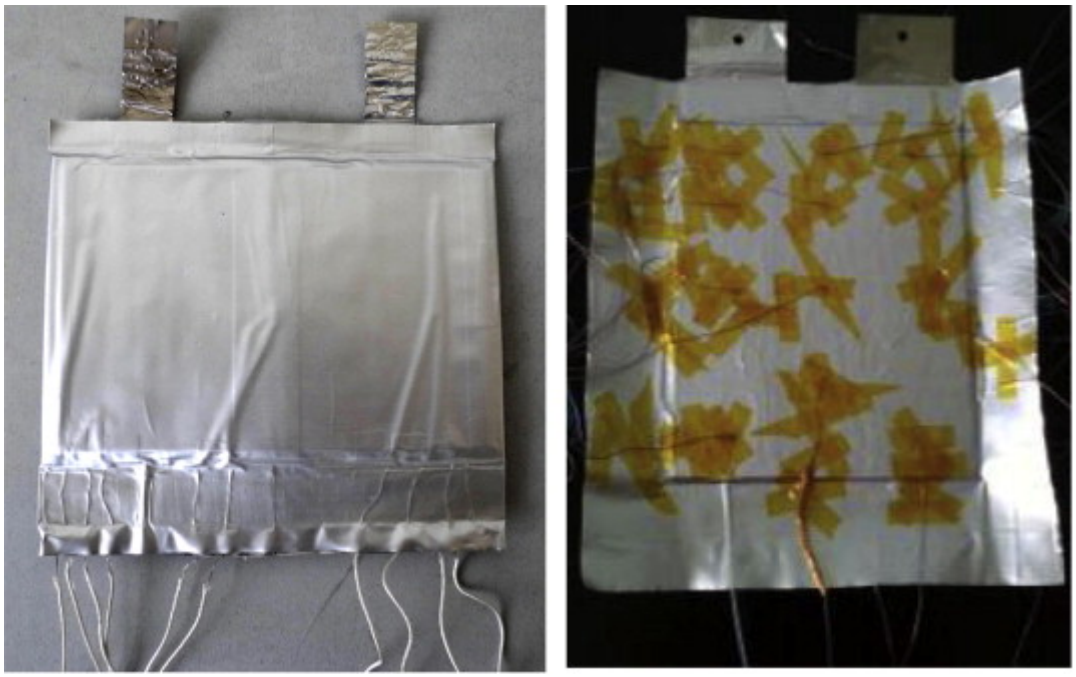

Figure 3.3: Internal sensors embedded in the cell [28]

Multiple/ segmented electrode measurement

- A newer and very difficult approach, it is possible to measure current and SOC distribution with the help of shunt resistors [25].
- It is expensive, know-how expertise is required for the measurement setup, and complexity increases with an increase in cell size.
- It is suitable for capturing measurements for a long time, provided the sensors do not fail. The volume of the data measurements depends on the measurement sampling rate and cell size.
- This method is suitable for cylindrical, prismatic, and pouch cell forms, but there are many complexities, challenges exist in preparing the cell sample, and it is almost impossible for large-format cells.
- This technique is only being used by one research group, because of the complexities in the preparation of such cells, sealing the case and non-reactive sensors with the cell components, and so on.
- Cell characteristics might be affected, and the reproducibility of the results depends on the quality of the cell, as most of these cells are produced in laboratories without advanced equipment for cell construction.

Local potential measurement through modified commercial cells

- Commercial A123 26650 cells with multiple tab configurations were used for the measurement of local potential [26].
- The cells were modified by opening the cell and separating the tabs, which allows the voltage measurement across four different positions on the electrode.
- This is an inexpensive method that can be adapted to high-quality commercial cells for in-situ measurements.
- In comparison to the unmodified cell, the performance of modified cells was affected by opening and hermetically sealing the cell again.
- This method can only be adapted to those cylindrical cell types, that come with multi-tab electrodes, but it is difficult to make such cell designs for commercial pouch cells.

In-situ and ex-situ diffraction/neutron imaging

- This is an old and easier approach to measuring current and SOC distribution [35, 36].
- X-ray diffraction and neutron imaging are the commonly used tools.
- Even though it is easier, these are highly expensive measurement setups, as not many research groups can afford such a facility, especially for neutron imaging.
- The samples can only be measured at different stages of aging and not throughout the length of the experiment.
- Only predefined dimensions of the sample cell that fit the measuring device can be used. Therefore, the cells need to have customized dimension for in-situ measurements. Cells that are outside the measurement dimensions have to undergo ex-situ measurements.
- This method has been published by many authors, hence it is a reliable method.
- Cell characteristics will be affected in ex-situ measurements, and it is not possible to continue testing further, but the cell characteristics are not affected during in-situ measurements. The results can be reproduced.

3D/pseudo-3D battery models

- This is an existing method for evaluating temperature, current, and SOC distribution.
- Computer simulation tools such as COMSOL, ANSYS, or any equivalent Multiphysics platform can be used.
- It is an easier and much faster approach, and almost every research group employs this method to obtain results. There are numerous publications on 3D modelling and simulation.
- Cell measurements may be required to obtain some parameters required for the mathematical equations and to validate the results. Most parameters can be found in the literature, but few parameters have to be obtained experimentally.

- Data handling depends on the complexity of models and accuracy of the simulation results.
- This method is suitable for all cell forms and sizes available commercially, and it is also possible to obtain any number of combinations of designs that are not commercially available. Overall, it is a very versatile tool.

Volume expansion in pouch cells

- This is a new method for evaluating cell volume expansion during the charge and discharge process; the schematic is shown in Fig. 3.4.
- Although it is not used to measure inhomogeneous temperature, current, or SOC distribution, non-uniform volume expansion has a strong connection to aging, especially at the edge of the pouch cell.
- Displacement sensors are used to measure the thickness change or volume expansion at different locations on the cell surface.
- This method is suitable for pouch and prismatic cell forms of all sizes. A large cell size requires more sensors to record spatial displacement.
- The sample measurements can be done at different aging intervals, usually once when the cells are new and once when they reach the end of life.
- The main objective of the study is to evaluate intercalation-induced stress during the charge and discharge process and its influence on cycle life aging of the cell.
- Recent publications show that, this method can be used to study lithium plating [45].

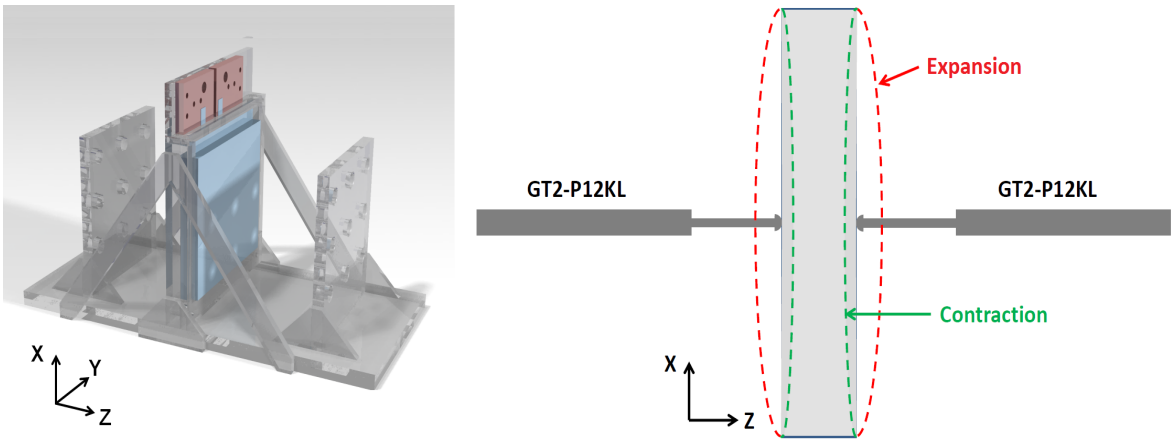

Figure 3.4: Schematic of cell volume expansion along the thickness of pouch cells [107]

3.2 Selection of Cells for Sizing Investigation

The choice of the cells is very critical to the investigation of sizing influence on their performance and lifetime. Different sizes, from small to medium, to large cells, have been considered in this investigation. The microscopic parameters, such as the active material composition, separator, current

collector material, cell chemistry, particle size, diffusion coefficient, equilibrium potential, reaction rate, thermodynamic parameters, thermal and electrical conductivity, heat capacity of active materials, and different components of a cell, should be identical in all cell sizes to have the same electrochemical, thermal characteristics. Otherwise, these parameters may have additional influence on performance and lifetime. However, the macroscopic parameters such as cell form, aspect ratio, thickness of active materials, current collector and separator, tab size, and its location attain significance when studying the influence of cell size. Besides these criterion, the cells should have a superior quality of manufacturing, with a low tolerance limit on geometry and cell performance to obtain reproducible results. Therefore, commercial cells from a renowned manufacturer were chosen for the sizing investigation. The cells were selected from the same manufacturer, so that the effect of cell manufacturing would have a similar influence on their electrochemical and thermal performances. The different cell sizes were chosen strictly on the basis of availability of the cells on the market. The specification of the cells are shown in Tabs. 3.1, 4.2 and 4.3.

Table 3.1: Specification of investigated pouch cells; also refer to Tabs. 4.2 and 4.3

Nominal Capacity (Ah)	Size (mm) (WxHxT)	Weight (g)	Electrode Area Ratio (Cathode/Anode)	No. of layers[1]
8	105 × 100 × 7.05	157	0.952	16
25	225 × 224 × 6	570	0.963	14
53	225 × 224 × 12.3	1,200	0.965	29
75	263 × 266 × 11.2	1,500	0.983	28

Fig. 3.5 shows the visual comparison of the cells used for the sizing investigation. These cells belong to the category of high-energy pouch cells, with a nominal voltage of 3.6 V. According to the data sheet of the manufacturer, the active material consists of a NMC cathode and a graphite anode. The electrolyte is made of a solution of lithium hexafluoro phosphate ($LiPF_6$) in a mixture of the organic solvent ethylene carbonate (EC) and ethyl methyl carbonate (EMC).

Figure 3.5: Visual comparison of different cell sizes

Besides pouch cells, the cylindrical cells were also chosen in the sizing investigations, but the tests were limited to calendar and cycle aging tests. The specification of cylindrical cells are shown in Tab.

[1]The electrodes are double-side-coated, except for two single-side-coated cathodes at the top-most and bottom-most layers of the pouch cell. Hence, the number of cathode layers are one more than the anode layers.

3.2. These cells are an LFP-based cathode and a graphite-based anode. The electrolyte is $LiPF_6$ in a mixture of the organic solvent EC, propylene carbonate (PC), diethyl carbonate (DEC), dimethyl carbonate (DMC), and EMC. These cells belong to the category of high-power cylindrical cells, with a nominal voltage of 3.3 V.

Table 3.2: Specification of investigated cylindrical cells

Nominal Capacity (Ah)	Diameter (mm)	Length (mm)	Weight (g)
1.1	18	65	39
2.5	26	65	76

3.3 Short-term Characterization Tests

Several tests were performed on the cells to evaluate their characteristics and to obtain parameters for battery modelling. The battery models can be used to simulate the results and validate them with the experimental data. In some cases, the battery models can be used to simulate certain results, which may not be possible to determine them experimentally, particularly the cell-sizing investigation. The tests can be basically classified into short-term tests, where the duration of a test is between several hours and less than one week, and long-term or aging tests, where the duration of a test extends beyond a week and up to an year. This section describes the experimental setups with the measurement techniques used for the short-term tests. The next section, 3.4, describes the measurement setups for the long-term tests.

3.3.1 Discharge Capacity Test

This test determines the cell capacity at a given temperature, the discharge C-rate, and the cell's aging history. Due to the dependency of the cell capacity on these factors, the discharge capacity test was standardized at 25±1°C and 1C discharge current from a fully charged state (100% SOC). Prior to this test, the given cell was fully charged in constant current constant voltage (CCCV) mode at 1C, cut-off voltage at 4.2 V, and cut-off current at 0.05C, and rested for 1h to obtain temperature and voltage equilibrium. This test was performed when the cell was new as well as at different aging intervals to evaluate the remaining capacity, SOH, and the remaining useful life (RUL) of the cell. Additionally, this test was done at different temperatures and C-rates to evaluate the performances, such as rate capability, Ragone plots, and energy and charge efficiency. Fig. 3.6 shows the voltage profile used for the standard discharge capacity measurement of a 75 Ah cell. The discharge was stopped at the lower cut-off voltage 2.7 V.

3.3.2 Impedance Characterization Test

The impedance characterization of the cells can be performed with two different methods. They are classified as time-domain-based measurements, also known as hybrid pulse power characterization (HPPC), and frequency-domain-based measurements, also known as electrochemical impedance spectroscopy (EIS).

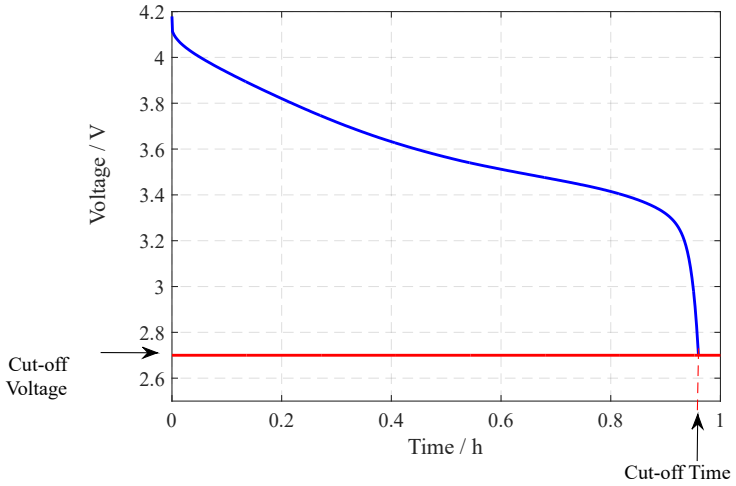

Figure 3.6: Discharge voltage profile to measure the cell capacity of a 75 Ah cell at 25±1°C and 1C discharge rate

3.3.2.1 Hybrid Pulse Power Characterization

This is a very commonly used technique, wherein a cell is charged and discharged with a high current pulse, typically a 3C current with a duration of 10 s. The voltage response of the cell is recorded as an output. The cell impedance is calculated as the ratio of change in the voltage response to change in the input current. The current and voltage measurement sampling rate should be greater than 1 kHz range to obtain a more accurate impedance value. This technique has certain drawbacks due to limitations in the measurement sampling rate caused by measurement noises and inaccuracies of the current sensors. However, this method is often used because of its simplicity.

The cell impedance is also sensitive to temperature, current, SOC, and its aging history. Therefore, to obtain impedance parameters for different operating conditions, additional measurements need to be performed, for example, at a different temperature and SOC range. In this thesis, the HPPC measurements were used mainly for aging characterization and battery-modelling-parameter extraction. For the aging characterization, this measurement was standardized, and the tests were done at 25°C. The cells were pulse discharged at a 10% SOC step from a fully charged state, as described in the following steps:

1. Fully charge the cell in CCCV at 1C C-rate until the upper cut-off voltage and 0.05C current cut-off.
2. Pause for 1 h to obtain temperature and voltage equilibrium.
3. Repeat the following test sequence for each of the SOC steps (starting from 100% SOC and down to 0% SOC at a 10% SOC step):
   (a) Apply discharge pulse for 10 s.
   (b) Pause for 3 min.
   (c) Apply charge pulse for 10 s.
   (d) Pause for 3 min.
   (e) Discharge the cell at 1C until the next SOC step.

(f) Pause for 1 h to obtain temperature and voltage equilibrium.

The current amplitude for the pulse current was 3C for all cells except 75 Ah, where the current amplitude was restricted to 200 A due to the limitation of maximum current from the battery tester. Fig. 3.7 shows the voltage and current profile of HPPC measurement for a 75 Ah cell.

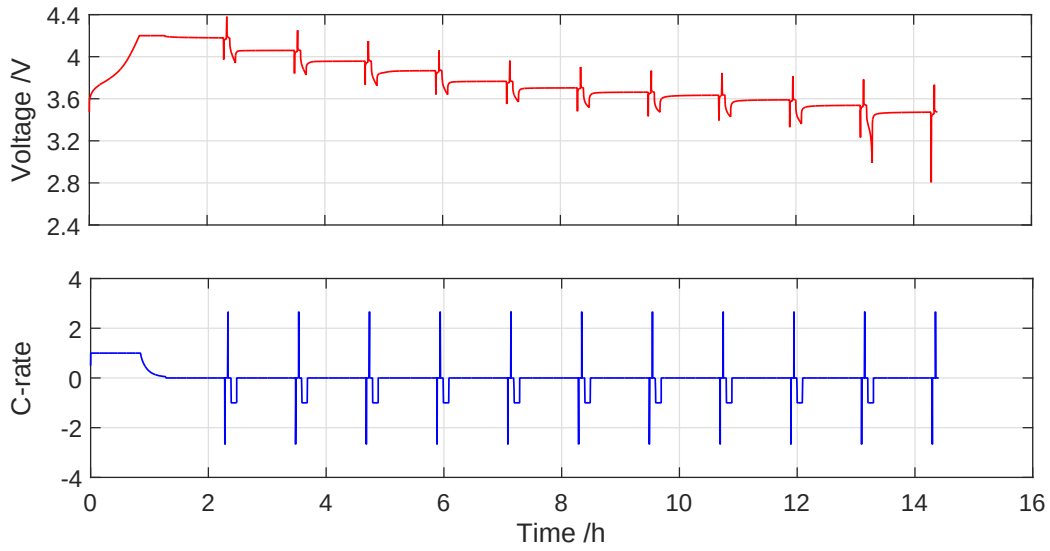

Figure 3.7: HPPC test profile of the 75 Ah cell at 25°C

A closer view into the voltage response of the HPPC profile, as can be seen in Fig. 3.8, shows an immediate voltage drop when the current pulse is applied. This is a clear indication that the battery has some internal resistance. It can be also observed that there is a time-varying voltage, which can be interpreted as the presence of additional elements, like a capacitor (in combination with resistance). The time-varying voltage part can be divided into short-transient and long-transient RC elements because of different time constants in the voltage profile. The mathematical representation of these elements is shown in Eqns. (3.1) – (3.3).

$$R_i = \frac{\Delta V_0}{I_p} \tag{3.1}$$

$$R_1 = \frac{\Delta V_1}{I_p} \tag{3.2}$$

$$R_2 = \frac{\Delta V_2}{I_p} \tag{3.3}$$

The time period t_1 for the short time resistance (R_1) is approximated to about 500 ms after the immediate drop, and the time period t_2 for the long time resistance (R_2) is approximated to about 9.5 s after the end of t_1. However, the time constants vary for different cell sizes and their aging histories.

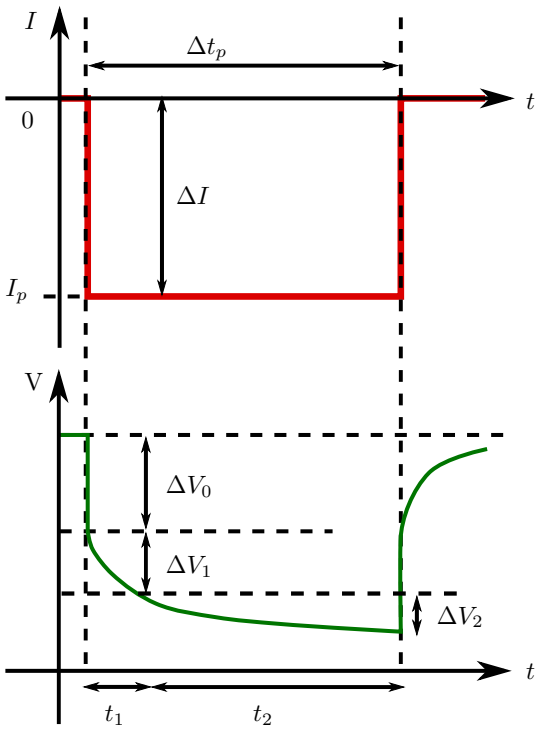

Figure 3.8: Closeup view of the voltage response and current pulse of the HPPC profile

3.3.2.2 Electrochemical Impedance Spectroscopy

Electrochemical impedance spectroscopy (EIS) is a common analysis used in electrochemistry to evaluate the impedance characteristics of a battery by applying an excitation signal at a wide range of frequencies. EIS is also a special case of impedance spectroscopy. It is a powerful and non-invasive measurement technique to investigate the complex impedance of a battery that is connected to different electrochemical processes occurring inside a cell. EIS measurement is performed by employing a small sinusoidal excitation signal at different frequencies, ranging from 5 mHz to 10 kHz. The great advantage of EIS measurements over HPPC measurements is the ability to separate different electrochemical activities occurring simultaneously inside a cell and accurately determine the impedance of the battery with the application of a multi-frequency excitation signal, also known as a frequency sweep. The impedance is calculated as the ratio of output response to input excitation [108]. The excitation signal can be applied in the form of voltage to produce an output current, which is called as potentiostatic method, or it can be applied in the form of current to produce an output voltage, which is called as galvanostatic method.

As batteries are best known as current-controlled devices, the galvanostatic method is preferred for EIS measurements. In this method, a small sinusoidal excitation current is applied to the battery to measure its voltage response. The cell impedance at a given frequency is calculated as the ratio of voltage response to its current input by assuming the cell behaviour to be in the linear region, as shown in Eqn. (3.4).

$$\bar{Z}(f) = \frac{\bar{V}(f)}{\bar{I}(f)} \tag{3.4}$$

When doing an EIS measurement, three important points must be considered: linearity, stability, and causality of the test system [109].

- Linearity: Batteries are highly non-linear, especially when operated under high currents. To avoid non-linearity, the applied AC amplitude must be small enough. Nevertheless, the amplitude must still be large enough to measure a voltage response without noise in the measurements.
- Stability: Battery electrode materials change their structure during charge and discharge. In addition to this, variations in temperature and SOC change the electrochemical behaviour of a battery. To ensure good results, the overall state of the system must not change significantly during the EIS measurement.
- Causality: The output of the system has to correlate with the applied excitation. Therefore, the cell must be shielded from outside perturbations. For example, a sinusoidal input should produce a corresponding sinusoidal output response.

The impedance spectroscopy has different regions, a high-frequency region that consists of a series inductance and resistance, a mid-frequency region that is a depressed semi-circle, and a low-frequency tail representing diffusion impedance. The series inductance might be due to connection cables, the type of wiring, porous electrode structure, and so on. The series resistance is mainly caused by the electronic resistance of current collectors, active material, electrolyte resistance, contact resistance, and so on. It is denoted by R_i, calculated as the value at the x-intercept on the Nyquist plot, typically at 1 kHz frequency[2]. The mid-frequency arc is the result of the electrode-electrolyte interface (SEI layer), charge transfer, and double-layer capacitance. The low frequency slope is associated with Warburg impedance, representing the diffusion of ions in the solid phase [110]. Fig. 3.9, shows the typical impedance spectrum of a lithium-ion battery.

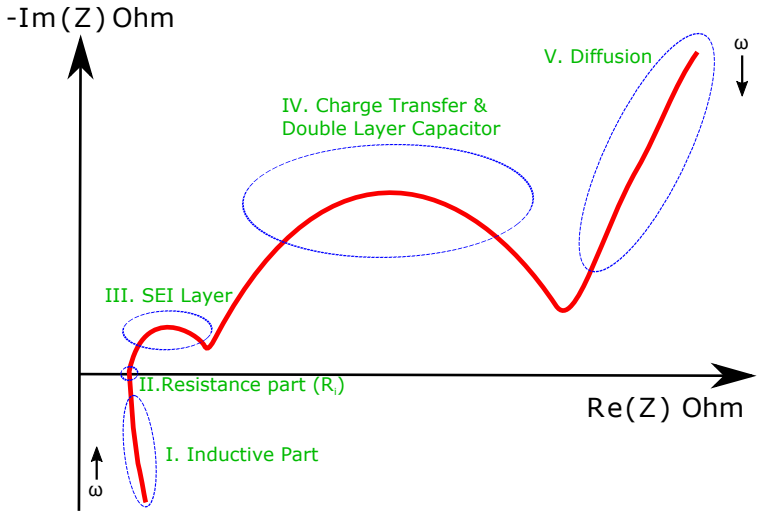

Figure 3.9: Schematic impedance spectrum in a Nyquist plot for a lithium-ion battery (based on [110]).

Even though this method is more accurate compared to HPPC, it has seldom been used in the impedance parameterization of batteries for aging studies. This is due to the complexity of extracting different impedance for a battery, longer measurement duration in comparison to the HPPC technique, and the high volume of impedance measurements. However, this technique is still used to extract the

[2] The frequency is not always 1 kHz; on the 75 Ah pouch cell, it varied from 500 to 700 Hz, depending on its SOH.

impedance parameters for multiphysics-based battery models (Section 4.4) as well as in determining the evolution of SEI resistance under the different aging conditions of the battery. Additional results are shown in App. A4.

The impedance behaviour for the cells was investigated at different temperatures and SOCs. The procedures for the EIS measurements have been adapted from Waag et al. [111] as described here:

1. Fully charge the cell in CCCV at 1C C-rate until the upper cut-off voltage and 0.05C current cut-off.

2. Pause for 1 h to obtain temperature and voltage equilibrium.

3. Repeat the following test sequence for each SOC (starting from 100% SOC and down to 0% SOC at 10% SOC step).

   (a) EIS measurement in the frequency range 10 kHz – 5 mHz.

   (b) Discharge the cell at 1C until the next SOC step (based on actual cell capacity).

   (c) Pause for 1h to obtain temperature and voltage equilibrium.

The test temperatures were 15, 25, and 40°C. The measurements were performed within the selected frequency range at 8 points per decade, with an excitation current input 0.05C, and the output voltage response was expected to be around 10 mV AC amplitude. However, the EIS measurements for aging tests were only performed at 50% SOC and 25°C, with an interval of four weeks between the successive tests.

3.3.3 Open Circuit Voltage Measurements

The OCV is the measurement of terminal voltage of a battery under no-load conditions (I = 0). In addition to this, the battery must be in complete equilibrium, w.r.t. voltage and temperature, such that there are no dynamic reactions within the cell. The OCV for most cell chemistries are dependent on the cell SOC, except for LFP chemistry (nearly flat OCV characteristics). Besides SOC, OCV is also a function of temperature, aging, and, to some extent, battery hysteresis.

There are two methods for measuring the OCV of the cell. In the first method, the cell from a fully charged state is discharged stepwise at different SOC intervals. The shorter the interval between two SOCs, the more accurate the result. In general, 5% and 10% SOC steps are commonly used measurement techniques. In this work, a 10% SOC step was used in most of the OCV measurements (refer to the HPPC profile in Fig. 3.7). The second method is more accurate, and it is mainly used for multiphysics simulation purposes. In this method, the cell is discharged from 100% SOC with a very low C-rate for the reason that voltage polarization is very low. The voltage measured at the battery terminal is taken as OCV. Even with the low C-rate (0.05C) discharge, the polarization voltage cannot be completely neglected. Hence, after the complete discharge, the cell is charged again with the same C-rate used for the discharge. Finally, the OCV is calculated as the average of the charge voltage and the discharge voltage to negate the effect of polarization. Fig. 3.10 shows the OCV measurement for a 75 Ah cell. This technique is also known as pseudo-OCV measurement.

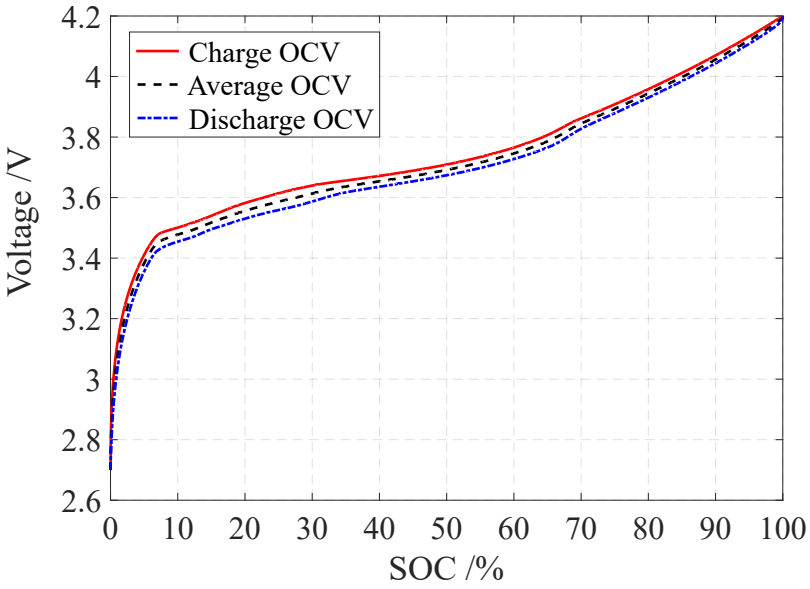

Figure 3.10: Measurement data of charge and discharge pseudo-OCV and evaluation of average OCV on a 75 Ah cell at 25°C ambient temperature

3.3.4 Spatial Temperature Measurements

As explained in section 3.1, this technique can be used to measure the temperature inhomogeneity on the surface of the cell. As this technique is feasible for the pouch dimension, only the cells from Tab. 3.1 were considered for the measurements. The surface measurement points were chosen to be equidistant from one another in the form of a square matrix. The total number of measurement points were chosen to be nine for 8 Ah cells and twenty-five for 25, 53, and 75 Ah cells. The schematic representation of spatial temperature measurements on a 75 Ah cell is shown in Fig. 3.1. The temperature sensor is a thermocouple Type K with a fine-gauge, exposed welded tip. The dimensions of the thermocouple were 1 mm in length and 0.0076 mm in diameter. Some measurements were done with aluminium plates attached as cooling plates[3] for the thermal management of the cell. The temperature sensors attached to the cell surface should be very thin (µm scale) to ensure very good contact between the cooling plate and the cell surface. The test profile for the spatial temperature measurements are described in the following steps:

1. The cell is rested for 3 h before the start of the test to attain temperature and voltage equillibrium.
2. Fully charge the cell in CCCV mode at a 1C C-rate with the cut-off criterion described by the manufacturer's datasheet.
3. Relaxation for 3 h to attain an equilibrium state, and all the dynamic reactions fade away.
4. Discharge the cell in CC mode at a 0.5C C-rate.
5. Pause for 10 min before repeating steps 2 to 4, but replace step 4 with discharge C-rates 1C, 2C, and 3C.
6. Steps 1 to 5 can be repeated at different ambient temperatures, such as 15, 25, and 40°C.

[3]Water is circulated through the cooling plates, which absorbs the excess heat transferred to the aluminium plates

In order to study the effect of the cooling medium, the spatial temperature measurements were performed with and without the cooling plates. The test setup with the cooling plates is shown in Fig. 3.11. More pictures of this test setup are shown in App. A1.

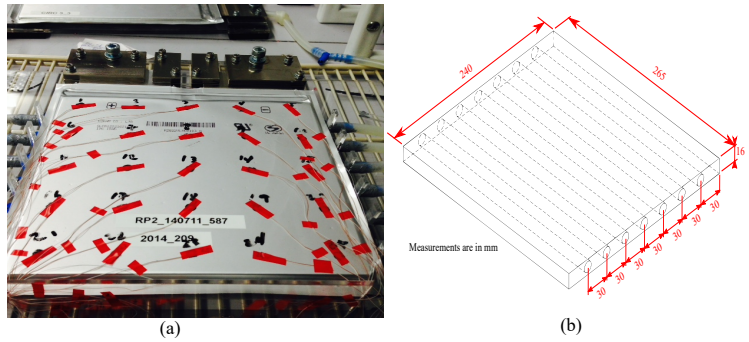

Figure 3.11: Test setup of spatial temperature measurements on a 75 Ah cell with aluminium plates as the cooling medium (a) temperature sensors on the cell in a 5x5 matrix, (b) dimensions of the aluminium cooling plate, (c) the cooling plate on the cell surface, and (d) the Julabo chiller unit

3.3.5 Volume Expansion Measurements

This section describes the experimental setup to evaluate the cell expansion behaviour via displacement measurements on the surface of lithium-ion cells, especially pouch cells. The setup comprises five parts, as listed here:

1. Investigated cell and the cell fixture
2. Sensors (displacement and temperature)
3. Temperature Chamber
4. Battery test system
5. Data-acquisition unit

Additional items include control and data storage to operate the equipment and store the measurement data, respectively. The work mainly focuses on the normal operations of the cells, hence, the cell expansion is relatively small (∼1.5–2% displacement compared to the cell thickness) from a macroscopic perspective. Given these preconditions, the fixture should be solid enough to minimize the measurement error, hence, a proper design of the structure is critical to the reliability of the results. Fig. 3.12

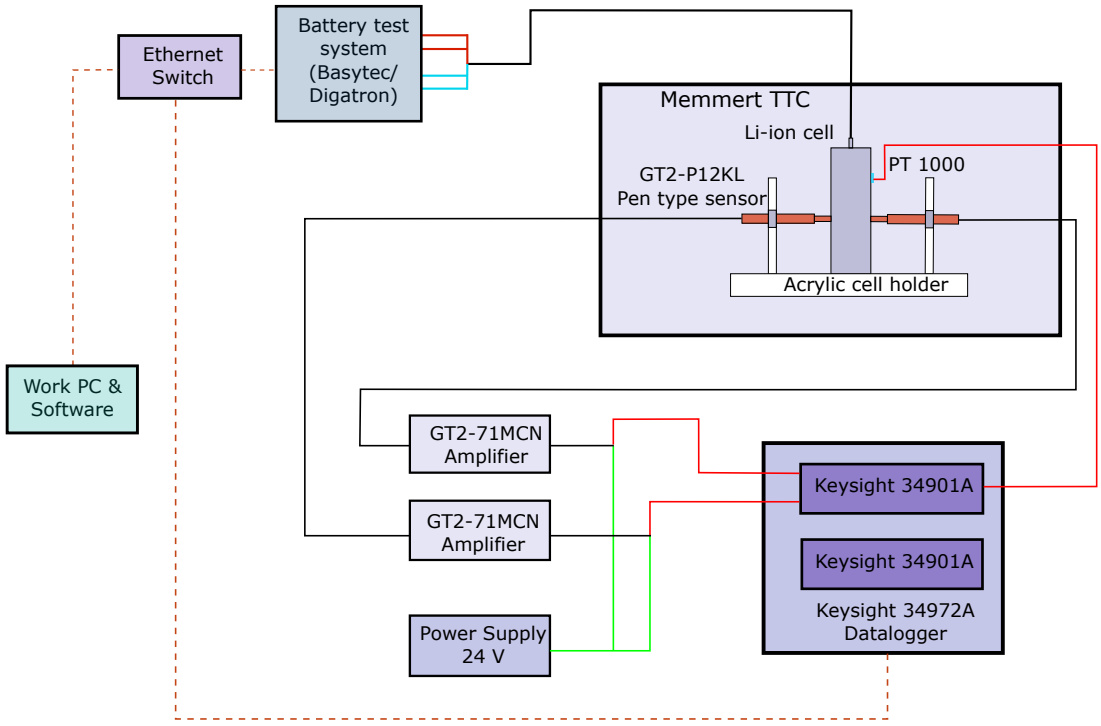

Figure 3.12: Schematic diagram for displacement measurement on the pouch cell. Measurement points are shown in Fig. 3.13.

shows the schematic of the displacement test setup. Additional details about the setup construction can be found in App. A2.

Fig. 3.13 shows the number of measured data points for the volume displacement of different cell sizes. The 8 Ah cells had nine measuring points (a 3x3 matrix) on the front surface and correspondingly equal points on the back surface (hidden from view). The larger cells 25, 53, and 75 Ah had ten measurement points, selected from a 5x5 matrix. The total displacement at a given point on the cell is calculated as the sum of front and back displacements. The number of sensors used in the measurements were four, and it was possible to measure displacement at two given points. The experiment was repeated to measure the displacement on remaining positions. As depicted in Fig. 3.4, the cells were mounted vertically in order to measure the displacement along the thickness direction, which allowed free expansion on the cell without any constraints. This would not have been possible if the cells had not been mounted horizontally, because that could have restricted the displacement on the bottom surface. This is also applied to the cell's geometric edges, where there were no constraints caused by the mounting of the cell. However, some constraints did occur due to the sealing of the external pouch laminate as well as to spot welding near the current-collector tabs. This situation could not be avoided because of the process involved in the cell manufacturing.

The displacement measurements were performed on the cells, as shown in the following steps. The precondition before the start of a displacement test was that the cell was assumed to be at 0 % SOC, if otherwise, it was completely discharged using the CCCV discharge regime at a 1C discharge C-rate, 2.7 V cut-off voltage, and 0.05C cut-off current.

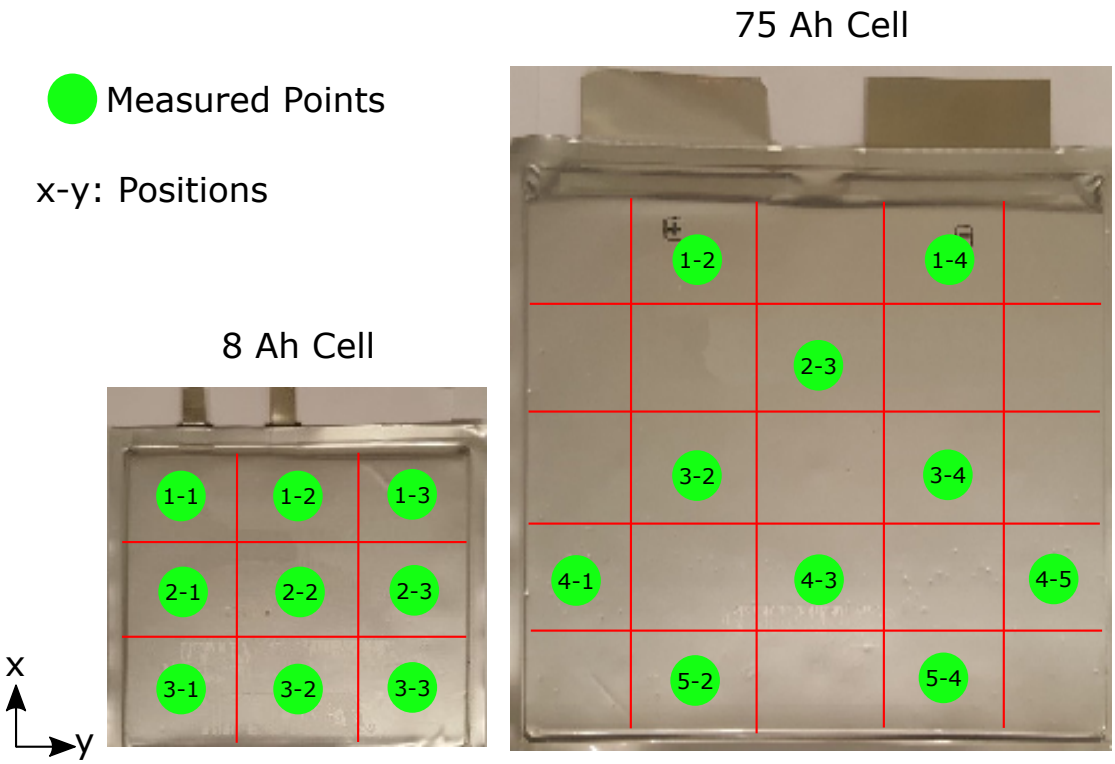

Figure 3.13: Front view of measurement points on the surface of (a) 8 Ah and (b) 75 Ah pouch cells

1. At 0 % SOC, the cell was rested for 4 h to attain consistency in the displacement sensor[4] readings. During this long pause, the temperature and voltage equilibrium could be attained simultaneously.
2. After the long pause, the cells were completely charged with the standard CCCV regime.
3. Pause for 2 h to attain displacement relaxation, as well as temperature and voltage relaxation.
4. Discharge the cell at a given C-rate (0.5, 1, 1.5, & 2C) in the CCCV regime.
5. Repeat step 3 to attain displacement relaxation.
6. Steps 1 to 5 can be repeated at different ambient temperatures.

3.4 Aging Characterization Tests

As described in section 1.2, an increase in the cell size leads to certain inherent disadvantages in the cell performance, such as temperature, SOC, and current density distribution. The hypothesis proposed in this work has led to conclusion that inhomogeneous cell characteristics could affect the lifetime of the battery. It was also proposed in the hypothesis that only cycle aging affected the cell inhomogeneity due to increase in cell size, but not the calendar aging. Therefore, for the aging characterization, calendar and cycle-life tests were performed on all the cell sizes to evaluate the proposed hypothesis. Some operating conditions are also well explained in section 2.4, such as low ambient temperature

[4] The sensor readings showed time-related drift with an increase in value that was significant in the initial 2 h. The drift effect significantly faded away after 3 h, and hence a 4 h pause was chosen to minimize the drift effect.

(15°C) and high C-rate (3C) increasing the cell inhomogeneity. This condition could make a perfect case study for aging inhomogeneity. However, these conditions are also favourable for lithium plating, another aging process occurring in the cell. As this aging inhomogeneity study is based on the influence of sizing in the context of cell geometry, 40°C and 1C cycling conditions (1C CCCV charge and 1C CC discharge) were preferred for cycle aging. The ambient temperature of 40°C was chosen for another reason, that is, to compare the results of cycle and calendar aging. It has been well established that calendar aging can be accelerated by high ambient temperature. Hence, to obtain the aging results in a defined time frame, the conditions for calendar aging were set as 40°C and 100% SOC (i.e., the cells were fully charged before the storage) [16].

Prior to the aging tests, the discharge capacity of the cells was measured at 100% SOC, 25°C, and a 1C discharge C-rate. The HPPC and OCV tests were performed as described in sections 3.3.2.1 and 3.3.3, respectively. These tests can be collectively put together as a reference performance test (RPT). The cells were divided into two groups each for calendar and cycle aging tests. The aging tests were briefly interrupted at specific intervals, 4 weeks and 100 cycles for calendar and cycle aging tests, respectively. During the brief interruption, the RPT was performed on the aged cells to obtain the aging parameters of cells, such as remaining capacity, pulse power, impedance, and OCV. After the completion of these tests, the aging tests were continued until the remaining capacity of the cells dropped below 70% of its nominal capacity value or at the end of 40 weeks, whichever one was earlier. In addition to these tests, long characterizations were performed every 12^{th} weeks, for calendar tests and every 400^{th} cycles for cycle aging tests. The tests included an EIS test at 50% SOC and one cycle of 0.05C charge and discharge, a pseudo-method to evaluate the OCV of a given cell. The schematic of the aging tests is shown in Fig. 3.14.

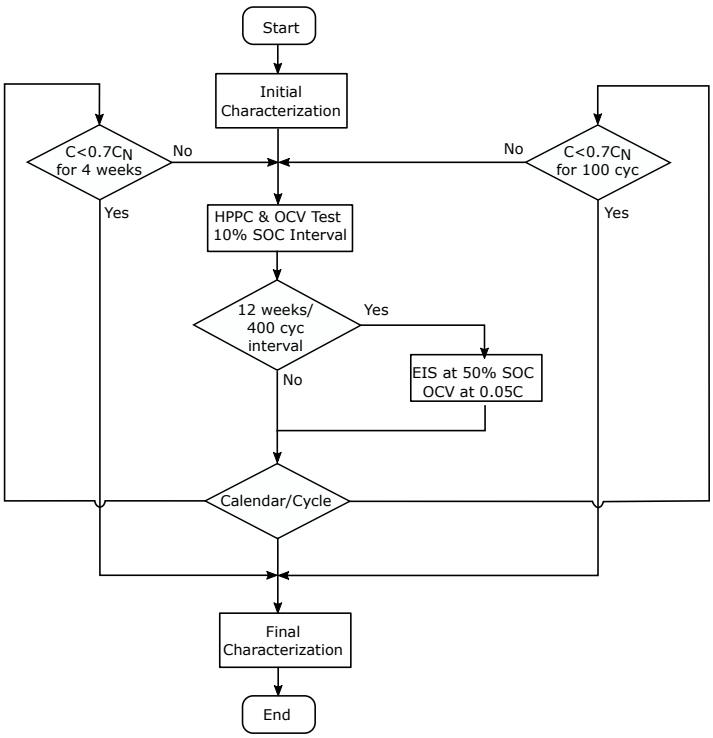

Figure 3.14: Schematic of calendar and cycle aging tests for the selected cells

3.4.1 Calendar Aging Test

The calendar aging test determines the shelf life of a battery under storage conditions. Prior to the start of the tests, the cells were charged to the target SOC and temperature, that is, 100% SOC and 40°C. The cells can be aged under float or storage conditions. In float conditions, the storage voltage of the cells was kept constant (without allowing the cell to self-discharge), whereas, in storage conditions, the voltage was not maintained at a constant level, allowing self-discharge in the cell caused by side reactions inside the cell. After four weeks of storage, the cells were brought to 25°C. At first, they were completely discharged to measure the self-discharge during the storage aging. After this step, the cells were charged to 100% SOC. In the next step, the discharge capacity of the cells was measured, and this was later followed by charging the cells again to 100% SOC, before starting the HPPC test. These charge and discharge protocols were ensured to measure the self-discharge, and reversible and irreversible capacity losses in the cells. After the completion of the HPPC test, the cells were charged again to 100% SOC and stored at 40°C for another period of four weeks of calendar aging.

3.4.2 Cycle Aging Test

The cycle aging test determines the usable life of the battery under cycling conditions. The cycle life aging tests were always started in the complete discharge state (0% SOC) and at 40°C ambient temperature. During the tests, the voltage, current, Ah charge and discharge, and temperature parameters were closely monitored. The following procedure describes the cycling regime.

1. Charge the cell in CCCV mode at 1C C-rate, 3.6 V and 4.2 V cut-off voltages, respectively, for LFP and NMC cells, and 0.05C cut-off current.
2. Pause for 15 min.
3. Discharge the cell in CC mode at 1C C-rate, 2 V and 2.7 V cut-off voltages, respectively, for LFP and NMC cells.
4. Pause for 15 min.
5. Repeat steps 1 to 4 one hundred times.

After 100 cycles, the cells were brought to 25°C before starting the HPPC test. Once these tests were completed, the cells were discharged to 0% SOC and cycled at 40°C ambient temperature for another period of 100 cycles. Additional results of the aging tests can be seen in App. A1.7.

3.5 Cell Disassembly and Coin-cell Characterization

These tests were performed by disassembling the commercial cells inside the argon-filled glovebox. The objective of these tests is to evaluate the half-cell characterization of cells, such as discharge capacity, OCV measurements, and the calculation of the entropic coefficient from a given half/full cell. These measurements provide input parameters for the multiphysics COMSOL models. Some results are shown in the appendix.

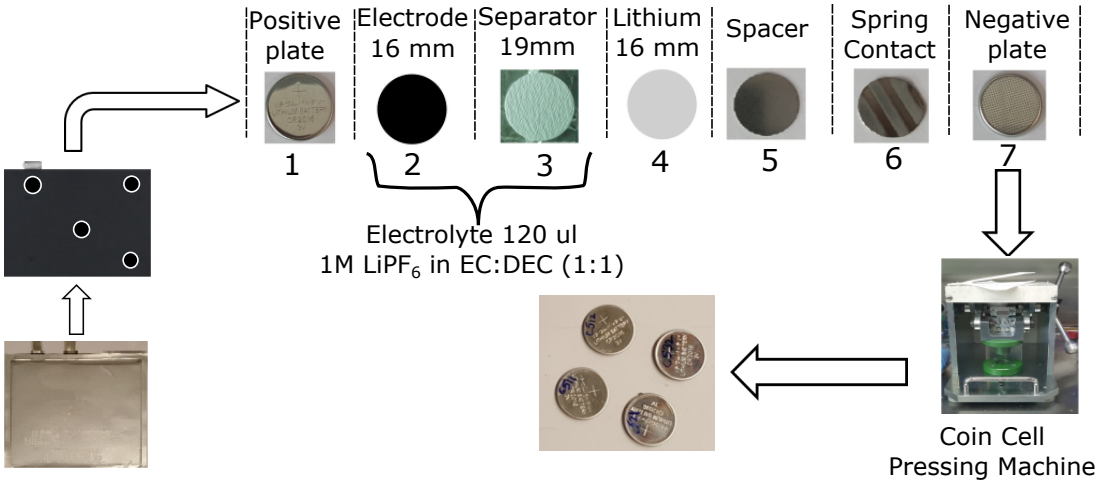

Figure 3.15: Schematic of coin-cell (half-cell) preparation from a commercial lithium-ion pouch cell.

3.5.1 Coin-cell Preparation

The cells were completely discharged in the CCCV regime at a 0.5C discharge C-rate at 2.5 V cut-off voltage, before going inside the Argon glovebox. The reason was to discharge the cell to the extent that it would not cause any mishap during the cell disassembly process. Even the tools used for disassembly, such as scissors, a knife, and tweezers, were either made of ceramic or plastic material to avoid an accidental short circuit. Once the outer pouch laminate was removed, the positive and negative electrodes were separated. The separators used in the original cells were discarded, because they had already been damaged during the aging process or some damages had been caused during the disassembly. The selected electrodes were washed in DMC and dried to remove the remaining traces of the original electrolyte and any impurities. The electrodes were cut into a coin-cell shape with a 16 mm diameter. The separator used was a commercial glass microfiber filter (CAT No. 1825-047), cut to a 19 mm diameter. For full cell preparation, the counter electrode was 16 mm graphite, whereas the half cell had lithium metal as the counter electrode (16 mm diameter). The commercial electrolyte Tomiyama was used in the coin-cell preparation. The specifications of the electrolyte are 1M $LiPF_6$ in EC and DEC (1:1 by volume). The coin cells were assembled as shown in Fig. 3.15 (steps 1 to 7 as indicated in the schematic). After assembling the components, the coin cells were pressed against the machine for strong mechanical and electrical contact. The coin cells were punched out of the electrodes from specific locations and layers, as indicated in App. A1.9. Meanwhile, the remaining layers were used to measure the electrode dimensions, tab dimensions, thicknesses of electrodes, current collectors, separator, and pouch laminate foil. Finally, the number of layers were counted. These measurements were used as cell parameters for multiphysics-based models.

3.5.2 Coin-cell Characterization

The assembled coin cells cycled at a 0.1C C-rate and 25°C ambient temperature to measure the remaining capacity [112]. The coin-cells were divided into full-cells, cathode half-cells, and anode half-cells. The full-cells and cathode half-cells had 4.2 V and 2.7 V as upper and lower cut-off voltages, respectively, whereas the anode half-cells had 2 V and 5 mV as upper and lower cut-off voltages. The following steps were used to measure the remaining capacity of the cells:

1. Discharge the cell at 0.1C to the lower cut-off voltage, to remove the cell's residual capacity.
2. Pause for 1 h.
3. Charge the cell at 0.1C to the upper cut-off voltage.
4. Pause for 1 h.
5. Repeat step 1 to measure the discharge capacity.

The OCV measurements for the half-cells were done using the same measurement technique explained in section 3.3.3. Fig. 3.16 shows the half-cell OCV measurements performed on the NMC cathode and the graphite anode. The cathode OCV measurement was performed by preparing coin cells from the disassembled 75 Ah cell, while the anode measurements were adopted from the previous measurements [113]. The entropic coefficient calculation for the half-cells are explained in App. A1.6.

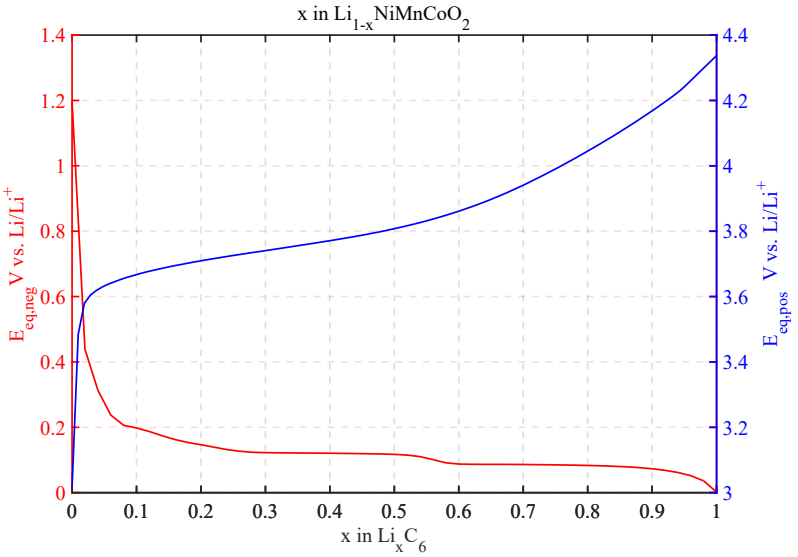

Figure 3.16: Open circuit voltage measurements of the NMC cathode and graphite anode half-cells

In addition to these tests, aged cells were also disassembled in the glovebox. Only two cell sizes were considered for this investigation, namely, 8 Ah and 75 Ah cells. There are many tests to determine the extent of the deterioration of the primary components of the aged cells, such as positive and negative electrodes, a separator, current collectors, and so on. The degradation of the materials can be linked to several sources, such as SEI formation, lithium plating, exfoliation of electrode coating from the current collector, and damage to the separators. This characterization requires extensive post-mortem diagnostic tools, equipment, and so on, and they are beyond of scope of this study. The disassembled aged cells have been compared with the fresh cells for visual inspection to identify the extent of the damage caused by aging of the cathode and anode electrodes. These results are discussed in chapter 5.5.

Chapter 4

Battery Modelling

This chapter deals with various battery modelling approaches that are widely used in different applications based on various motives. Each type of battery modelling varies in accuracy and complexity.

- *Diagnosis*: In this approach, not all variables in a battery are directly measurable. Even if it is possible to monitor the status of a specific variable, it can be very complex. Therefore, these models assist in diagnosing the battery and determining some of its unknown variables [114].
- *Monitoring and Controlling*: This approach is mainly used in real-time systems, where the internal state variables of the battery can be monitored and it is possible to adapt the operation parameters by controlling the state variables to achieve the desired results.
- *Battery Design*: This is mainly used before the development stage of the cell to study its desired characteristics. Prototypes are costly and time-consuming, whereas simulation tools that provide endless combinations of design variations can help to minimize the development cost.
- *System Design*: This approach is mainly used in the design of the battery pack size, capacity, power requirements, lifetime, and thermal management for a given driving condition. The system simulations can estimate driving range, state of function (SOF) derived from power capability, cranking power, cooling power requirements, energy throughput during its lifetime, and so on. These models are generally simplified to 0D, which reduces the model complexity and computational effort.

4.1 Classification of Battery Models

The models can be classified mainly based on the level of the physical interpretation of the battery characteristics. They are mathematical, electrical equivalent circuit, and physical-chemical-based models classified according to many literature sources [115–118]. Each model type find its own relevance and application based on the area of study. They have their own advantages and drawbacks in terms of accuracy, computational complexity, and configuration effort. As a battery is a complex electrochemical system, the fundamental approach helps us to understand its distinct nonlinear behaviour, such as electrochemical kinetics, explained by Newman and Doyle's porous electrode and concentrated solution theory, diffusion, charge transfer, aging mechanism, and so on. These characteristics can be best explained by physical-chemical models with relevant equations, parameters, and boundary conditions

[119, 120]. In other words, physical-chemical model is a white box model with a complete understanding of all the entities existing in various stages of modelling. These models have the highest accuracy, but require a complex approach and are computationally very time-consuming. A relatively easier approach is the depiction of the cell's physical-chemical behaviour as electrical circuit parameters. This method is best known as equivalent circuit modelling. The battery can be modelled as a combination of OCV, resistors, capacitors, and cell capacity [121–123]. Its accuracy is lower compared to the fundamental approach, but the complexity and computational effort can be reduced significantly. As this model is in the electrical system domain, it is easier to implement in a real-time application, such as BMS, to monitor and control the operation of the battery within the defined safety criteria. Although it is in the electrical domain, it still has some physical relevance to the battery characteristics; for example, this modelling approach is applied in different battery chemistry, but with some grey areas where some battery characteristics cannot be depicted by an equivalent component in the electrical domain. The last modelling technique is like a complete black box, without any knowledge about the intermediate stages between the input and output. This is also known as a mathematical model, where the mathematical equations have very little or no physical meaning to describe the battery characteristics. Some examples of these modelling techniques are polynomial equations generated by curve-fitting methods, fuzzy logic, artificial neural networks (ANN), and so on [124–126]. These models are generally less accurate and very simple to develop. They find application in system-level simulation for the overall diagnosis. Tab. 4.1 shows the evaluation summary of different battery modelling techniques.

Table 4.1: Evaluation of different battery models and their application

Model	Accuracy	Comp. Complexity	Config. Insight	Physical	Application
Mathematical	Low	Low	Low (2–5 params)	Low	Diagnosis System Simulation
Electrical Circuit	Medium	Medium	Medium (10–20 params)	Medium	Real-time Systems
Physical Chemical	High	High	High (>100 params)	High	Battery Design Reference Models

4.2 Mathematical Model

Mathematical models can be built from the past experimental data without necessarily understanding the fundamentals of battery dynamics. They are developed to simulate battery output voltage, temperature, SOC, as well as to estimate the battery capacity, RUL, and SOH. Some models include simple mathematical expressions, such as polynomial, exponential, power, and trigonometric functions, or the combination of these functions to simulate the battery. The common examples are Peukert's expression for battery capacity as a function of current and the OCV expression with a sigmoidal function, as shown in Eqns. (4.1) and (4.2), respectively [127]. These models are simplistic and do not take into account of load profiles, cell chemistry, reaction kinetics, aging mechanism, and so on. They are not accurate for predicting the exact performance of the battery, and, hence, their application is restricted mainly to diagnostic application.

$$C = I^p \cdot t \tag{4.1}$$

$$OCV(z) = K_0 + K_1 \frac{1}{1+e^{\alpha_1(z-\beta_1)}} + K_2 \frac{1}{1+e^{\alpha_2(z-\beta_2)}} + K_3 \frac{1}{1+e^{\alpha_3(z-1)}} + K_4 \frac{1}{1+e^{\alpha_4 z}} + K_5 z \tag{4.2}$$

where K_0, K_1..., α_1, α_2..., β_1, β_2 are constants and z is SOC between 0 and 1.

The model estimation can be improved by applying statistical tools, so-called known as stochastic models. These methods take into account the unknown internal state variables that are inaccessible to the measurement system and whose performance is affected by external and load conditions (taking into account modelling inconsistency, process noise, measurement noise, etc.) [128–130]. Instead of assuming mean estimate, these models generate a probability distribution over time, encapsulating the uncertainties inherent to the system, and provide a more realistic estimation of the output. Some tools, such as the relevance vector machine (RVM), support vector machine (SVM), and particle filter (PF), are generally used in the stochastic models.

New methods, such as ANN and fuzzy logic, are increasingly being used in the estimation of battery output, as shown in Fig. 4.1. These models are fast compared to high-fidelity physical-chemical models, but nevertheless are still accurate to a certain extent compared to other simple mathematical models. The improvement in the accuracy can be achieved by collecting a significant amount of data required to train the ANN [131]. Because of its open-loop characteristic, the trained ANN data for new cells cannot be accurate for aged cells. Furthermore, change in cell chemistry requires new training data for ANN to estimate the battery output. The accuracy of the model depends on the amount of training data and the number of hidden layers with the interconnection of neurons. This method is known as the direct estimation of battery output with ANN.

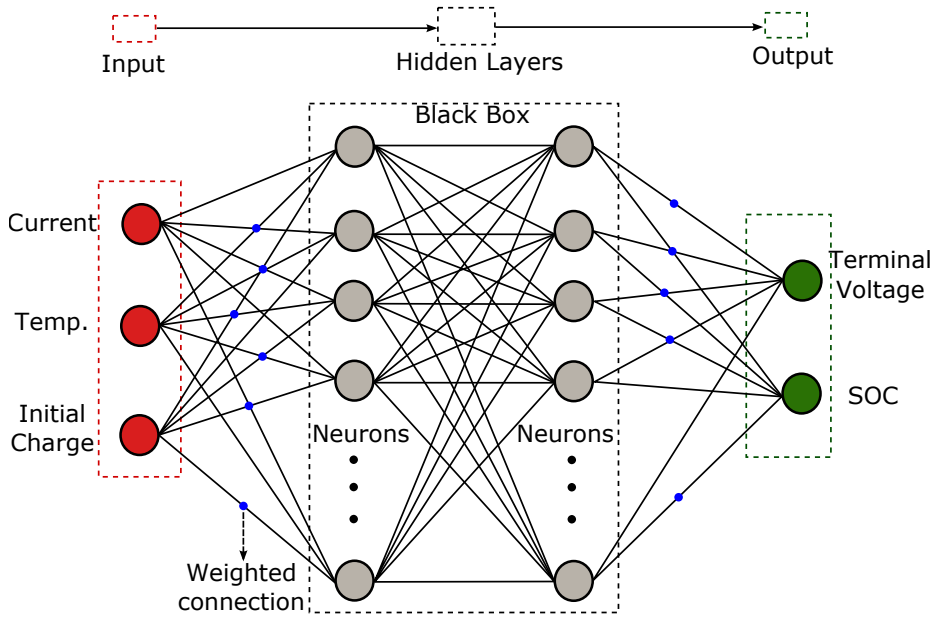

Figure 4.1: Schematic of Artificial Neural Network (ANN) for battery output estimation

If ANN is combined with other techniques, such as closed-loop SOC estimation based on the extreme

learning machine (ELM) together with the extended kalman filter (EKF), the results improve due to the adaptivity of the model [126]. Another advantage of closed-loop or adaptive estimation is that the training of the ANN data can be done during the online operation of the battery (i.e., the same model can be used for new-cell and aged-cell data). ANN models are used in different fields of science, like engineering and medicine, and, more recently, in battery-state determination. These models could also be used in evaluating inhomogeneity in large-format cells. Of course, this requires a completely different approach to train the hidden layers in the black box model. If the hidden layers can be trained using the historical data with the specific objective of evaluating, for example, inhomogeneity in large cells or the impact of cell design and form, it could be possible to obtain the desired results with this modelling approach. However, training these models can be very time-consuming and requires a big pool of data from different cell sizes over a long period. Such modelling approaches have not been attempted yet, nor have the results been published.

4.3 Equivalent Circuit Model

This is the most widely used approach for battery modelling. It strikes a perfect balance between accuracy and complexity. The models can be embedded in micro-controllers that can provide the real-time results of the battery output. The equivalent circuit model (ECM) can be further classified based on the measurement technique, time domain, and frequency domain, as described in sections 3.3.2.1 and 3.3.2.2. Even in the time-domain methods, there are different versions of the model based on the number of resistors in parallel with the capacitor (RC) elements. The number of RC elements in a circuit determines the order of the ECM. The schematic of ECMs with different orders are shown in Fig. 4.2.

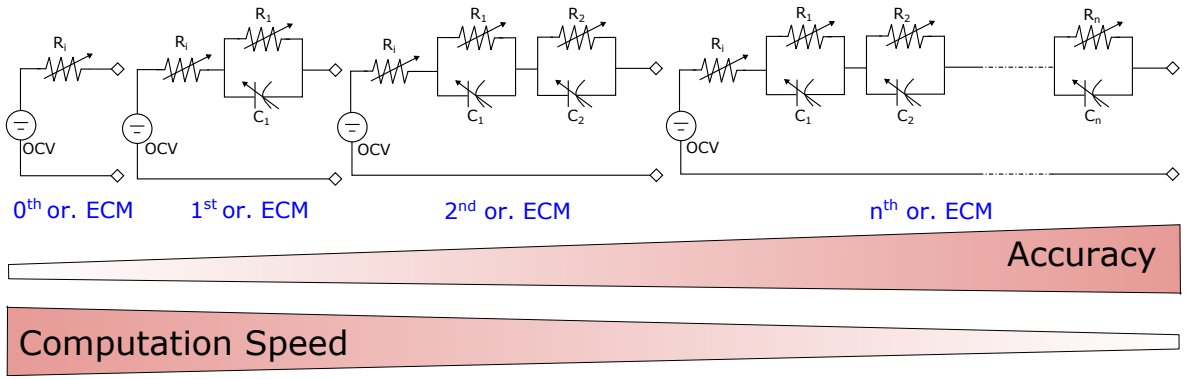

Figure 4.2: Equivalent Circuit Model (ECM) based on time-domain measurements

The ECM models are quite flexible with accuracy and complexity. Higher accuracy at the cost of complexity and low computation speed can be achieved by increasing of the order of the ECM, and vice versa. The simplest of all is the 0^{th} order ECM, which is seldom used or has become obsolete. The more common variants are the 1^{st} order and 2^{nd} order ECM. Beyond the 2^{nd} order model, the improvement in the accuracy is negligible compared to the increased complexity, configuration effort, and so on. Hence, the 2^{nd} order model can be considered as a benchmark model for lithium-ion batteries. The estimation of the circuit parameters along with the OCV values are explained in detail in section 3.3. The electrical equation of a 2^{nd} order model is shown in Eqn. (4.3). The time-domain ECM are real-time implementable and can be run on Hardware in Loop (HiL) platforms. Hence, they

are useful for BMS development and serve as a part of vehicle-level simulation studies for battery-pack sizing and range-estimation calculations [121].

$$V(t) = OCV + I(t)R_i + I(t)R_1(1 - e^{-\frac{t}{\tau_1}}) + I(t)R_2(1 - e^{-\frac{t}{\tau_2}}) \tag{4.3}$$

$$\tau_1 = R_1C_1 \tag{4.4}$$

$$\tau_2 = R_2C_2 \tag{4.5}$$

The 2nd type of ECM, that is, frequency-domain-based impedance models, are also used as alternatives to time-domain models. The main advantage of the impedance model is the accuracy with which the battery impedance can be measured. The impedance spectra also give the complete range of battery dynamics, starting from the high frequency inductance, internal resistance to the slow process of solid-state diffusion (towards the lower frequency spectrum). At high frequencies, inductive behaviour dominates the impedance characteristics of the cell. This behaviour is caused by geometry, especially in a cylindrical cell. Additionally, the measurement setup including the connection cables, type of wiring, and so on, influences its inductance. This is not a battery dynamic phenomenon, and hence this element is neglected in the ECM. The next element is internal resistance or pure Ohmic resistance, and it is one of the key parameters for evaluating power capability, heat generation, and temperature evolution in the battery. Frequency-domain measurements are more accurate compared to time-domain measurements. In a way, many parameters, such as SEI resistance, charge transfer, and diffusion coefficients, evaluated by EIS measurements can be used in the physical-chemical models. The semi-circular parts in the mid-frequency range (see Fig. 3.9) do not have circular contour; instead, they appear to be bulged or depressed semicircles. CPE elements are used instead of pure capacitors because the spatially distributed reactions in the layers result in different time constants [108]. In the low-frequency range (below 10 Hz), diffusion processes dominate in the anode and cathode. This is represented by Warburg impedance (Z_W), which describes the mixed electronic and/or ionic conduction in electrodes. The course of the impedance spectrum corresponds to a 45° slope in the Nyquist plot [110, 132]. The impedance parameters are extracted from the Nyquist plot (see Fig. 3.9). The parameters extracted from the Nyquist plot can be represented in the form of an electrical circuit, as shown in Fig. 4.3.

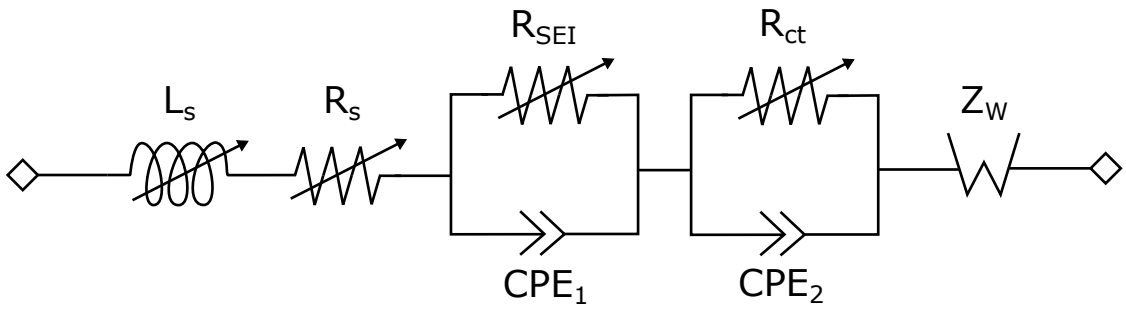

Figure 4.3: Equivalent Circuit Model (ECM) based on EIS measurements in the frequency domain

The expression for the complex impedance of the cell in different frequency spectra is shown in Eqn. 4.6. The circuit parameters are estimated by the least-square-curve-fitting method. Once the impedance

parameters are estimated, the battery SOH can be predicted by changes in the impedance values. For example, the change in the internal resistance and the SEI resistance serves as an indication of SOH. If these resistances increase, the SOH of the battery is lowered as an indication of fast degradation [133, 134]. Despite these great advantages, the EIS method does not easily estimate the battery capacity or SOH, as the results are hard to reproduce, mainly due to the fact that the system being monitored needs to maintain a steady state behaviour throughout the testing. This method is also costlier and requires bulky measurement equipment to generate a small signal AC and to analyze the responses in the Nyquist plot [135, 136]. Moreover, for practical reasons, it is preferable to use simple models (time-domain-based ECM) that facilitate on-board monitoring and control. As a result, EIS cannot be used to implement the real-time SOC and SOH estimation function of a battery [137].

$$\bar{Z}(\omega) = j\omega \cdot L_s + R_s + \frac{R_{SEI} \cdot CPE_1}{R_{SEI} + CPE_1} + \frac{R_{ct} \cdot CPE_2}{R_{ct} + CPE_2} + Z_W \tag{4.6}$$

$$\omega = 2\pi f \tag{4.7}$$

$$CPE = A \cdot (j\omega)^{-\xi} \tag{4.8}$$

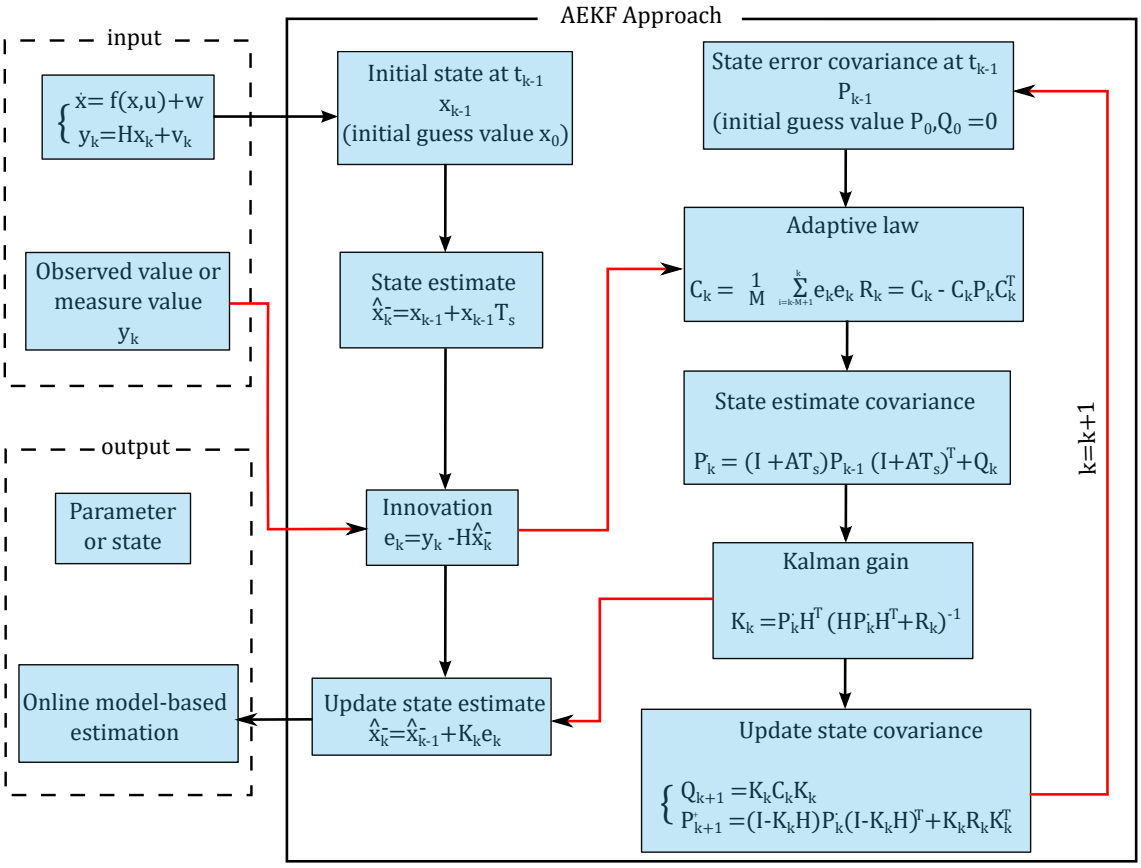

Figure 4.4: Flowchart implementation of the Adaptive Extended Kalman Filter (AEKF) [138]

Even though the ECM are quite effective in evaluating battery output characteristics, in reality, they suffer from measurement noise, process error, and other disturbances, which could be the result of

sensors degraded by harsh working environment. Besides these factors, some initial parameters also determine the accuracy of the results. To overcome these limitations, the ECMs are combined with filtering approaches by means of state-space battery models. Some of the widely used filter techniques are EKF, adaptive extended kalman filter (AEKF), sliding mode observer (SMO) [139]. The EKF-based algorithms strongly depend on the accuracy of the battery model, as well as the measurement and process noise, covariance matrices, and so on. If these settings are incorrect, it results in less accuracy and deviations from the measurements. Therefore, AEKF comes in handy to improve the accuracy of the output estimation by adaptively updating the process and measurement noise covariances [140, 141]. Fig. 4.4 shows the flowchart implementation of AEKF. Here, x is the state vector; y is the output; u is the system input; w and Q represent process noise and its noise covariance, respectively; v_k and R_k represent measurement noise and its noise covariance, respectively; H is the observer matrix; P is the covariance matrix; C_k is the innovation covariance matrix; K_k is the Kalman gain matrix; and e_k is the difference between observation and predicted observer [138]. The SMO has been known to have robustness in the presence of parameter variations and noise. It has a robust tracking performance in modelling uncertainties, environment and simple control structure [142]. However, the main disadvantage of these filtering methods is the estimation of battery SOC and SOH, that requires high computation power. The calculation involving complex matrix operation (covariance and inverse covariance matrices) could lead to numerical instabilities, and it additionally leads to complexities in the implementation of the algorithms in low-cost processors [116].

4.4 Electrochemical Thermal Multiphysics Model

Electrochemical thermal multiphysics models are based on physical-chemical models that follow the fundamental approach to describing the non-linear battery characteristics. The term, multiphysics, is often used in battery modelling of such complexity because of interactions between different physics, such as electrochemistry, Joule heating, and thermal characteristics, of the components used in the battery. A simple example to illustrate the interaction of the different physics involved in a battery is explained here. The electrochemical reactions in the battery produce either endothermic or exothermic heat, depending on charge or discharge. Additionally, irrespective of charge or discharge current, Joule heat is produced. These combined heats can act on the components, which results in an increase or decrease in the temperature of the battery. The temperature influences the electrochemical reactions in the battery, and this entire process results in the interaction of many physics, and hence the battery models of these types are multiphysics in nature. These models employ partial differential equations along the spatial geometry of the cell. They are very useful in the study of temperature, current density, and voltage distribution within the cell, which cause inhomogeneity. With the existing methodologies, it is difficult to evaluate cell inhomogeneity, but it can be overcome by adopting an electrochemical thermal model.

The model framework in this thesis is based on a multiscale multiphysics platform. A 3D electrochemical thermal model is an ideal platform for evaluating different inhomogeneities in the cell. However, it is very computationally challenging and expensive, especially if the cell dimensions are larger in magnitude (large-format cells). Several modelling approaches propose a trade-off by reducing certain dimensions of a given physics under consideration without significantly compromising on the accuracy of the results. This greatly helps to achieve computational effort and modelling efficiency. Therefore, a multiscale modelling approach is presented in this thesis that consists of:

- 1D electrochemical sub-model
- 2D current collector model
- 3D thermal model

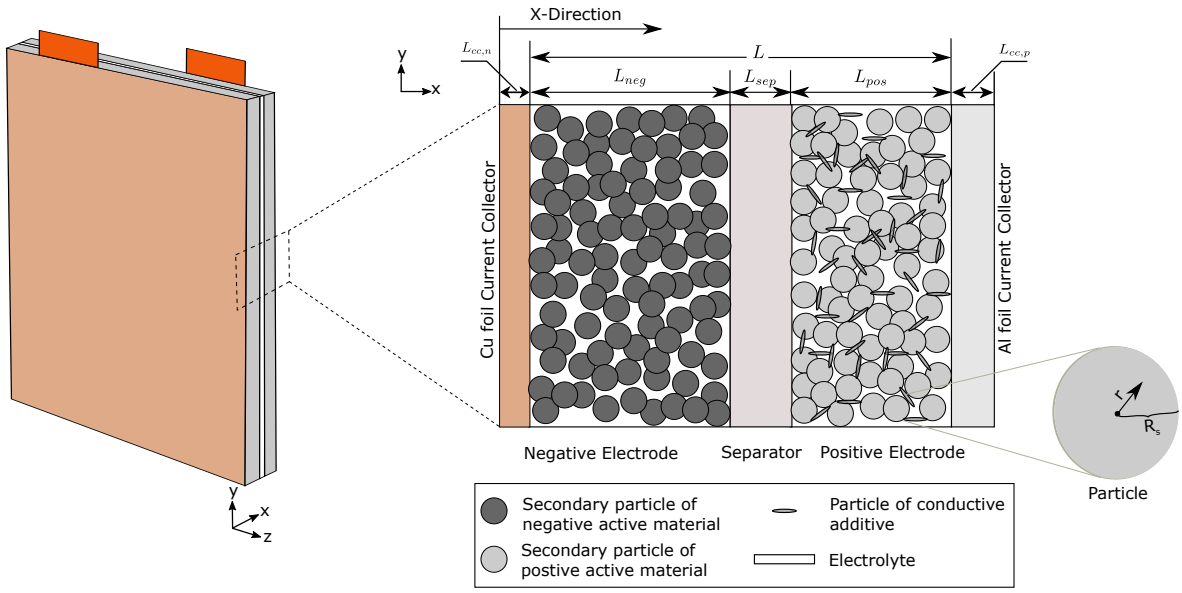

Figure 4.5: A 2D view of an electrochemical cell along the thickness plane

The cross-sectional representational view of a single-layer cell along the thickness plane is shown in Fig. 4.5. It consists of a cathode, an anode, an electrolyte, additives, a separator, and two current collectors. These components are essential to the electrochemical modelling of a cell. The electrochemical model is further divided into a 1D electrochemical sub-model (Fig. 4.7) that includes porous electrodes (cathode and anode), a separator, and a 2D current-collector model that includes both current collectors.

Tabs. 4.2 and 4.3 show the microscopic and macroscopic geometric properties of all the pouch cells used in the simulation. Most of these parameters were obtained by measurements. Therefore, one cell of every cell type was carefully opened in a glove box. After opening the cells, the number of anode and cathode layers was counted. Additionally, the sizes of the electrode and the separator were measured, as well as their thickness. The measurements show that the macroscopic geometric parameters of the cells differ in the size and number of layers and the size and position of the current collector tabs. However, the thickness of all the layers is equal for every cell. Fig. 4.6 is a schematic representation of macroscopic geometric parameters.

Table 4.2: Microscopic geometry parameters for all the cells used in the simulation

Symbol	Explanation	Value	Source
L_{pos}	Thickness cathode in m	63×10^{-6}	measured
L_{sep}	Thickness separator in m	20×10^{-6}	measured
L_{neg}	Thickness anode in m	75×10^{-6}	measured
$L_{cc,neg}$	Thickness current collector anode in m	7.5×10^{-6}	measured
$L_{cc,pos}$	Thickness current collector cathode in m	10×10^{-6}	measured

In porous electrode theory, the electrode is treated as a superimposed continuous sequence of active material, electrolyte, binders, and so on, which is actually related to its micro-structure. To simplify

[1] double-side coated layers; actual number of layers = Nca×2

Table 4.3: Macroscopic geometry parameters for individual cells used in the simulation

Symbol	Explanation	8 Ah	25 Ah	53 Ah	75 Ah	Source
H	Height of electrode plane in mm	83.5	183.5	183.5	222	measured
W	Width of electrode plane in mm	100	203	203	244	measured
$L_{tab,t}$	Thickness of tab in mm	0.3	0.3	0.3	0.3	measured
$L_{tab,W}$	Width of tab in mm	10	81	81	86	measured
$L_{tab,H}$	Height of tab in mm	12.5	32	32	32	measured
$d_{p,tab}$	Position of positive tab in mm	14	17	17	17	measured
$d_{n,tab}$	Position of negative tab in mm	42	105	105	141	measured
Nca[1]	Number of layers	16	14	29	28	measured
V	Volume in cm^3	60.35	227.61	449.80	602.89	calculated
A	Surface area in cm^2	87.72	387.09	387.09	551.04	calculated
S/A	Surface area to volume ratio in cm^{-1}	1.453	1.701	0.861	0.914	calculated

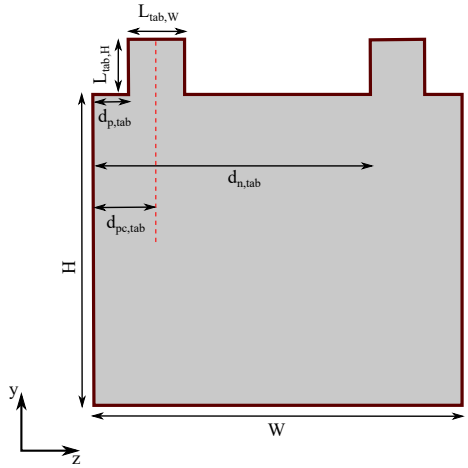

Figure 4.6: Schematic representation of the macroscopic geometry of the pouch cells used in simulation

further, the particles are assumed to be of spherical geometry with a known porosity. The conservation of lithium in a single particle is described by Fick's diffusion law [120].

$$\frac{\partial c_s}{\partial t} = \frac{D_s}{r^2}\frac{\partial}{\partial r}\left(r^2\frac{\partial c_s}{\partial r}\right) \tag{4.9}$$

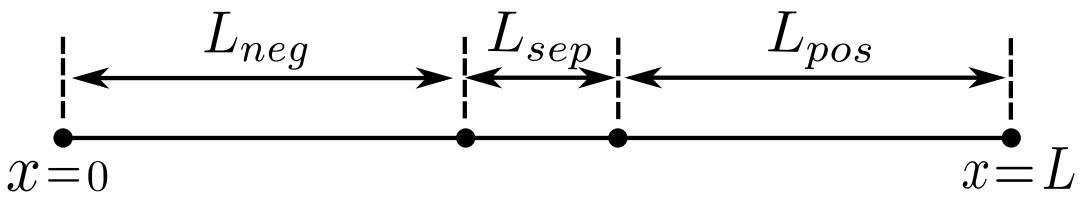

Figure 4.7: Schematic of a 1D electrochemical sub-model

with boundary conditions:

$$\left.\frac{\partial c_s}{\partial r}\right|_{r=0} = 0 \tag{4.10}$$

$$D_s \left.\frac{\partial c_s}{\partial r}\right|_{r=R_s} = \frac{-j^{Li}}{a_s F} \tag{4.11}$$

In Eqns. (4.9), (4.10), and (4.11), c represents Li concentration, and the subscript s denotes the solid phase. D_s is the solid phase diffusion coefficient, j^{Li} is the volumetric rate of electrochemical reaction at the particle surface, a_s is the specific interfacial surface area, and F is Faraday's constant (96487 C/mol).

For spherical active-material particles of radius R_s occupying electrode volume fraction ϵ_s, the interfacial surface area is given by:

$$a_s = \epsilon_s \frac{3}{R_s} \tag{4.12}$$

The electrochemical model of the particle surface at the electrode/electrolyte interface is given by $c_{s,e}(x,r,t) = c_s(x,R_s,t)$. The lithium conservation in the electrolyte phase is given by:

$$\frac{\partial(\epsilon_e c_e)}{\partial t} = \frac{\partial}{\partial x}\left(D_e^{eff}\frac{\partial}{\partial x}\,c_e\right) + (1-t_+^0)\frac{j^{Li}}{F} \tag{4.13}$$

where c_e is the Li concentration in the electrolyte phase, ϵ_e is the electrolyte phase volume fraction, and t_+^0 is the transference number of Li^+ with respect to the velocity of solvent.

There is zero flux boundary condition at the current collectors[2]:

$$\left.\frac{\partial c_e}{\partial x}\right|_{x=0} = \left.\frac{\partial c_e}{\partial x}\right|_{x=L} = 0 \tag{4.14}$$

The effective diffusion coefficient is calculated from the relative diffusion coefficient using the Bruggeman factor, taking into account of the mean Li^+ flow path (Tortousity) through the porous medium.

$$D_e^{eff} = D_e \tau_e^p \tag{4.15}$$

where D_e is the diffusion coefficient in the electrolyte phase, and τ_e^p is the Tortuosity correction factor.

The potential in the solid phase can be described by Ohm's law:

[2] Lithium cannot be transported through the current-collector and the external circuit.

$$\frac{\partial}{\partial x}\left(\sigma^{eff}\frac{\partial}{\partial x}\,\phi_s\right) - j^{Li} = 0 \tag{4.16}$$

$$\sigma^{eff} = \sigma\epsilon_s \tag{4.17}$$

where σ^{eff} is the effective conductivity of active material (S/m), and p, n indices indicate positive and negative electrodes, respectively; ϕ_{s} is the potential in the solid phase (V).

The boundary conditions at the current collector are:

$$-\sigma_n^{eff}\frac{\partial\phi_s}{\partial x}\bigg|_{x=0} = \sigma_p^{eff}\frac{\partial\phi_s}{\partial x}\bigg|_{x=L} = \frac{I_{cell}}{A} \tag{4.18}$$

Followed by zero electronic current at the separator boundaries:

$$\frac{\partial\phi_s}{\partial x}\bigg|_{x=L_{neg}} = \frac{\partial\phi_s}{\partial x}\bigg|_{x=L_{neg}+L_{sep}} = 0 \tag{4.19}$$

The potential in the electrolyte phase can be described as:

$$\frac{\partial}{\partial x}\left(\kappa^{eff}\frac{\partial}{\partial x}\,\phi_e\right) + \frac{\partial}{\partial x}\left(\kappa_D^{eff}\frac{\partial}{\partial x}\,\ln c_e\right) + j^{Li} = 0 \tag{4.20}$$

$$\kappa^{eff} = \kappa\epsilon_e^p \tag{4.21}$$

where κ^{eff} is the effective Li^+ conductivity of the electrolyte (S/m), and $\kappa_{\text{D}}^{\text{eff}}$ is the effective Li^+ diffusional conductivity of the electrolyte (A/m).

With the following boundary conditions:

$$\frac{\partial\phi_e}{\partial x}\bigg|_{x=0} = \frac{\partial\phi_e}{\partial x}\bigg|_{x=L} = 0 \tag{4.22}$$

The effective diffusion conductivity can be derived from concentrated solution theory.

$$\kappa_D^{eff} = \frac{2RT\,\kappa^{eff}}{F}(t_+^0 - 1)\left(1 + \frac{d\ln f_\pm}{d\ln c_e}\right) \tag{4.23}$$

These governing PDEs Eqns. (4.9), (4.13), (4.16), (4.17), (4.20), and (4.21) describing lithium conservation and potential in solid and liquid phases, respectively are coupled in the Butler Volmer equation [143], which describes the electrochemical kinetics as being expressed as:

$$j^{Li} = a_s i_0 \left\{ exp\left[\frac{\alpha_a F}{RT}\, \eta \right] - exp\left[-\frac{\alpha_c F}{RT}\, \eta \right] \right\} \tag{4.24}$$

$$i_0 = k(c_e)^{\alpha_a}(c_{s,max} - c_{s,e})^{\alpha_a}(c_{s,e})^{\alpha_c} \tag{4.25}$$

The cell over-potential is given by:

$$\eta = \phi_s - \phi_e - E_{eq} \tag{4.26}$$

The potential distribution in current collectors is described by two 2D models, one part representing the cathode and other part the anode. The 2D current collectors are coupled with the 1D electrochemical sub model along the thickness direction of the cell to represent a pseudo two-dimensional (P2D) electrochemical model. While building the 1D sub-model, it was assumed that a single sub-model represented the whole of the electrochemical cell. But, in reality, there is always spatial inhomogeneity that needs to be taken into account. Hence, to overcome this problem, the 2D current collector models were subdivided into nine parts, wherein each of these parts was connected individually to 1D sub-models, as shown in Fig. 4.8.

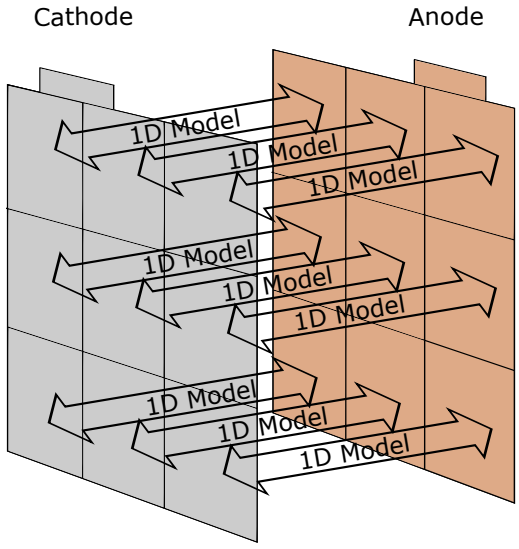

Figure 4.8: 2D current collectors coupled with 1D electrochemical sub-models

The charge balance in the current collectors is described as:

$$\sigma_{cc,j} \frac{\partial^2 \phi_{cc,j}}{\partial y^2} + \sigma_{cc,j} \frac{\partial^2 \phi_{cc,j}}{\partial z^2} + \frac{J \cdot \hat{u}}{\delta_{cc,j}} = 0 \quad (j = p, n) \tag{4.27}$$

where J is the current density (A/m^2), δ_{cc} is the thickness of the current collector (m), and p and n indices indicate positive and negative current collectors, respectively.

The boundary conditions at the interface between the current collectors and tabs of the positive and negative are:

$$\hat{u} \cdot (-\sigma_{cc,p} \nabla \phi_{cc,p}) = \frac{I_{cell}}{L \delta_{cc,p}} \tag{4.28}$$

$$\phi_{cc,n} = 0 \tag{4.29}$$

The remaining boundaries are assumed to be electrically insulated and can be represented as:

$$\hat{u} \cdot (\nabla \phi_{cc,j}) = 0 \quad (j = p, n) \tag{4.30}$$

The thermal model of the cell is constructed in 3D geometry, which is based on these works [23, 33, 144, 145]. Similar to the 2D current collector model, this model is subdivided into nine equally divided segments and coupled with the corresponding segments of the P2D electrochemical model to achieve non-uniform heat generation, and hence inhomogeneous temperature distribution in the cell. In a commercial pouch cell, there are several layers consisting of active materials, current collectors, and separators stacked one above the other, and they together constitute a cell sandwich, that is, a cell with a single layer. A multi-layered cell can be assembled by Z-folding. Fig. 4.9 shows the schematic of a multi-layered pouch cell. The active material used in this model is a composite material consisting of a cathode, anode, and separator.

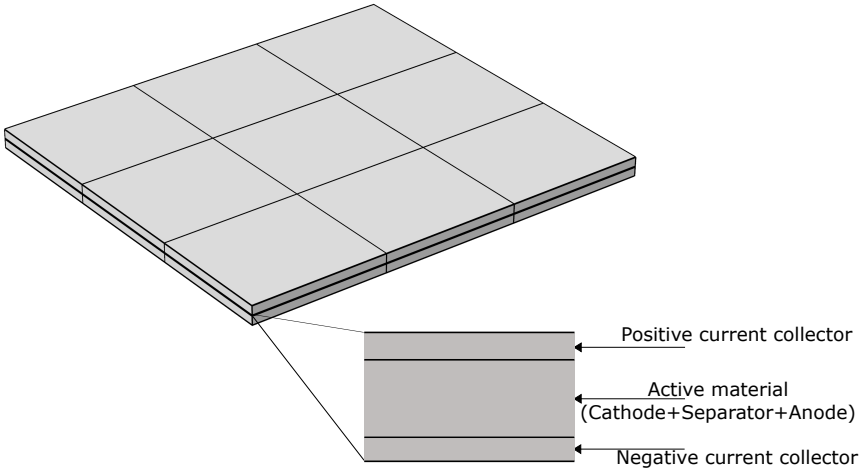

Figure 4.9: Schematic of a multi-layered pouch cell used in the 3D thermal model

The thermal parameters used for the active material is the average value of all the parameters (cathode, separator, and anode) calculated from a single layer. The average specific heat and average density of the material is calculated as shown in Eqns. (4.31) and (4.32).

$$C_{p,act} = \frac{\sum_i L_i C_{p,i}}{L} \tag{4.31}$$

$$\rho_{act} = \frac{\sum_i L_i \rho_{,i}}{L} \tag{4.32}$$

where L_i is defined as the thickness of the cathode, separator, and anode. Besides the average heat capacity and density, another important thermal parameter is the thermal conductivity of the composite material. The thermal conductivity accounts for heat transfer in the material, and it is also dependent on ambient temperature. Lower thermal conductivity reduces heat transfer (thermal insulation) and results in non-uniform heat distribution, whereas higher thermal conductivity improves the heat transfer (heat sink) and the heat distribution in the cell. The thermal conductivity also depends on the in-plane (along the surface) and through-plane (along the thickness direction) of the cell. The average thermal conductivity in a composite material is shown in Eqns. (4.33) and (4.34), for in-plane and through-plane direction respectively.

$$\lambda_{act,y} = \lambda_{act,z} = \frac{\sum_i L_i \lambda_{p,i}}{L} \tag{4.33}$$

$$\lambda_{act,x} = \frac{L}{\sum_i L_i / \lambda_{p,i}} \tag{4.34}$$

Furthermore, the thermal contact resistance between the layers is not taken into account, because most of the pores and gaps are filled with an electrolyte, which has a comparable thermal conductivity to the separator and the electrodes.

The thermal model is described by the set of equations:

The energy conservation in the cell core is described by Eqn. (4.35).

$$\rho C_p \frac{\partial T}{\partial t} = \frac{\partial}{\partial x}\left(\lambda_x \frac{\partial T}{\partial x}\right) + \frac{\partial}{\partial y}\left(\lambda_y \frac{\partial T}{\partial y}\right) + \frac{\partial}{\partial z}\left(\lambda_z \frac{\partial T}{\partial z}\right) + \dot{Q} - q_{conv} \tag{4.35}$$

The heat source mainly comes from the cell over-potential or Ohmic drop during charge/discharge; this heat is also known as irreversible heat. This heat is dissipated in the cell irrespective of the direction of current flow. The second source of heat is the entropic heat or reversible heat. In addition to these, heat is dissipated due to current flow in the tabs and is described in Eqns. (4.36), (4.37), (4.38), and (4.39).

$$\dot{Q} = q_r + q_j + q_{tab} \tag{4.36}$$

$$q_r = j^{Li}(\phi_s - \phi_e - U_{eq}) \tag{4.37}$$

$$q_j = \sigma^{eff}\nabla\phi_s \cdot \nabla\phi_s + \kappa^{eff}\nabla\phi_e \cdot \nabla\phi_e + \kappa_D^{eff}\nabla \ln c_e \nabla\phi_e \tag{4.38}$$

$$q_{tab} = \frac{I_{cell}^2 \cdot R_{tab,j}}{A_{tab,j} \cdot \delta_{cc,j}} \tag{4.39}$$

where $R_{tab,j}$ is the resistance of the cell tab (Ω), and $A_{tab,j}$ is the surface area of the cell tab (m^2).

Heat flow also depends on the ambient temperature. If the cell temperature is different than the ambient temperature, convective heat should be considered, as shown in Eqn. (4.40).

$$q_{conv} = \frac{2 \cdot h_{conv}(T - T_{ref})}{\delta_{cell}} \tag{4.40}$$

In Eqn. (4.38), the first part is the Joule heat from the solid phase, the second part is contributed by the electrolyte phase, and last part of the heat source comes from the concentration gradient in the electrolyte, which is also called the heat of mixing. The heat of mixing contributes little to the irreversible heat generation, and hence it is neglected.

Coupling is required between the electrochemical models, the current collector models, and the thermal model in order to determine the temperature distribution throughout the cell and to study the influence of temperature changes on the electrochemical performance. To couple all the sub-models, two basic rules were applied and illustrated in Fig. 4.10.

- To couple higher hierarchy domain variables with lower hierarchy domain sub-models, the variables are averaged and no spatial dependence is kept.
- To couple lower hierarchy domain variables with higher hierarchy domain sub-models, source terms are used. The variables are averaged over that domain's geometry, eliminating the coordinate system dependence, and then are converted into volumetric source terms in the higher hierarchy domain sub-model.

The 1D model receives temperature and current collector potentials as input and provides transverse current density and electrochemical heat generation as output. The input parameters of 2D current-collector model are the electrode current density and the electrode current source from the 1D model. As output, the Joule heating (irreversible heat generation) and electrode potential are provided. The inputs of the 3D thermal model are the initial temperature, ambient temperature, convective heat coefficient, and heat generation. The heat generation consists of irreversible heat, reversible heat, heat-mixing, and phase-change heating. Heat mixing and phase-change heating were neglected, as they did not contribute significantly.

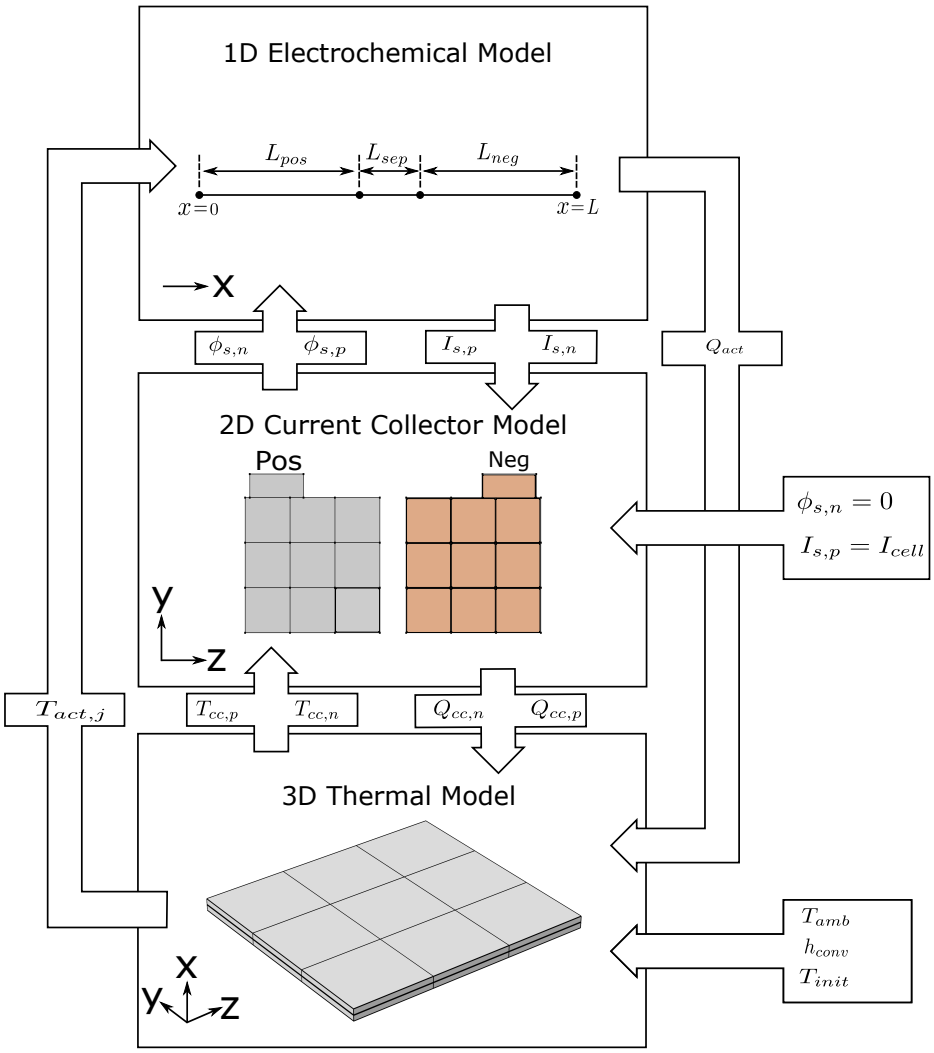

Figure 4.10: Schematic of the coupling of the electrochemical and thermal models of a cell

The electrochemical thermal model was simulated using the finite element method (FEM) software developed by COMSOL multiphysics. This multiphysics tool can solve different physics interfaces, in this case, an electrochemical battery module and heat transfer in a solid physics module. A segregated approach was used for the simulation of multi-physics. The 3D thermal sub-model was evaluated using the parallel direct solver (PARADISO), whereas the 1D electrochemical and 2D current collector sub-models were solved with the multi-frontal massively parallel solver (MUMPS). Both solvers were set to a relative convergence tolerance of 10^{-4}. Although the segregated approach generally needs more iterations until convergence, it requires less memory and time for each sub-step. Therefore, the total solution time and memory usage is low. This tool offers two types for meshing the geometries. The fastest and the easiest approach is physics-controlled mesh, depending on the type of physics. However, it is not applicable for complex geometries. The second type of meshing is user-controlled, wherein the user has the flexibility to define mesh according to the contours and complexity of the geometry. This type of meshing is suitable for 3D models, keeping in mind that certain sections of the geometry can have finer or coarser mesh depending on the accuracy and complexity of the model. Hence, the 1D and 2D models have physics-controlled mesh, and the 3D model has user-controlled mesh.

Table 4.4: Electrochemical and thermal parameters of cells used in the simulations

Symbol	Description	Value	Source
$r_{s,neg}$	Solid particle radius anode [m]	3.5×10^{-6}	[33]
$r_{s,pos}$	Solid particle radius cathode [m]	0.7×10^{-6}	[33]
$c_{s,neg,max}$	Maximum lithium concentration anode [mol/m^3]	30555	[33]
$c_{s,pos,max}$	Maximum lithium concentration cathode [mol/m^3]	49500	[33]
$c_{s,neg,0}$	Initial lithium concentration anode [mol/m^3]	$0.0287 * c_{s,neg,max}$	fitted
$c_{s,pos,0}$	Initial lithium concentration cathode [mol/m^3]	$0.82 * c_{s,pos,max}$	fitted
$c_{e,0}$	Initial electrolyte concentration [mol/m^3]	1000	assumption
$\sigma_{s,neg}$	Electronic conductivity anode [S/m]	100	[33]
$\sigma_{s,pos}$	Electronic conductivity cathode [S/m]	25	[146]
$D_{s,neg,0}$	Solid diffusion coefficient anode [m^2/s]	3.9×10^{-14}	[147]
$D_{s,pos,0}$	Solid diffusion coefficient cathode [m^2/s]	4×10^{-11}	[148]
D_e	Electrolyte diffusion coefficient [m^2/s]	Lookup table	fitted
$U_{eq,neg}$	Equilibrium potential anode [V]	Lookup table	[113]
$U_{eq,pos}$	Equilibrium potential cathode [V]	Lookup table	fitted
t_+^0	Transference number	0.38	[149]
$\frac{\partial \ln f_\pm}{\partial \ln c_e}$	Thermodynamic factor	Lookup table	fitted
$k_{a,0}$	Anodic reaction rate	1.7×10^{-11}	fitted
$k_{c,0}$	Cathodic reaction rate	1.7×10^{-11}	fitted
α_a	Anodic transfer coefficient	0.5	[147]
α_c	Cathodic transfer coefficient	0.5	[147]
$\sigma_{cc,neg}$	Electronic conductivity copper [S/m]	5.99×10^7	COMSOL library
$\sigma_{cc,pos}$	Electronic conductivity aluminium [S/m]	3.78×10^7	COMSOL library
h_{conv}	Heat transfer coefficient [W/(m^{2}K)]	9	measured
$C_{p,neg}$	Heat capacity anode [J/(kg K)]	1437.4	[38]
$C_{p,pos}$	Heat capacity cathode [J/(kg K)]	1269.21	[150]
$C_{p,sep}$	Heat capacity separator [J/(kg K)]	1978.2	[38]
$C_{p,al}$	Heat capacity aluminium [J/(kg K)]	900	[38]
$C_{p,cu}$	Heat capacity copper [J/(kg K)]	385	[38]
λ_{neg}	Thermal conductivity anode [W/(m K)]	1.04	[38]
λ_{pos}	Thermal conductivity cathode [W/(m K)]	1.58	[150]
λ_{sep}	Thermal conductivity separator [W/(m K)]	0.3344	[38]
λ_{al}	Thermal conductivity aluminium [W/(m K)]	238	[38]
λ_{cu}	Thermal conductivity copper [W/(m K)]	400	[38]
ρ_{neg}	Mass density anode [kg/m^3]	1347.33	[151]
ρ_{pos}	Mass density cathode [kg/m^3]	2328.5	[150]
ρ_{al}	Mass density aluminium [kg/m^3]	2700	[38]
ρ_{cu}	Mass density copper [kg/m^3]	8900	[38]
$\epsilon_{e,neg}$	Electrolyte porosity at anode	0.33	[152]
$\epsilon_{e,pos}$	Electrolyte porosity at cathode	0.35	[152]
$\epsilon_{e,sep}$	Electrolyte porosity at separator	0.35	[145]
$\epsilon_{s,neg}$	Anode volume fraction	$1 - \epsilon_{l,neg} - \epsilon_{non,neg}$	[153]
$\epsilon_{s,pos}$	Anode volume fraction	$1 - \epsilon_{l,pos} - \epsilon_{non,pos}$	[153]
$\epsilon_{non,neg}$	Volume fraction of non-active material anode	0.1	[146]
$\epsilon_{non,pos}$	Volume fraction of non-active material cathode	0.3	[146]

Chapter 5

Results and Discussion

5.1 Aging Test Results

This chapter evaluates the performance of different cell sizes and cell forms by performing the aging tests on the selected cells. The selection of the cells for this investigation can be seen in Tab. 3.1. In addition to this, the influence of cell form was also evaluated with comparison of aging results of a pouch cell form (Tab. 3.1) and a cylindrical cell form (Tab. 3.2). The cylindrical cells of different size and NMC chemistry were not commercially available for comparison. Therefore, the LFP chemistry with two different sizes was chosen for the investigation. The subsequent sections compare capacity fade, impedance rise, OCV and SOC characteristics, storage, and cycling characteristics of the selected cells.

5.1.1 Capacity Fade

The capacity fade was measured by comparing the discharge capacity of the cells with respect to their initial discharge capacity. As the discharge capacity of the cell varies with temperature and discharge C-rate, these conditions were kept constant at 25°C and 1C discharge current, respectively. The end of the test criteria was reached if the cell capacity dropped below 70% of its initial value (C_0). Fig. 5.1 shows the remaining capacity under cycle aging conditions for different cell sizes. The results consisted of two parts, (a) pouch cells and (b) cylindrical cells. The evolution of capacity fade in pouch cells were different for different cell sizes. The capacity fade showed non-linear characteristics, that is, the rate of capacity fade was not constant throughout the cycles. There was an increase in the cell capacity for pouch cells, except for the 8 Ah cells in the initial cycles, that is, between 0 and 2 weeks. This strange phenomenon has not been discussed in the literature related to aging studies. In general, the cell capacity decreases rapidly in the initial cycles, due to the formation and growth of SEI layer. After the initial phase, the growth of SEI layer decreases, thereby reducing the consumption of cyclable Li^+ [11, 154, 155]. On the one hand, the growth of SEI indicates the existence of side reactions in the cell, but, on the other hand, the SEI layer also functions as a protective layer and reduces the rate of side reactions. Hence, the rate of capacity loss decreases after the initial cycles. The 8 Ah cells shows similar behaviour to this. However, the capacity increase in 25, 53, and 75 Ah cells indicate that there might be high initial self-discharge reaction on the anode, which during the initial cycling weeks resulted in more active Li^+ upon reversible self-discharge during subsequent charge and discharge steps.

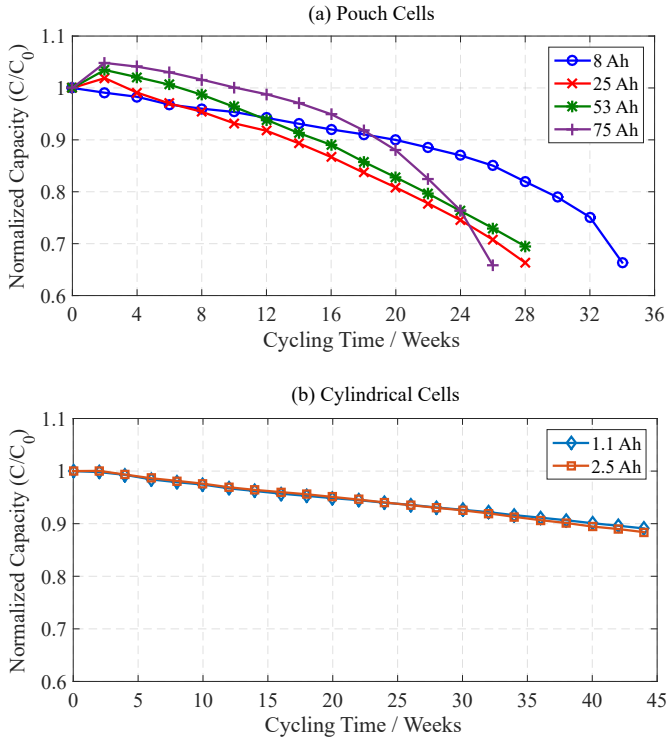

Figure 5.1: Remaining capacity (normalized) for different cell sizes under cycle aging conditions, (a) pouch cells, (b) cylindrical cells

Capacity balancing of the anode and cathode is done by the manufacturer to obtain optimal performance, electrochemical and thermal stability, and safety of the lithium-ion batteries. Both electrode materials have different gravimetric energy densities. This value in combination with useful stoichiometry of the electrode material provides the active mass of the electrode. The ratio of the active masses of the anode and cathode determines the capacity balancing of a cell, as shown in Eq. (5.1).

$$\gamma = \frac{m_+}{m_-} = \frac{\Delta x C_-}{\Delta y C_+} \tag{5.1}$$

The notations Δx and Δy are the stoichiometric ranges ($0 < \Delta x, \Delta y < 1$) of negative and positive electrodes, respectively. The electrode's active mass and coulombic capacity (in mAh) are denoted as m and C, respectively. In ideal conditions, the active mass ratio (γ) does not change over time or with frequent cycles of charge and discharge, that is, its value remains constant throughout. However, in practical conditions, there are many side reactions occurring inside the cell that alter the active mass ratio. The most common side reactions are the formation and growth of the SEI layer, lithium plating, and other aging processes (described in section 2.2). As the SEI layer has both, positive and negative contributions to cell performance, cell designers keep the active mass ratio higher at the beginning to aid the formation process, that is, the excess capacity is the measure of the amount of lithium required to form a stable SEI layer. However, the active mass ratio (γ) cannot be increased to an indeterminate value, as an excess positive material could lead to a lithium plating process, under favourable conditions. Hence, the anode material is slightly oversized (in dimensions) with respect to the cathode to prevent lithium plating on its surface. Tab. 3.1 shows the ratio of the electrode area of the cathode and anode. It is apparent that the active mass ratio of the cell increases from 8 Ah to

75 Ah. In larger cell sizes, a higher self-discharge reaction followed by capacity recovery contributes to a slight increase in the cell capacity in the initial stages of the cycle aging. However, at the later stages of cycling, the side reactions from the cell contributed to the loss of cyclable Li^+, thereby resulting in a loss of capacity. The quantity of the cyclable Li^+ was determined by the range of stoichiometry. This range should be chosen carefully such that the electrochemical reaction is reversible and the cell is used in the safe operating window [156]. Hence, in most cases, the full range of stoichiometry is avoided, and only a limited range is used for a stable reversible reaction.

The cylindrical cells 1.1 and 2.5 Ah showed capacity fade similar to the 8 Ah cell, that is, loss of capacity from the start of cycling. Even after 44 weeks of cycling, the capacity loss rate was linear. In comparison to the 8 Ah cell, the cylindrical cells of both dimensions showed excellent capacity retention, and there was only 10% capacity loss after 44 weeks, whereas the 8 Ah cell lost nearly 35% capacity after 34 weeks. The aging of cylindrical cells towards the end was linear compared to the aging of pouch cells. In spite of different cell chemistries of cylindrical and pouch cells, the results showed that there was a strong influence of cell size when the cells were subjected to cycle aging.

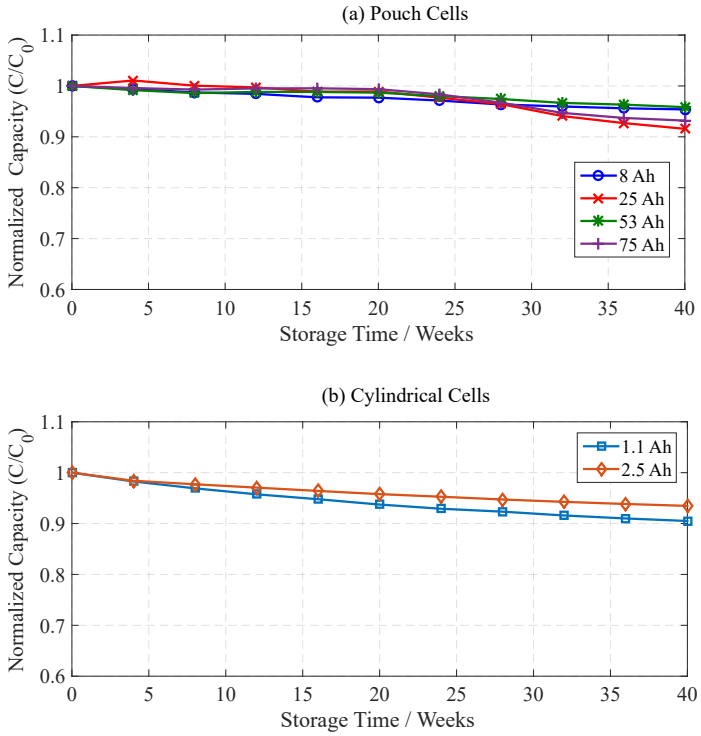

Figure 5.2: Remaining capacity (normalized) for different cell sizes under 40°C and 100% SOC storage conditions, (a) pouch cells, (b) cylindrical cells, measured at room temperature

The performance and aging characteristics of the cells under storage conditions determine the shelf life of the cells. In most private HEVs/EVs, the battery packs are not used for 90% of the operational time. Therefore, the cells are predominantly subjected to calendar aging under different SOCs and storage temperatures. Fig. 5.2 shows the remaining capacity of cells stored at 40°C and 100% SOC storage conditions. In this research, the cell capacities were measured at room temperature, as described in section 3.4.1. The results showed that calendar aging is nearly the same among different cell sizes, subjected to ±2% variation in remaining capacity. The variation in the measurements can be contributed by multiple factors, such as actual cell temperature inside the storage chamber, measurement inaccuracies, cell manufacturing conditions, and so on. The results of the storage test for the cylindrical-form

2.5 Ah cell was also similar to that of the pouch cells. However, the 1.1 Ah cylindrical cell form showed a slightly higher capacity loss. This could be attributed to the measurement inaccuracies contributed by differences in the manufacturing processes.

5.1.1.1 Calendar Aging and Cycle Aging Comparison

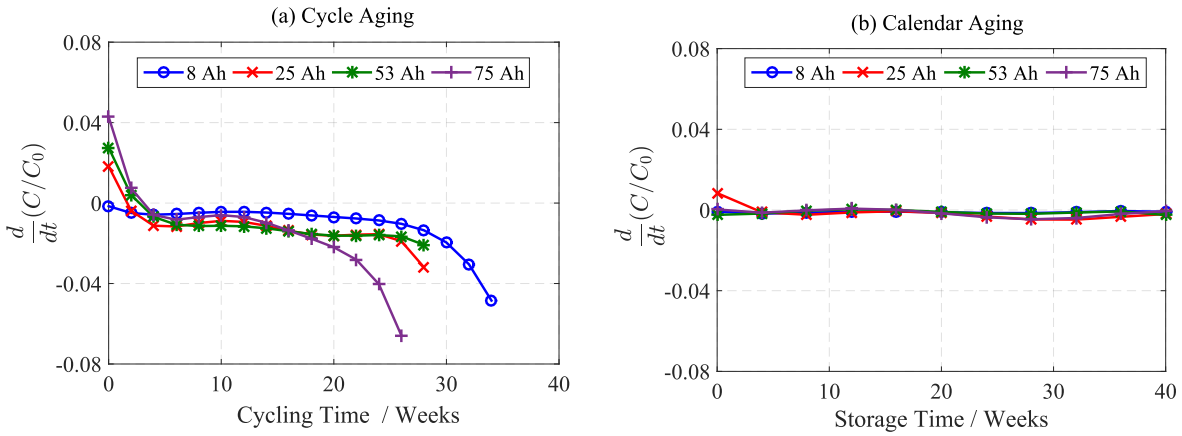

Figure 5.3: Plot of differential capacity fade with respect to time; (a) cycle aging, (b) calendar aging

The comparison of capacity loss during calendar and cycle aging tests on the selected cells clearly indicated that calendar aging has little influence on overall aging during the same period as compared to that of cycle aging. It shows that cycle aging induces more stress and causes the cells to degrade faster during a selected period of time in comparison to cells stored at the same ambient temperature. It was also observed that calendar aging was nearly the same among different cell sizes, subjected to ±2% variation in the cell capacities due to measurement inaccuracies. These results gave an indication that calendar aging had very little or no influence arising due to variation in cell size, that is, irrespective of whether the cell size is smaller or larger, of whether calendar aging was similar under the same chemistry, or cell composition and manufacturing process. To further validate this, a closer view of Fig. 5.3(a) revealed that there were different stages of aging where the capacity loss rate was either linear or non-linear and the loss rate was not same for all cell sizes, especially for cycle aged cells. The differential plots indicated that sizing did have an influence on cycle aging. At the initial stages of cycling, the cells of larger size had a negative capacity loss rate, owing to increase in cell capacity. The 8 Ah cell showed nearly constant capacity loss up to 24 weeks, which is similar to capacity loss rate for the 25 and 53 Ah cells between 4 to 24 weeks of cycling time. However, the 75 Ah cell showed an increased rate of capacity loss throughout the cycling time. Towards the EOL, all pouch cells showed non-linear aging. Hence, these results concluded that pouch cells of different sizes experienced non-linear aging, which is strongly related to inhomogeneity, and the degree of non-linearity increased with the increase in cell size. In comparison, the cells that experienced calendar aging (Fig. 5.3(b)) had constant capacity loss rate. This behaviour is slightly different from the square-root-of-time characteristics described in the literature. However, if the aging factor or capacity loss factor is slow [157], the square root and linear function results are similar, that is, there is no significant loss of capacity in the calendar aged cells.

Therefore, these results have proved the following hypotheses, proposed in Chapter 1.2 of the thesis.

- Cell sizing influences cycle aging, that is, when the cells are charged and discharged regularly.

- Cell sizing should not influence calendar aging, as the inhomogeneities do not occur when the cells are stored in OCV relaxation state.

5.1.1.2 Self-Discharge During Storage

The scope of the aging tests on different cell sizes were not intended to develop a holistic aging model, but rather to prove that cell size has an influence on cycle life aging. Nevertheless, with limited tests performed to evaluate calendar aging, it is interesting to study the self-discharge losses in cells. Self-discharge is a phenomenon in batteries wherein the internal electrochemical reactions reduce the storage capacity, without any external connection. It reduces the calendar life of the battery by being able to discharge less capacity than its previously charged capacity. Lithium-ion cells have low self-discharge rates compared to other battery technologies, such as NiCd and NiMH. Self-discharge in lithium-ion cells consists of reversible and irreversible losses. Reversible capacity loss can be defined as a process wherein the cyclable Li^+ can be recovered by charging and discharging the cell again, whereas irreversible losses is the capacity that cannot be recovered. The following steps explain the calculations of these losses [157]:

1. The discharge capacity of the cell is measured at 25°C, as explained in section 3.3.1.
2. Fully charge the cell in CCCV at 25°C, 1C C-rate until the upper cut-off voltage 4.2 V and 0.05C current cut-off.
3. Calendar aging test at 40°C for 4 weeks.
4. Measure the discharge capacity as explained in step 1.
5. Calculate the difference between the cell capacity measured in step 1 and step 4 to obtain self-discharge loss.
6. Charge the cell as described in step 2.
7. Discharge the cell again as described in step 1. The difference between measured capacity in step 1 and the current step is the irreversible capacity loss.
8. The difference between the self-discharge and irreversible capacity loss is known as the reversible capacity loss.
9. Repeat steps 2 and 3 to continue the calendar aging tests.

The formation and growth of SEI layers due to electrolyte decomposition and consumption of cyclable Li^+ is one of the by-products of irreversible capacity losses. Other irreversible side reactions, such as metal-oxide dissolution, solvent dissolution, and lithium plating can also contribute to irreversible capacity loss. The rate of self-discharge depends on the nature of the electrolyte and solvents. Additionally, pore blockage due to oxidation products and high internal resistance also contribute to self-discharge. The reversible capacity losses can be recovered mainly by reversible insertion of Li^+ into the positive electrode structure. This can be done by recharging the cell. The reversible losses can also be attributed to the leakage currents through the separator of the cell due to impurities that exist in the separator. This capacity can be recovered with low C-rate cycling.

Fig. 5.4 shows the comparison of self-discharge and reversible and irreversible capacity losses during the calendar aging tests of the pouch cells. In the initial weeks, the self-discharge rate was high for the cells.

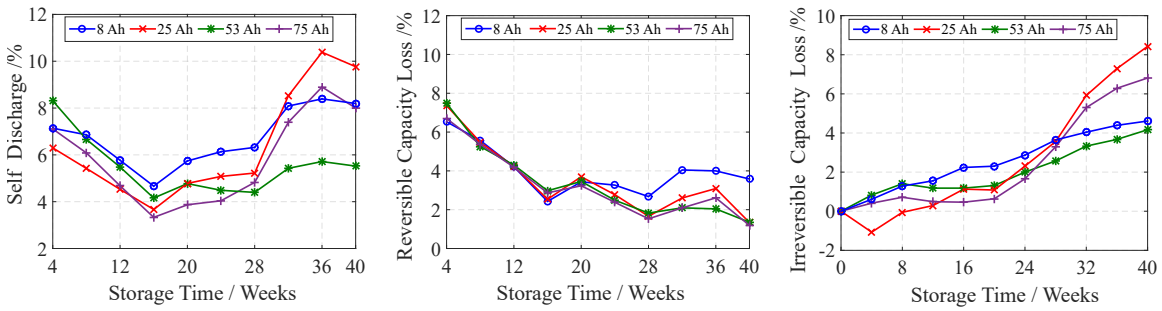

Figure 5.4: Comparison of self-discharge, reversible capacity loss, and irreversible capacity loss during calendar aging

After the self-discharge was measured, the cells were recharged to 100% SOC and discharged again to measure reversible capacity loss and the capacity fade due to irreversible losses. The capacity retention was excellent, with very low losses due to irreversible reactions. Hence, during the initial weeks of the storage, the cells exhibited an overall good capacity retention during the second discharge, which followed the self-discharge tests. As the weeks progressed, the self-discharge rate was low compared to that of the initial weeks, but the capacity recovery gradually decreased, and, at the same time, the irreversible losses also increased. Towards the end of 40 weeks of storage, the self-discharge again increased due to the significant contribution of irreversible capacity losses.

Hence the results can be summarized as follows:

- High capacity recovery during the initial weeks ensured that cells were able to retain most of the lost capacity during self-discharge.
- As the storage time increases, the reversible losses decreased and irreversible losses increased as an indication of the continuing aging process in the cells.
- Accumulated irreversible losses towards the end of 40 weeks were high, assuming that the aging process was influenced by the growth of SEI layers, dissolution of cathode materials, and other side reactions.

5.1.2 Power Fade

Power fade is the loss of power capability during the operation of a battery, resulting from an increase in its internal resistance or impedance. It reduces the efficiency of the battery, especially at high C-rate cycling, inducing rate capability losses. It also reduces the charge and discharge capacity of the cell because of higher voltage polarization, which causes the cut-off voltage to be reached sooner. The resistance increase is also an indication of the low SOH of the battery, for example, a battery with low SOH attains the upper cut-off voltage faster when it is charged in the CC phase and remains in the CV for a longer duration. Fig. 5.5 shows the plot of resistance over cycling time at 20, 50, and 80% SOC intervals for different cell sizes. The cell resistance was calculated from the 10 s current pulse and by measuring its voltage response, as shown in Fig. 3.8. Eqns. (5.2) and (5.3) were used to calculate the resistance and discharge power of the cell, respectively. It can be observed that, irrespective of the size, the resistance of the cells increased with cycling time, that is, the capacity increase in the initial

stages of the cycling of 25, 53, and 75 Ah cells had no effect on the evolution of the resistance.

$$R_{cell} = \left(\frac{\Delta V^{1}}{\Delta I}\right)_{t=10s,3CDCH} \tag{5.2}$$

$$P_{DCH} = \frac{V_{min} \cdot (OCV - V_{min})}{R_{cell}}$$

where $V_{min} \approx \frac{1}{3} \cdot OCV$

$$= 2/9 \cdot \frac{OCV^2}{R_{cell}} \tag{5.3}$$

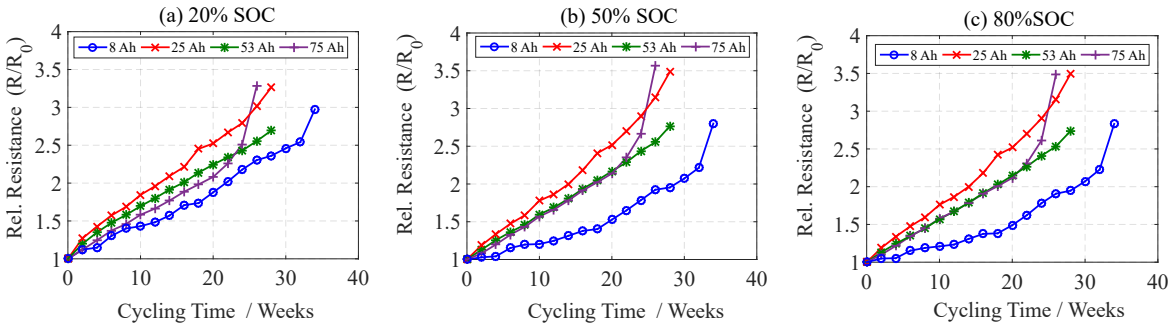

Figure 5.5: Normalized 10 s DC resistance vs. the cycle time of different cell sizes and SOC intervals

The results show the resistances of the 25 Ah cells at different SOCs were higher compared to the other pouch cells. Similar results were also observed with respect to capacity loss in the selected cells. However, the 75 Ah cell showed significant increase in its resistance between 20 and 26 weeks. This phenomenon coincides with its rapid capacity loss during the same duration. Hence, there is a strong relation between the capacity loss and resistance increase. At 20% SOC, it is not clear which cell size had a higher resistance increase, but, at 80% SOC, it became clearer that the 8 Ah cell and 75 Ah cell had respectively lower and higher resistance increases, with the exception of the 25 Ah cell.

Fig. 5.6 shows the normalized discharge power of selected pouch cells plotted with respect to the cycling time. These values were directly derived from their respective cell resistances. When these results were compared with the discharge power from the calendar aging tests shown in Fig. 5.7, cycle aging had a maximum impact on the discharge power of the cell. The actual discharge power was reduced to less than 40% of its nominal value throughout different SOC levels. It was expected that the discharge power capability of cells undergoing calendar aging would be similar across different cell sizes, as it was the same in the case of discharge capacity. Nevertheless, the differences in the discharge capacity were less in calendar aging when compared with cycle aging results. Even though there is a correlation between measured capacity and power capability, they are still different cell parameters. While the former arises due to loss of cyclable Li^+, structural degradation, active material dissolution, the latter is due to SEI film resistance, electrolyte resistance, loss of contact between active material and current collectors, and so on.

[1] $\Delta V = \Delta V_0 + \Delta V_1 + \Delta V_2$ as shown in Fig. 3.8

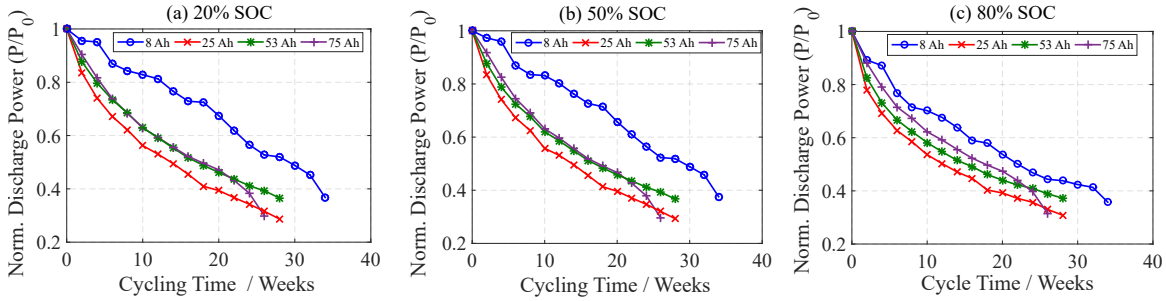

Figure 5.6: Plot of discharge power at different SOCs during cycle aging for different cell sizes

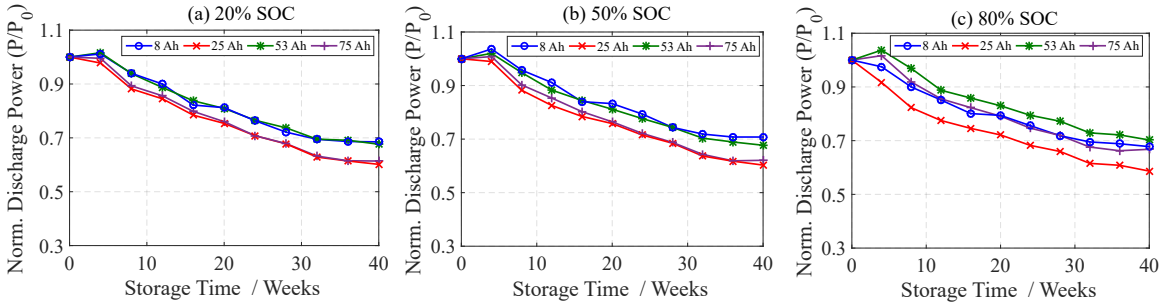

Figure 5.7: Plot of discharge power at different SOCs during calendar aging for different cell sizes

5.1.3 OCV and SOC Dependency on Aging

SOC is an indication of the amount of charge remaining in the battery. When the battery is new, the rated or nominal capacity refers to its actual capacity. Aging of a battery introduces capacity loss, and hence towards the EOL, the actual SOC would not attain 100% of its rated value. This constant changing of SOC definition throughout the lifetime of the battery could influence the functioning of BMS. OCV is closely related to SOC in most battery technologies, with the exception of LFP-based materials. The estimation of SOC requires accurate evaluation of OCV and hence is an important step towards the prediction of battery performance and its safe operation window.

From a modelling and simulation perspective, the cell OCV, resistance, and capacitance values are dependent on SOC. The evaluation of these parameters at different SOC intervals was done by SOC definitions based on the actual capacity remaining at every aging interval. Thereafter, the battery models were simulated based on these parameter adjustments to obtain output voltage, power capability, and so on. Fig. 5.8 shows measurements of OCV with respect to actual SOC at different aging intervals for 8, 25, 53, and 75 Ah cells.

A 2D lookup table for OCV comprised of SOC interval and cycling time, together with lookup tables for other parameters were passed on to the battery model to simulate terminal voltage, as described in section 5.4. At first glance, it appeared as though there was not much change in the OCV values in different aging histories, but a closer observation at 100% SOC state showed a slight drift in the OCV value. To quantify this deviation, the OCV values at 100% SOC for a 75 Ah cell were plotted versus cycling time, as shown in Fig. 5.9 (a). At the beginning of cycling, the OCV value at 100% SOC was high, but, as the cycling time increased, the OCV value dropped by nearly 30 mV towards the EOL. The gradual decrease in the OCV could be an indication of consumption of Li^+ inventory, thereby

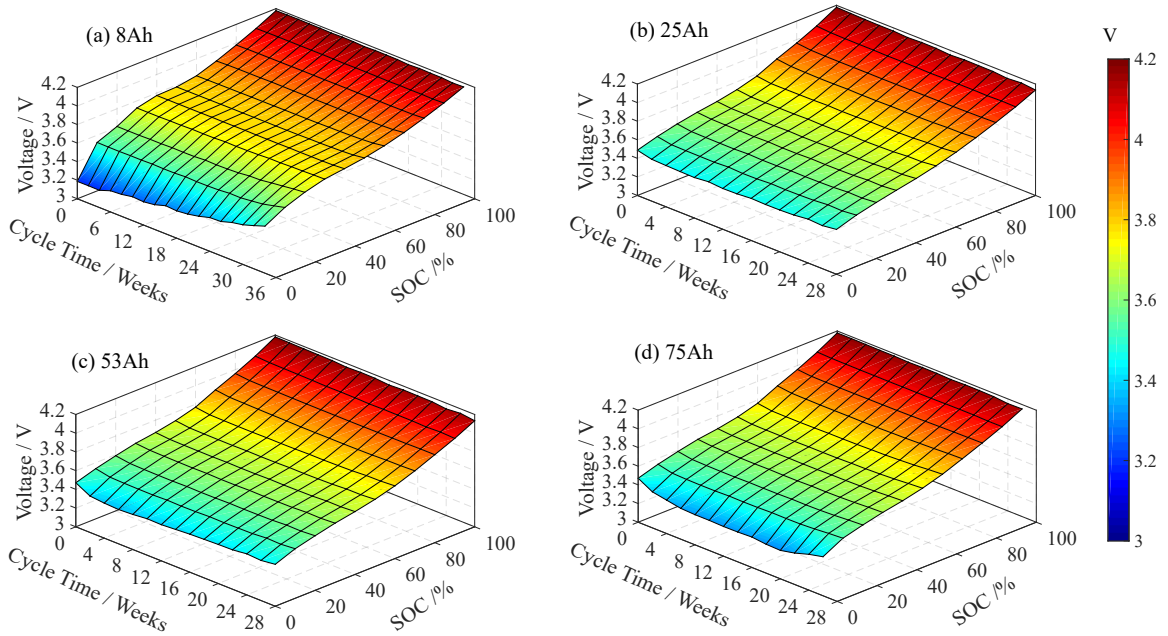

Figure 5.8: Open circuit voltage as a function of SOC and cycling time for 8, 25, 53, and 75 Ah pouch cells

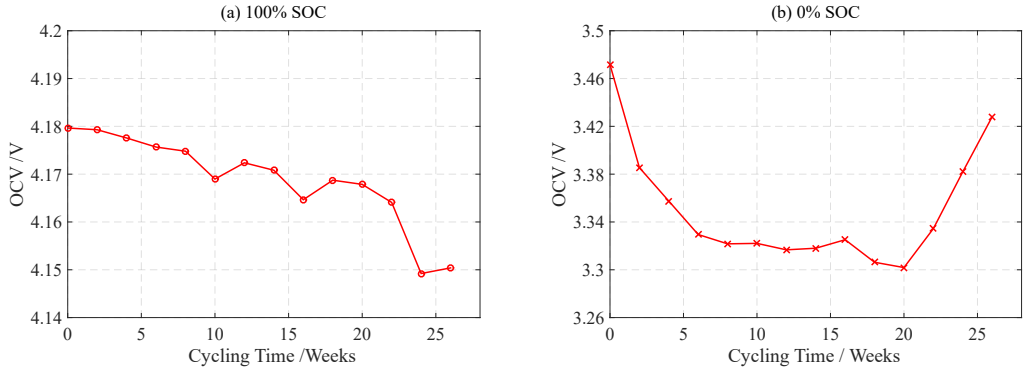

Figure 5.9: Open circuit voltage plotted vs. cycling time for a 75 Ah cell at (a) 100% SOC, (b) 0% SOC

affecting the stoichiometry of the cathode material or an increase of the resistance [158]. Fig. 5.9 (b) shows the OCV value versus cycling time at complete discharge state (0% SOC). The OCV value had significantly decreased in the initial weeks and continued to decrease until 20 weeks. This was similar to the voltage drop at 100% SOC. Thereafter, it started increasing again until the end of its life. The sharp increase in the OCV might have been influenced by the cell cut-off voltage being attained faster due to an increase in the cell resistance during the same time [26]. Therefore, high polarization voltage close to 0% SOC and followed by 1 h of rest time could have resulted in the voltage relaxing to a higher value.

5.2 Spatial Measurements to Evaluate Inhomogeneity

Spatial measurements of the battery is a widely used method to evaluate temperature and volume expansion inhomogeneity. These measurement techniques are explained in section 3.1 and employed in the pouch cells, where it is easier to place sensors on the cell surface. The spatial measurements consist of temperature and displacement measurements on different cell sizes. The results of these measurements are discussed in this section.

5.2.1 Spatial Temperature Profile

The spatial temperature measurements were recorded on the pouch cells with different sizes at different ambient temperatures and C-rates, as described in section 3.3.4. The measurements were done by employing different cooling techniques, forced air convection, and aluminium cooling plates, placed on the two largest cell surfaces. At first, these measurements were done on fresh cells before the commencement of aging tests. These measurements were repeated when the cells reached their EOL. The measurements were evaluated to find the maximum temperature gradient (ΔT_{max}) at each temperature and C-rate. Fig. 5.10 shows ΔT_{max} measured among different cell sizes, plotted over different C-rates and temperatures. In this setup, the cells were cycled inside the temperature chamber at a constant ambient temperature. Hence, the heat dissipation from the cell occurred through forced air convection. It was observed that ΔT, the temperature inhomogeneity, increases with increase in ambient temperature and C-rate. ΔT also increases with an increase in cell size, with the exception of 25 Ah, whose ΔT value is lower than that of the 8 Ah cell, even though its geometric size is large. It was observed that 25 Ah cells had the smallest thickness of all the cells (Tab. 3.1). The slimmer cell could have resulted in less heat trapped in the volumetric heat source and might have resulted in better heat exchange with the outside [22, 37]. Fig. 5.11 shows ΔT_{max} measured among different cell sizes at different ambient temperatures and C-rates, with aluminium cooling plates on the cell surface. Indirect cooling with aluminium cooling plates was more effective than forced air convection, as the two largest surfaces of the pouch were in contact with the plates.

In comparison to the forced air circulation, the ΔT_{max} was always greater for the cooling plates setup for all temperatures, C-rates and cell sizes. But the similarities in both cases were that ΔT was determined by temperature, C-rate, and cell size. Again, there was an exception for the 25 Ah cell, where ΔT was much lower than for the other cells for all test conditions. The explanation is the same as described in the previous paragraph, based on the cell thickness.

The cooling plates employed on the cells improved the overall thermal management of the battery by dissipating the heat generated in the cells, which reduced the temperature rise significantly. Tab.

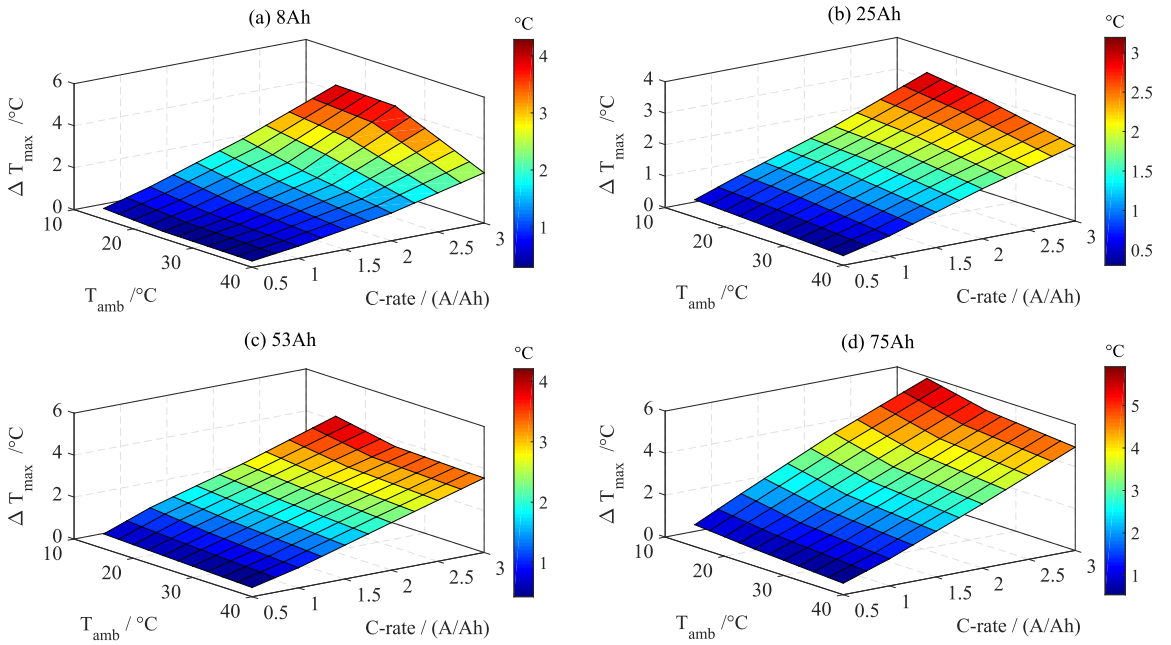

Figure 5.10: Maximum temperature gradient measured on the cell surface, plotted against C-rate and temperature for an a) 8 Ah cell, b) 25 Ah cell, c) 53 Ah cell, and d) 75 Ah cell under forced air convection

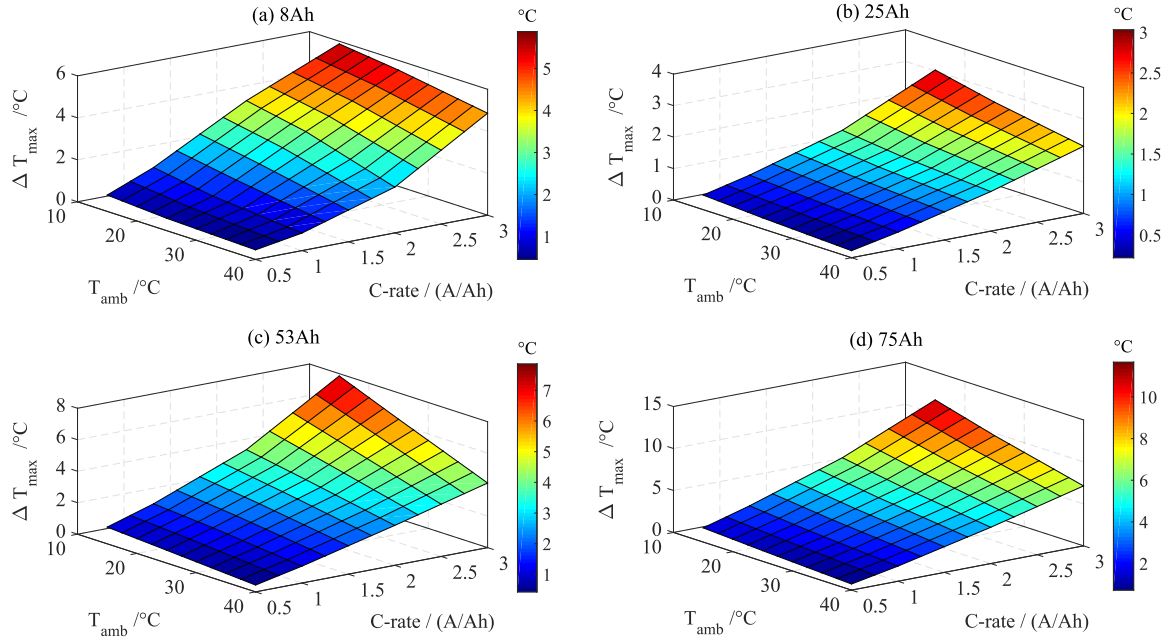

Figure 5.11: Maximum temperature gradient measured on the cell surface, plotted against C-rate and temperature for an a) 8 Ah cell, b) 25 Ah cell, c) 53 Ah cell, and d) 75 Ah cell with Al. cooling plates

5.1 shows the comparison of the maximum temperature attained by the cells during 3C discharge current, with different cooling methods. The cells cooled with forced air convection did not dissipate the heat efficiently, resulting in a large difference between the temperature attained by the cell and the ambient temperature. It is a well established theory that temperature accelerates the aging of the cells, explained by the Arrhenius equation. If this temperature evolution were to continue over many cycles of charge and discharge, the expected lifetime of the cell would be reduced significantly. According to Arrhenius relations, the life expectancy of the cell reduces at temperatures above 20°C [61]. In addition to lifetime reduction, the safety of the cells could be compromised if the cell temperature exceeds 60°C, especially for the larger cell sizes. This situation arises especially at high ambient temperatures and C-rates (e.g., 40°C and 3C discharge current). If battery packs are to be built with large format cells (e.g., 75 Ah cells), forced air cooling might be ineffective due to stressful operating conditions.

Table 5.1: Comparison of maximum temperature attained with a 3C discharge C-rate; (a) forced air convection, (b) aluminium cooling plates at different ambient temperatures

Cell Type	Max. Temperature [°C]					
	Forced air convection			Al. cooling plates		
	15°C	25°C	40°C	15°C	25°C	40°C [2]
8 Ah	42.1	49.1	54.8	22.8	32.3	46.3
25 Ah	35.8	47.8	59.4	22	30.8	44.5
53 Ah	42.9	52.5	63.7	29.8	36	47
75 Ah	43.8	54.8	65.2	32.7	39	50.1

As observed in Tab. 5.1, large-format cells are relatively safer to work with when aluminium cooling plates are employed for the thermal management. Even though aluminium cooling plates reduce the overall cell temperature, they increase the temperature inhomogeneity, and this leads to different regions of the cell experiencing varied temperatures. If the non-uniform temperature distribution continues for many cycles, the cell undergoes inhomogeneous aging.

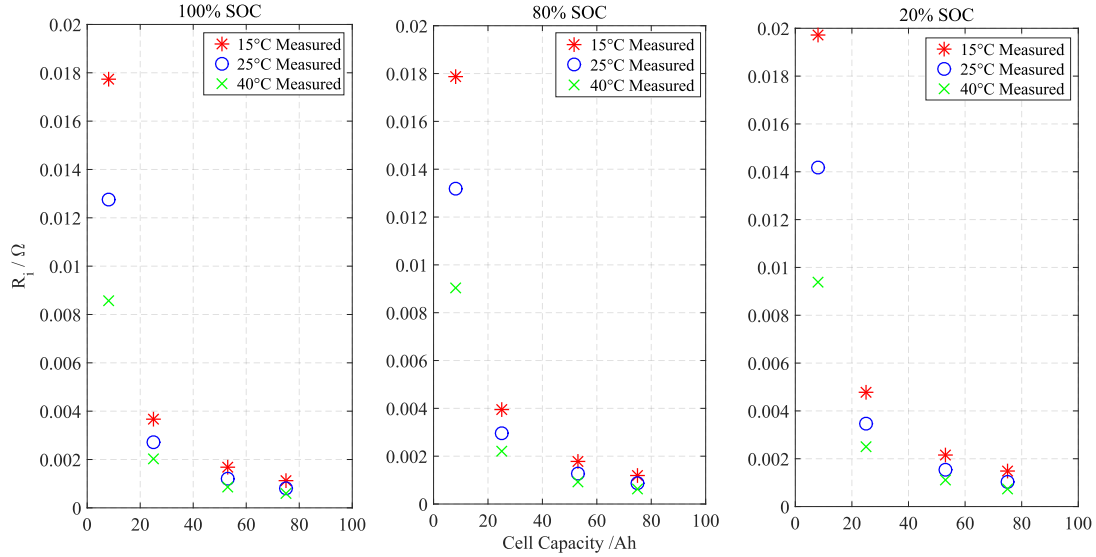

Figure 5.12: Internal resistance of the cell measured with electrochemical impedance spectroscopy (EIS) at different temperatures and SOCs

To study the impact of ambient temperature on ΔT, the sources of heat generation in the cells were evaluated. One of the main sources of heat generation comes from Joule heating, which depends

[2] Ambient temperature

on input current and the internal resistance of the cell. The EIS tests were performed on these cells at different temperatures and SOCs, as explained in section 3.3.2.2, to evaluate their internal resistance (R_i). The internal resistance is the sum of electrolyte resistance, current collector resistance, active material resistance, and so on. Other resistances, like solid electrolyte interface resistance (R_{SEI}), charge transfer resistance (R_{ct}), diffusion impedance (Z_W), and double layer capacitor (C_{dl}) also contribute to irreversible heat loss, but not to the extent of R_i. Fig. 5.12 shows the plot of R_i, calculated from EIS measurements at different temperatures, SOCs, and cell capacities. It can be observed that the value of R_i is sensitive to temperature changes, and the value increases nearly by a factor of two, from 40°C to 15°C. Hence, it can be assumed that the ΔT value is maximum at low ambient temperature, because of the effect of change in cell impedance along the cell surface that results in different localized temperatures, as shown in Fig. 5.10.

It is a well known fact that the aging mechanism in the cell causes a loss of its capacity and an increase in its impedance. One of the main reasons for an increase in the overall temperature in the aged cells is impedance rise. After the completion of the cycle aging tests, the spatial temperature measurements were repeated on these cells. The original test matrix was used, except with one alteration. The 3C discharge C-rate was omitted from the scope of the tests because the cell surface temperature exceeded 60°C during this high current discharge. Fig. 5.13 shows ΔT_{max} measured on aged cells of different sizes, plotted over temperature and C-rate.

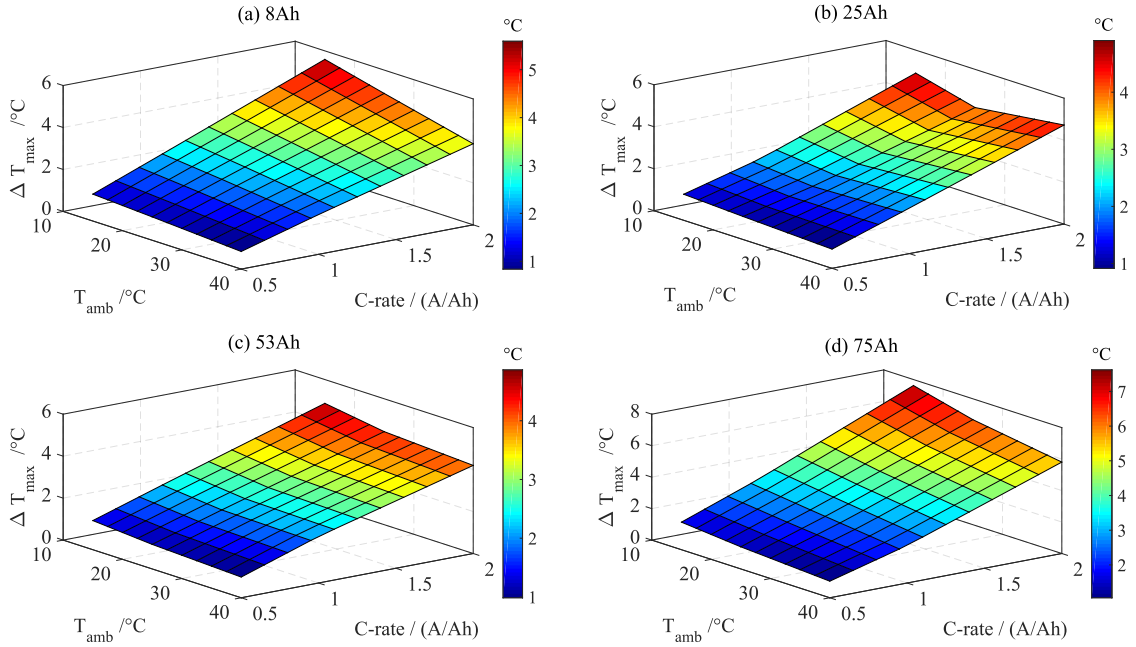

Figure 5.13: ΔT_{max} measured on aged cells, plotted over C-rate and temperature for an a) 8 Ah cell, b) 25 Ah cell, c) 53 Ah cell, and d) 75 Ah cell under forced air convection

As the ΔT_{max} surface plots of fresh and aged cells are plotted in different scales of C-rates, it is not easy to compare the results. Tab. 5.2 shows the ΔT_{max} values of fresh and aged cells under the same testing conditions. It can be seen that the ΔT_{max} value of aged cells increased by at least by double in relation to fresh cells, that is, before the commencement of the cycle aging tests. Hence, these results prove that aging increased the temperature inhomogeneity in the cells irrespective of their sizes. The increase in temperature non-uniformity means that heat generation was inhomogeneous across the cell. As the Joule heat was the major contributor to heat generation, it was an indication

that different regions of the cell exhibit varied resistance. As resistance increase is directly related to the aging mechanism (see Fig. 5.5), it can be concluded that cells undergo inhomogeneous aging. Additionally, the spatial temperature measurement on aged cells with aluminium cooling plates could not be performed accurately, because the aging introduced uneven growth of the cell thickness. This resulted in an uneven surface with many peaks and valleys. Hence, many parts of the cell surface could not come into contact with the cooling plates. This problem was non-existent in cells before the start of cycling. Thickness growth during the aging process is seldom discussed in the literature [159]. Section 5.2.2 describes this phenomenon and also discusses the measurement of volume displacement in pouch cells.

Table 5.2: Comparison of ΔT_{max} for fresh and aged cells of different sizes under forced air cooling conditions

ΔT_{max} [°C]							
	8 Ah				25 Ah		
	Fresh\Aged				Fresh\Aged		
	15°C	25°C	40°C		15°C	25°C	40°C
0.5C	0.51\1.28	0.34\1.11	0.30\0.84	0.5C	0.55\1.24	0.46\1.10	0.31\0.92
1C	1.13\2.71	0.77\2.40	0.59\1.90	1C	1.08\2.24	0.95\1.99	0.65\2.17
2C	2.57\5.60	1.97\4.89	1.32\3.86	2C	2.04\4.91	1.94\4.18	1.59\4.72
	53 Ah				75 Ah		
	Fresh\Aged				Fresh\Aged		
	15°C	25°C	40°C		15°C	25°C	40°C
0.5C	0.70\1.39	0.59\1.17	0.44\0.99	0.5C	1.05\1.75	0.81\1.40	0.55 \1.05
1C	1.53\2.57	1.24\2.29	0.96\2.22	1C	2.10\3.55	1.63\3.08	1.29\2.39
2C	2.78\4.87	2.54\4.43	2.26\4.2	2C	4.14\7.62	3.45\6.67	3.06\5.81

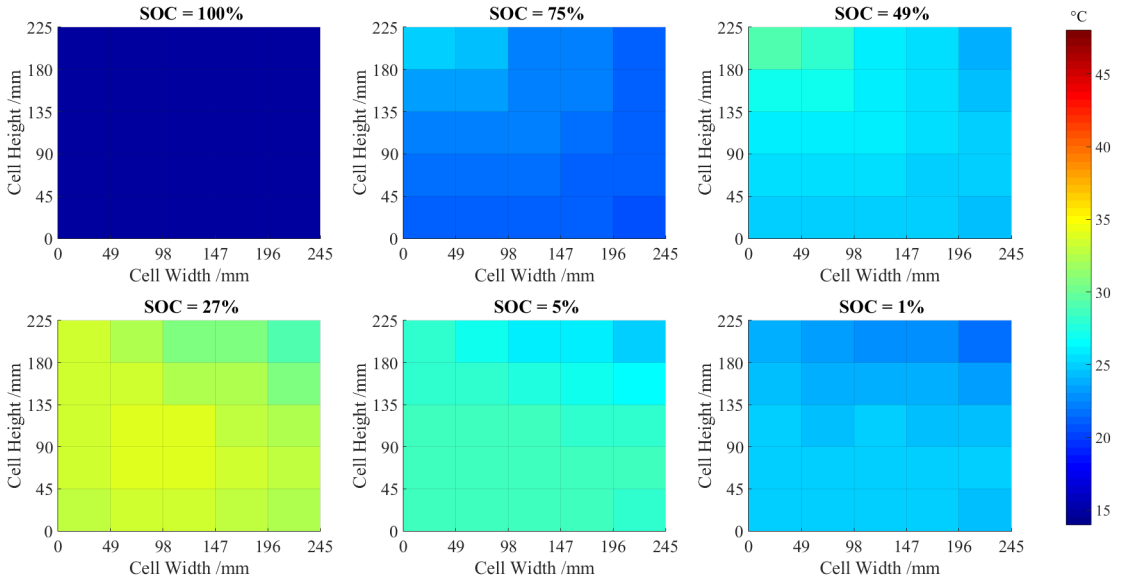

Figure 5.14: Temperature map on the cell surface of fresh 75 Ah cell during CCCV discharge with 2C discharge current under forced air cooling at 15°C ambient temperature

Figs. 5.14 and 5.15 compare the surface temperature plot on fresh and aged cells. The cells were completely discharged in CCCV mode[3] at 2C current from a fully charged state at 15°C ambient

[3] This discharge regime was chosen because the ambient temperature was low and discharge current was high. It could lead to rate capability loss if the cell is discharged only in CC mode

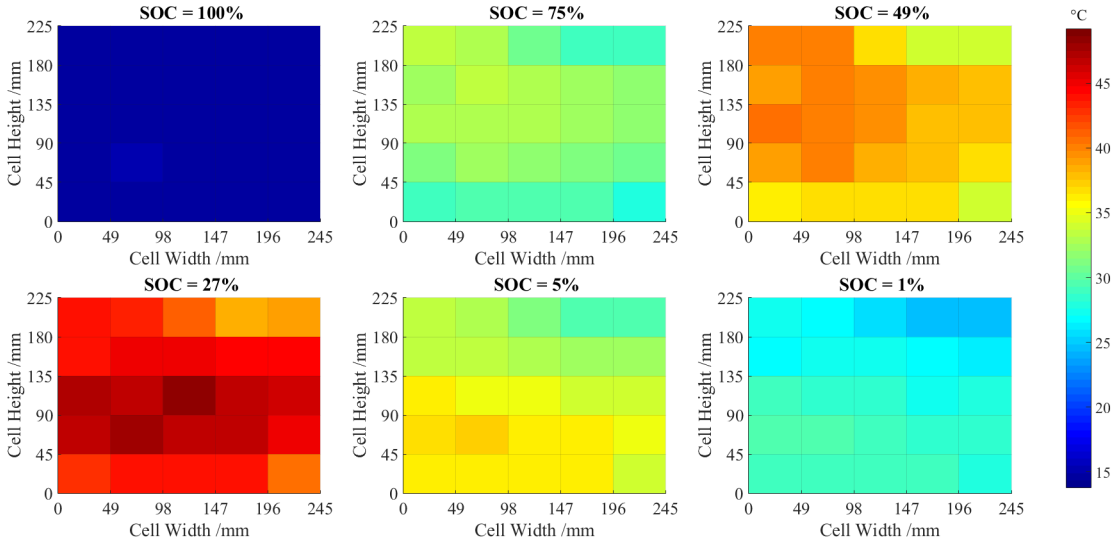

Figure 5.15: Temperature map of the cell surface of an aged 75 Ah cell during CCCV discharge with 2C discharge current under forced air cooling at 15°C ambient temperature

temperature under the forced air cooling. Each of these plots shows temperature distribution at six selected SOCs. The color bars used for the indication of temperature value has the same scales throughout for fresh and aged cells. Both results showed temperature gradually increasing from the beginning of discharge and reaching the point of culmination when the cells reached around 25% SOC, that is, about the end of CC discharge mode. After the discharge phase entered CV mode, the cell temperature reduced towards the end of discharge. It can be observed that, when the cell was relatively new (before cycling) during the continuous discharge process, the gradients started developing near the positive tab. Later, they spread towards the middle part of the cell, and, finally, the lower regions experienced higher ΔT. In comparison to the results with the aged cell, the ΔT was observed in similar hot spots throughout the continuous discharge. The overall temperature and ΔT increased in aged cells. This led to the conclusion that cell regions with high temperatures aged faster than the cell regions with low temperatures.

The results of the spatial temperature measurements and evaluation leads to the following conclusion:

- Low ambient temperature and high C-rate increase temperature inhomogeneity, and vice versa.
- ΔT increases with the following order of precedence; isothermal conditions, natural convection, force convection, direct/indirect contact cooling, that is, the type of cooling medium influences temperature distribution in the cell.
- ΔT increases with an increase in cell size irrespective of test conditions and cooling methods.
- The aging mechanism increases the temperature inhomogeneity irrespective of cell size.
- ΔT introduces aging inhomogeneity.

5.2.2 Spatial Volume Expansion Profile

The cell volume expansion occurs during the charge step and contracts to the cell's original volume during the discharge step[4]. The phenomenon of volume expansion and contraction can be explained by the intercalation/deintercalation process. During the charging process, the Li^+ are deintercalated from the cathode and they intercalate into the layers of anode. This results in an increase of the volume of the anode electrode, while the volume of the cathode contracts simultaneously. The percentage of volume expansion in the anode is greater than that in the cathode in the chosen cell chemistry, which results in its thickness increase. The cell volume is primarily expanded along the thickness direction, and hence the volume expansion can be correlated to the thickness increase. In the deintercalation process, it is reversed, as the occupied Li^+ are returned to their original lattice positions. Thermal expansion of the cell due to temperature rise also contributes to the volume expansion, but it is in lower proportion compared to intercalation-related expansion. As different cathode materials exhibit different structures, the percentages of volume expansion are different. Tab. 5.3 shows the volume expansion properties of commonly used cathode materials. The volume change values are based on the state of charge of a full cell.

Table 5.3: Volume expansion properties of some commonly used cathode materials [160–163]

Material	Crystalline Structure	Volume change	Average Voltage (V)
LCO	Layered	2.3%	3.8
NMC 111	Layered	2.4%	3.7
NMC 442	Layered	-2.4%	3.7
LFP	Olivine	-7%	3.4

Transition metal oxide and poly-anion compounds have drawn much academic as well as commercial attention due to their higher operating voltage resulting in higher energy density. These intercalation cathodes have an average voltage vs. Li/Li^+ between 3 and 4 V. Research done by Koyama et al. [160] compared the unit volume of oxide based cathode materials. The exhibition of good cyclability, shelf life, and rate capacity was due to its low volume change of NMC 111 (-2.4%), the lowest among the oxide-based cathodes. In anode materials, the most commercialized graphite shows up to 10% volume change[5]. Tab. 5.4 shows the comparison of volume expansion in different anode materials. The volume changes in LTO of about 0.2% is significantly lower than in other anode materials. Its zero-strain intercalation mechanism in combination with the high potential of lithiation ensures a high rate capability and excellent cycle life. Despite these advantages, LTO has drawbacks due to reduced cell voltage and, as a result, low gravimetric energy density. Graphite has around 10% strain during the intercalation process, but it has a higher gravimetric energy density along with a good cycle life and rate capability. Hence, it is the most commercially used anode material. Si, Ge, and Sn all have greater theoretical capacity, but are not preferred anode materials, the reason being huge volume changes resulting in a higher cyclic stress. Therefore, the higher strain leads to structural collapse and, as a result, poor capacity retention after a few cycles of charge and discharge.

The comparison of cathode and anode materials shows that volume changes are dominant in the anode materials. Therefore, many investigations are carried out on these materials with methods such as X-ray diffraction, neutron diffraction, and dilatometer and displacement sensor techniques. The expansion of cell volume consists of two components, reversible and irreversible thickness. The reversible part follows the SOC of the battery, that is, when the SOC increases, the cell volume expands, and vice

[4] This section was contributed by the Master's thesis work of Mr. Yizhi Gao.
[5] In cells where the utilization is not 100%, the typical volume change is between 6 and 7% [163].

Table 5.4: Volume expansion comparison in anode materials [161, 164]

Material	Lithiation potential (V)	Delithiation potential (V)	Gravimetric energy density (mAh g^{-1})	Diffusivity (cm^2s^{-1})	Volume change
Graphite	0.07, 0.10, 0.19	0.1, 0.14, 0.23	372	10^{-11}–10^{-7}	10%
LTO	1.55	1.58	175	10^{-12}–10^{-11}	0.2 %
Si	0.05, 0.21	0.31, 0.47	4212	10^{-13}–10^{-11}	270 %
Ge	0.2, 0.3, 0.5	0.5, 0.62	1624	10^{-12}–10^{-10}	240 %
Sn	0.4, 0.57, 0.69	0.58, 0.7, 0.78	994	10^{-16}–10^{-13}	255 %

versa. The irreversible part corresponds to thickness increase due to the formation and growth of SEI layers on the anode surface and other effects. Such a large strain may damage the SEI layers and reduce the lifetime of the cell. The mechanical stress of the anode is strongly related to stress in the SEI, which could lead to a breakup of the layers [165]. A study by Lee et al. [166] conducted on LG pouch cells exhibited a 4% irreversible increase of the cell thickness, which may have resulted from the SEI formation. However, the actual magnitude of that change depends on many parameters, such as cell design, thickness, mechanical construction, and so on. The irreversible thickness increase can also be caused by lithium plating. Under certain operating conditions, Li^+ are reduced to metallic lithium and deposited on the anode instead of intercalating into the graphite lattice [167]. Plating could lead to a growth in the cell thickness by 16 μm per plated Ah, and it does not depend on the number of layers inside the cell [45]. A large part of the lithium plating is reversible [167–171]. The reduction of deposited lithium can occur either through subsequent intercalation into the graphite layers, which needs sufficient relaxation time, or by dissolution during the following discharge. In the latter situation, lithium oxidizes at a potential of about 100 mV greater than the deintercalation potential of lithium in graphite, causing a higher voltage when discharging at low current [45, 167].

5.2.2.1 Volume Expansion in the 8 Ah cell

The expansion in the 8 Ah pouch cell is described in this section. During the intercalation process, aided by the softness of the laminate material, the expansion occurs along the thickness direction. Due to the smaller Young's modulus of the laminate material, the volume expansion along the thickness direction is not restricted that much. Therefore, it can be assumed that the swelling of the active material can be translated into the swelling of the pouch cell [163]. The nominal thickness of the cell according to Tab. 3.1 is 7.05 mm.

$$t_{cell} = 7050\ \mu m \tag{5.4}$$

The cell expansion is measured as the sum of the readings from the displacement sensors connected to the front and back surfaces.

$$Expansion = \frac{(L_{front} + L_{back})}{t_{cell}} \tag{5.5}$$

In Tab. 3.1, the number of layers of active material is shown as 16, but they are coated on either side of the current collector. Hence, the actual number of layers is doubled, to 32.

The percentage of individual material thickness is shown here.

$$Ratio_{anode} = (32 \cdot t_{anode})/t_{cell} = 35.4\% \tag{5.6}$$
$$Ratio_{cathode} = (32 \cdot t_{cathode})/t_{cell} = 30.5\% \tag{5.7}$$
$$Ratio_{sep} = (32 \cdot t_{sep})/t_{cell} = 9.1\% \tag{5.8}$$
$$Ratio_{lam} = (2 \cdot t_{lam})/t_{cell} = 4.2\% \tag{5.9}$$

The sum of values from Eqns. (5.6) - (5.9) only add up to 79.2%. The rest comes from current collectors (positive and negative), electrolyte, and other additives. As described in this section, the graphite anode undergoes 10% volume expansion during the intercalation process (i.e., during charge), while the NMC material undergoes 3% contraction during the same time. Therefore, the expansion of the cell is the sum of expansion of the anode and contraction of the cathode.

$$S_{anode} = Ratio_{anode} \times 7\% = 2.48\% \tag{5.10}$$
$$S_{cathode} = Ratio_{cathode} \times (2.4\%) = 0.73\% \tag{5.11}$$
$$S_{cell} = S_{anode} - S_{cathode} = 1.75\% \tag{5.12}$$

These calculations estimate that the anode expansion is nearly 2.48% and the cathode contraction is 0.73%, whereas the overall cell expansion is close to 1.75%. Fig. 5.16 shows the volume expansion in a 8 Ah cell at different surface points on the cell during a 1 CCCV charge and discharge.

During the measurements, the cell volume changed along the thickness direction. Under all circumstances, there was no restriction to the expansion or contraction of cell thickness caused by external factors[6]. The measurements started when the cell was at 0% SOC. At this SOC, the cell is assumed to be at its minimum thickness. Its thickness increased during the charge process and vice versa during the discharge process. The increase in displacement was proportional to the cell voltage and SOC. The displacement was maximum in a fully charged state, but slowly settled down during the voltage and temperature relaxation. After a long pause of 2 h, the cell was discharged in the CCCV regime. The cell had residual displacement at the end of CC discharge. Under normal cell discharge, the CV phase would be discarded. However, due to residual displacement (20 – 40 μm), the cell was further discharged in the CV phase to minimize the residual expansion. The volume expansion was not uniform at all positions on the cell surface. It varied between 1.83 and 2.15%; this range is close to the theoretical calculation of 1.75%. In other words, each measured point expands by a different amount. For a better illustration of displacement at all nine points, surface plots were drawn at different SOC intervals, as shown in Fig. 5.17.

In these plots, the expansion is shown in actual value instead of percentage, as it indicates a clear distinction in thickness between each of the measured point along the cell surface. The middle and

[6] The horizontal placement of the cell could have restricted the volume change on the bottom surface of the cell. Hence, it was hanging vertically to freely expand/contract along the thickness direction. No part of the active cell surface was in contact with the cell holder.
[7] The sensors were set to 0 μm at 0% SOC at the beginning of the experiment.

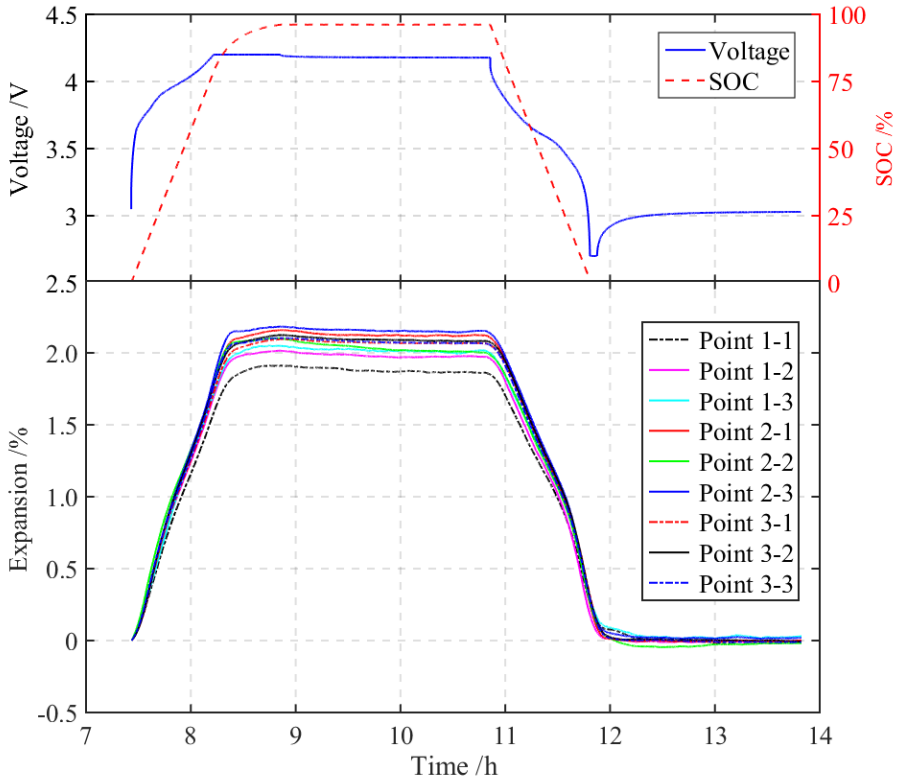

Figure 5.16: Volume expansion in the 8 Ah cell at different surface points during 1 CCCV discharge at 25°C ambient temperature.

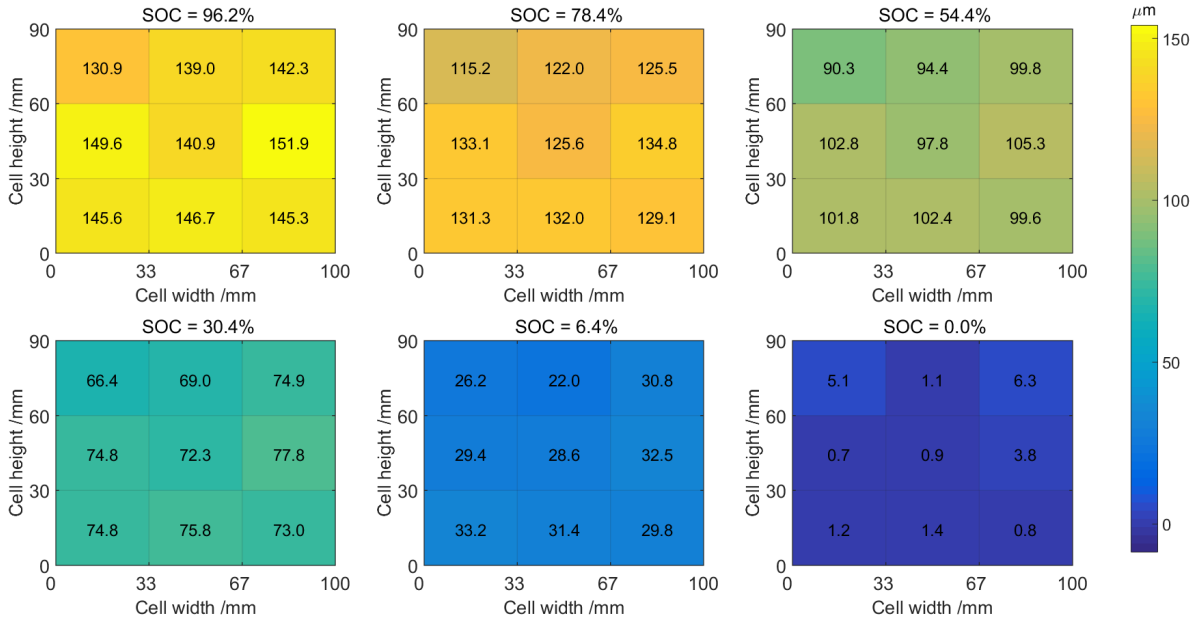

Figure 5.17: Surface plot of the thickness change[7] in the 8 Ah cell at different SOC steps during 1 CCCV discharge at 25°C ambient temperature.

the lower parts of the cell experienced larger thickness increase compared to the parts of the cell closer the tabs at ∼96%. This type of displacement profile comes from the mechanical construction of the cell. Positions 1–1 and 1–2 (see Fig. 3.13) are near the tabs, where the extension of the current collector foils are joined together by spot welding and hence restrict the free expansion of active material in this region. The residual displacement at the end of the CC discharge could be caused by the residual capacity remaining in the cell and its actual temperature. Therefore, removing the residual cell capacity using CV discharge and attaining the temperature and voltage equilibrium might explain the residual displacement. The cell voltage polarization and temperature depend the discharge C-rate. Fig. 5.18 shows the volume expansion, voltage, and temperature profile of the 8 Ah at two surface points on the cell, one closer to the cell tab and the other the farthest away from the tabs. The volume expansion and temperature at these points were measured with the spatial sensors, whereas the voltage was measured across the external tabs. As the displacement measurements at all points could not be measured simultaneously, only two points (1–1) and (3–3) were considered for the evaluation. These two points were selected because point (1–1) was the point closest to the tabs and (3–3) was the farthest from the tabs.

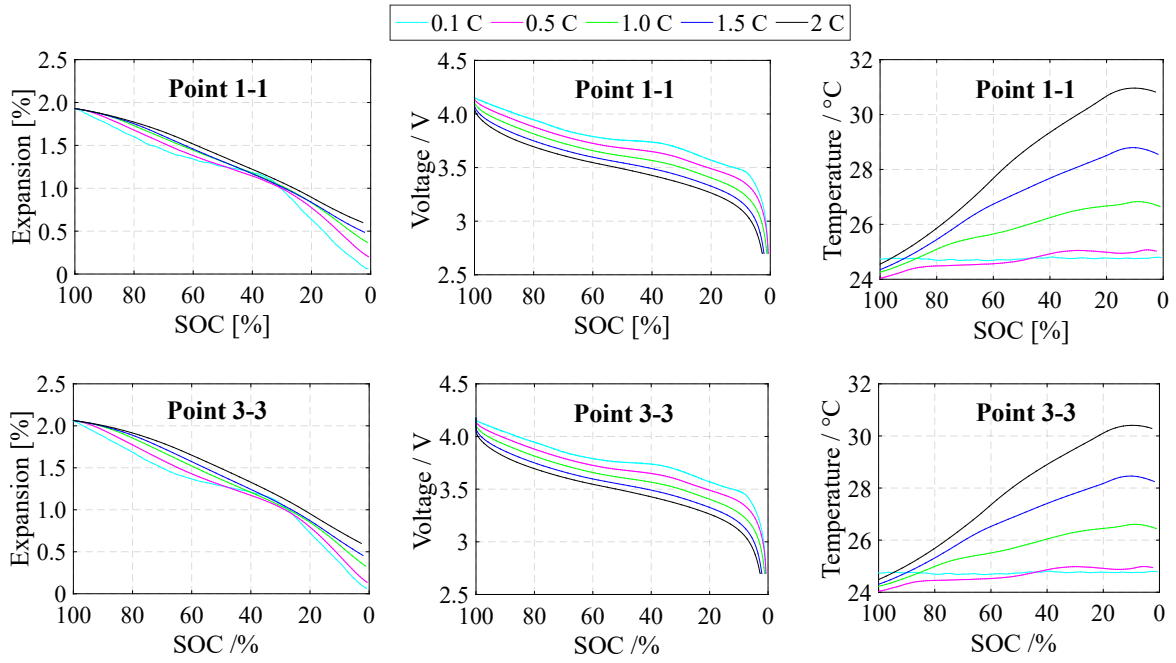

Figure 5.18: Volume expansion, voltage, and temperature profile of the 8 Ah cell versus SOC during the discharge at different C-rates

The intercalation and deintercalation of Li^+ into and out of the graphite anode material is the primary source of volume changes in the cell. The most intuitive exhibition of the amount of intercalation and deintercalation is the cell capacity or in other words the SOC. Hence, the expansion of the cell is closely related to its actual SOC, or the real capacity in the cell. The discharge C-rate 0.1C has less voltage polarization and almost no change in the temperature during the entire discharge. Hence, it can be safely assumed that thermal expansion of this material at this C-rate does not contribute to the volume changes, and it is purely due to the intercalation and deintercalation process. The residual displacement at the end of CC discharge was nearly zero. However, at other C-rates, the residual displacement is related to the increase in discharge C-rate. A higher C-rate increases the voltage polarization, leading to rate capability losses, which is directly related to the residual displacement. In terms of residual displacement, both points shows similar results by different C-rate discharge currents.

There was a marginal increase in the temperature at point 1–1 in comparison with point 3–3. The displacement plateau was observed during 0.1C discharge in the SOC range 30–60%, which corresponds to the voltage plateau under the same operating conditions. It can be concluded that a higher C-rate leads to large residual swelling. In addition, at high C-rates, the cell did not return to its original thickness, because its SOC did not reach zero at the end of CC discharge. The operation at higher discharge C-rates also led to a higher temperature increase, as shown in the temperature subplot of Fig. 5.18. Based on these observations and conclusions, it is safe to infer that the residual expansion is mainly attributed to the residual capacity and the thermal expansion of the cell components. The thermal expansion of the cell due to temperature rise is difficult to estimate because of the different thermal characteristics of each material based on these measurements.

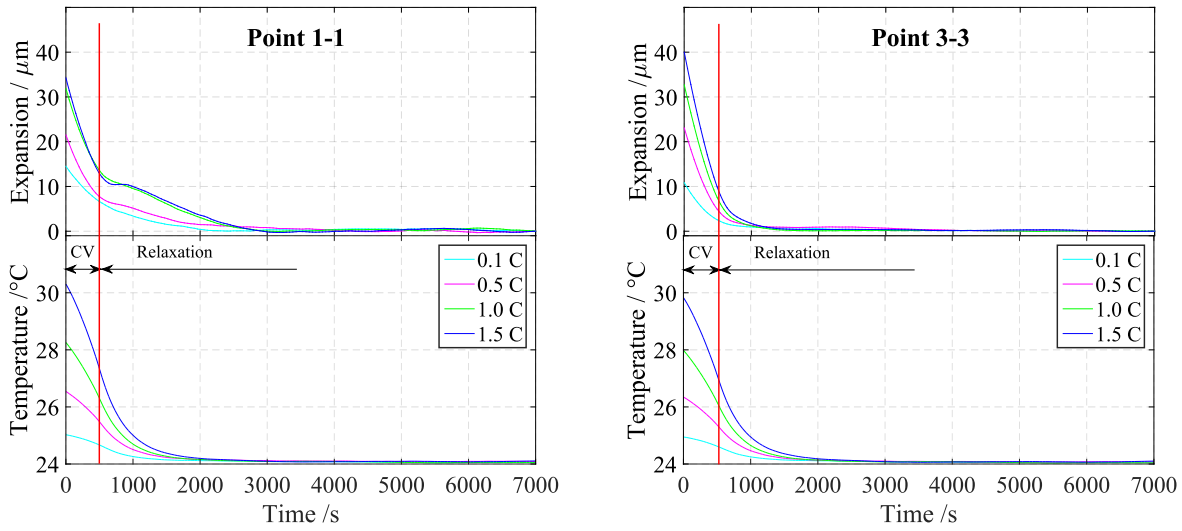

Figure 5.19: Residual displacement relaxation in the 8 Ah cell during the CV phase and rest time at the end of discharge at points 1–1 and 3–3

Fig. 5.19 shows the relaxation profile of residual displacement after the CC discharge at different C-rates. The profile was studied during the CV discharge and the rest time to follow after the complete discharge of the cell. There is a red demarcation line between the end of CV discharge and the beginning of cell relaxation, during the rest time. The CV phase was generally shortened to a duration of 10 min. During this period, the temperature started decreasing due to an exponential drop in the current, whereas, during the rest time, it was much slower. The relaxation in the residual displacement also followed a similar pattern. This led to the conclusion that displacement relaxation has two parts, due to two different time constants. Eqn. (5.13) describes the exponential decay of displacement.

$$S = a_0 + a_1 e^{-t/\tau_1} + a_2 e^{-t/\tau_2} \tag{5.13}$$

where S is the expansion at a given point, and τ_1 and τ_2 are two time constants representing the time constants of thermal relaxation and relaxation between the different phases of graphite, [172] respectively, on the cell at a given discharge current. These time constants varied at different C-rates, as it can be observed in the plots at high C-rates that both displacement and temperature relaxation occurred at a faster rate. As seen in Fig. 5.19, the thermal relaxation contributed to the faster response, more than the relaxation of different phases of graphite, which took hours to relax until the

cell thickness was nearly back to its original value. However, the relaxation at point 1–1 did not follow a smooth profile as it appeared in point 3–3. It took a much longer time to return to the original cell thickness, and there was a plateau during the relaxation process. Given that the temperature profile was similar to that of point 3–3, the thermal relaxation response at point 1–1 should be identical to point 3–3. The cell construction plays a bigger role in the overall volume expansion and its relaxation at point 1–1. A possible explanation could be that point 1–1 is closer to the cell tabs, where the current collectors at different layers are spot-welded together. This creates mechanical constraint in this region, as explained in this section, and could possibly lead to more mechanical stress in this part than in any other parts of the cell.

These results illustrate that, at a high C-rate, the cell expansion leads to a larger residual displacement due to the temperature rise. The residual displacement increases the mechanical stress in the cell. This situation could get worse if there is no proper thermal management of the battery. In a real-time situation, the battery pack of an EV is subjected to much harsher conditions, where the cooling medium may not be sufficient to dissipate the heat generated by the cells. In such a scenario, the cells in the battery pack remain at a higher temperature, which means the cells experience residual volume expansion and thermal stress for a long duration.

Oh et al. [44] correlated the expansion of the cell at different C-rates with the role of individual electrodes during the process. The analysis was done by differentiating the volume expansion with respect to the charge accumulated in the cell, in other words, SOC. At first, the direct difference method, as shown in Eqn. (5.14), was used to calculate the derivative, but the sample rate of the test was relatively high (1 Hz), considering the test lasted for several hours, this led to significant noise, and no clear trends were observed in this method. To eliminate the noise from the derivative, the relationship between expansion and SOC was described by a polynomial function, as shown in Eqn.(5.15). The derivative of the polynomial function was used to plot the dS/dSOC curve versus SOC, as shown in Fig. 5.20.

$$y'_n = (y_{n+1} - y_n)/(x_{n+1} - x_n) \tag{5.14}$$

$$f(x) = a_6x^6 + a_5x^5 + a_4x^4 + a_3x^3 + a_2x^2 + a_1x + a_0 \tag{5.15}$$

$$f'(x) = 6a_6x^5 + 5a_5x^4 + 4a_4x^3 + 3a_3x^2 + 2a_2x + a_1 \tag{5.16}$$

The local maxima corresponded to the phase shift in the graphite material, as reported in previous works [173, 174]. The phase transition in NMC material does not appear to have a strong impression, because the NMC lattice does not fill in stages the way the graphite lattice does, and hence they undergo smaller volume changes (∼3%). Therefore, the volume expansion at low C-rates appears to be dominated by the graphite electrodes, that is well within the 2% volume changes in the positive and negative electrodes calculated in this section. The apparent shift in the peaks corresponding to Fig. 5.20 towards the right for a higher discharge rate indicates a phase transition at the later stage. The reason for the peak shift could also be due to lagging thermal expansion, as shown in the relaxation plots (see Fig. 5.13).

The concept of aging has been extensively discussed in this thesis. Besides many aging effects explained in chapter 2, it also increases the overall thickness of the battery. In the pouch cell, the volume expansion is mainly confined to the cell's thickness. Fig. 5.21 compares the cell thickness at different

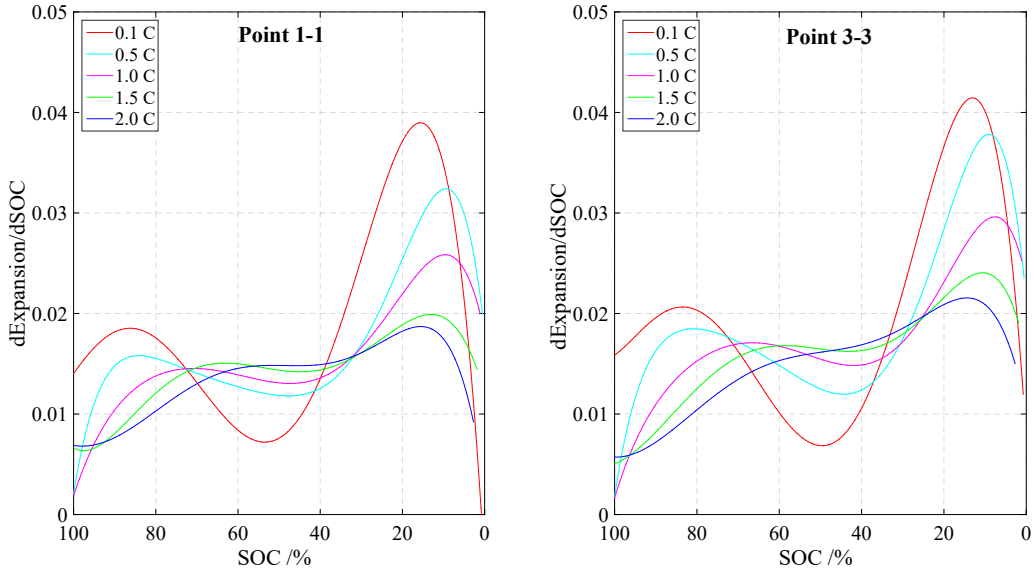

Figure 5.20: Derivative of expansion with respect to SOC the during the discharge process at points 1–1 and 3–3 at 25°C ambient temperature

surfaces on the new 8 Ah cell and the same cell when it was aged. The aging history of this cell can be seen in section 5.1.1. The increase in the thickness in the aged cell may be a consequence of different factors, such as gas formation, SEI formation, breakdown and reformation, lithium plating, and macroscopic deformation, such as buckling of different layers of the cell. It can be observed that the thickness increase is not uniform throughout the cell surface. The points closer to the tabs (1–1, 1–2, and 1–3) have maximum thicknesses among all the measured points on the cell. The inhomogeneity in the thickness increase could be related to the inhomogeneous temperature distribution, SEI layer growth, mechanical stress evolution during the volume expansion, and contraction due to the mechanical construction of the cell. These results once again confirm that the position near the cell tabs experiences maximum stress, leading to early aging compared to other positions far away from the cell tabs.

5.2.2.2 Volume Expansion in the 75 Ah Cell

Fig. 5.22 shows the expansion in the 75 Ah cell at ten surface points (see Fig. 3.13) during 1 CCCV cycling at 25°C ambient temperature. As expected, the cell volume increased during charge and contracted during discharge. The large-format 75 Ah cell expanded by ∼2% of the original thickness. The cell thickness reached its peak value after the end of the CC charge and in the middle of the CV charge. It was followed by relaxation in the cell displacement during the CV charge, and it continued further into the rest period. This is in complete contrast to the cell displacement in the 8 Ah cell, where the cell displacement more or less remained constant during the entire CV phase. It could also be observed that the peak displacement varied at different positions on the cell surface. The possibility of different peaks due to thermal expansion was also looked into, but the difference between the temperatures at the measured positions was close to 1°C. Therefore, the non-difference in the displacement peaks due to thermal expansion can be ignored. This could have been due to over-lithiation at some positions and redistribution of intercalated Li^+ in the anode material, owing to inhomogeneous characteristics of the cell. The discharge phase showed more difference in the distribution of cell thickness. There were plateaus in the expansion curve at points 1–2 and 1–4 when

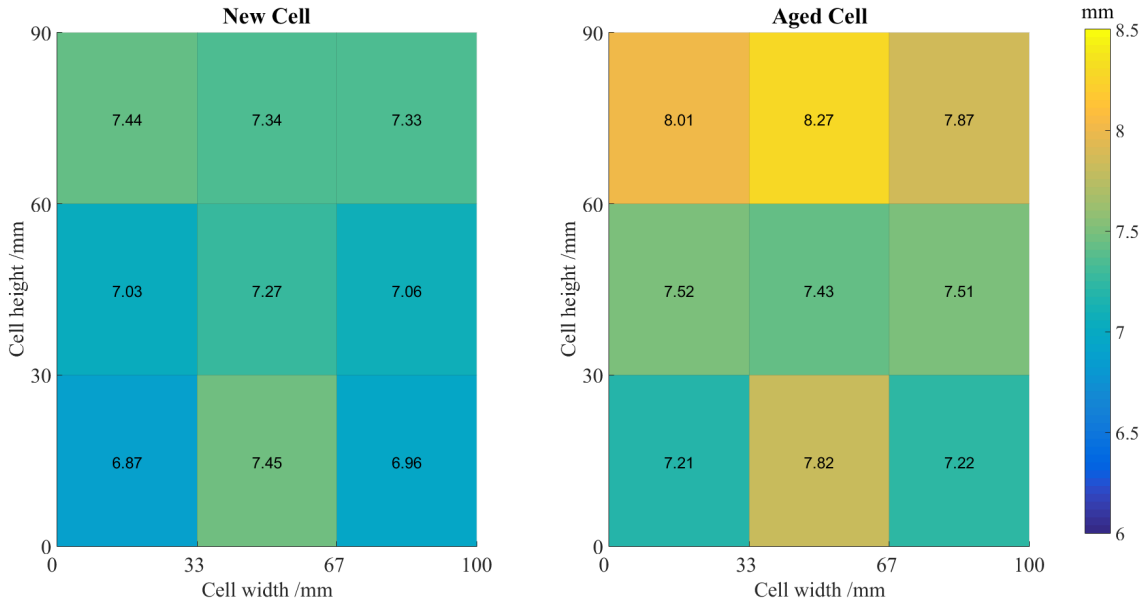

Figure 5.21: Comparison of absolute cell thickness measured at different points, before and after aging tests on the 8 Ah pouch cell

the cell entered into CV discharge. These points are close to the positive and negative tabs of the cell, respectively. The stresses due to cell design and construction may have caused these plateaus. There were large differences in the cell expansion throughout the discharge phase, and they culminated at the end of CV discharge. It is worth mentioning that the temperature gradient was the maximum in this instance, and that could be the primary reason for the large residual expansion, especially at the points that experienced maximum temperature. Therefore, thermal expansion may have contributed to the overall thickness changes in the cell. The large temperature gradient occurred despite the cell being cycled at the nominal C-rate and being kept inside the temperature chamber with strong cooling.

Even after 2 h of rest time following complete discharge, there was low residual expansion at some of the measured points. The excessive cell volume changes resulted from:

- formation of different phases of graphite
- slow diffusion of Li^+ in the electrode's active material [172]
- more structural changes in the outer region of the electrode particle
- expansion primarily occurring at the outer region of the electrode particle

According to these explanations, the excessive cell volume change is determined by the input C-rate, the Li^+ diffusion coefficient, and the rate at which structural changes occur in the electrode material. It can be relaxed by sufficient pause time. However, during the continuous operation of the cell, the pause time may not be sufficient for the excess volume change to relax to its original state. Therefore, the residual volume in each cycle develops gradually. As a result, the cell volume changes increase with cycling [43]. The detrimental effect of this excess volume change causes structural damage to the electrode material, loss of Li^+ to the formation and growth of SEI layers on the anode surface, lithium plating, and so on. Eventually, the volume changes result in the loss of cell capacity due to cycling.

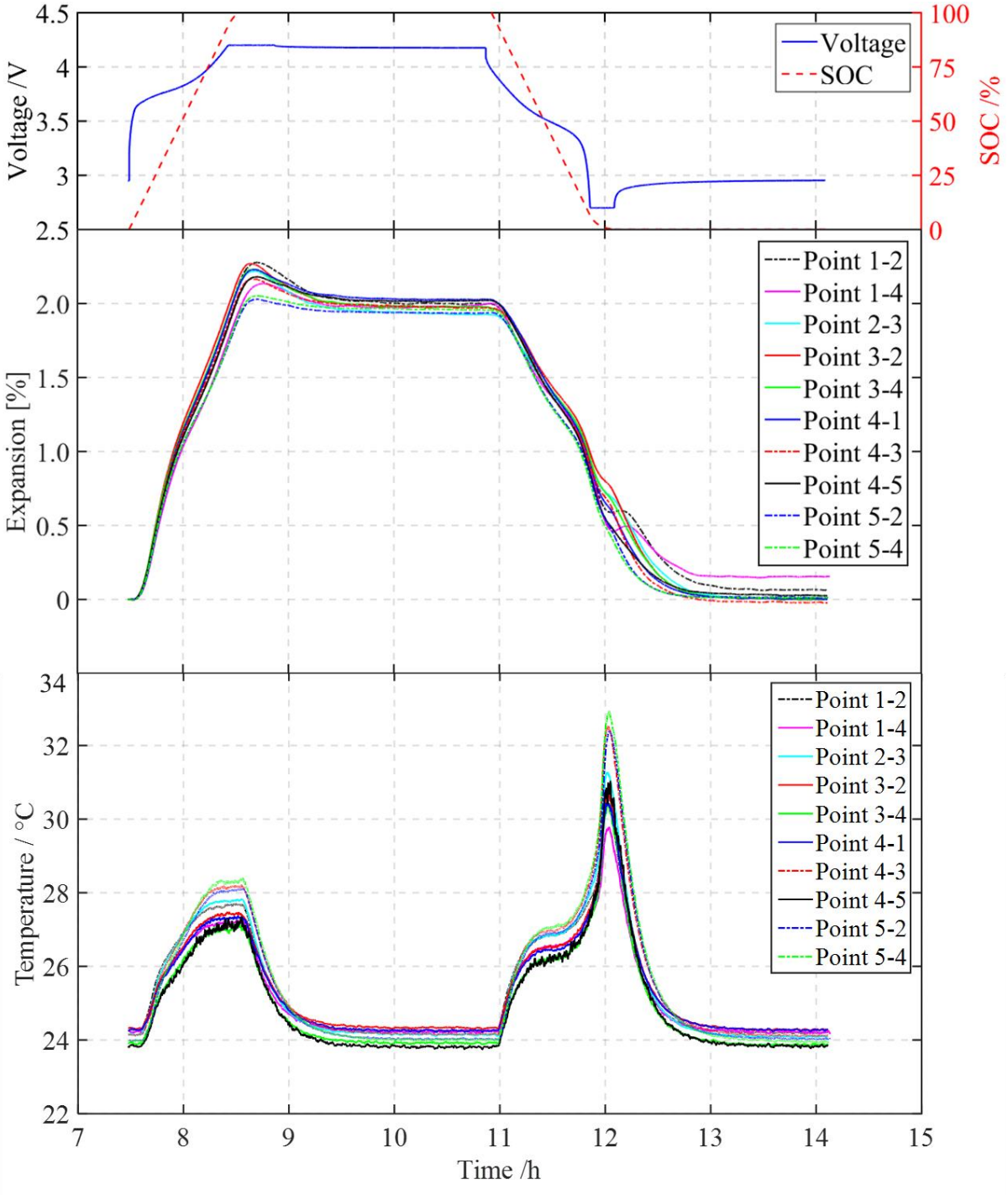

Figure 5.22: Time series plot of cell voltage, expansion, and temperature distribution at ten selected points on the surface of the 75 Ah cell during 1 CCCV cycling at 25°C ambient temperature (best viewed in color)

Fig. 5.23 compares the displacement of fresh and aged 75 Ah cells on position 1–2 (closer to the positive). The same cell was used in both measurements, once before the start of the aging test and again after the end of the aging test. When the cell was aged, it had ∼66% remaining capacity after 1300 full cycles, equivalent to 26 weeks of cycling time. The testing conditions were the same, that is, 1 CCCV charge and discharge and 25°C ambient temperature. The most intriguing observation from this result was that the cell displacement profiles were vastly different. It was expected that the voltage profile of an aged cell is characterized by high polarization due to an increase in the internal resistance and reduction in the charging and discharging time. However, the reversible thickness increase in the aged cell was significantly lower than the fresh cell, despite reaching similar displacement peaks during the charge phase. There was a huge displacement swing from the end of the charge to the beginning of discharge phase in the aged cell. The magnitude of the displacement relaxation can be attributed to large residual expansion caused by high temperature and redistribution of intercalated Li^+ in the anode material. Hence, this result leads to the conclusion that cell inhomogeneity increases in the aging process. The reduction in the cell expansion showed that less of the Li^+ were intercalated into the anode, caused primarily by the loss of capacity. It can be concluded that the amount of cell expansion is related the remaining capacity of the cell, an indirect method to estimate SOH.

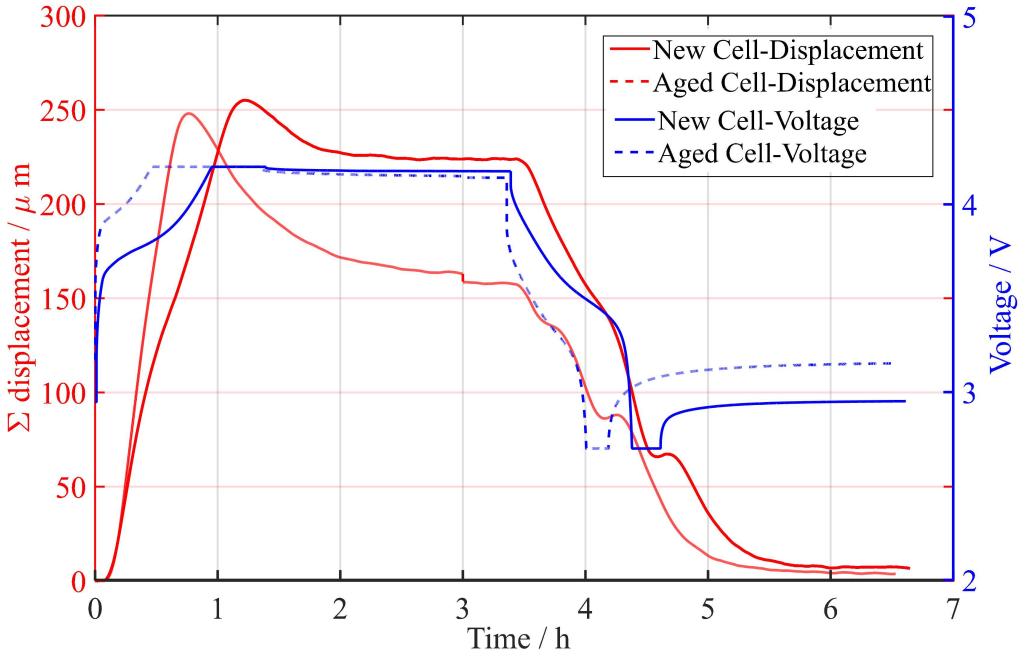

Figure 5.23: Cell displacement comparison between fresh and aged 75 Ah cells during 1 CCCV charge and discharge, measured at point 1–4, at 25°C ambient temperature (best viewed in color)

The cycle aging also caused irreversible thickness increase in the cell. Fig. 5.24 shows that the evolution of cell thickness averaged at 25 points at different cycling intervals. At the end of life, the average cell thickness was increased from 11.47 mm to 12.98 mm, that is, by ∼13.2%. The cell had an average thickness increase of 15.2%, assuming a 2% increase during the charge phase, especially when it was aged. Considering the cell thickness is inhomogeneously distributed, some of the surface of the cell accumulated more thickness than the rest. Fig. 5.25 shows the comparison of surface thickness for a new cell and when it was completely aged.

Before the cycle aging, the surface had maximum deviation (δ_t) and standard deviation (σ_t) values

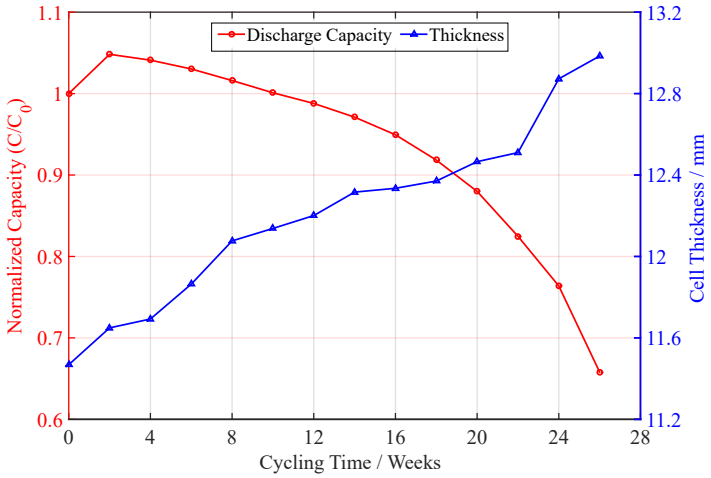

Figure 5.24: Average thickness accumulation at 0% SOC in the 75 Ah cell during cycle aging

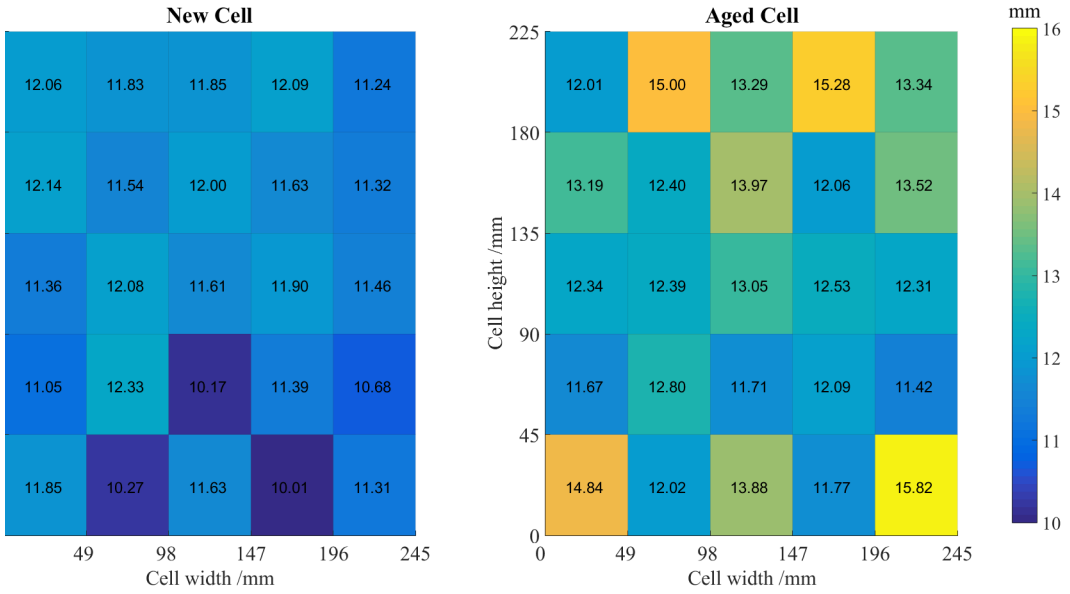

Figure 5.25: Surface plot of absolute cell thickness measured on 25 points in a 75 Ah cell at 0% SOC; (a) new cell, (b) aged cell

of 2.32 mm and 0.6 mm respectively. The δ_t value was already significant in the new cell, which indicated that the surface was less uniform at the BOL. The actual image of the new cell is shown in Fig. 5.40(a). After aging, the surface became more erratic, with δ_t and σ_t increased to 4.15 mm and 2 mm respectively. This corresponds to the maximum thickness increase of ∼28.3%[8], assuming that a 2% increase in the thickness during charging leads to a thickness increase of over 30% from its original value. This thickness allowance should be maintained when the cells are housed in the battery pack case in order to prevent the external stresses from acting on the cell surface. The surface plot of the aged cell also showed that there was maximum thickness accumulation near the tabs (1–2 & 1–4). In addition, the maximum cell inhomogeneity near the cell tabs, post-manufacturing stresses due to spot welding of the current collectors to the external tab, and the stress from the external sealing of the polymer foil could have contributed to the maximum thickness accumulation. The cell thickness increase during cycling is a good indication of reduced SOH.

5.3 Multiscale and Multiphysics Simulation

In this section, a comprehensive, qualitative, and quantitative validation of the P2D electrochemical and 3D thermal model approach is presented[9]. The measurements as described in section 3.3.4 were used as the basis of the model validation by comparing the simulation results with the measurement data with respect to voltage profile, temperature profile, and temperature distribution on the cell surface. Except for macroscopic geometries parameters (Tab. 4.3), all other parameters (Tabs. 4.2 & 4.4) were the same for all cells. The simulation results of 25, 53, and 75 Ah cells are discussed in this section.

5.3.1 Voltage Validation

The first simulation started with the validation of the OCV profile. To validate the OCV profile, the pseudo-OCV current profile (section 3.3.3) was used in the simulation conditions. At 0.05C current, the output voltage was nearly equal to the OCV of the cell. Fig. 5.26 shows the comparison between the measured discharge voltage at 0.05C (assumed to be pseudo-OCV) and the simulated result. As the OCV is the same for all the selected cells, only the results for the 25 Ah cell are shown here. It is observable that the simulation fits very well with the experimental data of the OCV measurement. From the beginning until the 65% SOC mark, the curves are almost identical, and the maximum discrepancy is less than 5 mV. Only in the range of 30% and 15% SOC as well as at very low SOCs does the simulated OCV behave slightly differently to the measured OCV. The profiles show a difference of less than 20 mV for the range between 30% and 15% SOC and a 40 mV voltage drop at very low SOCs. The cause of these divergences could be attributed to the graphite anode OCV used, as OCV measurements for the anode were not performed, but merely adopted from [113]. In general, the results show that the initial SOCs for the anode and cathode are well balanced.

The accurate simulation of the voltage behaviour under some current flow is more significant than the simulation with no current flowing in the cell, that is, OCV condition. This section depicts different discharge scenarios for voltage validation. Fig. 5.27 presents the voltage simulation results for the 25, 53, and 75 Ah cells for different discharge rates and ambient temperatures compared against the measured data. It is apparent that the simulations show very good agreement with the experimental

[8] This is calculated by taking the maximum cell thickness values in both fresh and aged cells.
[9] This section was contributed by the Master's thesis work of Mr. Tim Pixis.

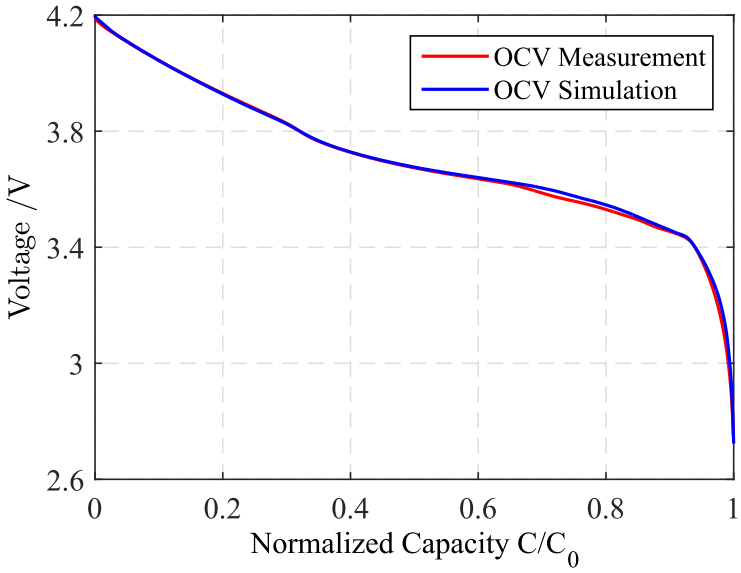

Figure 5.26: Comparison of OCV simulation and discharge voltage measured at 0.05C for a 25 Ah cell at 25°C

data for the discharge rates of 1C, 2C, and 3C discharge currents, but it is not so in the case of the 0.5C current. At the ambient temperatures 15°C and 40°C, the simulated voltage was over-estimated and under-estimated, respectively, especially towards the end of discharge. This is because the model uses a fixed capacity, whereas, in the experiment, we get a higher capacity at higher temperatures. There is good agreement with the experimental and simulation results at 25°C, because the simulation parameters were optimized for the ambient temperature 25°C. Furthermore, it was not possible to simulate the cells at the ambient temperature 15°C with a discharge rate of more than 2C, because the solutions could not achieve the targeted convergence, hence the simulations stopped abruptly without any results. Therefore, these conditions were discarded from the results. These results also show that the models adapted well to cell size and geometric dimensions.

Tabs. 5.5, 5.6, and 5.7 show the modelling accuracies for the 75 Ah cell. The runtime error was low when the ambient temperature was 25°C. The goodness of fit (R^2 value) was close to 1 for all C-rate discharges. The average error voltage was within 20 mV throughout the simulation. These factors are a good indication of how accurate the simulation results are when compared to the measured data. The maximum error voltage is just an indication of the maximum deviation from the measured data. There are entries that indicate a high maximum voltage error, but other deciding factors are very low. The maximum error mostly occurred towards the end of discharge. The change in ambient temperature to 15°C and 40°C reduced the accuracy of the model. However, the runtime error and R^2 value were within the acceptable limits at $<6\%$ and >0.9, respectively, but the average error voltage was slightly higher, which needs to be improved. The model tends to slightly underestimate the cell capacity for low and high temperatures. This indicates that the temperature dependency is satisfactory, but there is still some room for improvements by adjusting, for example, the anodic and cathodic reaction rates individually. The close agreement between simulation results and experimental data indicates that the proposed electrochemical battery model predicts runtime and voltage responses accurately.

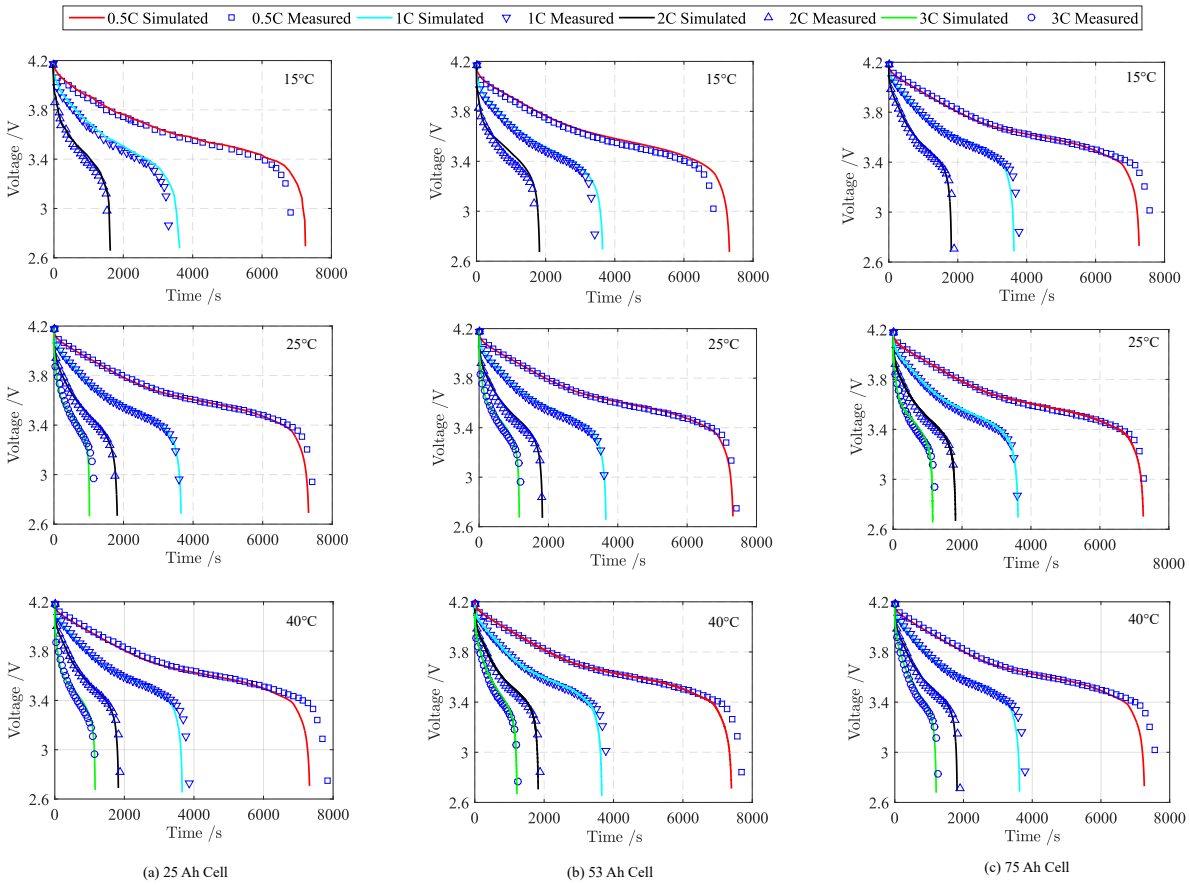

Figure 5.27: Comparison of measured and simulated voltage results at different discharge C-rates and ambient temperatures for a (a) 25 Ah cell, (b) 53 Ah cell, and (c) 75 Ah cell

Table 5.5: Modelling accuracies of a 75 Ah cell at 15°C ambient temperature

Current rate	Avg. Error Voltage (mV)	Max. Error Voltage (mV)	R^2	Runtime Error[10](%)
0.5C	30.1	468	0.935	3.13
1C	46.6	497	0.90	5.43
2C	39.9	331	0.914	4.38

Table 5.6: Modelling accuracies of a 75 Ah cell at 25°C ambient temperature

Current rate	Avg. Error Voltage (mV)	Max. Error Voltage (mV)	R^2	Runtime Error (%)
0.5C	20.6	257	0.98	1.52
1C	12.6	64.3	0.996	0.03
2C	1.7	120	0.986	0.314
3C	2.4	279	0.985	1.30

[10] It is calculated as the difference between the measured and simulated value with respect to the measured value, expressed in percentage.

Table 5.7: Modelling accuracies of a 75 Ah cell at 40°C ambient temperature

Current rate	Avg. Error Voltage (mV)	Max. Error Voltage (mV)	R^2	Runtime Error (%)
0.5C	65.2	465	0.930	5.44
1C	47.7	452	0.953	4.68
2C	37.3	302	0.954	4.34
3C	41.2	391	0.901	4.71

5.3.2 Temperature Validation

Fig. 5.28 shows the plot of measured and simulated temperature on the centre of the cell surface for 25, 53, and 75 Ah cells at different discharge C-rates and temperatures. In general, the simulation results show the same profile compared to the measurements. The best results of the model were observed at 25°C, where the simulated results were close to the measured data. A maximum temperature difference of up to 3°C existed, mainly at a high C-rate discharge. It can also be observed that, under some simulation conditions at 15°C and 40°C ambient temperature, there is a steep increase in the temperature at the beginning of discharge, resulting in a widening of the gap at mid-SOC levels between measured and simulated data. This could be attributed to over-estimation of the internal resistance of the cell under those conditions. It results in higher irreversible heat generation compared to the measurements. The behaviour described is thereby independent of the cell size and input current. The model also over-estimated the simulated temperature in all cell sizes at a 3C discharge rate towards the end of discharge. The maximum over-estimation was observed in the 75 Ah cell at 3C discharge rate, where a difference of up to 5°C can be observed. It should be noted that, even in measurement data, there is a higher end-temperature from the 25 Ah to the 75 Ah cell. This transformation could be the effect of an increase in cell size, as explained in section 2.4. Despite these additional effects arising from cell size, the model adapted to the changes. Furthermore, the discrepancy between the simulated and measured temperature profiles could be explained by limited thermal parameters and the assumptions used in the thermal model to simplify it. In conclusion, the model shows good adaptability to the measured temperature for different cell sizes, based on the same microscopic cell parameters with a certain degree of accuracy and limitations. This model serves as a good prediction of the electrochemical and thermal characteristics of a battery of any arbitrary cell geometry, size, whether it is a scale-up or scale-down design approach.

5.3.3 Current Density Distribution

The current density gradient causes different current flow in different parts of the cells. It gradually affects the SOC distribution in the cell and also introduces differential heat generation, leading to a temperature gradient. When the change in SOC and temperature becomes significant, the internal resistance of the cell changes, causing the reversal of the current density distribution. Fig. 5.29 shows the variation in local currents during a 3C discharge at 40°C ambient temperature on 53 and 75 Ah cells at different points on the cell. The selection of simulation points is shown in App. A3. The current value is normalized to the nominal current of the cell to compare the current distribution in different cell capacities. At the beginning of discharge, as expected, the current was maximum near to the location of tabs compared to the rest of the cell surface. The current flow pattern remained like this throughout the mid-SOC range. The next part was the reversal of the current distribution. This happened when all the current values merged at around 75–80% DOD, and reversal of current density distribution started from this point. The exact meaning of reversal is that the regions that experienced

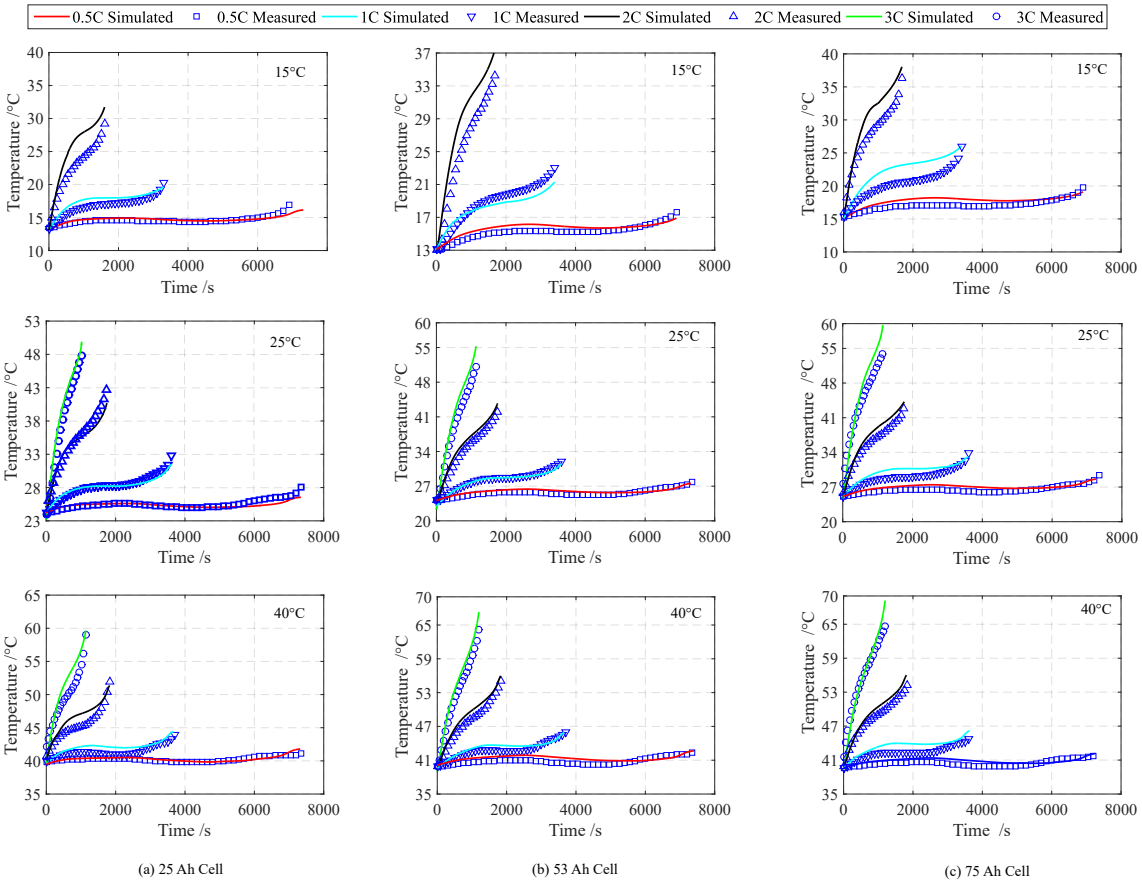

Figure 5.28: Comparion of measured and simulated temperature results at different discharge C-rates and ambient temperatures on the centre of the cell surface for a (a) 25 Ah cell, (b) 53 Ah cell, and (c) 75 Ah cell

high current distribution changed to low current density regions, and vice versa. This phenomenon has been described by Zhang et al. [25]; the reversal of current density distribution is attributable to non-homogeneous local SOC due to uneven current flow in the early stages of discharge. Moreover, towards the end of discharge, there was a steep increase in the current density gradient, with low current density near the vicinity of the tabs and rising current density at the distance far away from the tabs.

5.3.4 Temperature Distribution

Fig. 5.30 shows the temperature distribution in the positive and negative electrodes of a 75 Ah cell in simulation conditions, 40°C and 3C discharge rate. The simulated electrodes are placed on the outer stack, that is, close to the top cell surface of the cell. It should be noted that the cell's external tabs were excluded from the geometry of the battery thermal model. The surface graphs depict the temperature on the electrode at the time intervals 100 s, 800 s, and 1203 s. The positive electrode showed an initially high temperature in the vicinity of its tab, due to higher current density in this region. It increased the heat generation in the cell, leading to high temperature. In the middle of discharge, around 800 s, the high temperature region shifted towards the upper-middle region of the electrode surface, that is, between the positive and negative tabs. Towards the end of the discharge, the temperature hot spots moved further away from the tabs. In the real temperature measurements, the temperature hot spots

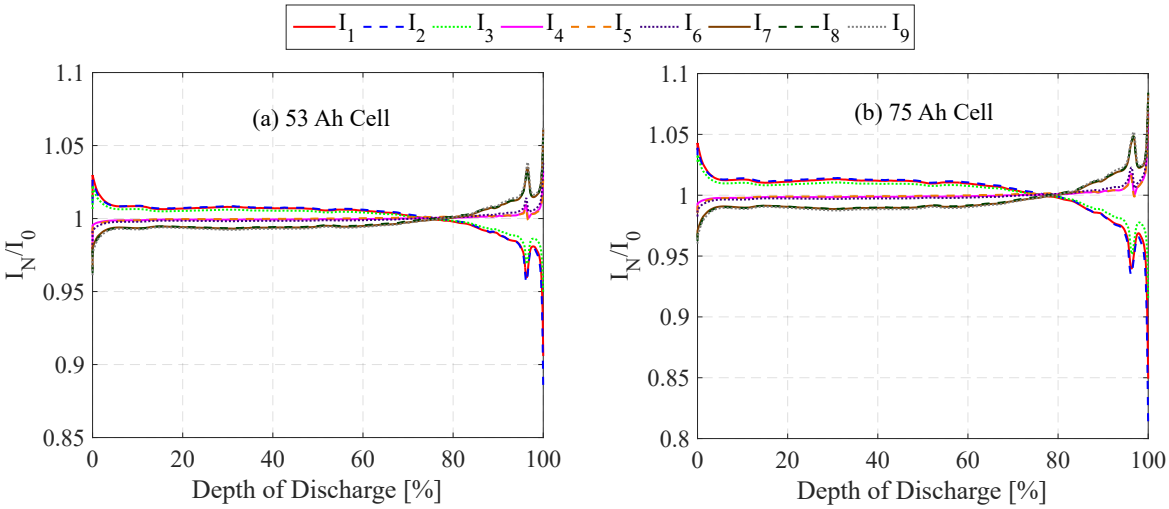

Figure 5.29: Variation of local currents during 3C discharge of the 53 Ah and the 75 Ah cells at $T_{amb} = 40°C$ (best viewed in color). The selected points for simulation are shown in App. A1.4

can be seen near the cell tabs, then gradually move towards the centre of the cell and towards the end of discharge further away from the tabs. It is at this point that the simulation results differ from the actual measurement data (see Fig. 5.14). In the simulation, the temperature results were strongly affected by the convection heat transfer along the borders of the cell surface. An indication of this was the relatively low temperature along the lower region of the cell (farthest away from the tabs). In the simulation conditions, the air flow was assumed to be laminar and there was strong convection at the surface boundaries. This simulation condition is not the true reflection of the actual convection inside the temperature chamber. There was forced air convection inside the temperature chamber caused by rotating fans or the blowing of cool air into the chamber. This resulted in more turbulent air flow inside the temperature chamber. The boundary conditions in the simulation were strongly influenced by the difference in the ambient and cell temperatures, that is, higher temperature led to stronger convection at the boundaries, and, in addition, the temperature sensors with the wiring do not exactly measure the surface temperature, as the cables act as a cooling system. Hence, the temperature distributions are not similar in measured and simulated results, especially towards to the end of discharge.

Fig. 5.31 shows the comparison of ΔT_{max} in large-format cells at different ambient temperatures and C-rates, (a) on the cell surface with soft pouch casing and (b) along the single cell layer excluding the soft pouch case. The temperature gradients were similar in both simulation conditions, suggesting that external casing had little or no influence on the temperature distribution. The ΔT_{max} was significantly higher in the 75 Ah cell compared to the other two cell types. This difference could be attributed to different surfaces of each cell type. The large surface area in the 75 Ah cell caused a higher current density gradient, resulting in inhomogeneous temperature distribution. Comparing the 25 Ah and 53 Ah cells, and both cells, with identical surface area and current density distribution, the temperature gradient was slightly higher in the 53 Ah cell. This is due to a higher number of layers being present in the cell and causing a higher temperature gradient. There is more volumetric heat generation in the 53 Ah cell when compared to the 25 Ah cell for the same surface area (Fig. 2.10). The simulated temperature gradient values were significantly lower compared to the measured data, for example, ΔT_{max} value for the 75 Ah cell at 25°C and 3C discharge was close to 5°C, whereas the simulation results show only 2°C. This huge difference shows that the thermal model did not adapt well to the temperature gradients. The thermal model needs some improvement with better

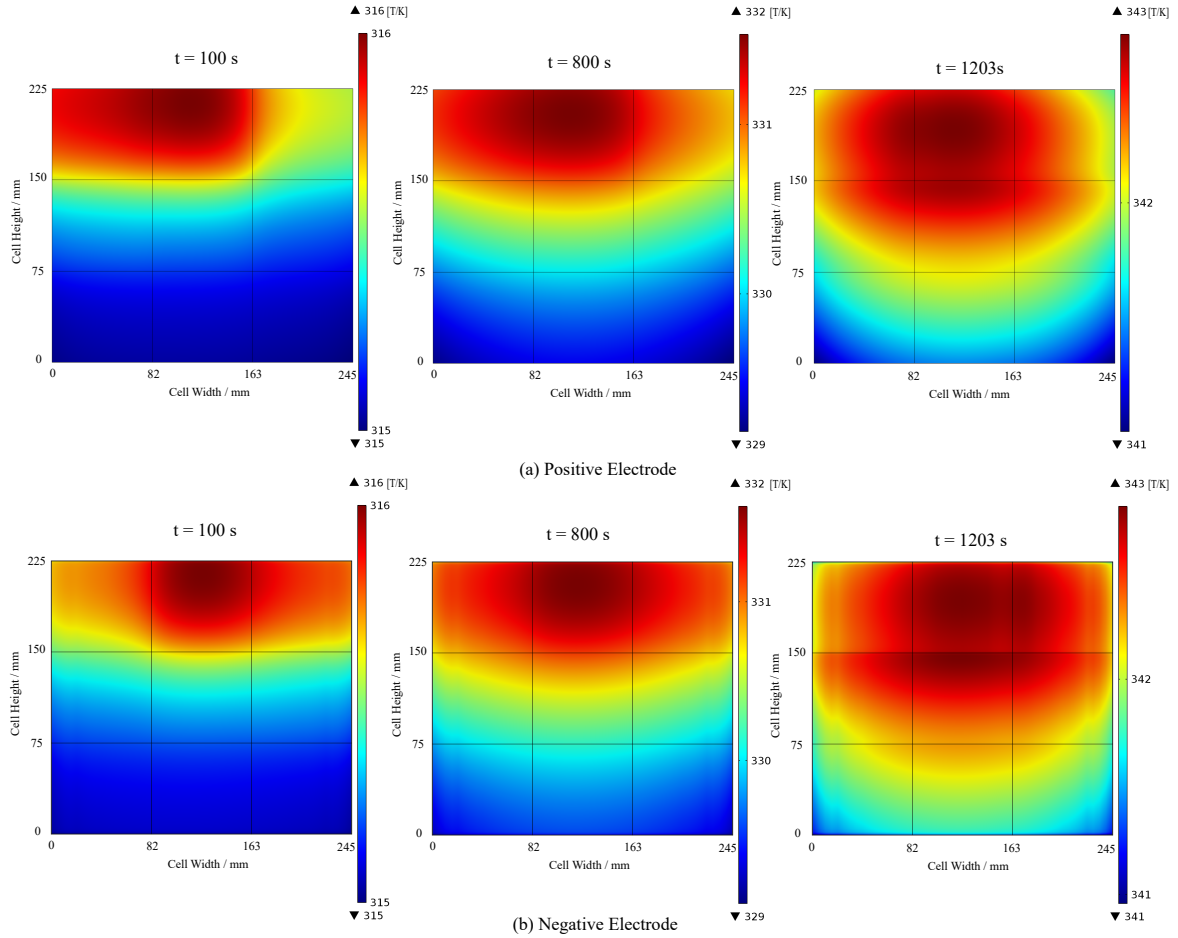

Figure 5.30: Temperature distribution on the (a) positive and (b) negative electrodes of the 75 Ah cell at 40°C ambient temperature, 3C discharge rate at time intervals of 100 s and 800 s and at the end of discharge

parameterization, especially for the convective heat transfer and thermal conductivity of the materials used in the battery. These parameters were either obtained from literature or through estimation. Despite these shortcomings of the thermal model, the temperature rise in the cells from the simulation results were nearly equal to the measurement values, as shown in Fig. 5.31.

It can be observed in Fig. 5.32 that the maximum temperature rise in the 53 Ah cell was much higher than that of the 25 Ah cell. This can be explained by the effective surface-area-to-volume ratio of cells, as calculated in Tab. 4.3. And increase in the cell size reduced the surface-area-to-volume ratio, which subsequently reduced the cooling surface area per volumetric heat generation. The result also show that a surface-area-to-volume ratio similar to that of the 53 Ah and 75 Ah cells show a similar temperature rise. In contrast, this ratio in the 25 Ah cell is significantly higher, leading to a much lower temperature rise in the selected test conditions.

The influence of layer position on temperature, current density, and SOC gradients in the cell is also important to cell inhomogeneity studies. Additional simulation results have been obtained by changing the layer positions from 1 to 0.25 and 0.5[11]. Tab. 5.8 shows the simulation results of temperature inhomogeneity within a layer for different layer positions. The results show very little

[11] Where $0 \leq k \leq 1$ refers to the position of a layer along the cell thickness direction, and k=0.5 indicates the middle layer of the cell

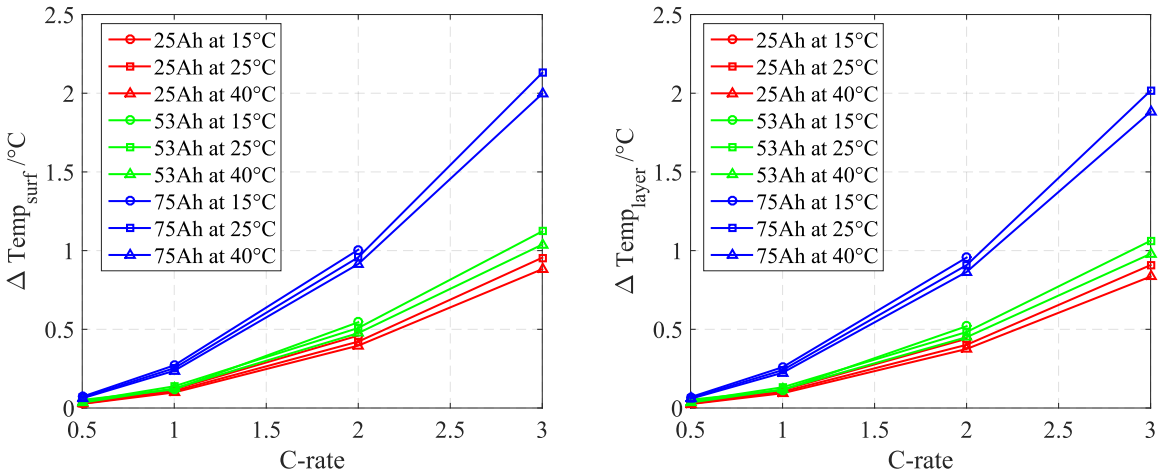

Figure 5.31: Maximum temperature gradient recorded during simulation on the (a) cell surface and (b) single layer located closer to the cell surface

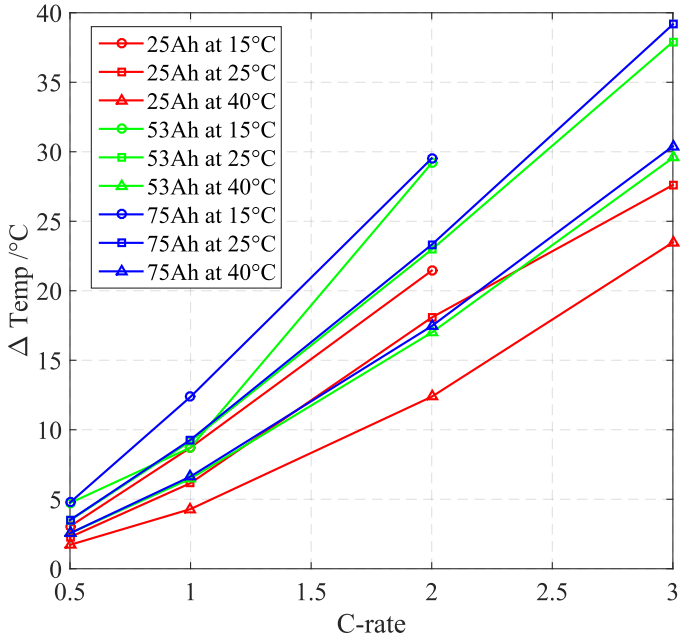

Figure 5.32: Maximum temperature rise observed during the cell simulation at different ambient temperatures and C-rates

difference or no difference in value, indicating that, along the thickness direction at different layer positions, temperature inhomogeneity can be neglected. This is according to the fact that all layers have identical geometry and equal current flows in each layer. The heat transfer, especially in the middle layers, were not the same compared to the cell layers closer to the surface. This could lead to more hot spots in the middle layers. However, due to approximation applied to the P2D electrochemical model, that is, the volume temperature from the 3D thermal model averaged with surface temperature and coupled with the 2D electrochemical model, the gradients through the cell thickness are hardly noticeable. To overcome this limitation, a full 3D electrochemical and thermal model should be used in the simulation. However, many references indicate (see chapter 2) that cell inhomogeneity exists primarily along the in-plane direction (surface), and it is negligible along the through-plane direction (thickness).

Cell Type	k =0.5	k =0.25
25 Ah	0.4015	0.3962
53 Ah	0.4829	0.4030
75 Ah	0.9077	0.9159

Table 5.8: Comparison of the maximum temperature gradient within a layer at different layer positions at ambient temperature of 25°C, 2C discharge rate

5.3.5 Modelling Limitations

As models are only approximations of real systems, they are only valid for specific scenarios and are inherently inexact. The models used in this thesis are subject to limitations. As described in chapter 4.4, the cell models are built as P2D models and are divided into nine equally-sized segments. Due to the small number of segments, the influence of current density distribution, temperature distribution, and SOC distribution in the simulations is probably smaller, compared to the actual cell. Hence, an increase in the number of segments and an adaptation of the segment distribution could improve the results. Especially next to the current collector tabs, where a strong current density gradient is expected, higher resolution could generate better results.

In addition to the resolution limitations, such a model requires more than 100 parameters. The cell manufacturer discloses very little information due to proprietorship, and this leads to inaccurate estimation of microscopic cell parameters, for example, exact cell chemistry, electrolyte information, thermal properties of cell components, and so on, are not disclosed by the cell manufacturer. Most parameters are obtained from literature, and some of them are obtained through experimentation and estimation. Hence, inaccurate cell parameters also limit the accuracy of the models. Two main parameters could be the reason for the differences in the temperature validation. The first one is the adopting of the entropic heat coefficient measurement for the graphite anode from [113], without actual half cell measurements of the selected cells. As the reversible heat generation has a significant impact on the total heat generation, especially at a charge and discharge current lower than 1C, the difference in the temperature profile of the 0.5C and 1C discharge can be partly ascribed to the entropic heat coefficient. Besides the entropic heat coefficient, detailed information about the electrolyte used are also unavailable. Due to the fact that the properties of the electrolyte have a significant influence on the ohmic resistance of a cell and, therefore, on the irreversible heating of the cell, inaccurate values could lead to an incorrect voltage profile and heat generation rate.

Overall, the simulations are limited to specific temperature and discharge current ranges, caused by

non-convergence of the solution due to the sensitivity of the parameters used in the multiphysics simulation platform. For the ambient temperatures of 25°C and 40°C, the COMSOL models are able to simulate all discharge currents from 0.5C to 3C. However, it was not possible to simulate discharge currents higher than 2C, especially at low ambient temperatures such as 15°C. The simulation results validated with the experimental data are good in some parts, but show a significant difference in the temperature gradients. The SOC and current density distribution results could not be validated because these parameters could not be measured directly. The presentation of SOC and current density gradients towards the end of discharge in the simulations might have some errors, especially when the simulated voltages have differences in comparison with the measurement data (Tabs. 5.5 – 5.7). The pattern of simulated results and experimental data were similar, which is still good for qualitative analysis.

5.4 Spatially Resolved Battery Model

This model is derived from the 2nd-order ECM[12] based on the time domain measurements described in section 3.3. A 2nd-order ECM as explained in section 4.3 is a 0-dimensional (0D) time-dependent model, as it assumes that the cell characteristics are identical at all spatial coordinates in a battery. This assumption is true if the geometric size of the battery is very small. If the dimensions are up-scaled, that is, as the cell size increases, all spatial coordinates in a battery will not have similar electrochemical or thermal characteristics, but they rather differ from one point to another. Therefore, the cell inhomogeneity inherently occurs when the size increases. Hence, to evaluate inhomogeneity, these effects are incorporated by transforming a 0D model into a spatially-resolved equivalent circuit model (SRECM). Fig. 5.33 shows the schematic of a SRECM, developed from a 2nd-order ECM.

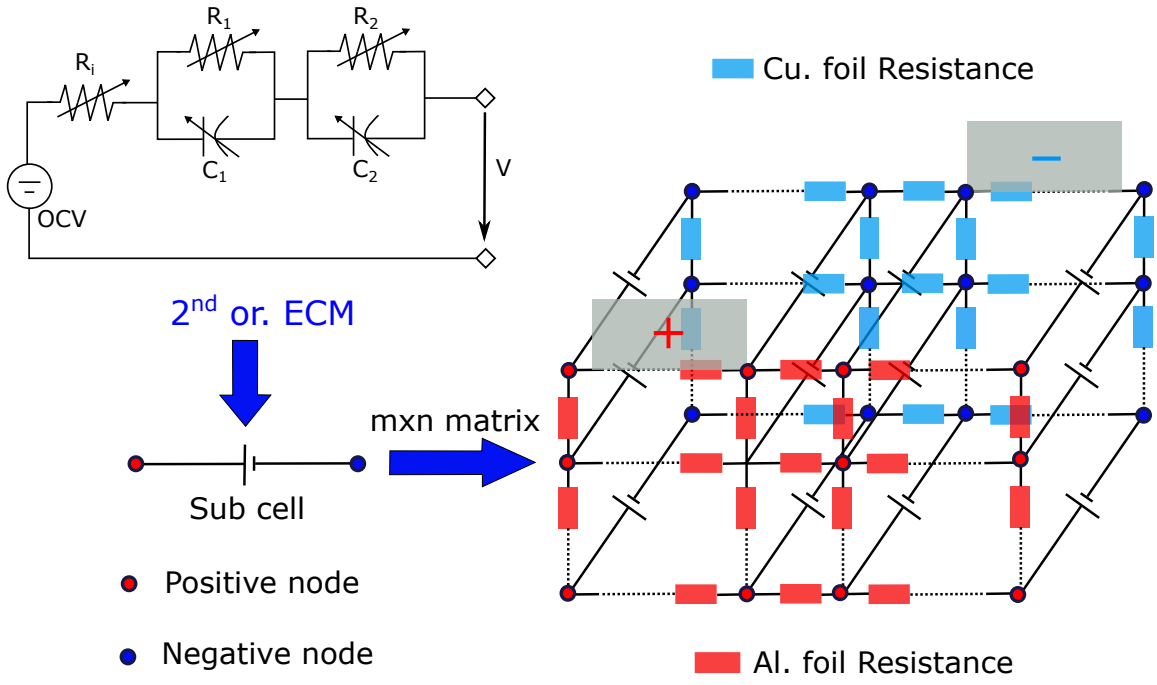

Figure 5.33: Schematic of a spatially resolved battery model derived from a 2nd-order ECM

[12] This section has been contributed by the internship work of Mr. Chethan Parthasarathy.

A cell consists of components such as positive and negative current collectors, positive and negative electrodes, and a separator. The active material part, that is, two electrodes and a separator representing a 2nd-order ECM, is connected between the nodes of positive and negative current collector plates. Therefore, the resistance of the current collectors have not been taken into account; instead, the current collectors are represented as 2D resistance grids with the consideration that the current collector thickness is much smaller compared to its length and width. The 8 Ah and 75 Ah cells were selected for SRECM, these cells being the smallest and the largest sizes, respectively. These cells would make a comparative study of how sizing influences the cell inhomogeneity. The number of the sub-cells were also selected based on the cell size, that is, a 5x5 matrix for the smaller 8 Ah cell and a 12x12 matrix for the larger 75 Ah cell. Irrespective of the position of the sub-cells along the plane, they are all connected in parallel (if the resistance between two nodes is neglected) in a way that the positive terminal of the sub-cells are connected to the positive current collector nodes, and the negative terminal of the sub-cells is connected to the negative current collector nodes. The grid resistances of the current collectors are evaluated based on the number of nodes selected for each current collector material by a discretization process. With these settings, the parameters of the sub-cells are calculated as shown in the Eqns. (5.17) – (5.21), where N is the number of nodes, and Cap is the cell capacity in Ah.

$$R_{i,subcell} = R_{i,fullcell} \cdot N \tag{5.17}$$

$$C_{i,subcell} = \frac{C_{i,fullcell}}{N} \tag{5.18}$$

$$OCV_{i,subcell} = OCV_{i,fullcell} \tag{5.19}$$

$$Cap_{i,subcell} = \frac{Cap_{i,fullcell}}{N} \tag{5.20}$$

$$SOC_{i,subcell} = \frac{\int I_{i,subcell} \cdot dt}{Cap_{i,subcell}} \tag{5.21}$$

The parameters R_i, R_1, C_1, R_2, and C_2 were estimated by running an optimization script in Matlab® using the Eqns. (4.3) - (4.5). The parameterization was performed at a 10% SOC interval between 0% and 100% SOC from the input current and voltage response of the HPPC profile, as shown in Fig. 3.7. The aged cells were also parametrized with the same procedure, using the HPPC profile at different aging intervals. The parameterization of the 8 Ah and 75 Ah cells are shown in App. A1.7, in Tabs. A5 & A6, respectively. The OCV parameters of both cell types were evaluated as described in section 5.1.3. The model was then improvised to incorporate the aging effects, by regularly updating the cell parameters at different cycling intervals. The spatially resolved battery model was built in Simulink/Simspace® to simulate the cell behaviour. The input values of the simulation were a 1C discharge C-rate and 25°C ambient temperature from a fully charged cell at 100% SOC. The output of the Simulink model provides the current, voltage, and SOC of each sub-cell and the output voltage of the complete cell. The simulation of the 8 Ah and 75 Ah cells were performed using their respective cell parameters. The simulation conditions for the aged cell were same, except that some parameters,

such as OCV, resistance, capacitance, and remaining discharge capacity, were different [175]. A lookup table function was used to handle the aging parameters of the cell.

5.4.1 Simulation Results

The battery model was simulated in two stages. At first the output voltage was validated with the measurement data to compare the accuracy of the model. In the next steps, the surface distribution of the current, SOC, and voltage were simulated.

5.4.1.1 Comparison of Simulated and Measured Voltage

The 2nd-order spatially resolved ECM was simulated by providing the cell parameters for a given cell with its aging history. Fig. 5.34 shows the comparison of the measured and simulated voltage of a 75 Ah cell. The plot with the marker indicates the measured data, and the continuous lines are simulation results. It can be observed that, at each passing aging interval, the discharge capacity was reduced as a result of capacity loss and impedance increase. The lower discharge time and the increase in polarization voltage denote the capacity fade and impedance rise, respectively. The simulated voltage at different cycle numbers matched the measured data very closely. The simulation results are reasonably accurate, except for at the beginning of discharge and towards the end of discharge. The mean relative error was close to 2%, and, in some cases, the error was greater than 5%, especially towards the EOD. At very low SOCs, the dynamics of the battery changed very quickly, with a significant increase in the diffusion resistance. The model response and adaptation to the change in battery aging was very good.

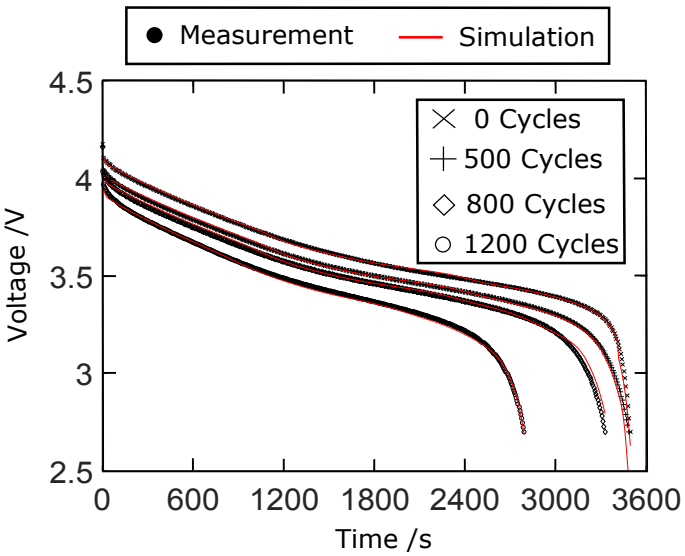

Figure 5.34: Comparison of the measured and simulated discharge voltage of a 75 Ah cell at different aging intervals, 1C rate and 25°C

5.4.1.2 Surface Plots to Evaluate Inhomogeneity

The surface plots were aimed at studying the current, SOC, and voltage distribution in the cell during a continuous discharge process. Fig. 5.35 shows the current distribution on the surface of the 8

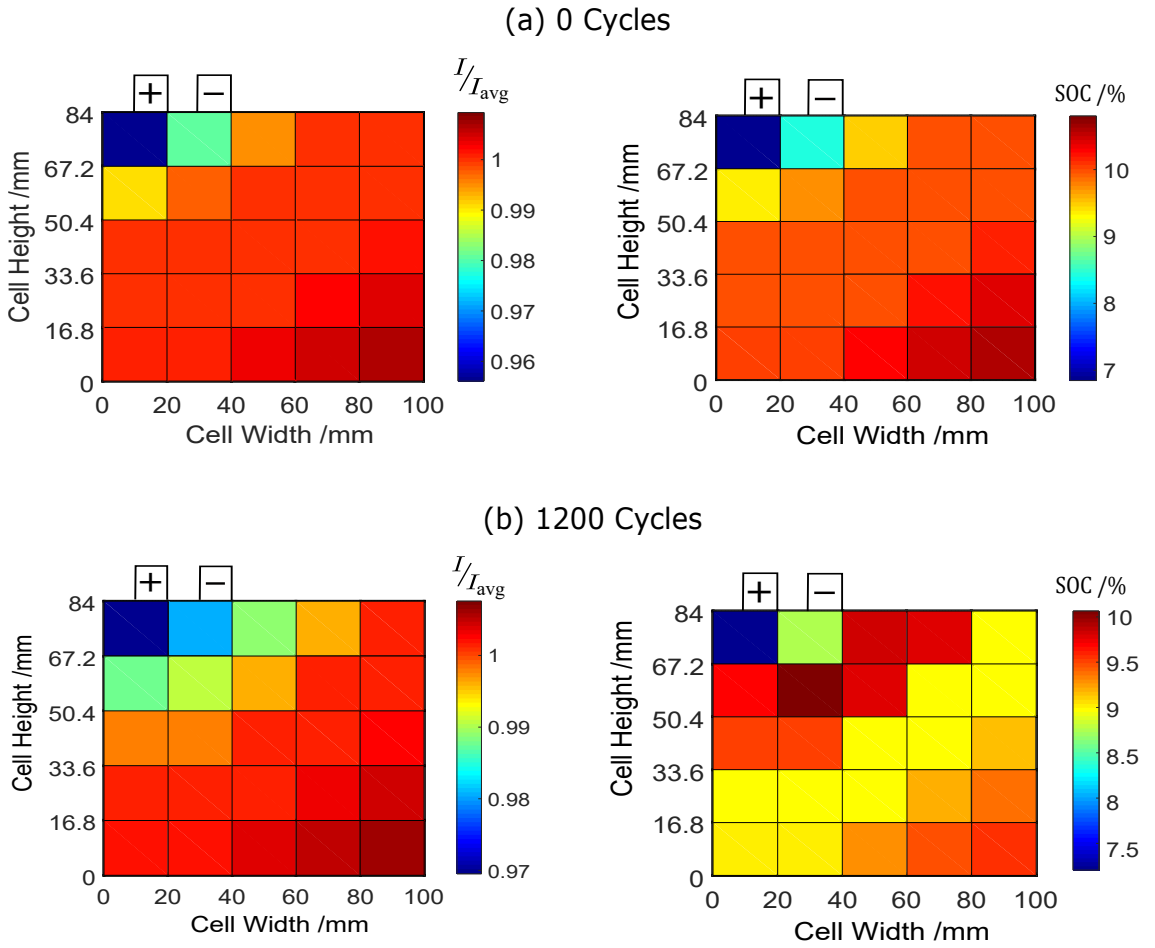

Figure 5.35: Comparison of the current and SOC distribution of 8 Ah cells in fresh and aged cells (1,200 cycles) at 10% SOC and 25°C

Ah cell at 10% SOC during a 1C discharge process. Due to the small geometric dimensions, the current distribution was more or less uniform throughout the surface. In addition to this, there was no significant difference in the current gradient between the fresh and aged cell. This shows that the aging was more or less homogeneous in the investigated small-format cells. In contrast, the current and the SOC distribution in the large-format 75 Ah cell was non-homogeneous. The cell aging increased the inhomogeneity, as illustrated in Fig. 5.36. In the aged cell at 1200 cycles, the currents are inhomogeneously distributed, that is, near the cell tabs, towards the centre of the cell, and in the region farthest away from the tabs. This is a clear indication of inhomogeneous aging, where some regions of the cell exhibit different characteristics. It should be noted that the current distribution is not constant throughout the discharge process. It can fluctuate between lower and higher values. In the beginning of discharge, the positions near the cell tab experience higher current distribution than positions that are farther away from the tabs. However, towards the EOD, there was a reversal of current distribution. The reversal of the current distribution was observed in the multiphysics simulation results (Fig. 5.29), and it can also be seen in previous works [21, 25, 176].

This occurs due to the change in the local impedance characteristics of the cell influenced by local SOC and temperature. The SOC gradient is the result of inhomogeneous current distribution. When the local SOC decreases, it increases the impedance of the region, thereby forcing the current to follow the

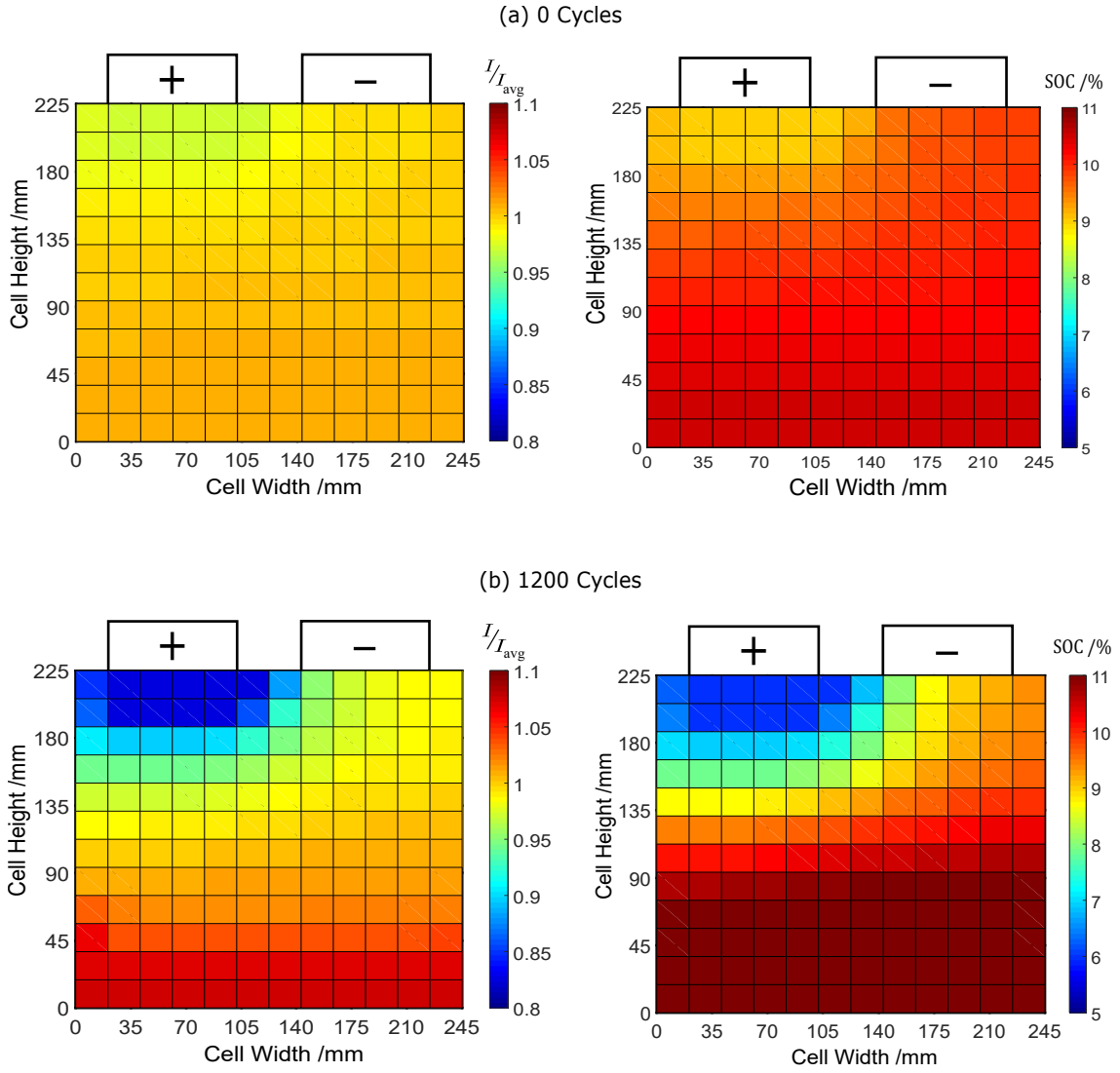

Figure 5.36: Comparison of the current and SOC distribution of 75 Ah cells in fresh and aged cells (1,200 cycles) with a 1C discharge rate at 10% SOC and 25°C

path of least resistance. Fig. 5.37 shows the current distribution pattern in a 75 Ah cell, aged at 1200 cycles at a 1C discharge current at various SOC intervals. At the beginning stage of the discharge, that is, at 98% SOC, the current distribution is at the maximum proximity to the positive tab of the cell and gradually reduces at the positions farther away. This high concentration of current decreases the SOC level at a faster rate to create an SOC imbalance. This process influences the local cell impedance and the local OCV, as the impedance and OCV are functions of SOC. After the initial inrush of current near the cell tab, the current distribution throughout the cell improves due to different impedance and OCV along the cell. The regions with high impedance and/or low OCV experience lesser current, and vice versa. Hence, the magnitude of current gradually reduces near the tabs and increases towards the positions farthest away from the cell, as illustrated at 80%, 60%, and 40% SOCs. At these SOC levels, the currents near the cell tabs are still marginally higher than at other locations. Towards the EOD, the cell impedance starts increasing at a greater rate, thereby restricting the current flow near the tabs, and, at the same instance, the SOC levels in the region farthest away from the tab are considerably high. Hence, the current distribution in this region increases. This process is called reversal of current

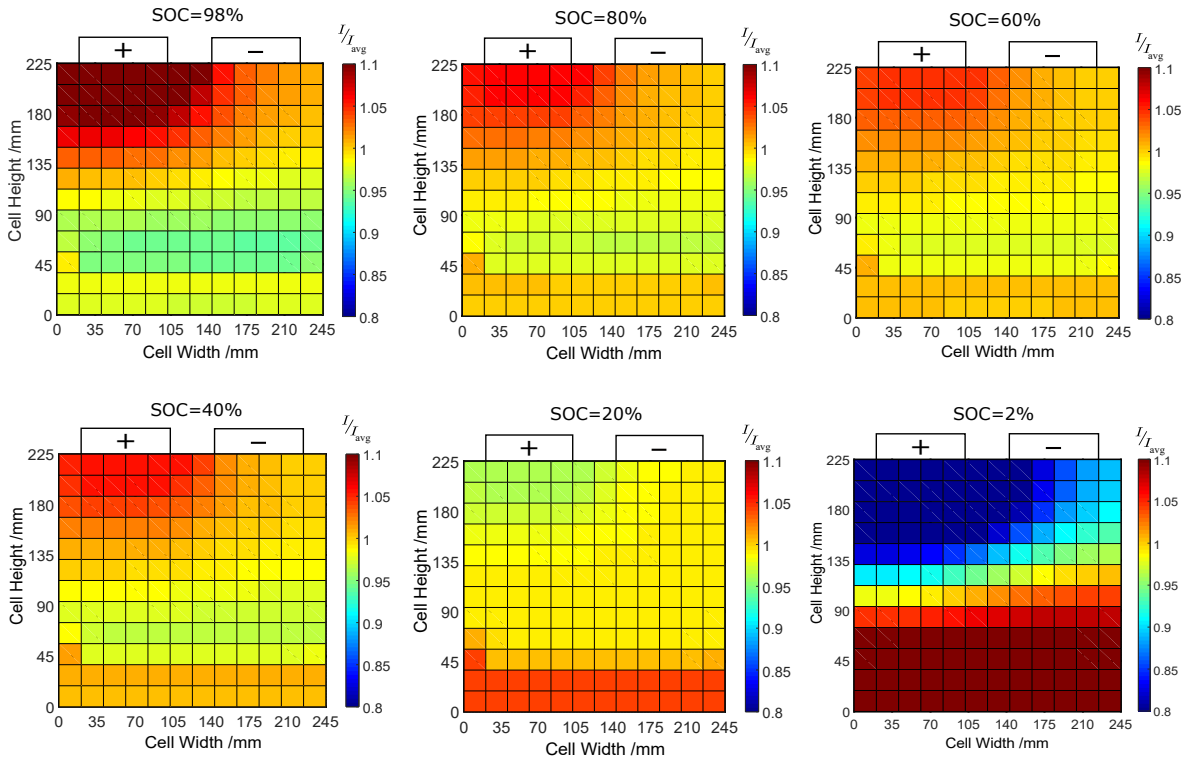

Figure 5.37: Comparison of surface current distribution in 75 Ah cells at different SOCs; after 1,200 cycles, 25°C, and 1C discharge rate

distribution, which happens between 40% and 20% SOC. At the point close to complete discharge (2% SOC), the current distribution is completely opposite to that at the beginning of discharge (98% SOC).

The location near the cell tabs is always subjected to fluctuation in current density inherently present due to the design of the cell. Therefore, it is important to study the current flow pattern near the cell tabs. Fig. 5.38 shows the current flow pattern in a 75 Ah cell during a 1C discharge at different stages of aging. The reversal of current distribution is not very significant in the new cell. As the cell ages, it can be observed that current flow near the positive tab further reduced towards the EOD. This is an indication that this region has a lower capacity due to aging, or it has entered into the deep discharge phase, where the cell impedance is very high. This could perhaps explain why the capacity fade is very nonlinear in the 75 Ah cell in comparison to the 8 Ah cell, which could be the reason for its early EOL.

It should also be noted that voltage distribution is inhomogeneous due to current distribution, as shown in the voltage drop at different regions in the aged 75 Ah cell in Fig. 5.39. The region near the positive tab shows the highest voltage polarization throughout the discharge, followed by regions close to the negative tab, centre, and right bottom edge of cell. Similar results were observed by Erhard et al. [27] in a cylindrical cell, where the positions farther away from the cell tab experience lesser voltage polarization during a continuous discharge. However, this gradient appears to be nearly constant throughout the discharge process, which is in contrast to the reversal of current distribution. Nevertheless, the positive and the negative tab regions are always stressed and susceptible due to inhomogeneity. Therefore, localized or inhomogeneous aging provides strong case of performance degradation in the large-format cells.

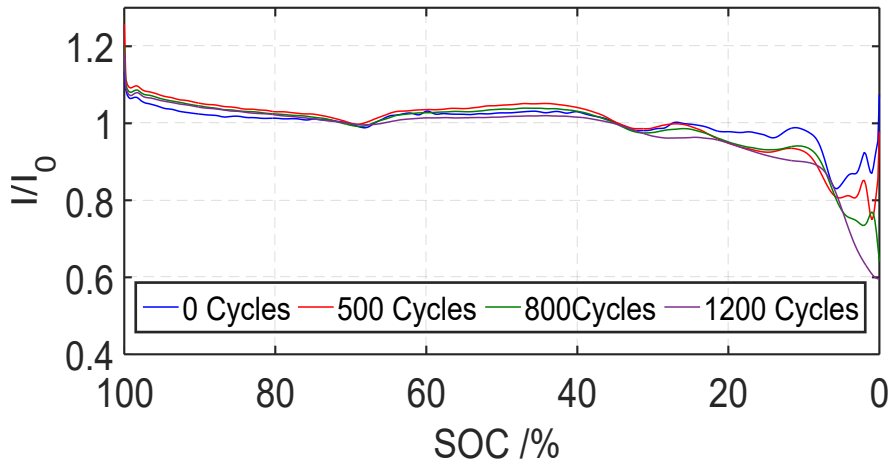

Figure 5.38: Current distribution near the positive tab of the 75 Ah cell under different aging conditions, 1C discharge current, and 25°C

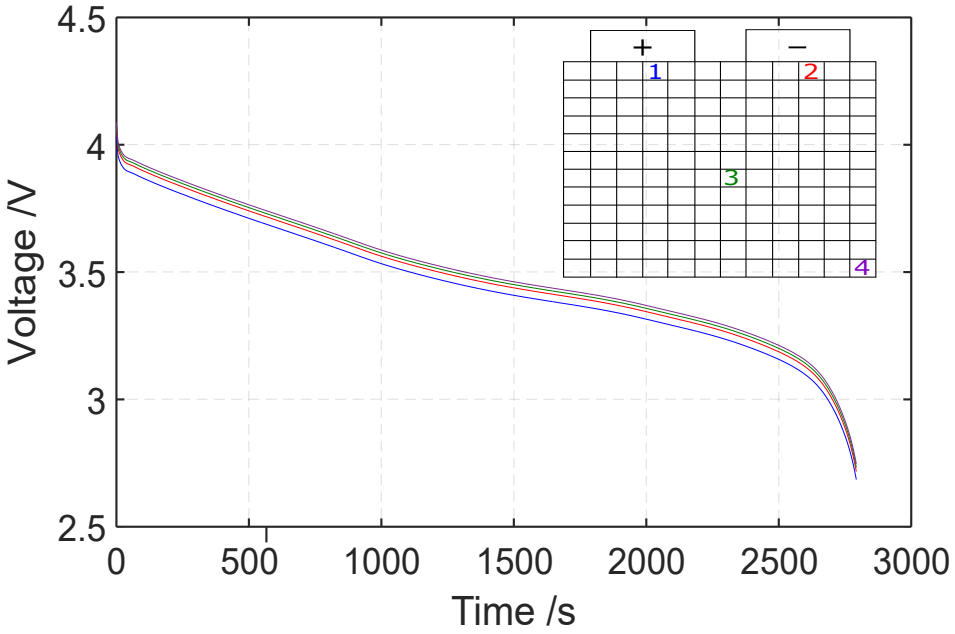

Figure 5.39: Discharge voltage simulation at different regions in a 75 Ah cell after 1200 cycles at 1C discharge current and 25°C

5.4.2 Computational Effort

The battery model simulation was done in a Matlab/Simulink® environment, and the Simspace block was used for the computation of electrical equivalent circuits. Tab. 5.9 shows the computation summary of the simulated cells. A variable step type ode15s (Stiff/NDF) solver with a relative tolerance value of 10^{-3} was used as configuration parameters for the simulation. It is visible that the solution time increases with the increase in the number of sub-cells. This is due to the fact that the number of energy storage elements (capacitors) in the circuit significantly increases with the number of sub-cells. Another advantage of this modelling approach is that aging parameters can be easily obtained from the experimental results in comparison to the parameters required to solve a Newman model. The computation efforts and model complexities are much greater in this approach, that is, for COMSOL P2D and 3D models, respectively. The simulations were performed on a server with 96 GB of installed memory (RAM) and 2.90 GHz CPU [146]. In a simple comparison, a full 3D model requires 4.6 times more memory space and consumes 380 times more computation time than a SRECM.

Table 5.9: Comparison of computation time and required memory for different simulation platforms

Simulation Platform	Cell	Solution Time [s]	No. of Sub-cells	Memory Used [GB]
Matlab SRECM	8 Ah	25.28	25	2
Matlab SRECM	75 Ah	144	144	2.56
COMSOL P2D	75 Ah	1020	9	1.44
COMSOL 3D	75 Ah	54845	full 3D	11.78

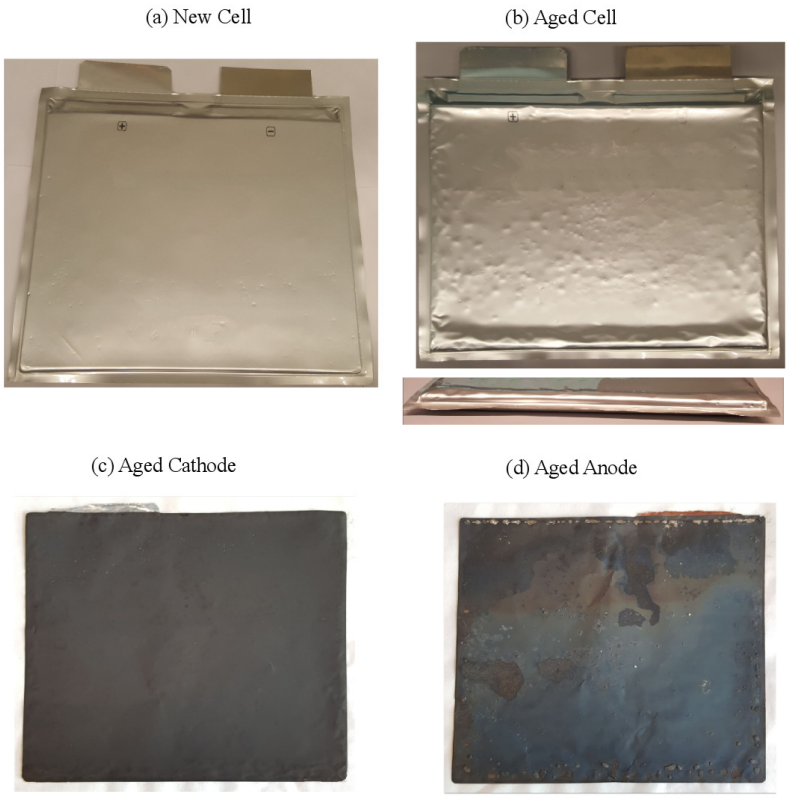

Figure 5.40: Visual inspection of the new 75 Ah cell and the same cell at the end of life

5.5 Visual Inspection of Disassembled Cells

This section discusses the visual inspection of a large-format 75 Ah cell. Fig. 5.40 shows the captured images of the cell in fresh and aged condition as well as the snapshots of aged cathode and anode electrodes. When the cell was new, its surface appeared to be pristine and flat with an average thickness of about 11.47 mm. At the end of life, the cell surface was uneven with small spots at some places. It also appears to be bulged at the edges along the length of the cell. The thickness increase can be noticed in the side view of Fig. 5.40 (b) and measured on the cell as shown in Fig. 5.25. As explained in section 5.2.2, the cell thickness accumulated during the cycling aging to a maximum thickness up to 28% from its original value. The average thickness at the EOL was 12.98 mm, that is, 13.2% increase.

The aged cell was opened inside the argon-filled glove box in a completely discharged state. The electrodes were separated and washed with DMC and dried to remove the remaining traces of electrolytes and impurities. Fig. 5.40 (c) & (d) shows the images of the aged cathode and anode electrodes, respectively. It could be observed that there were no major damages to the cathode, except at the edges where the surface appeared to have undergone mechanical strain. There were tiny white spots on the surface, which could have been some by-products due to irreversible reactions mainly caused by the aging process. The anode surface appeared to be completely damaged by the aging process. Metal deposits could be seen on the edges of the electrode at the locations where the unopened cell had bulged. They may have formed due to mechanical pressure enforced by the sealing process. These metal deposits have been reported as lithium plating on the anode surface [167]. In some parts of the electrode surface, the graphite materials were exfoliated from the current collector. This occurs due to cracking of the SEI layer, solvent co-intercalation, gas evolution, and so on, as explained in section 2.3.

These visual inspections indicate that the aging process is triggered by the deterioration of anode electrode. The optical view represents the inhomogeneous aging (according to Fig. 5.36) and the current/SOC distribution (according to Fig. 5.37). Similar images of the 8 Ah cells can be found in App. A1.9.

Chapter 6

Benefits of Cell Sizing Investigation

6.1 Selection of the Right Cell

Selection of the right cell type is critical for the design and development of the battery pack to match the vehicle energy and power demands. Tab. 6.1 shows the characteristics of different cell forms. Each format presents certain advantages and disadvantages in the context of vehicle application. Cylindrical cells comes in standard format, and they have great advantage in manufacturing compared to non-standardized pouch and prismatic forms. This cost advantage is not going to continue much longer, as the cost of manufacturing flat cells has come down significantly over the years and getting closer to the cylindrical cells. To overcome poor packing efficiency, cell manufacturers started producing prismatic and later pouch cells. The prismatic form has a lower energy density due to the hard casing; hence, to improve the energy density, soft polymer cases were used in the pouch cells. However, this light weight design advantage is lost at the pack level, as they require more packing for mechanical strength.

Table 6.1: Comparison of Different Cell forms [177]

	Prismatic	Cylindrical	Pouch
Heat rejection/cooling	Good	place between cells can be used for cooling	Good
Stacking	Easiest	Requires extra parts	Requires extra parts
Assembly in module	Good	Requires integration	Hardest: requires more housing to add rigidity
Recycling/disassembly	Good	Good	Difficult if tabs are laser welded
Packing efficiency	Good	Worse	Best
Casing	Aluminium, steel or hard plastic	Steel/Aluminium	Polymer
Use in vehicles	In production BMW i3	Panasonic cells in Telsa EV	LG Cells in Chevrolet Volt

The great advantage of pouch and prismatic forms is that they are available in larger sizes, that is, more energy per cell. This allows a reduction in the number of cells with a parallel connection in a module and thus reduces the pack assembly cost. However, due to the non-standardized shapes, they are more difficult to manufacture. If only the costs of the cells are considered in a battery pack, cylindrical cells are much cheaper than the other forms. Cylindrical cells are mostly available in 18650 configurations, either as high-energy or high-power cells. The high-energy cells are preferred for EV applications and high-power cells in HEV applications. A typical high-energy 18650 cell has a capacity of ∼3 Ah. The battery pack for EVs is built by assembling cells in a series and parallel to enhance voltage and cell capacity, respectively. It requires several thousands of cells to build a battery pack for EV application. The cost of BMS may increase with the number of cells to monitor in a battery pack. Here, a large-format pouch and prismatic cells have a clear advantage, where individual cells have capacity up to 60 Ah. Irrespective of any cell size, each cell has a nominal voltage between 3–4 V,

and, on average, more than 90 cells are connected in a series to bring the voltage above 360 V. In such a scenario, a few hundreds of large-format pouch/prismatic cells, including the parallel connections, are required to build a battery pack.

Going from cell level to module and pack level, the gravimetric energy density and power density are reduced significantly. The number of passive components gets added at each level from the cells to the pack. These passive components are essential to ensuring the cells are performing at their best to deliver required energy and power to the vehicle. They consist of the following parts:

- A battery management system, an assembly of circuit boards programmed to monitor, the voltage, current, and temperature from cell level to pack level. It also monitors the SOC, SOH, SOF, and SOS, of the battery.
- Power electronics distribute the high currents and include DC-DC converters, safety devices, shunts, fuses, connectors, and safety disconnector.
- Wiring to connect the cells in a series and parallel, connecting different cell-modules, and communication wires in the battery, such as CAN.
- Mechanical support material such as casing with plastic or metals, insulation between the electrical and cooling components.
- Thermal management of the battery, such as cooling, heating, heat sinks, fans, liquid channels, and so on.

Table 6.2: Battery Pack Details

Manufacturer	Battery Pack Energy [kWh]	Cell Capacity [Ah]	Cooling Type	Topology	No. of Cells
VW [178]	18.7	25 /Prismatic	Air	2P102S[1]/17[2]	204
Smart EV [179]	17.6	52 /Pouch	Liquid	1P93S/3	93
i-MiEV [180]	16.3	50 /Prismatic	Air	1P88S/12[3]	88
Tesla S [181]	85	3.1 /Cylindrical	Liquid	74P96S/16	7104
Nissan Leaf [182]	24	32.5 /Pouch	Air	2P96S/48	192

6.2 Challenges Due to Size Increase

In the last years, battery packs have been built with large-format cells, with exceptions in Tesla cars where the small-format cylindrical cells are the preferred choice. The large-format cells are mainly produced in prismatic or pouch forms. This idea was derived from batteries for mobile devices that are geometrically flat and in which it is not possible to use cylindrical cells for such devices. Due to their non-standardized shapes and sizes, there exist many variants of large-format cells; they are more expensive than many cylindrical cells put together to match the capacity. The cost factor also comes from the complexity of the manufacturing process. Its mechanical integration in the stages of pick and place, stacking and winding are more difficult to accurately ensure the critical alignment of the electrode stack with high uniformity. Large-format-cell manufacturing currently results in typically

[1] 2P102S: two cells in parallel and 102 cells in a series; a total of 204 cells
[2] No. of modules; they are connected in series to boost the battery voltage
[3] The battery pack is composed of 88 serially connected cells assembled in 12 modules (10 modules of 8 cells and 2 modules of 4 cells)

lower cell yield and slightly higher cell-to-cell variation compared to short-format cells. The optimal cell capacity for an EV application is between 40 and 60 Ah per cell, in some cases, up to 100 Ah per cell (example, the new BMWi3 has 93 Ah cells). Even though they have an advantage in weight distribution, volume distribution, and packing efficiency in a battery pack, it is only possible to match these parameters at the battery pack level if its energy density at the cell level is comparable to cylindrical cells. The energy density of the battery pack for the Tesla S at cell level is significantly higher than the rest. Such an improvement can make the battery pack lighter and more compact.

Figs. 5.10 and 5.11 show that the temperature gradient was highest in the 75 Ah cell, irrespective of cooling conditions. It is interesting to note that the temperature gradient was higher when aluminium cooling plates were in contact with the cell surface. However, without the cooling plates, the maximum temperatures in the cell would be significantly higher, as shown in Tab. 5.1. The surfaces close to the cell tabs experience high temperatures, and this increases the temperature gradient in the cell. On the one hand, cooling plates placed on the cell reduce the cell temperature, and, on the other hand, they increase temperature inhomogeneity. An optimal solution should be considered to reduce the average cell temperature and also keep the temperature gradient to a minimum value. Otherwise, large-format cells experience inhomogeneous aging, leading to premature end of life, as shown in Fig. 5.1. Air-cooled systems are less expensive than aluminium cooling plates because the pack and module designs can integrate the air channels into the mechanical structure without additional cost to the system. On the other hand, it reduces the volumetric energy density at battery level pack, because a lot of empty spaces are consumed in the process [183]. The cooling plates between the cell surfaces not only increase temperature inhomogeneity, but they also may not be efficient if they are not completely in contact with the cell surface. Moreover, surface cooling is inefficient because it creates a high thermal gradient perpendicular to the layers. This leads to non-uniform impedance and therefore non-uniform currents between the layers, thereby reducing the useable cell capacity. Therefore, surface cooling leads to inhomogeneous aging, whereas tab cooling can result in uniform current distribution in each layer [184]. In such a scenario, the tab cooling can be cost-efficient, reduce capacity loss, and remove excess heat from the cell tabs where the maximum cell temperature is expected, as described in [185].

The volume expansion poses additional challenges to the mechanical stability of the cell. Frequent expansion and contraction causes visco-elastic deformation of the materials, resulting in accumulation of cell thickness. There should be a sufficient gap or spacer material between cells and external casing to prevent unwanted stress acting on the cell. Swelling is another problem that is persistent in pouch cells, especially when the cell is at high SOC. It increases with battery overcharge, resulting from faulty BMS, and jeopardizes the safety of the battery pack. This problem is not so prevalent in prismatic cells due to their hard casing. Additionally, it is difficult to provide fool-proof protection from an internal short circuit or thermal runaway at the initial stages, as explained in section 2.1. The cylindrical cells are equipped with CIDs, PTCs, and a pressure vent, which are enabled to function in the event of overcharge, high temperature, and pressure, respectively. To a certain extent, prismatic cells have PTCs and a pressure vent, but these devices are not present in pouch cells due to their inherent design. Therefore, pouch cells are extremely vulnerable to risk compared to other cell forms, relying completely on the BMS unit to prevent such undesirable events. Finally, the inhomogeneous aging reduces the lifetime of the battery pack, and this means early replacement of the battery pack and additional costs to the end user. This price is significant when the cost of the battery pack is around 30% of the vehicle price.

These challenges are not meant to discourage the usage of large-format cells in EV applications; they should be viewed from a perspective of addressing them sooner than later.

6.3 Improvement in Design to reduce Cell Inhomogeneity

This section proposes improvement in the cell design to reduce the current density gradient, thereby reducing the cell inhomogeneity. There are several design parameters that affect current distribution in the cell, as explained in section 2.3.3. In this example, a large-format 75 Ah cell has been chosen for the study. The cell aspect ratio is kept constant, and, by varying tab size and location, different cell designs were studied. Tab 6.3 shows four different tab configurations, namely NT, CT, wide tab design (WT), and a combination of wide and counter tabs (WCT) with varied tab size and location.

Table 6.3: Difference in tab configurations for 75 Ah

Dimensions[4]	NT	WT	CT	WCT
$d_{p,tab}$ in mm	17	0	80	32
$L_{tab,W}$ in mm	86	110	86	180
W in mm	245	245	245	245
$d_{pc,tab}$ in mm	60	55	123	122
ϵ_{tab}	0.245	0.224	0.5	0.498

The $L_{tab,W}$ values for WT and WCT were increased to reduce the constriction and spreading resistance, which helped to reduce the current density distribution near the tabs. Another design parameter is tab eccentricity (ϵ_{tab}), that is, how much the tabs are centrally positioned along the width of the cell. The optimum value for ϵ_{tab} is 0.5, whereas any smaller or larger fraction will distribute the current unevenly along two halves of the cell width. Eqn. (6.1) shows the calculation of ϵ_{tab}.

$$\epsilon_{tab} = \frac{\text{Distance of tab centre from Y-axis } (d_{pc,tab})}{\text{Cell width (W)}} \tag{6.1}$$

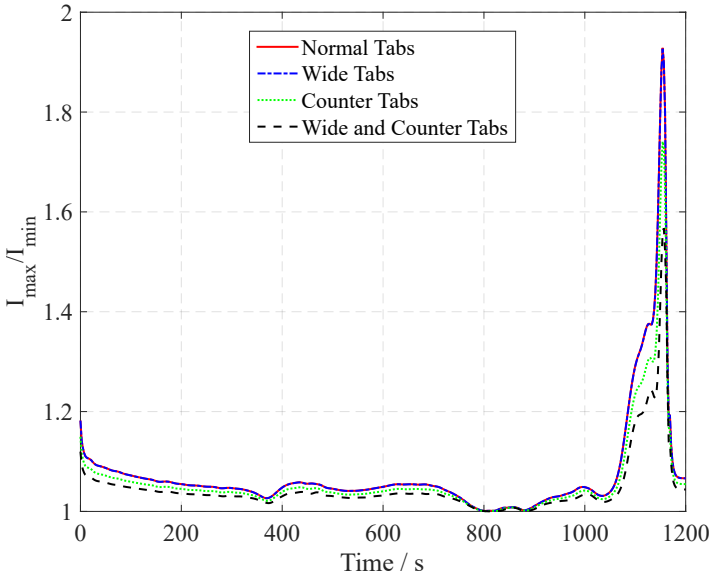

Figure 6.1: Ratio of the maximum to minimum current distribution on the electrode surface during 3C discharge at 25°C for different tab designs

The proposed cell designs were simulated using the SRECM approach (explained in section 5.4) to evaluate the current and SOC distribution in the cell. Fig. 6.1 shows the ratio of the maximum to

[4]The schematic of the parameters is shown in Fig. 4.6.

minimum current simulated along the cell surface during a 3C discharge at 25°C ambient temperature for different tab designs. The result shows a higher gradient for both the NT and WT designs compared to CT and WCT. The current distribution in the NT and WT designs were nearly similar, and it did not improve the current distribution because of the WT design. This could be due to reduced tab eccentricity, and hence the advantage due to the widening of tabs was neutralized. The difference in the current gradient for different tab designs may appear smaller, but, over a length of discharge, the SOC difference increased with each passing time step. The CT and WCT designs improved the current distribution and also saw a reduction in the maximum current gradient compared to other designs. It should be observed that the tab eccentricities for both designs were close to the optimal value of 0.5.

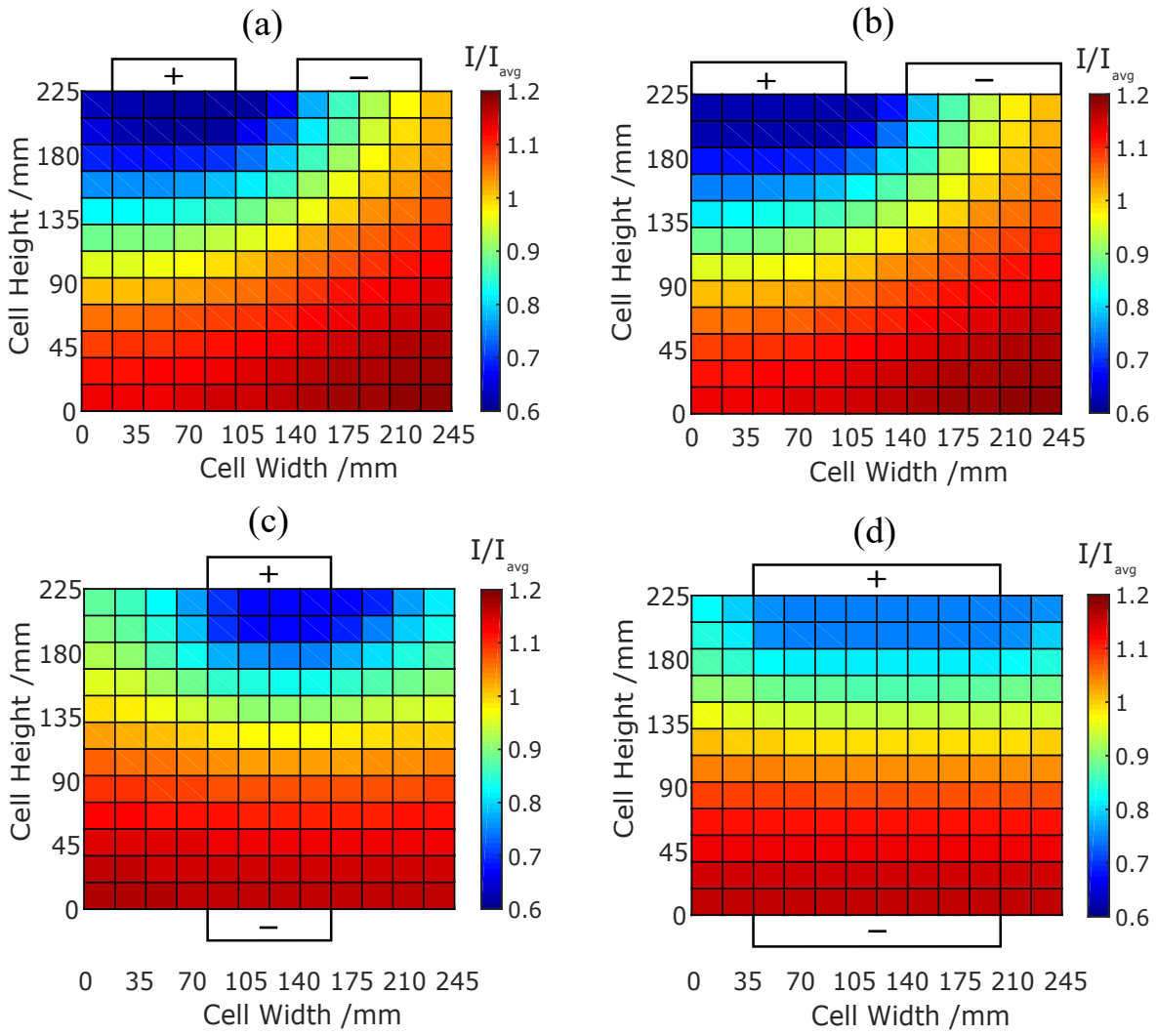

Figure 6.2: Maximum current distribution on the electrode surface during 3C discharge at 25°C for (a) Normal Tabs, (b) Wide Tabs, (c) Counter Tabs, & (d) Wide and Counter Tabs, cell SOC = 4%

The maximum current gradient occurs around 4% SOC for all cell designs. Fig. 6.2 shows the surface distribution at the maximum current gradient. The current distribution reversal can be observed for all tab configurations, that is, positions near the positive tab experience low current density compared to positions farthest from the tab. The current gradient is lowest in WCT, followed by the CT, WT, and NT designs. This surface plot is the best illustration of reducing the current density gradient in large-format cells. These results are in agreement with the proposed tab configurations in [21, 87]. Hence, increasing the tab width and improving the tab eccentricity in large-format pouch cells can reduce

the cell inhomogeneity. In the cylindrical cells, the current gradients can be reduced by introducing multiple tabs to the cell. This type of configuration is available in commercial A123 26650 cells, which have four tabs each for positive and negative terminals [186].

Despite this design improvement, it is critical to evaluate the cost of production and the gravimetric and volumetric energy densities of these cells. A CT design may not increase the cost of production, but it could increase the geometric length of the cell (including the length of the tabs) when the cell tabs are placed on the opposite side and decrease the overall volume of the cell, thereby reducing the volumetric energy density at the cell level. However, going to the module and pack level, it could serve as an advantage in the placement of cells to connect them either in a series or in parallel. The volumetric energy densities of module and packs can match the cells of the NT design or even improve it. However, a cell design with WCT requires additional current collector materials, both copper and aluminium, and the costs add up with an increase in kWh capacity. Both gravimetric and volumetric energy density are reduced with an increase in the amount of materials that do not take part in the electrochemical conversion of energy. Therefore, these design aspects need to be considered in finding an optimal solution for the overall performance of the cell.

Chapter 7

Conclusion and Outlook

7.1 Conclusion

It is a well known fact that the large-format cells have advantages in the EV battery compared to the short-format cells due to lesser connections and wiring for the battery pack, lower integration and assembly costs, higher weight to volume ratio, and so on. However, it was also observed that large cells age faster than small cells. With this sizing phenomenon, this thesis has found reasons for the faster aging in large-format cells and, if possible, avoid it with better design of cells and optimal thermal management.

This thesis begins with studying the influence of sizing on different cells, 8, 25, 53, and 75 Ah NMC cells, chosen for investigation. Through an extensive literature study, the effects of cell size increase have been evaluated. These studies have concluded that an increase in cell size increases cell inhomogeneity, additionally influenced by operating conditions, such as C-rate and ambient temperature. Hypotheses were developed proposing that cell inhomogeneity occurs only during cycling and not under storage conditions. Several experimental methods were reviewed and adopted to evaluate cell inhomogeneity. Results of aging tests proved the proposed hypotheses, as explained in section 5.1.1. The aging tests also proved that large-format cells age faster, and the aging is nonlinear when the cell is near its EOL. Additional aging results from 1.1 Ah and 2.5 Ah LFP cylindrical showed better capacity retention compared to the pouch cells.

Spatial temperature measurements showed that there is a strong influence of cell size on temperature inhomogeneity up to 10°C in 75 Ah cells, along with operating conditions such as ambient temperature and C-rate. The influence of operating conditions on temperature inhomogeneity agreed with the literature findings. It has also been demonstrated that cooling methods influence the temperature distribution in the cells irrespective of cell size. As temperature is a dominant stress factor in cell aging, a high temperature gradient leads to stronger aging inhomogeneity.

Cell volume expansion and contraction occurs during the charge and discharge process, respectively. A pouch cell expands by about 2% of its original volume, mainly restricted along its thickness. The measurements showed that volume expansion is non-uniform throughout the cell surface. It depends on the mechanical construction of the cell and the prestress caused by the manufacturing process. The volume expansion is directly related to cell voltage or SOC. High C-rate cycling led to large residual volume expansion in the cell due to temperature rise and residual cell capacity. This increases the

mechanical stress on the cell. The aging process caused thickness accumulation in the cell, due to SEI layer growth, lithium plating, gas evolution, and so on. In the large-format 75 Ah cell, its average thickness increased by 13%, and, due to inhomogeneous thickness growth, the maximum thickness increase was 28% at the EOL. Its thickness increase during cycling is an indication of diminishing SOH. The cell volume expansion measurement is critical for the design of battery packs. Sufficient thickness allowance should be provided between the cells and external casing in order to prevent external stresses from acting on the cell, when the cell remains in expanded state.

The results of multi-scale multi-domain models proved that the same cell parameters can be used to upscale the cell size to evaluate the performance of large-format cells. This simulation tool is particularly useful to study the performance of large-format cells in EV battery packs beforehand. The voltage and temperature measurements were validated against the simulation results with reasonable accuracy. These models were also used to evaluate current, SOC, and temperature distribution in the cell, which otherwise were not possible to measure with the existing techniques. However, these models have a few limitations, and these models were only used to perform a qualitative analysis. The limitations of this modelling technique are discussed in section 5.3.5.

SRECM was developed to evaluate aging inhomogeneity in two sizes, 8 Ah and 75 Ah cells, respectively. The simulation results showed that 75 Ah cells had greater inhomogeneity, especially toward the EOL. Inhomogeneous current and SOC lead to localized or inhomogeneous aging. The final part of the thesis explains the benefits of the cell sizing investigation, especially choosing the right cell type for a battery pack. It also explains various challenges caused by cell size increase and possible improvements to cell design, for example, changes to tab configuration to reduce inhomogeneity.

The major contributions of this thesis are:

- Calendar aging and cycle aging evaluation of commercial lithium-ion pouch cells with NMC chemistry, for the different sizes 8, 25, 53, and 75 Ah.
- A temperature inhomogeneity study through spatial measurements in different cooling medium: (a) forced air convection and (b) aluminium cooling plates.
- Volume expansion study of 8 Ah and 75 Ah cells, (a) fresh cells and (b) aged cells, and evaluation of thickness accumulation during the aging process.
- Electrochemical and thermal modelling of 25, 53, and 75 Ah cells with the same parameters (except for cell geometry) as the given cell types using the scale-up approach.
- Simulation of aging inhomogeneity by SRECM in Matlab/Simulink®.

7.2 Outlook

This thesis presents cell sizing investigations by comparing the performance and aging of commercially available cells. The cells chosen were not ideal for these investigations, and some compromises were made, as it is difficult to manufacture custom cell designs at laboratory or pilot scales that match tolerance and performance to obtain reproducible results.

- The tab configuration for the 8 Ah cell was different from that of the rest of the cells
- All the cells did not have identical thickness or number of layers

- The external sealing of the soft case was different for the selected cell types

For future sizing investigations, these aspects should be taken into consideration. The spatial measurements provided a good overview of temperature distribution on the cell surface. However, the inner layers of the cells were considerably hotter than the surface temperature due to less heat exchange with the surroundings. Efforts should be made to place temperature sensors inside commercial cells for further investigations. The displacement sensors used in the measurements are point-based, and they should be replaced with more accurate and higher-resolution laser sensors that construct 2D/3D images to evaluate the volume expansion in pouch cells. Moreover, future investigations of volume expansion should include cylindrical cells. Such investigations could be interesting for observing the influence of the cell size (diameter) on the mechanical stress applied in the electrodes.

The multi-scale multi-physics COMSOL model has few limitations in simulating the temperature, SOC, and current gradients. The simulated temperature gradients were much lower compared to the actual measurements. A full 3D electrochemical and thermal model with more detailed parameterization could improve the accuracy of the model. However, it is computationally more expensive, and it is difficult to obtain a complete set of parameters for a given cell without simplification of the model. The present model is not suitable for the simulation of aged cells, as many parameters change during the aging process, and new parameters have to be introduced, for example, SEI layer growth, lithium plating, and so on. The model should be improvised to adopt aging characteristics to evaluate aging inhomogeneity.

The SRECM is a much more simplified approach compared to a FEM-based tool like COMSOL. It has a limited set of parameters, and aging parameters were easily adopted from the available measurements. This model also needs further improvement by coupling the thermal model to the existing electrical model. The surface current and SOC distribution can be simulated more accurately by increasing the number of sub-cells. The modelling approach can be used to optimize the cell design, as it provides endless iterations of changes to the parameters to simulate the cell performance. This saves a lot of cost, time, and resources to manufacture high performance cells.

Bibliography

[1] Y. Zhang and C.-Y. Wang, "Cycle-life Characterization of Automotive Lithium-ion Batteries with $LiNiO_2$ Cathode," *Journal of the Electrochemical Society*, vol. 156, no. 7, pp. A527–A535, 2009. [Online]. Available: http://dx.doi.org/10.1149/1.3126385

[2] J. W. Fergus, "Recent developments in cathode materials for lithium ion batteries," *Journal of Power Sources*, vol. 195, no. 4, pp. 939–954, 2010. [Online]. Available: http://dx.doi.org/10.1016/j.jpowsour.2009.08.089

[3] D. Hurst and J. Gartner, "Global Forecasts for Light Duty Hybrid, Plug-in Hybrid and Battery Electric Vehicles: 2013-2020 ," http://www.navigantresearch.com/wp-assets/uploads/2013/06/EVMF-13-Executive-Summary.pdf, accessed: 21.12.2016.

[4] S. S. N. Kassatly, "The lithium-ion battery industry for electric vehicles," Ph.D. dissertation, Massachusetts Institute of Technology, 2010. [Online]. Available: http://hdl.handle.net/1721.1/61873

[5] "TUM CREATE EVA, Taxi for Tropical Megacities," http://www.eva-taxi.sg/index.php, accessed: 21.12.2016.

[6] D. L. Anderson, "An Evaluation of Current and Future Costs for Lithium-Ion Batteries for Use in Electrified Vehicle Powertrains," Ph.D. dissertation, Duke University, 2009. [Online]. Available: http://dukespace.lib.duke.edu/dspace/handle/10161/1007

[7] C. Pillot, "Battery Market Development for Consumer Electronics, Automotive, and Industrial: Materials Requirements and Trends," *The 11th China International Battery Fair, ShenZhen, China*, 2014. [Online]. Available: http://www.avem.fr/docs/pdf/AvicenneDiapoXining.pdf

[8] R. Gogoana, M. B. Pinson, M. Z. Bazant, and S. E. Sarma, "Internal resistance matching for parallel-connected lithium-ion cells and impacts on battery pack cycle life," *Journal of Power Sources*, vol. 252, pp. 8–13, 2014. [Online]. Available: http://dx.doi.org/10.1016/j.jpowsour.2013.11.101

[9] M. Wohlfahrt-Mehrens, C. Vogler, and J. Garche, "Aging mechanisms of lithium cathode materials," *Journal of power sources*, vol. 127, no. 1, pp. 58–64, 2004. [Online]. Available: http://dx.doi.org/10.1016/j.jpowsour.2003.09.034

[10] J. Vetter, P. Novák, M. Wagner, C. Veit, K.-C. Möller, J. Besenhard, M. Winter, M. Wohlfahrt-Mehrens, C. Vogler, and A. Hammouche, "Ageing mechanisms in lithium-ion batteries," *Journal of power sources*, vol. 147, no. 1, pp. 269–281, 2005. [Online]. Available: http://dx.doi.org/10.1016/j.jpowsour.2005.01.006

[11] A. Barré, B. Deguilhem, S. Grolleau, M. Gérard, F. Suard, and D. Riu, "A review on lithium-ion battery ageing mechanisms and estimations for automotive applications," *Journal of Power Sources*, vol. 241, pp. 680–689, 2013. [Online]. Available: http://dx.doi.org/10.1016/j.jpowsour.2013.05.040

[12] R. Arunachala, S. Arnold, L. Moraleja, T. Pixis, A. Jossen, and J. Garche, "Influence of cell size on performance of lithium ion battery," in *Oral presentation at Advanced Battery Power Conference Aachen*, 2015.

[13] R. E. Gerver and J. P. Meyers, "Three-dimensional modeling of electrochemical performance and heat generation of lithium-ion batteries in tabbed planar configurations," *Journal of The Electrochemical Society*, vol. 158, no. 7, pp. A835–A843, 2011. [Online]. Available: http://dx.doi.org/10.1149/1.3591799

[14] M. Fleckenstein, O. Bohlen, M. A. Roscher, and B. Bäker, "Current density and state of charge inhomogeneities in Li-ion battery cells with $LiFePO_4$ as cathode material due to temperature gradients," *Journal of Power Sources*, vol. 196, no. 10, pp. 4769–4778, 2011. [Online]. Available: http://dx.doi.org/10.1016/j.jpowsour.2011.01.043

[15] J. B. Gerschler, F. N. Kirchhoff, H. Witzenhausen, F. E. Hust, and D. U. Sauer, "Spatially resolved model for lithium-ion batteries for identifying and analyzing influences of inhomogeneous stress inside the cells," in *Vehicle Power and Propulsion Conference, 2009. VPPC'09. IEEE*. IEEE, 2009, pp. 295–303. [Online]. Available: http://dx.doi.org/10.1109/VPPC.2009.5289836

[16] R. Arunachala, L. Moraleja, A. Jossen, and J. Garche, "Aging Inhomogeneity influenced by Cell Size in Commercial Pouch Cells," in *European Electric Vehicle Congress (EEVC)*. European Electric Vehicle Congress, 2015. [Online]. Available: https://www.researchgate.net/publication/285593039_Aging_Inhomogeneity_influenced_by_Cell_Size_in_Commercial_Pouch_Cells

[17] N. B. Chemistries, "Diagnose A Problem Before It Begins," http://www.batterypoweronline.com/images/MayJuneDigital.pdf, 2010, accessed: 28.12.2015.

[18] M. Alamgir, S. Ketkar, and K. Yoo, "Recent progresses of LG Chem's large-format Li ion polymer batteries," in *Power and Energy Society General Meeting, 2011 IEEE*. IEEE, 2011, pp. 1–4. [Online]. Available: http://dx.doi.org/10.1109/PES.2011.6039774

[19] U. S. Kim, C. B. Shin, and C.-S. Kim, "Modeling for the scale-up of a lithium-ion polymer battery," *Journal of Power Sources*, vol. 189, no. 1, pp. 841–846, 2009. [Online]. Available: http://dx.doi.org/10.1016/j.jpowsour.2008.10.019

[20] A. A. Pesaran, G. Kim, K. Smith, S. Santhanagopalan, and K. Lee, *Overview of Computer-aided Engineering of Batteries and Introduction to Multi-scale, Multi-dimensional Modeling of Li-Ion Batteries*. National Renewable Energy Laboratory, 2012. [Online]. Available: http://www.nrel.gov/transportation/energystorage/pdfs/54425.pdf

[21] P. Taheri, A. Mansouri, B. Schweitzer, M. Yazdanpour, and M. Bahrami, "Electrical constriction resistance in current collectors of large-scale lithium-ion batteries," *Journal of The Electrochemical Society*, vol. 160, no. 10, pp. A1731–A1740, 2013. [Online]. Available: http://dx.doi.org/10.1149/2.041310jes

[22] G.-H. Kim, K. Smith, K.-J. Lee, S. Santhanagopalan, and A. Pesaran, "Multi-domain modeling of lithium-ion batteries encompassing multi-physics in varied length scales," *Journal*

of The Electrochemical Society, vol. 158, no. 8, pp. A955–A969, 2011. [Online]. Available: http://dx.doi.org/10.1149/1.3597614

[23] S. Du, M. Jia, Y. Cheng, Y. Tang, H. Zhang, L. Ai, K. Zhang, and Y. Lai, "Study on the thermal behaviors of power lithium iron phosphate (LFP) aluminum-laminated battery with different tab configurations," *International Journal of Thermal Sciences*, vol. 89, pp. 327–336, 2015. [Online]. Available: http://dx.doi.org/10.1016/j.ijthermalsci.2014.11.018

[24] A. Samba, N. Omar, H. Gualous, O. Capron, P. Van den Bossche, and J. Van Mierlo, "Impact of Tab Location on Large Format Lithium-Ion Pouch Cell Based on Fully Coupled Tree-Dimensional Electrochemical-Thermal Modeling," *Electrochimica Acta*, vol. 147, pp. 319–329, 2014. [Online]. Available: http://dx.doi.org/10.1016/j.electacta.2014.08.115

[25] G. Zhang, C. E. Shaffer, C.-Y. Wang, and C. D. Rahn, "In-situ measurement of current distribution in a Li-Ion cell," *Journal of The Electrochemical Society*, vol. 160, no. 4, pp. A610–A615, 2013. [Online]. Available: http://dx.doi.org/10.1149/2.046304jes

[26] P. Osswald, S. Erhard, J. Wilhelm, H. Hoster, and A. Jossen, "Simulation and measurement of local potentials of modified commercial cylindrical cells i. cell preparation and measurements," *Journal of The Electrochemical Society*, vol. 162, no. 10, pp. A2099–A2105, 2015. [Online]. Available: http://dx.doi.org/10.1149/2.0561510jes

[27] S. Erhard, P. Osswald, J. Wilhelm, A. Rheinfeld, S. Kosch, and A. Jossen, "Simulation and measurement of local potentials of modified commercial cylindrical cells ii: Multi-dimensional modeling and validation," *Journal of The Electrochemical Society*, vol. 162, no. 14, pp. A2707–A2719, 2015. [Online]. Available: http://dx.doi.org/10.1149/2.0431514jes

[28] Z. Li, J. Zhang, B. Wu, J. Huang, Z. Nie, Y. Sun, F. An, and N. Wu, "Examining temporal and spatial variations of internal temperature in large-format laminated battery with embedded thermocouples," *Journal of Power Sources*, vol. 241, pp. 536–553, 2013. [Online]. Available: http://dx.doi.org/10.1016/j.jpowsour.2013.04.117

[29] U. S. Kim, J. Yi, C. B. Shin, T. Han, and S. Park, "Modelling the thermal behaviour of a lithium-ion battery during charge," *Journal of Power Sources*, vol. 196, no. 11, pp. 5115–5121, 2011. [Online]. Available: http://dx.doi.org/10.1016/j.jpowsour.2011.01.103

[30] J. Liu, M. Kunz, K. Chen, N. Tamura, and T. J. Richardson, "Visualization of charge distribution in a lithium battery electrode," *The Journal of Physical Chemistry Letters*, vol. 1, no. 14, pp. 2120–2123, 2010. [Online]. Available: http://dx.doi.org/10.1021/jz100634n

[31] C. Veth, D. Dragicevic, R. Pfister, S. Arakkan, and C. Merten, "3D Electro-Thermal Model Approach for the Prediction of Internal State Values in Large-Format Lithium Ion Cells and Its Validation," *Journal of The Electrochemical Society*, vol. 161, no. 14, pp. A1943–A1952, 2014. [Online]. Available: http://dx.doi.org/10.1149/2.1201412jes

[32] B. Wu, Z. Li, and J. Zhang, "Thermal Design for the Pouch-Type Large-Format Lithium-Ion Batteries I. Thermo-Electrical Modeling and Origins of Temperature Non-Uniformity," *Journal of The Electrochemical Society*, vol. 162, no. 1, pp. A181–A191, 2015. [Online]. Available: http://dx.doi.org/10.1149/2.0831501jes

[33] A. Awarke, S. Pischinger, and J. Ogrzewalla, "Pseudo 3D modeling and analysis of the SEI growth distribution in large format Li-ion polymer pouch cells," *Journal of*

the Electrochemical Society, vol. 160, no. 1, pp. A172–A181, 2013. [Online]. Available: http://dx.doi.org/10.1149/2.022302jes

[34] C. Veth, D. Dragicevic, and C. Merten, "Thermal characterizations of a large-format lithium ion cell focused on high current discharges," *Journal of Power Sources*, vol. 267, pp. 760–769, 2014. [Online]. Available: http://dx.doi.org/10.1016/j.jpowsour.2014.05.139

[35] L. Cai, K. An, Z. Feng, C. Liang, and S. J. Harris, "In-situ observation of inhomogeneous degradation in large format Li-ion cells by neutron diffraction," *Journal of Power Sources*, vol. 236, pp. 163–168, 2013. [Online]. Available: http://dx.doi.org/10.1016/j.jpowsour.2013.02.066

[36] A. Senyshyn, M. Mühlbauer, O. Dolotko, M. Hofmann, T. Pirling, and H. Ehrenberg, "Spatially resolved in operando neutron scattering studies on Li-ion batteries," *Journal of Power Sources*, vol. 245, pp. 678–683, 2014. [Online]. Available: http://dx.doi.org/10.1016/j.jpowsour.2013.06.158

[37] G.-H. Kim, A. Pesaran, and R. Spotnitz, "A three-dimensional thermal abuse model for lithium-ion cells," *Journal of Power Sources*, vol. 170, no. 2, pp. 476–489, 2007. [Online]. Available: http://dx.doi.org/10.1016/j.jpowsour.2007.04.018

[38] G. Guo, B. Long, B. Cheng, S. Zhou, P. Xu, and B. Cao, "Three-dimensional thermal finite element modeling of lithium-ion battery in thermal abuse application," *Journal of Power Sources*, vol. 195, no. 8, pp. 2393–2398, 2010. [Online]. Available: http://dx.doi.org/10.1016/j.jpowsour.2009.10.090

[39] G.-H. Kim, K. Smith, J. Ireland, and A. Pesaran, "Fail-safe design for large capacity lithium-ion battery systems," *Journal of Power Sources*, vol. 210, pp. 243–253, 2012. [Online]. Available: http://dx.doi.org/10.1016/j.jpowsour.2012.03.015

[40] Y. Zhang, C.-Y. Wang, and X. Tang, "Cycling degradation of an automotive $LiFePO_4$ lithium-ion battery," *Journal of Power Sources*, vol. 196, no. 3, pp. 1513–1520, 2011. [Online]. Available: http://dx.doi.org/10.1016/j.jpowsour.2010.08.070

[41] J. Christensen and J. Newman, "Stress generation and fracture in lithium insertion materials," *Journal of Solid State Electrochemistry*, vol. 10, no. 5, pp. 293–319, 2006. [Online]. Available: http://dx.doi.org/10.1007/s10008-006-0095-1

[42] R. Fu, M. Xiao, and S.-Y. Choe, "Modeling, validation and analysis of mechanical stress generation and dimension changes of a pouch type high power Li-ion battery," *Journal of Power Sources*, vol. 224, pp. 211–224, 2013. [Online]. Available: http://dx.doi.org/10.1016/j.jpowsour.2012.09.096

[43] X. Wang, Y. Sone, and S. Kuwajima, "In situ investigation of the volume change in li-ion cell with charging and discharging satellite power applications," *Journal of The Electrochemical Society*, vol. 151, no. 2, pp. A273–A280, 2004. [Online]. Available: http://dx.doi.org/10.1149/1.1635827

[44] K.-Y. Oh, J. B. Siegel, L. Secondo, S. U. Kim, N. A. Samad, J. Qin, D. Anderson, K. Garikipati, A. Knobloch, B. I. Epureanu *et al.*, "Rate dependence of swelling in lithium-ion cells," *Journal of Power Sources*, vol. 267, pp. 197–202, 2014. [Online]. Available: http://dx.doi.org/10.1016/j.jpowsour.2014.05.039

[45] B. Bitzer and A. Gruhle, "A new method for detecting lithium plating by measuring the cell thickness," *Journal of Power Sources*, vol. 262, pp. 297–302, 2014. [Online]. Available: http://dx.doi.org/10.1016/j.jpowsour.2014.03.142

[46] M. Broussely, S. Herreyre, P. Biensan, P. Kasztejna, K. Nechev, and R. Staniewicz, "Aging mechanism in Li ion cells and calendar life predictions," *Journal of Power Sources*, vol. 97, pp. 13–21, 2001. [Online]. Available: http://dx.doi.org/10.1016/S0378-7753(01)00722-4

[47] P. Liu, J. Wang, J. Hicks-Garner, E. Sherman, S. Soukiazian, M. Verbrugge, H. Tataria, J. Musser, and P. Finamore, "Aging mechanisms of $LiFePO_4$ batteries deduced by electrochemical and structural analyses," *Journal of the Electrochemical Society*, vol. 157, no. 4, pp. A499–A507, 2010. [Online]. Available: http://dx.doi.org/10.1149/1.3294790

[48] Y. Baba, S. Okada, and J.-i. Yamaki, "Thermal stability of Li_x CoO_2 cathode for lithium ion battery," *Solid State Ionics*, vol. 148, no. 3, pp. 311–316, 2002. [Online]. Available: http://dx.doi.org/10.1016/S0167-2738(02)00067-X

[49] H. P. Jones, T. Chapin, M. Tabaddor *et al.*, "Critical Review of Commercial Secondary Lithium-Ion Battery Safety Standards," in *ESA Special Publication*, vol. 680, 2010, p. 55. [Online]. Available: http://adsabs.harvard.edu/abs/2010ESASP.680E..55J

[50] C. J. Orendorff, E. P. Roth, and G. Nagasubramanian, "Experimental triggers for internal short circuits in lithium-ion cells," *Journal of Power Sources*, vol. 196, no. 15, pp. 6554–6558, 2011. [Online]. Available: http://dx.doi.org/10.1016/j.jpowsour.2011.03.035

[51] E. Sahraei, J. Campbell, and T. Wierzbicki, "Modeling and short circuit detection of 18650 Li-ion cells under mechanical abuse conditions," *Journal of Power Sources*, vol. 220, pp. 360–372, 2012. [Online]. Available: http://dx.doi.org/10.1016/j.jpowsour.2012.07.057

[52] Q. Wang, P. Ping, X. Zhao, G. Chu, J. Sun, and C. Chen, "Thermal runaway caused fire and explosion of lithium ion battery," *Journal of power sources*, vol. 208, pp. 210–224, 2012. [Online]. Available: http://dx.doi.org/10.1016/j.jpowsour.2012.02.038

[53] K. Edström, T. Gustafsson, and J. O. Thomas, "The cathode–electrolyte interface in the Li-ion battery," *Electrochimica Acta*, vol. 50, no. 2, pp. 397–403, 2004. [Online]. Available: http://dx.doi.org/10.1016/j.electacta.2004.03.049

[54] K. Xu and A. von Cresce, "Interfacing electrolytes with electrodes in Li ion batteries," *Journal of Materials Chemistry*, vol. 21, no. 27, pp. 9849–9864, 2011. [Online]. Available: http://dx.doi.org/10.1039/C0JM04309E

[55] A. Millner, "Modeling lithium ion battery degradation in electric vehicles," in *Innovative Technologies for an Efficient and Reliable Electricity Supply (CITRES), 2010 IEEE Conference on*. IEEE, 2010, pp. 349–356. [Online]. Available: https://dx.doi.org/10.1109/CITRES.2010.5619782

[56] I. Bloom, B. G. Potter, C. S. Johnson, K. L. Gering, and J. P. Christophersen, "Effect of cathode composition on impedance rise in high-power lithium-ion cells: Long-term aging results," *Journal of power sources*, vol. 155, no. 2, pp. 415–419, 2006. [Online]. Available: http://dx.doi.org/10.1016/j.jpowsour.2005.05.008

[57] M.-S. Wu and P.-C. J. Chiang, "High-rate capability of lithium-ion batteries after storing at elevated temperature," *Electrochimica Acta*, vol. 52, no. 11, pp. 3719–3725, 2007. [Online]. Available: http://dx.doi.org/10.1016/j.electacta.2006.10.045

[58] P. Ramadass, B. Haran, R. White, and B. N. Popov, "Capacity fade of Sony 18650 cells cycled at elevated temperatures: Part I. Cycling performance," *Journal of power sources*, vol. 112, no. 2, pp. 606–613, 2002. [Online]. Available: http://dx.doi.org/10.1016/S0378-7753(02)00474-3

[59] D. Abraham, E. Reynolds, P. Schultz, A. Jansen, and D. Dees, "Temperature dependence of capacity and impedance data from fresh and aged high-power lithium-ion cells," *Journal of The Electrochemical Society*, vol. 153, no. 8, pp. A1610–A1616, 2006. [Online]. Available: http://dx.doi.org/10.1149/1.2210668

[60] G. Ning and B. N. Popov, "Cycle life modeling of lithium-ion batteries," *Journal of The Electrochemical Society*, vol. 151, no. 10, pp. A1584–A1591, 2004. [Online]. Available: http://dx.doi.org/10.1149/1.1787631

[61] T. Waldmann, M. Wilka, M. Kasper, M. Fleischhammer, and M. Wohlfahrt-Mehrens, "Temperature dependent ageing mechanisms in Lithium-ion batteries–A Post-Mortem study," *Journal of Power Sources*, vol. 262, pp. 129–135, 2014. [Online]. Available: http://doi.org/10.1016/j.jpowsour.2014.03.112

[62] I. Bloom, B. Cole, J. Sohn, S. Jones, E. Polzin, V. Battaglia, G. Henriksen, C. Motloch, R. Richardson, T. Unkelhaeuser *et al.*, "An accelerated calendar and cycle life study of Li-ion cells," *Journal of Power Sources*, vol. 101, no. 2, pp. 238–247, 2001. [Online]. Available: http://dx.doi.org/10.1016/S0378-7753(01)00783-2

[63] M. Ecker, N. Nieto, S. Käbitz, J. Schmalstieg, H. Blanke, A. Warnecke, and D. U. Sauer, "Calendar and cycle life study of Li(NiMnCo)O_2-based 18650 lithium-ion batteries," *Journal of Power Sources*, vol. 248, pp. 839–851, 2014. [Online]. Available: http://dx.doi.org/10.1016/j.jpowsour.2013.09.143

[64] J. Wang, P. Liu, J. Hicks-Garner, E. Sherman, S. Soukiazian, M. Verbrugge, H. Tataria, J. Musser, and P. Finamore, "Cycle-life model for graphite-$LiFePO_4$ cells," *Journal of Power Sources*, vol. 196, no. 8, pp. 3942–3948, 2011. [Online]. Available: http://dx.doi.org/10.1016/j.jpowsour.2010.11.134

[65] R. P. Ramasamy, R. E. White, and B. N. Popov, "Calendar life performance of pouch lithium-ion cells," *Journal of Power Sources*, vol. 141, no. 2, pp. 298–306, 2005. [Online]. Available: http://dx.doi.org/10.1016/j.jpowsour.2004.09.024

[66] J. Belt, V. Utgikar, and I. Bloom, "Calendar and PHEV cycle life aging of high-energy, lithium-ion cells containing blended spinel and layered-oxide cathodes," *Journal of Power Sources*, vol. 196, no. 23, pp. 10 213–10 221, 2011. [Online]. Available: http://dx.doi.org/10.1016/j.jpowsour.2011.08.067

[67] P. Keil, S. F. Schuster, J. Wilhelm, J. Travi, A. Hauser, R. C. Karl, and A. Jossen, "Calendar Aging of Lithium-Ion Batteries I. Impact of the Graphite Anode on Capacity Fade," *Journal of The Electrochemical Society*, vol. 163, no. 9, pp. A1872–A1880, 2016. [Online]. Available: http://dx.doi.org/10.1149/2.0411609jes

[68] K. Kato, A. Negishi, K. Nozaki, I. Tsuda, and K. Takano, "PSOC cycle testing method for lithium-ion secondary batteries," *Journal of power sources*, vol. 117, no. 1, pp. 118–123, 2003. [Online]. Available: https://doi.org/10.1016/S0378-7753(03)00157-5

[69] K. Takei, K. Kumai, Y. Kobayashi, H. Miyashiro, N. Terada, T. Iwahori, and T. Tanaka, "Cycle life estimation of lithium secondary battery by extrapolation method and accelerated aging test," *Journal of Power Sources*, vol. 97, pp. 697–701, 2001. [Online]. Available: http://dx.doi.org/10.1016/S0378-7753(01)00646-2

[70] T. Guena and P. Leblanc, "How depth of discharge affects the cycle life of lithium-metal-polymer batteries," in *Telecommunications Energy Conference, 2006. INTELEC'06. 28th Annual International*. IEEE, 2006, pp. 1–8. [Online]. Available: http://dx.doi.org/10.1109/INTLEC.2006.251641

[71] S. S. Choi and H. S. Lim, "Factors that affect cycle-life and possible degradation mechanisms of a Li-ion cell based on $LiCoO_2$," *Journal of Power Sources*, vol. 111, no. 1, pp. 130–136, 2002. [Online]. Available: http://dx.doi.org/10.1016/S0378-7753(02)00305-1

[72] M. Ecker, J. B. Gerschler, J. Vogel, S. Käbitz, F. Hust, P. Dechent, and D. U. Sauer, "Development of a lifetime prediction model for lithium-ion batteries based on extended accelerated aging test data," *Journal of Power Sources*, vol. 215, pp. 248–257, 2012. [Online]. Available: http://dx.doi.org/10.1016/j.jpowsour.2012.05.012

[73] J. Schmalstieg, S. Käbitz, M. Ecker, and D. U. Sauer, "A holistic aging model for Li (NiMnCo) O_2 based 18650 lithium-ion batteries," *Journal of Power Sources*, vol. 257, pp. 325–334, 2014. [Online]. Available: https://doi.org/10.1016/j.jpowsour.2014.02.012

[74] J.-W. Lee, Y. K. Anguchamy, and B. N. Popov, "Simulation of charge–discharge cycling of lithium-ion batteries under low-earth-orbit conditions," *Journal of power sources*, vol. 162, no. 2, pp. 1395–1400, 2006. [Online]. Available: http://dx.doi.org/10.1016/j.jpowsour.2006.07.045

[75] B. Lunz, Z. Yan, J. B. Gerschler, and D. U. Sauer, "Influence of plug-in hybrid electric vehicle charging strategies on charging and battery degradation costs," *Energy Policy*, vol. 46, pp. 511–519, 2012. [Online]. Available: http://dx.doi.org/10.1016/j.enpol.2012.04.017

[76] G. Ning, B. Haran, and B. N. Popov, "Capacity fade study of lithium-ion batteries cycled at high discharge rates," *Journal of Power Sources*, vol. 117, no. 1, pp. 160–169, 2003. [Online]. Available: http://dx.doi.org/10.1016/S0378-7753(03)00029-6

[77] K. Zaghib, A. Guerfi, P. Hovington, A. Vijh, M. Trudeau, A. Mauger, J. Goodenough, and C. Julien, "Review and analysis of nanostructured olivine-based lithium recheargeable batteries: Status and trends," *Journal of Power Sources*, vol. 232, pp. 357–369, 2013. [Online]. Available: http://dx.doi.org/10.1016/j.jpowsour.2012.12.095

[78] A. Burke, M. Miller, and H. Zhao, *Fast Charging Tests (up to 6C) of Lithium Titanate Cells and Modules: Electrical and Thermal Response.* Institute of Transportation Studies, University of California, Davis, 2012. [Online]. Available: http://pubs.its.ucdavis.edu/download_pdf.php?id=1638

[79] M. Okubo, E. Hosono, J. Kim, M. Enomoto, N. Kojima, T. Kudo, H. Zhou, and I. Honma, "Nanosize effect on high-rate Li-ion intercalation in $LiCoO_2$ electrode," *Journal*

of the american chemical society, vol. 129, no. 23, pp. 7444–7452, 2007. [Online]. Available: http://dx.doi.org/10.1021/ja0681927

[80] X. Zhang, G. Pan, G. Li, J. Qu, and X. Gao, "Si–Si_3N_4 composites as anode materials for lithium ion batteries," *Solid State Ionics*, vol. 178, no. 15, pp. 1107–1112, 2007. [Online]. Available: http://dx.doi.org/10.1016/j.ssi.2007.05.011

[81] J. Zhou and P. Notten, "Studies on the degradation of Li-ion batteries by the use of microreference electrodes," *Journal of Power Sources*, vol. 177, no. 2, pp. 553–560, 2008. [Online]. Available: http://dx.doi.org/10.1016/j.jpowsour.2007.11.032

[82] K. Kang, Y. S. Meng, J. Bréger, C. P. Grey, and G. Ceder, "Electrodes with high power and high capacity for rechargeable lithium batteries," *Science*, vol. 311, no. 5763, pp. 977–980, 2006. [Online]. Available: http://dx.doi.org/10.1126/science.1122152

[83] B. Xu, D. Qian, Z. Wang, and Y. S. Meng, "Recent progress in cathode materials research for advanced lithium ion batteries," *Materials Science and Engineering: R: Reports*, vol. 73, no. 5, pp. 51–65, 2012. [Online]. Available: http://dx.doi.org/10.1016/j.mser.2012.05.003

[84] W.-J. Zhang, "Structure and performance of $LiFePO_4$ cathode materials: a review," *Journal of Power Sources*, vol. 196, no. 6, pp. 2962–2970, 2011. [Online]. Available: http://dx.doi.org/10.1016/j.jpowsour.2010.11.113

[85] D. A. H. McCleary, "Three dimensional computational modeling of electrochemical performance and heat generation in spirally and prismatically wound configurations," Ph.D. dissertation, University of Texas at Austin, 2012. [Online]. Available: http://hdl.handle.net/2152/20051

[86] G.-H. Kim and K. Smith, "Multi-Scale Multi-Dimensional Model for Better Cell Design and Management (Presentation)," National Renewable Energy Laboratory (NREL), Golden, CO., Tech. Rep., 2008. [Online]. Available: http://www.osti.gov/scitech/servlets/purl/940943

[87] A. Pesaran, G.-H. Kim, and K. Smith, "Accelerating Design of Batteries Using Computer-Aided Engineering Tools (Presentation)," National Renewable Energy Laboratory (NREL), Golden, CO., Tech. Rep., 2010. [Online]. Available: http://www.osti.gov/scitech/servlets/purl/1009286

[88] B. Rieger, S. V. Erhard, S. Kosch, M. Venator, A. Rheinfeld, and A. Jossen, "Multi-Dimensional Modeling of the Influence of Cell Design on Temperature, Displacement and Stress Inhomogeneity in Large-Format Lithium-Ion Cells," *Journal of The Electrochemical Society*, vol. 163, no. 14, pp. A3099–A3110, 2016. [Online]. Available: http://dx.doi.org/10.1149/2.1051614jes

[89] K.-J. Lee, K. Smith, A. Pesaran, and G.-H. Kim, "Three dimensional thermal-, electrical-, and electrochemical-coupled model for cylindrical wound large format lithium-ion batteries," *Journal of Power Sources*, vol. 241, pp. 20–32, 2013. [Online]. Available: http://dx.doi.org/10.1016/j.jpowsour.2013.03.007

[90] S. Bazinski and X. Wang, "The influence of cell temperature on the entropic coefficient of a lithium iron phosphate (lfp) pouch cell," *Journal of The Electrochemical Society*, vol. 161, no. 1, pp. A168–A175, 2014. [Online]. Available: http://dx.doi.org/10.1149/2.082401jes

[91] S. Paul, C. Diegelmann, H. Kabza, and W. Tillmetz, "Analysis of ageing inhomogeneities in lithium-ion battery systems," *Journal of Power Sources*, vol. 239, pp. 642–650, 2013. [Online]. Available: http://dx.doi.org/10.1016/j.jpowsour.2013.01.068

[92] V. Agubra and J. Fergus, "Lithium ion battery anode aging mechanisms," *Materials*, vol. 6, no. 4, pp. 1310–1325, 2013. [Online]. Available: http://dx.doi.org/10.3390/ma6041310

[93] J. Steiger, D. Kramer, and R. Mönig, "Mechanisms of dendritic growth investigated by in situ light microscopy during electrodeposition and dissolution of lithium," *Journal of Power Sources*, vol. 261, pp. 112–119, 2014. [Online]. Available: http://dx.doi.org/10.1016/j.jpowsour.2014.03.029

[94] S. F. Schuster, T. Bach, E. Fleder, J. Müller, M. Brand, G. Sextl, and A. Jossen, "Nonlinear aging characteristics of lithium-ion cells under different operational conditions," *Journal of Energy Storage*, vol. 1, pp. 44–53, 2015. [Online]. Available: http://dx.doi.org/10.1016/j.est.2015.05.003

[95] C. Daniel, "Materials and processing for lithium-ion batteries," *Jom*, vol. 60, no. 9, pp. 43–48, 2008. [Online]. Available: http://dx.doi.org/10.1007/s11837-008-0116-x

[96] E. Roth and D. Doughty, "Thermal abuse performance of high-power 18650 Li-ion cells," *Journal of power sources*, vol. 128, no. 2, pp. 308–318, 2004. [Online]. Available: http://dx.doi.org/10.1016/j.jpowsour.2003.09.068

[97] "Nageltests an kommerziellen Lithium-Ionen Zellen (Typ 18650)," Nationale Plattform Elektromobilität, accessed: 13.02.2016.

[98] P. Röder, B. Stiaszny, J. C. Ziegler, N. Baba, P. Lagaly, and H.-D. Wiemhöfer, "The impact of calendar aging on the thermal stability of a $LiMn_2O_4$–$Li(Ni_{1/3}Mn_{1/3}Co_{1/3})$ O_2/graphite lithium-ion cell," *Journal of Power Sources*, vol. 268, pp. 315–325, 2014. [Online]. Available: http://dx.doi.org/10.1016/j.jpowsour.2014.06.040

[99] "Examined in a Battery Testing Calorimeter," Kraftwerk Batterie Conference 2015, accessed: 13.02.2016.

[100] "Interaction of Aging and Safety," TÜV SÜD Battery Testing GmbH, accessed: 13.02.2016.

[101] M.-H. Yang, "Recent Li-Ion Battery Development for LEV Applications ," http://www.datei.de/public/extraenergy/2014_Veranstaltungen/EUROBIKE/HiTech-Energy-Storage-systems.pdf, accessed: 22.03.2017.

[102] Y. Saito, M. Shikano, and H. Kobayashi, "Heat generation behavior during charging and discharging of lithium-ion batteries after long-time storage," *Journal of Power Sources*, vol. 244, pp. 294–299, 2013. [Online]. Available: http://dx.doi.org/10.1016/j.jpowsour.2012.12.124

[103] J. Geder, R. Arunachala, S. Jairam, and A. Jossen, "Thermal behavior of aged lithium-ion batteries: calorimetric observations," in *Green Energy and Systems Conference (IGESC), 2015 IEEE*. IEEE, 2015, pp. 24–29. [Online]. Available: http://dx.doi.org/10.1109/IGESC.2015.7359386

[104] M.-S. Wu, P.-C. J. Chiang, J.-C. Lin, and Y.-S. Jan, "Correlation between electrochemical characteristics and thermal stability of advanced lithium-ion batteries in abuse testsâ€"short-circuit tests," *Electrochimica acta*, vol. 49, no. 11, pp. 1803–1812, 2004. [Online]. Available: http://dx.doi.org/10.1016/j.electacta.2003.12.012

[105] M. Fleischhammer, T. Waldmann, G. Bisle, B.-I. Hogg, and M. Wohlfahrt-Mehrens, "Interaction of cyclic ageing at high-rate and low temperatures and safety in lithium-ion

batteries," *Journal of Power Sources*, vol. 274, pp. 432–439, 2015. [Online]. Available: http://dx.doi.org/10.1016/j.jpowsour.2014.08.135

[106] A. Rheinfeld, S. Kosch, S. V. Erhard, P. J. Osswald, B. Rieger, and A. Jossen, "Electro-Thermal Modeling of Large Format Lithium-Ion Pouch Cells: A Cell Temperature Dependent Linear Polarization Expression," *Journal of The Electrochemical Society*, vol. 163, no. 14, pp. A3046–A3062, 2016. [Online]. Available: http://dx.doi.org/10.1149/2.0701614jes

[107] Y. Gao, "Investigation of Volume Expansion in Commercial Pouch Cells," Master's thesis, Technische Universität München, Lehrstuhl für Elektrische Energiespeichertechnik, 2015.

[108] O. Bohlen, S. Buller, R. W. De Doncker, M. Gelbke, and R. Naumann, "Impedance based battery diagnosis for automotive applications," in *Power Electronics Specialists Conference, 2004. PESC 04. 2004 IEEE 35th Annual*, vol. 4. IEEE, 2004, pp. 2792–2797. [Online]. Available: http://dx.doi.org/10.1109/PESC.2004.1355275

[109] E. Karden, S. Buller, and R. W. De Doncker, "A method for measurement and interpretation of impedance spectra for industrial batteries," *Journal of Power sources*, vol. 85, no. 1, pp. 72–78, 2000. [Online]. Available: http://dx.doi.org/10.1016/S0378-7753(99)00385-7

[110] A. Jossen, "Fundamentals of battery dynamics," *Journal of Power Sources*, vol. 154, no. 2, pp. 530–538, 2006. [Online]. Available: http://dx.doi.org/10.1016/j.jpowsour.2005.10.041

[111] W. Waag, S. Käbitz, and D. U. Sauer, "Experimental investigation of the lithium-ion battery impedance characteristic at various conditions and aging states and its influence on the application," *Applied Energy*, vol. 102, pp. 885–897, 2013. [Online]. Available: http://dx.doi.org/10.1016/j.apenergy.2012.09.030

[112] B. Stiaszny, J. C. Ziegler, E. E. Krauß, J. P. Schmidt, and E. Ivers-Tiffée, "Electrochemical characterization and post-mortem analysis of aged $LiMn_2O_4$–$Li(Ni_{0.5}Mn_{0.3}Co_{0.2})O_2$/graphite lithium ion batteries. Part I: Cycle aging," *Journal of Power Sources*, vol. 251, pp. 439–450, 2014. [Online]. Available: http://dx.doi.org/10.1016/j.jpowsour.2013.11.080

[113] K. Lee, "Voltage Relaxation of Li_yFePO_4 based Batteries," Master's thesis, Technical University Munich, Lehrstuhl für Elektrische Energiespeichertechnik, 2014.

[114] J. P. Schmidt, "Verfahren zur Charakterisierung und Modellierung von Lithium-Ionen Zellen," Ph.D. dissertation, Karlsruhe Institute of Technology, 2013. [Online]. Available: http://digbib.ubka.uni-karlsruhe.de/volltexte/documents/2887873

[115] A. Fotouhi, D. J. Auger, K. Propp, S. Longo, and M. Wild, "A review on electric vehicle battery modelling: From lithium-ion toward lithium–sulphur," *Renewable and Sustainable Energy Reviews*, vol. 56, pp. 1008–1021, 2016. [Online]. Available: http://dx.doi.org/10.1016/j.rser.2015.12.009

[116] W. Waag, C. Fleischer, and D. U. Sauer, "Critical review of the methods for monitoring of lithium-ion batteries in electric and hybrid vehicles," *Journal of Power Sources*, vol. 258, pp. 321–339, 2014. [Online]. Available: http://dx.doi.org/10.1016/j.jpowsour.2014.02.064

[117] T. Pixis, "Study the Influence of Cell Size from P-3D Lithium Ion Battery Models with COMSOL," Master's thesis, Technische Universität München, Lehrstuhl für Elektrische Energiespeichertechnik, 2014.

[118] M. R. Jongerden and B. R. Haverkort, "Which battery model to use?" *Software, IET*, vol. 3, no. 6, pp. 445–457, 2009. [Online]. Available: http://dx.doi.org/10.1049/iet-sen.2009.0001

[119] M. Doyle, T. F. Fuller, and J. Newman, "Modeling of galvanostatic charge and discharge of the lithium/polymer/insertion cell," *Journal of the Electrochemical Society*, vol. 140, no. 6, pp. 1526–1533, 1993. [Online]. Available: http://dx.doi.org/10.1149/1.2221597

[120] J. Newman and W. Tiedemann, "Porous-electrode theory with battery applications," *AIChE Journal*, vol. 21, no. 1, pp. 25–41, 1975. [Online]. Available: http://dx.doi.org/10.1002/aic.690210103

[121] S. Thanagasundram, R. Arunachala, K. Makinejad, T. Teutsch, and A. Jossen, "A cell level model for battery simulation," in *European Electric Vehicle Congress (EEVC)*, 2012. [Online]. Available: https://www.researchgate.net/profile/Suguna_Thanagasundram/publication/235602059_A_Cell_Level_Model_for_Battery_Simulation/links/0912f511db0c693ca1000000.pdf

[122] L. Chenglin, L. Huiju, and W. Lifang, "A dynamic equivalent circuit model of $LiFePO_4$ cathode material for lithium ion batteries on hybrid electric vehicles," in *Vehicle Power and Propulsion Conference, 2009. VPPC'09. IEEE.* IEEE, 2009, pp. 1662–1665. [Online]. Available: http://ieeexplore.ieee.org/stamp/stamp.jsp?arnumber=5289681

[123] X. Hu, S. Li, and H. Peng, "A comparative study of equivalent circuit models for Li-ion batteries," *Journal of Power Sources*, vol. 198, pp. 359–367, 2012. [Online]. Available: http://dx.doi.org/10.1016/j.jpowsour.2011.10.013

[124] C.-F. Chiasserini and R. R. Rao, "Pulsed battery discharge in communication devices," in *Proceedings of the 5th annual ACM/IEEE international conference on Mobile computing and networking.* ACM, 1999, pp. 88–95. [Online]. Available: http://dx.doi.org/10.1145/313451.313488

[125] S. Malkhandi, "Fuzzy logic-based learning system and estimation of state-of-charge of lead-acid battery," *Engineering Applications of Artificial Intelligence*, vol. 19, no. 5, pp. 479–485, 2006. [Online]. Available: http://dx.doi.org/10.1016/j.engappai.2005.12.005

[126] M. Charkhgard and M. Farrokhi, "State-of-charge estimation for lithium-ion batteries using neural networks and EKF," *Industrial Electronics, IEEE Transactions on*, vol. 57, no. 12, pp. 4178–4187, 2010. [Online]. Available: http://dx.doi.org/10.1109/TIE.2010.2043035

[127] D. Cadar, D. Petreus, I. Ciocan, and P. Dobra, "An improvement on empirical modelling of the batteries," in *Electronics Technology, 2009. ISSE 2009. 32nd International Spring Seminar on.* IEEE, 2009, pp. 1–6. [Online]. Available: http://dx.doi.org/10.1109/ISSE.2009.5207015

[128] E. Thomas, I. Bloom, J. Christophersen, and V. Battaglia, "Rate-based degradation modeling of lithium-ion cells," *Journal of Power Sources*, vol. 206, pp. 378–382, 2012. [Online]. Available: http://dx.doi.org/10.1016/j.jpowsour.2012.01.106

[129] B. Saha, K. Goebel, S. Poll, and J. Christophersen, "A bayesian framework for remaining useful life estimation," in *Proceedings Fall AAAI symposium: AI for prognostics. Arlington*, 2007. [Online]. Available: http://www.aaai.org/Papers/Symposia/Fall/2007/FS-07-02/FS07-02-014.pdf

[130] W. Prochazka, G. Pregartner, and M. Cifrain, "Design-of-experiment and statistical modeling of a large scale aging experiment for two popular lithium ion cell chemistries," *Journal of The Electrochemical Society*, vol. 160, no. 8, pp. A1039–A1051, 2013. [Online]. Available: http://dx.doi.org/10.1149/2.003308jes

[131] T. Weigert, Q. Tian, and K. Lian, "State-of-charge prediction of batteries and battery–supercapacitor hybrids using artificial neural networks," *Journal of Power Sources*, vol. 196, no. 8, pp. 4061–4066, 2011. [Online]. Available: http://dx.doi.org/10.1016/j.jpowsour.2010.10.075

[132] U. Westerhoff, K. Kurbach, F. Lienesch, and M. Kurrat, "Analysis of Lithium-Ion Battery Models Based on Electrochemical Impedance Spectroscopy," *Energy Technology*, vol. 4, no. 12, pp. 1620–1630, 2016. [Online]. Available: http://dx.doi.org/10.1002/ente.201600154

[133] A. Eddahech, O. Briat, N. Bertrand, J.-Y. Delétage, and J.-M. Vinassa, "Behavior and state-of-health monitoring of Li-ion batteries using impedance spectroscopy and recurrent neural networks," *International Journal of Electrical Power & Energy Systems*, vol. 42, no. 1, pp. 487–494, 2012. [Online]. Available: http://dx.doi.org/10.1016/j.ijepes.2012.04.050

[134] A. Eddahech, O. Briat, E. Woirgard, and J.-M. Vinassa, "Remaining useful life prediction of lithium batteries in calendar ageing for automotive applications," *Microelectronics Reliability*, vol. 52, no. 9, pp. 2438–2442, 2012. [Online]. Available: http://dx.doi.org/10.1016/j.microrel.2012.06.085

[135] Y. Xing, N. Williard, K.-L. Tsui, and M. Pecht, "A comparative review of prognostics-based reliability methods for lithium batteries," in *Prognostics and System Health Management Conference (PHM-Shenzhen), 2011.* IEEE, 2011, pp. 1–6. [Online]. Available: http://dx.doi.org/10.1109/PHM.2011.5939585

[136] J. Zhang and J. Lee, "A review on prognostics and health monitoring of Li-ion battery," *Journal of Power Sources*, vol. 196, no. 15, pp. 6007–6014, 2011. [Online]. Available: http://dx.doi.org/10.1016/j.jpowsour.2011.03.101

[137] M.-H. Hung, C.-H. Lin, L.-C. Lee, and C.-M. Wang, "State-of-charge and state-of-health estimation for lithium-ion batteries based on dynamic impedance technique," *Journal of Power Sources*, vol. 268, pp. 861–873, 2014. [Online]. Available: http://dx.doi.org/10.1016/j.jpowsour.2014.06.083

[138] H. He, R. Xiong, and H. Guo, "Online estimation of model parameters and state-of-charge of $LiFePO_4$ batteries in electric vehicles," *Applied Energy*, vol. 89, no. 1, pp. 413–420, 2012. [Online]. Available: http://dx.doi.org/10.1016/j.apenergy.2011.08.005

[139] S. M. Rezvanizaniani, Z. Liu, Y. Chen, and J. Lee, "Review and recent advances in battery health monitoring and prognostics technologies for electric vehicle (EV) safety and mobility," *Journal of Power Sources*, vol. 256, pp. 110–124, 2014. [Online]. Available: http://dx.doi.org/10.1016/j.jpowsour.2014.01.085

[140] R. Xiong, H. He, F. Sun, and K. Zhao, "Evaluation on state of charge estimation of batteries with adaptive extended kalman filter by experiment approach," *Vehicular Technology, IEEE Transactions on*, vol. 62, no. 1, pp. 108–117, 2013. [Online]. Available: http://dx.doi.org/10.1109/TVT.2012.2222684

[141] F. Sun, X. Hu, Y. Zou, and S. Li, "Adaptive unscented Kalman filtering for state of charge estimation of a lithium-ion battery for electric vehicles," *Energy*, vol. 36, no. 5, pp. 3531–3540, 2011. [Online]. Available: http://dx.doi.org/10.1016/j.energy.2011.03.059

[142] I.-S. Kim, "The novel state of charge estimation method for lithium battery using sliding mode observer," *Journal of Power Sources*, vol. 163, no. 1, pp. 584–590, 2006. [Online]. Available: http://dx.doi.org/10.1016/j.jpowsour.2006.09.006

[143] K. A. Smith, "Electrochemical modeling, estimation and control of lithium ion batteries," Ph.D. dissertation, The Pennsylvania State University, 2006. [Online]. Available: http://www.mne.psu.edu/MRL/theses/Dissertation_KandlerSmith2006.pdf

[144] S. Chen, C. Wan, and Y. Wang, "Thermal analysis of lithium-ion batteries," *Journal of Power Sources*, vol. 140, no. 1, pp. 111–124, 2005. [Online]. Available: http://dx.doi.org/10.1016/j.jpowsour.2004.05.064

[145] V. Srinivasan and C. Wang, "Analysis of electrochemical and thermal behavior of Li-ion cells," *Journal of The Electrochemical Society*, vol. 150, no. 1, pp. A98–A106, 2003. [Online]. Available: http://dx.doi.org/10.1149/1.1526512

[146] S. Li, "Implementation of 3D Electrochemical Li-ion Cell Model with COMSOL," Master's thesis, University of Ulm, Institut für Energiewandlung und -speicherung, 2013.

[147] W. Fang, P. Ramadass, and Z. J. Zhang, "Study of internal short in a Li-ion cell-II. Numerical investigation using a 3D electrochemical-thermal model," *Journal of Power Sources*, vol. 248, pp. 1090–1098, 2014. [Online]. Available: http://dx.doi.org/10.1016/j.jpowsour.2013.10.004

[148] S. Tippmann, D. Walper, L. Balboa, B. Spier, and W. G. Bessler, "Low-temperature charging of lithium-ion cells part i: Electrochemical modeling and experimental investigation of degradation behavior," *Journal of Power Sources*, vol. 252, pp. 305–316, 2014. [Online]. Available: http://dx.doi.org/10.1016/j.jpowsour.2013.12.022

[149] L. O. Valøen and J. N. Reimers, "Transport properties of $LiPF_6$-based Li-ion battery electrolytes," *Journal of The Electrochemical Society*, vol. 152, no. 5, pp. A882–A891, 2005. [Online]. Available: http://dx.doi.org/10.1149/1.1872737

[150] A. Blanchard, "Modelling the overcharge of lithium-ion cells," Master's thesis, Technische Universität München, Lehrstuhl für Elektrische Energiespeichertechnik, 2014.

[151] Z. Jiangong, S. Zechang, W. Xuezhe, D. Haifeng, and S. Li, "Preliminary Study of a Distributed Thermal Model for a LFP Battery in COMSOL Inc. Multiphysics (MP) Software," in *Vehicle Power and Propulsion Conference (VPPC), 2013 IEEE*. IEEE, 2013, pp. 1–5. [Online]. Available: http://dx.doi.org/10.1109/VPPC.2013.6671700

[152] S. G. Stewart, V. Srinivasan, and J. Newman, "Modeling the performance of lithium-ion batteries and capacitors during hybrid-electric-vehicle operation," *Journal of The Electrochemical Society*, vol. 155, no. 9, pp. A664–A671, 2008. [Online]. Available: http://dx.doi.org/10.1149/1.2953524

[153] J. Newman, K. E. Thomas, H. Hafezi, and D. R. Wheeler, "Modeling of lithium-ion batteries," *Journal of power sources*, vol. 119, pp. 838–843, 2003. [Online]. Available: http://dx.doi.org/10.1016/S0378-7753(03)00282-9

[154] M. Dubarry, C. Truchot, and B. Y. Liaw, "Synthesize battery degradation modes via a diagnostic and prognostic model," *Journal of power sources*, vol. 219, pp. 204–216, 2012. [Online]. Available: http://dx.doi.org/10.1016/j.jpowsour.2012.07.016

[155] D. Liu, Y. Wang, Y. Xie, L. He, J. Chen, K. Wu, R. Xu, and Y. Gao, "On the stress characteristics of graphite anode in commercial pouch lithium-ion battery," *Journal of Power Sources*, vol. 232, pp. 29–33, 2013. [Online]. Available: http://dx.doi.org/10.1016/j.jpowsour.2012.12.110

[156] P. Arora, R. E. White, and M. Doyle, "Capacity fade mechanisms and side reactions in lithium-ion batteries," *Journal of the Electrochemical Society*, vol. 145, no. 10, pp. 3647–3667, 1998. [Online]. Available: http://dx.doi.org/10.1149/1.1838857

[157] M. Kassem, J. Bernard, R. Revel, S. PÃ©lissier, F. Duclaud, and C. Delacourt, "Calendar aging of a graphite/$LiFePO_4$ cell," *Journal of Power Sources*, vol. 208, no. 15, pp. 296 – 305, 2012. [Online]. Available: https://doi.org/10.1016/j.jpowsour.2012.02.068

[158] L. Lavigne, J. Sabatier, J. M. Francisco, F. Guillemard, and A. Noury, "Lithium-ion Open Circuit Voltage (OCV) curve modelling and its ageing adjustment," *Journal of Power Sources*, vol. 324, pp. 694–703, 2016. [Online]. Available: http://dx.doi.org/10.1016/j.jpowsour.2016.05.121

[159] J. Sturm, F. Spingler, B. Rieger, A. Rheinfeld, and A. Jossen, "Non-Destructive Detection of Local Aging in Lithium-Ion Pouch Cells by Multi-Directional Laser Scanning," *Journal of The Electrochemical Society*, vol. 164, no. 7, pp. A1342–A1351, 2017. [Online]. Available: http://dx.doi.org/10.1149/2.0161707jes

[160] Y. Koyama, I. Tanaka, H. Adachi, Y. Makimura, and T. Ohzuku, "Crystal and electronic structures of superstructural $Li_{1-x}[Co_{1/3}Ni_{1/3}Mn_{1/3}]O_2$ ($0 \leq x \leq 1$)," *Journal of Power Sources*, vol. 119, pp. 644–648, 2003. [Online]. Available: http://dx.doi.org/10.1016/S0378-7753(03)00194-0

[161] N. Nitta, F. Wu, J. T. Lee, and G. Yushin, "Li-ion battery materials: present and future," *Materials today*, vol. 18, no. 5, pp. 252–264, 2015. [Online]. Available: http://dx.doi.org/10.1016/j.mattod.2014.10.040

[162] M. Ma, N. A. Chernova, B. H. Toby, P. Y. Zavalij, and M. S. Whittingham, "Structural and electrochemical behavior of $LiMn_{0.4}$ $Ni_{0.4}$ $Co_{0.2}$ O_2," *Journal of Power Sources*, vol. 165, no. 2, pp. 517–534, 2007. [Online]. Available: https://doi.org/10.1016/j.jpowsour.2006.10.022

[163] B. Rieger, S. V. Erhard, K. Rumpf, and A. Jossen, "A new method to model the thickness change of a commercial pouch cell during discharge," *Journal of The Electrochemical Society*, vol. 163, no. 8, pp. A1566–A1575, 2016. [Online]. Available: http://dx.doi.org/10.1149/2.0441608jes

[164] S. Goriparti, E. Miele, F. De Angelis, E. Di Fabrizio, R. P. Zaccaria, and C. Capiglia, "Review on recent progress of nanostructured anode materials for Li-ion batteries," *Journal of Power Sources*, vol. 257, pp. 421–443, 2014. [Online]. Available: http://dx.doi.org/10.1016/j.jpowsour.2013.11.103

[165] V. A. Sethuraman, N. Van Winkle, D. P. Abraham, A. F. Bower, and P. R. Guduru, "Real-time stress measurements in lithium-ion battery negative-electrodes," *Journal of Power Sources*, vol. 206, pp. 334–342, 2012. [Online]. Available: http://doi.org/10.1016/j.jpowsour.2012.01.036

[166] J. H. Lee, H. M. Lee, and S. Ahn, "Battery dimensional changes occurring during charge/discharge cyclesâ€"thin rectangular lithium ion and polymer cells," *Journal of power sources*, vol. 119, pp. 833–837, 2003. [Online]. Available: http://dx.doi.org/10.1016/S0378-7753(03)00281-7

[167] R. V. Bugga and M. C. Smart, "Lithium plating behavior in lithium-ion cells," *ECS Transactions*, vol. 25, no. 36, pp. 241–252, 2010. [Online]. Available: http://dx.doi.org/10.1149/1.3393860

[168] A. N. Jansen, D. W. Dees, D. P. Abraham, K. Amine, and G. L. Henriksen, "Low-temperature study of lithium-ion cells using a Li y Sn micro-reference electrode," *Journal of Power Sources*, vol. 174, no. 2, pp. 373–379, 2007. [Online]. Available: http://dx.doi.org/10.1016/j.jpowsour.2007.06.235

[169] W. Lu, C. M. López, N. Liu, J. T. Vaughey, A. Jansen *et al.*, "Overcharge effect on morphology and structure of carbon electrodes for lithium-ion batteries," *Journal of the Electrochemical Society*, vol. 159, no. 5, pp. A566–A570, 2012. [Online]. Available: http://dx.doi.org/10.1149/2.jes035205

[170] P. M. Gomadam and J. W. Weidner, "Modeling volume changes in porous electrodes," *Journal of The Electrochemical Society*, vol. 153, no. 1, pp. A179–A186, 2006. [Online]. Available: http://dx.doi.org/10.1149/1.2136087

[171] S. Zhang, K. Xu, and T. Jow, "Study of the charging process of a$LiCoO_2$-based Li-ion battery," *Journal of Power Sources*, vol. 160, no. 2, pp. 1349–1354, 2006. [Online]. Available: http://dx.doi.org/10.1016/j.jpowsour.2006.02.087

[172] M. Bauer, B. Rieger, S. Schindler, P. Keil, M. Wachtler, M. A. Danzer, and A. Jossen, "Multi-phase formation induced by kinetic limitations in graphite-based lithium-ion cells: Analyzing the effects on dilation and voltage response," *Journal of Energy Storage*, vol. 10, pp. 1–10, 2017. [Online]. Available: http://dx.doi.org/10.1016/j.est.2016.11.006

[173] I. Bloom, A. N. Jansen, D. P. Abraham, J. Knuth, S. A. Jones, V. S. Battaglia, and G. L. Henriksen, "Differential voltage analyses of high-power, lithium-ion cells: 1. Technique and application," *Journal of Power Sources*, vol. 139, no. 1, pp. 295–303, 2005. [Online]. Available: http://dx.doi.org/10.1016/j.jpowsour.2004.07.021

[174] H. M. Dahn, A. Smith, J. Burns, D. Stevens, and J. Dahn, "User-friendly differential voltage analysis freeware for the analysis of degradation mechanisms in li-ion batteries," *Journal of The Electrochemical Society*, vol. 159, no. 9, pp. A1405–A1409, 2012. [Online]. Available: http://dx.doi.org/10.1149/2.013209jes

[175] R. Arunachala, C. Parthasarathy, A. Jossen, and J. Garche, "Inhomogeneities in Large Format Lithium Ion Cells: A Study by Battery Modelling Approach," *ECS Transactions*, vol. 73, no. 1, pp. 201–212, 2016. [Online]. Available: http://dx.doi.org/10.1149/07301.0201ecst

[176] L. Höffer, "Entwicklung einer Modellzelle zur Nachbildung der Stromdichteverteilung in Lithium-Ionen-Batterien," Master's thesis, Technische Universität München, Lehrstuhl für Elektrische Energiespeichertechnik, 2013.

[177] C. Cluzel, C. Douglas *et al.*, "Cost and performance of ev batteries," *Element Energy, Final Report for the Committee on Climate Change*, 2012, accessed: 04.03.2017. [Online]. Available: https://www.yumpu.com/en/document/view/3901506/cost-and-performance-of-ev-batteries-final-report-element-energy

[178] "VW E-up!" accessed: 05.03.2017. [Online]. Available: https://de.wikipedia.org/wiki/VW_E-up!

[179] "Smart Electric Drive," accessed: 05.03.2017. [Online]. Available: https://en.wikipedia.org/wiki/Smart_electric_drive

[180] "Mitsubishi i-MiEV," accessed: 05.03.2017. [Online]. Available: https://en.wikipedia.org/wiki/Mitsubishi_i-MiEV

[181] "Tesla S Model, 85 kWh Battery Pack," accessed: 05.03.2017. [Online]. Available: https://electrek.co/2016/02/03/tesla-battery-tear-down-85-kwh/

[182] "Cell, Module, and Pack for EV Applications," accessed: 05.03.2017. [Online]. Available: http://www.eco-aesc-lb.com/en/product/liion_ev/

[183] J. Warner, "Lithium-ion battery packs for EVs," *Lithium-Ion Batteries: Advances and Applications*, pp. 127–150, 2014.

[184] I. A. Hunt, Y. Zhao, Y. Patel, and G. Offer, "Surface cooling causes accelerated degradation compared to tab cooling for lithium-ion pouch cells," *Journal of The Electrochemical Society*, vol. 163, no. 9, pp. A1846–A1852, 2016. [Online]. Available: http://dx.doi.org/10.1149/2.0361609jes

[185] S. J. Bazinski and X. Wang, "Thermal Effect of Cooling the Cathode Grid Tabs of a Lithium-Ion Pouch Cel," *Journal of The Electrochemical Society*, vol. 161, no. 14, pp. A2168–A2174, 2014. [Online]. Available: http://jes.ecsdl.org/content/161/14/A2168

[186] S. V. Erhard, P. J. Osswald, P. Keil, E. Höffer, M. Haug, A. Noel, J. Wilhelm, B. Rieger, K. Schmidt, S. Kosch *et al.*, "Simulation and Measurement of the Current Density Distribution in Lithium-Ion Batteries by a Multi-Tab Cell Approach," *Journal of The Electrochemical Society*, vol. 164, no. 1, pp. A6324–A6333, 2017. [Online]. Available: http://dx.doi.org/10.1149/2.0551701jes

[187] R. Arunachala, K. Makinejad, S. Athlekar, A. Jossen, and J. Garche, "Cycle life characterisation of large format lithium-ion cells," in *Electric Vehicle Symposium and Exhibition (EVS27), 2013 World*. IEEE, 2013, pp. 1–9. [Online]. Available: http://dx.doi.org/10.1109/EVS.2013.6914865

[188] C. Pillot, "The Rechargeable Battery Market and Main Trends 2014-2025," in *Proc. 3rd Israeli Power Sources Conf.*, 2013, pp. 9–34, accessed: 13.02.2017. [Online]. Available: http://www.avicenne.com/pdf/Fort_Lauderdale_Tutorial_C_Pillot_March2015.pdf

[189] "[electric vehicle market forecasts: Global forecasts for light duty hybrid, plug-in hybrid, and battery electric vehicles: 2013-2020."

[190] S. Arnold, T. Nguyen, R. Arunachala, and A. Jossen, "Study of Inhomogeneity in Large Format Li-Ion Cells with different Multiphysics Models," in *Proceedings of the 2015 COMSOL Conference in Kuala Lumpur*, 2015. [Online]. Available: https://www.comsol.co.in/paper/download/299861/arnold_paper.pdf

Appendix

A1.1 Battery Definitions

- **Charge Voltage Limit**
  The maximum allowed charge voltage specified by the manufacturer. The value depends on current rate, duration of current pulse during the pulse operation mode.
- **Discharge Voltage Limit**
  The minimum allowed discharge voltage specified by the manufacturer. The value depends on current rate, duration of pulse during the pulse operation mode.
- **End of Charge Voltage**
  It is the cut-off voltage specified by the manufacturer during CC and CV operation.
- **End of Discharge Voltage**
  It is the cut-off voltage for continuous discharge, specified by the manufacturer.
- **Nominal Voltage**
  It is the reference voltage of the battery, which is also referred to sometimes as normal voltage of the battery.
- **OCV**
  It is the voltage between the battery terminals under no load conditions. It depends on the SOC and temperature.
- **Terminal Voltage**
  It is the voltage between the battery terminals which it is being charged or discharged. It varies with SOC, charge/discharge current.
- **Nominal Capacity**
  It is the capacity in Ah, when the battery is discharged from a completely charged state (100% SOC) with a constant current until the end of discharge voltage at room temperature. The nominal capacity is specified by the manufacturer. If the experimentally determined capacity differs more than 5% from the manufacturer's specification, the measured capacity value should be used as nominal capacity.
- **C-rate**
  It is the discharge or the charge current, numerically expressed in the multiples of rated capacity in Ah of the battery. For example, if a cell of 5 Ah nominal capacity is discharged with a constant current of 5A, then the C-rate is 1C.

- **Actual Capacity**
  It is the amount of charge that can be removed from a battery, which is function of temperature, current and aging.

- **SOC**
  It is an expression of the battery capacity as a percentage of nominal capacity.

$$SOC_{nom} = 100 * \frac{\text{nominal capacity} - \text{dischargedcapacity}}{\text{nominal capacity}} \tag{A1.1}$$

$$SOC_{act} = 100 * \frac{\text{actual capacity} - \text{discharged capacity}}{\text{actual capacity}} \tag{A1.2}$$

$$\tag{A1.3}$$

- **DOD**
  It is the percentage of battery capacity that can be discharged, expressed as the percentage of nominal capacity.

$$\text{DOD} = 100 - \text{SOC} \tag{A1.4}$$

- **Calendar Life**
  The time required to reach the end of life of the battery at reference temperature (25°C) under open circuit condition.

- **Cycle Life**
  The time required to reach the end of life when the battery is in use, at a reference temperature.

- **BOL**
  It is the time at which the actual test begins. The characteristics of the cells at BOL are determined by discharge capacity measurement, HPPC & EIS test.

- **EOL**
  When a battery reaches 80% or 70% of its nominal capacity, the battery is considered to have reached the end of its life. This is an industry standard definition, which does not mean that the battery cannot be used anymore or it should be disposed.

- **Second Life**
  When an automotive battery reaches its EOL, it can be used for other less intensive application such as off-grid energy or photovoltaic application. This is termed as second life of the battery, where it can be reused.

- **End of Test (EOT)**
  It is the point of where the lifetime testing is halted, either because the criteria specified in the test plan are reached, or because it is not possible to continue testing.

- **Capacity Fade – ΔC**
  It is decrease in the capacity of the battery at a time during the lifetime test, measured with

respect to the capacity at BOL. The capacity fade is calculated using the following formula, where t_0 is the time at BOL and t_1 is the time during the test or after the test is completed.

$$\Delta C = 100 * \left(1 - \frac{C(t_1)}{C(t_0)}\right) \tag{A1.5}$$

- **SOH**
  It describes the health or the percentage of available performance remaining, before the EOL. A cell at BOL is at SOH = 100% and at EOL = 80% or 70%, depending on the criteria for EOL.

A1.2 Specifications of Measurement Equipment

Table A1: Specification BaSyTec CTS Battery Tester

Channels per Unit	32
Maximum Charging Current (A)	5
Maximum Discharging Current (A)	-5
Voltage Range (V)	0 - 5
Time Resolution (ms)	20
Current Range	5A/ 300mA/ 15mA/ 1mA
Accuracy (%)	± 0,05

Table A2: Specification Digatron (MCT 200-06-6 ME S) Battery Tester

Channels per Unit	6
Charge Current Rate (A)	0,2 - 200
Discharge Current Rate (A)	0,2 - 200
Voltage Range (V)	0 - 6
Time Resolution (ms)	20
Accuracy (%)	± 0,1

Table A3: Specification Digatron Impedance Spectroscope (EISmeter 2-20-4)

Resistance Range (mω	0,3 - 3000
Output Current AC (A)	2 (max. peak)
Frequency Range AC Current	10 mHz - 6,5 kHz
Meas. Accuracy abs(Z)	<1%
Meas. Accuracy arg(Z)	<1°

Table A4: Specification Biologic SP-240

Compliance (V)	-3,+14
Output Current AC (A)	1 µA - 4 A
Frequency Range AC Current	10 µHz - 3 MHz
Meas. Accuracy abs(Z)	<1%
Meas. Accuracy arg(Z)	<1°

A1.3 Special Measurements Setup

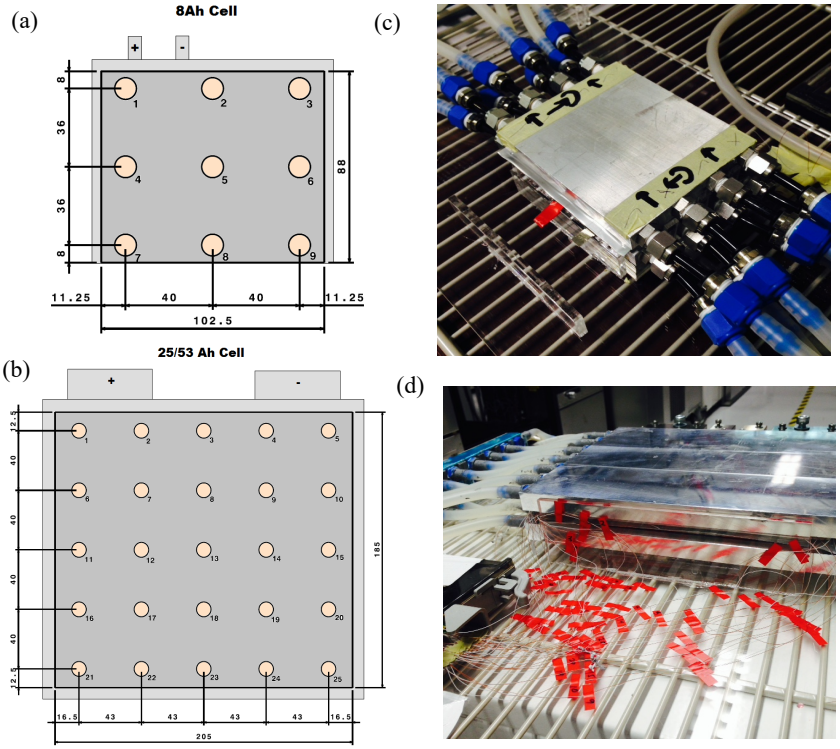

Figure A1: Spatial temperature measurements with Al. cooling plates (a) 8 Ah sensor positions (b) 25, 53 Ah sensor positions (c) snapshot of 8 Ah cooling setup (d) snapshot of 25 Ah cooling setup

- Fig. A1 (a) and (b) shows the location of sensors on the cell surfaces for respective sizes
- Sensors are placed equidistant from one another to generate the temperature map along the surface
- All dimensions shown are in mm
- Fig. A1 (c) and (d) the pictures of cooling setup for 8 Ah and 25 Ah cells respectively
- 25 Ah and 53 Ah cells have identical dimensions, hence the same cooling setup was used
- Temperature measurement were logged in Keysight datalogger 34980A

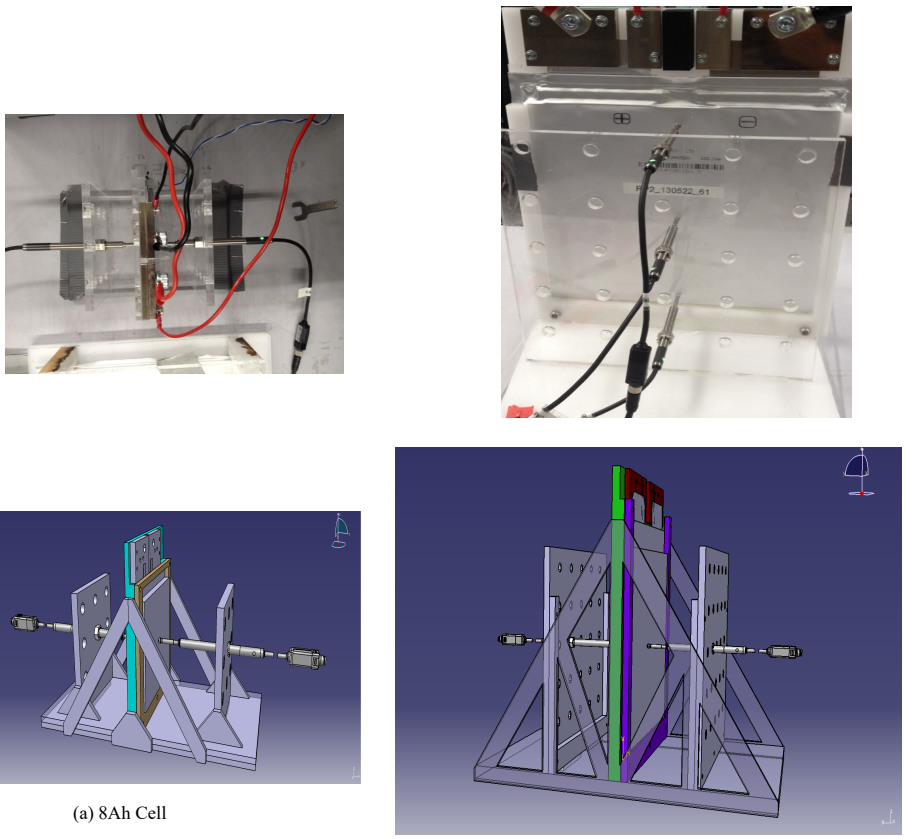

(a) 8Ah Cell

(b) 25, 53 & 75Ah Cell

Figure A2: Picture animation of displacement measurement setup for different cell sizes

- Fig. A2 (bottom) shows the animation of 8 Ah and 75 Ah displacement measurement setup
- Displacement sensors are placed in this fashion to allow the cell to freely expand along the thickness direction
- The details of the sensors and datalogging devices are shown in App. A1.8
- The entire measurement setup was placed inside a temperature chamber to have constant ambient conditions throughout the tests

A1.4 Simulation of Local Currents

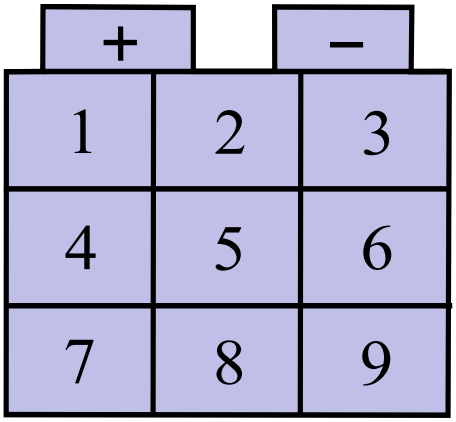

Figure A3: Simulation of Local Currents at different points on the large format pouch cells

- Fig. A3 shows the simulation of local currents in a large format cell at different points
- A P2D model is used in the COMSOL Multiphysics tool to perform simulation
- The simulation points are selected based on the model described in Fig. 4.5

A1.5 EIS Measurements for Different Cell Sizes

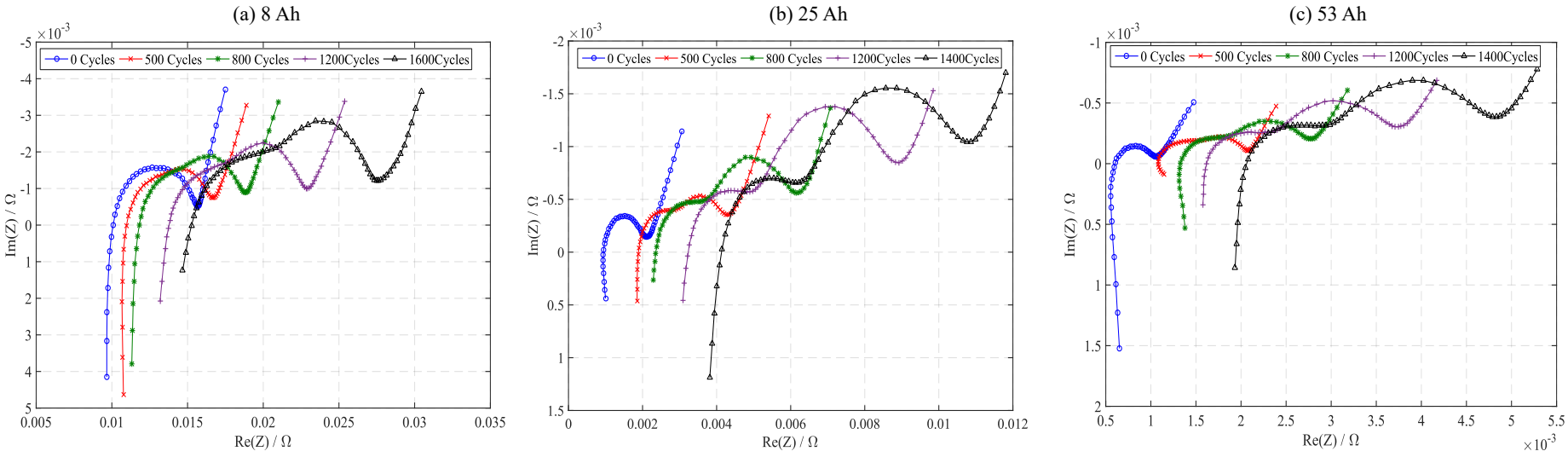

Figure A4: Electrochemical Impedance Spectroscopy measurements for different cell sizes

- Fig. A4 the impedance plot for 8, 25 & 53 Ah cells respectively.
- The impedance plot of 75 Ah cell is shown in Fig. 2.4
- As explained in section 2.3.1, cell impedance increases during the aging process
- The right shift in the x-intercept indicates increase in the cell internal resistance
- The growth of SEI layers can be seen as development of two semi circular region in the mid frequency range
- Two semi circular regions can be distinctively identified at later stages of aging or towards the EOL
- The semi circular grows bigger as the number of cycles increases, an indication of increase in charge transfer resistance and double layer capacitance

A1.6 Half Cell Entropy Calculations

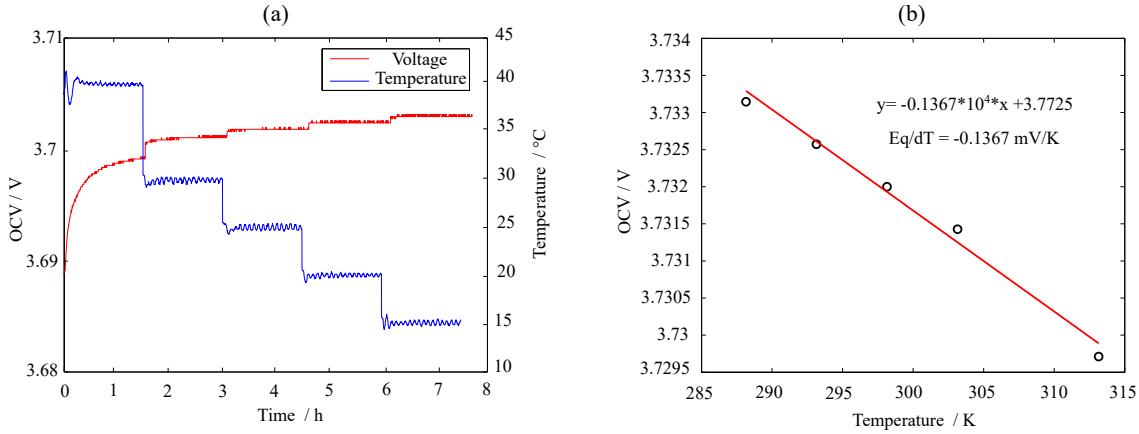

Figure A5: Calculation of Entropic Coefficient for NMC half cell at 20% SOC

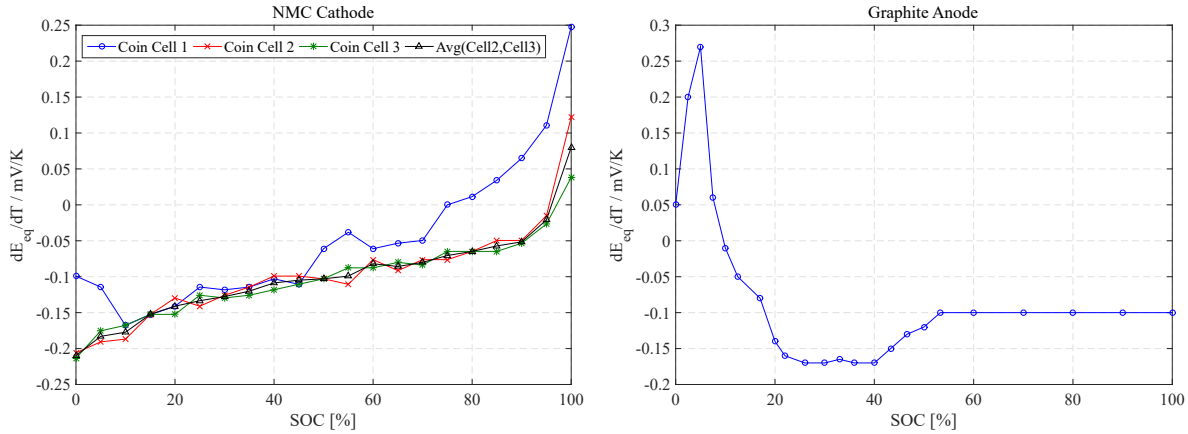

Figure A6: Entropic Coefficient of NMC and graphite at different SOC Intervals

A1.7 Additional Aging Results

- Tabs. A5 and A6 shows the complete set of parameters used in the SRECM for 8 Ah and 75 Ah cells
- These parameters were extracted from the HPPC tests at different SOC and aging intervals as explained in section 3.3.2.1
- The obtained pulse measurements were imported to Matlab and parameters were extracted using the Matlab function lsqcurvefit
- This is a nonlinear curve fitting solver which uses least square techniques by minimizing the user defined function in comparison with the measured data.
- The user defined function for the curve fitting solver is shown in Eqn. (4.3)
- The OCV measurements at different cycle aging intervals are explained in section 5.1.3

Table A5: SRECM parameters for 8 Ah cell at different aging conditions

SOC[%]	100	90	80	70	60	50	40	30	20	10	0
Cycles						R_i /Ω					
0	0.006599	0.007086	0.007131	0.007041	0.006565	0.006596	0.006672	0.006783	0.0069	0.007114	0.010081
500	0.00796	0.008556	0.008697	0.008711	0.008409	0.008477	0.008526	0.009046	0.009249	0.009548	0.011841
800	0.009328	0.009736	0.009834	0.00978	0.009576	0.009754	0.009905	0.010493	0.010752	0.011107	0.013134
1200	0.014389	0.014711	0.014856	0.014748	0.014831	0.014955	0.015052	0.015511	0.0161	0.016403	0.018134
1600	0.020051	0.020131	0.020187	0.020294	0.020095	0.019829	0.019928	0.020017	0.01956	0.019686	0.019675
						R_1 /Ω					
0	0.001922	0.001726	0.001647	0.001729	0.001923	0.002003	0.002113	0.002499	0.002787	0.003686	0.008026
500	0.002273	0.002243	0.002385	0.002567	0.002861	0.003106	0.003386	0.00441	0.005594	0.006128	0.009391
800	0.003054	0.003099	0.003141	0.003298	0.003439	0.003926	0.004338	0.005557	0.007382	0.007926	0.010099
1200	0.003239	0.003355	0.003485	0.003433	0.003828	0.004289	0.004756	0.005727	0.008597	0.009118	0.011231
1600	0.004074	0.004288	0.004413	0.004326	0.004676	0.005424	0.005848	0.00687	0.012071	0.012778	0.015824
						C_1 /F					
0	23.79429	44.67796	53.71054	41.69888	19.07796	19.67351	20.06327	18.44379	18.63367	17.32203	42.52576
500	20.40718	31.56421	29.80205	24.1197	14.22786	14.12523	14.09535	18.74231	16.94261	18.34654	34.42905
800	16.59958	19.87153	20.28564	17.09871	13.17313	12.74049	12.85085	16.97349	15.52427	16.8904	29.14673
1200	15.6822	17.21008	16.785	15.34144	12.5433	12.28067	12.19386	15.12032	15.49389	16.51551	25.18358
1600	40.01701	41.79295	41.59455	38.35706	34.71481	29.8646	28.39457	26.16503	17.9863	19.17803	18.79949
						R_2 /Ω					
0	0.00345	0.003377	0.003369	0.003132	0.00383	0.004059	0.004393	0.004714	0.004275	0.007695	0.051164
500	0.003606	0.00341	0.003322	0.002984	0.003527	0.003661	0.003927	0.005348	0.004657	0.00778	0.032254
800	0.003745	0.003556	0.003423	0.003022	0.00352	0.003613	0.003848	0.006224	0.005267	0.008361	0.022752
1200	0.003775	0.003614	0.003476	0.003089	0.003553	0.003614	0.003791	0.007049	0.005732	0.008187	0.020034
1600	0.004073	0.003867	0.003668	0.003444	0.003852	0.003954	0.004023	0.007307	0.006442	0.008169	0.017901
						C_2 /F					
0	2318.817	1889.245	1860.469	2081.776	1922.767	1919.75	1864.194	1718.812	1658.768	1072.908	354.4585
500	2226.526	1781.092	1707.03	1937.13	1918.712	1958.61	1885.035	1153.977	1212.519	867.5969	409.2008
800	2070.615	1676.604	1609.225	1846.407	1872.078	1850.8	1751.757	952.6472	1013.138	800.4667	389.8899
1200	2034.838	1697.587	1608.495	1918.736	1826.827	1813.71	1729.11	956.1175	897.4624	787.8595	401.4637
1600	2247.896	1905.635	1846.248	2002.255	1895.471	1911.288	1846.141	1286.671	928.4016	928.3706	463.7177

A1.8 Displacement Sensor

- ***Keyence* GT2-P12KL High-accuracy Digital Contact Sensor**
  To measure the displacement, which is on the scale of 100μm, high-precision contact type displacement sensors with 1μm accuracy and 0.1μm resolution were used. The range of displacement of this sensor is 0-12mm and a low-stress type head with contact force of less than 0.2N was used to minimize the force exerted on the battery's surface by the sensor head, so that the influence of the swelling behavior of cells has minimal effect on the displacement value. The sensor has to be

Table A6: SRECM parameters for 75 Ah cell at different aging conditions

SOC[%]	100	90	80	70	60	50	40	30	20	10	0
Cycles						R_i /Ω					
0	0.000744	0.000764	0.00077	0.000762	0.000778	0.000794	0.000807	0.000825	0.000853	0.000871	0.00088
500	0.001045	0.001094	0.001109	0.001134	0.001147	0.001161	0.001167	0.001185	0.001237	0.001251	0.001429
800	0.001301	0.001351	0.001383	0.001371	0.001419	0.001386	0.001415	0.001439	0.001495	0.001523	0.001773
1200	0.001679	0.001737	0.001778	0.001787	0.001844	0.001848	0.00186	0.001877	0.001944	0.001988	0.002295
						R_1 /Ω					
0	8.85×10^{-5}	0.000103	0.000121	0.000124	0.0001	9.95×10^{-5}	0.000113	0.000143	0.000201	0.000309	0.000618
500	0.000427	0.000379	0.000352	0.000328	0.000317	0.000311	0.000332	0.000371	0.000437	0.000629	0.001024
800	0.000506	0.00046	0.000416	0.000428	0.000385	0.000423	0.000421	0.000456	0.000527	0.000699	0.001092
1200	0.000671	0.000633	0.000581	0.000573	0.000531	0.000529	0.000536	0.000569	0.000622	0.000768	0.001149
						C_1 /F					
0	3.19×10^3	3189.298	2571.344	2739.441	2765.687	2.15×10^3	1908.381	1462.904	991.3762	779.3904	670.3273
500	403.3778	476.9462	562.5811	611.3689	571.2889	564.0167	534.0977	535.4952	495.3465	415.1539	407.5073
800	366.262	410.2748	485.9521	495.464	502.682	430.8826	438.0834	443.2554	411.1129	366.9773	365.1829
1200	282.7962	316.8225	344.0079	343.3718	379.8002	360.7225	362.1724	348.8948	336.4198	305.8111	317.5723
						R_2 /Ω					
0	0.000364	0.000379	0.000374	0.000362	0.000315	0.000374	0.000398	0.000422	0.000478	0.000608	0.012961
500	0.000382	0.00039	0.0004	0.000392	0.000364	0.000411	0.000434	0.000466	0.00052	0.000976	0.004207
800	0.000405	0.000411	0.000422	0.000417	0.000404	0.000457	0.000477	0.000513	0.000577	0.000971	0.003166
1200	0.00045	0.000468	0.000484	0.000491	0.000497	0.000555	0.000581	0.000621	0.000695	0.00095	0.002329
						C_2 /F					
0	30197.89	24475.69	21764.96	21379.66	26510	25383.47	25714.14	24364.22	19932.22	14078.85	4879.088
500	24784	19561.47	17836.5	17510.45	21164.78	21136.51	20789.54	19434.45	14663.58	9908.691	3582.931
800	21564.51	17553.04	16427.32	16655.01	18679.55	18342	17972.8	16888.29	13519.7	9384.17	3714.148
1200	17267.09	15354.05	14571.2	14455.37	15153.55	14080.36	13734.91	13084.62	10842.77	7944.628	3997.528

used together with an amplifier (*Keyence* GT2-71MCN), which powers the sensor and provides a digital display as well as an analog current output. The sensor and the amplifier are shown in Figure A7.

(a) GT2-P12KL (b) GT2-71MCN

Figure A7: GT2-P12KL Pencil-type Sensor head and GT2-71MCN Amplifier

- ***Keysight* 34972A LXI Data Logger**
  A *Keysight* 34972A Data Logger Switch Unit (Figure A8) was used to acquire the temperature and displacement data from the displacement and temperature sensors (PT1000). A board with 22 channels (34901A) is plugged from the back side of the data logger. The output of the displacement sensors is analog current between 4 and 20mA, corresponding to the displacement range of 0-12mm. The sensors are connected to the last 2 channels, which are the only ones that can measure direct current of all the 22 channels.

(a) Front Panel (b) Back Side

Figure A8: *Keysight* 34972A LXI Data Acquisition / Data Logger Switch Unit

A1.9 Cell Disassembly

- Fig. A9 shows the selected images of the 8 Ah cell when the cell was new and aged
- The aged cell appears to have increased in the thickness as explained in sections 3.3.5 and 5.5
- The aged anode of 8 Ah appears to have fewer damages compared to the same electrode of 75 Ah cell
- The aged cathode has some prominent white spots which was not observed in 75 Ah
- Apart from this there are no significant damages to the positive electrode

(a) New Cell (b) Aged Cell

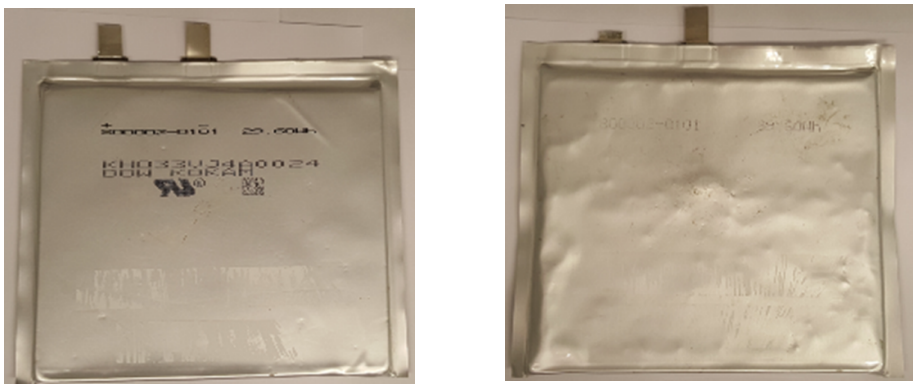

(c) Aged Cathode (d) Aged Anode

Figure A9: Visual inspection of new 8 Ah cell and the same cell at the end of life

A1.10 SOC Distribution for Different Tab Configurations in 75 Ah Cells

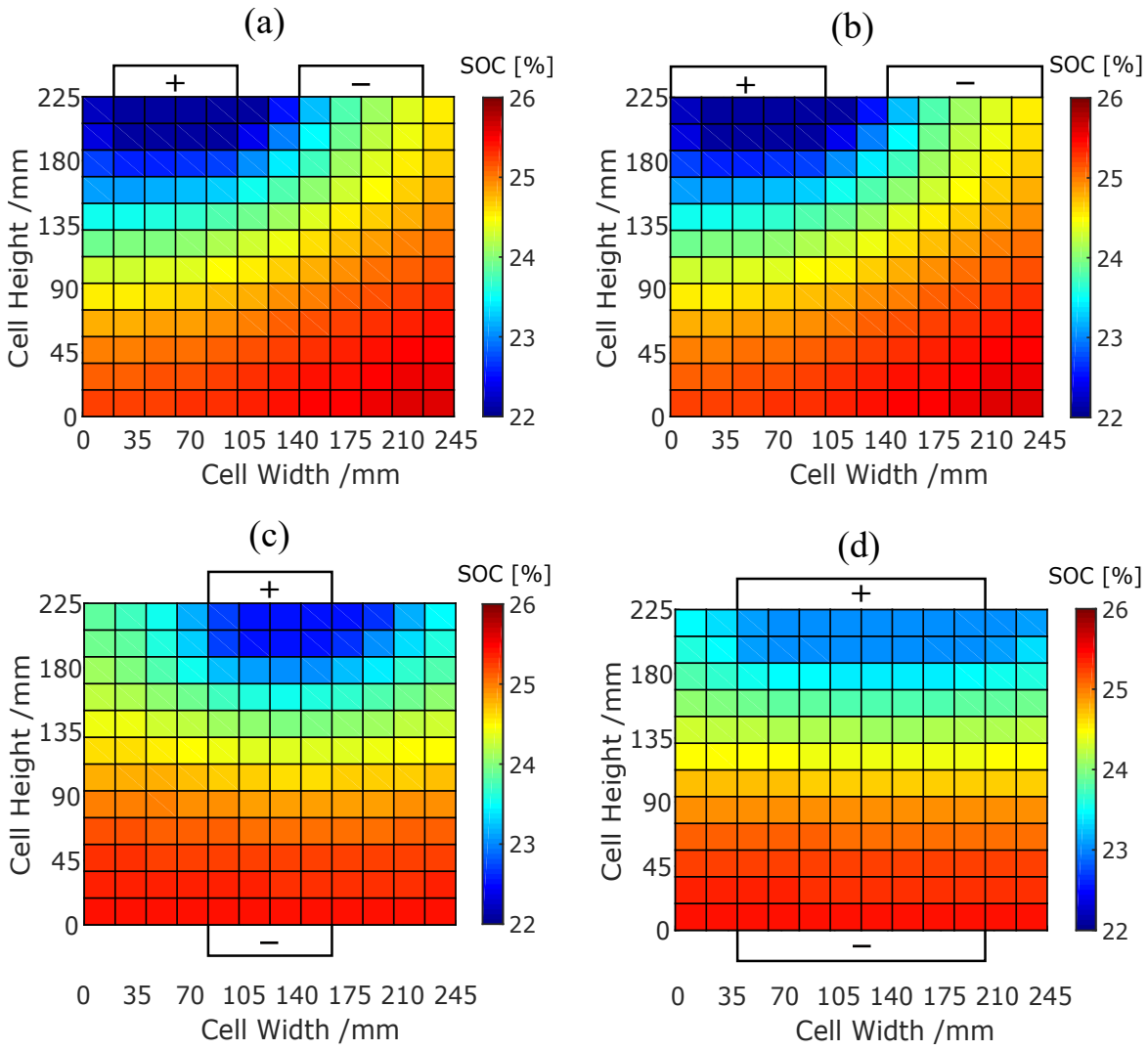

Figure A10: Maximum SOC gradient on the cell surface during 3C discharge at 25°C for (a) Normal Tabs, (b) Wide Tabs, (c) Counter Tabs & (d) Wide and Counter Tabs, cell SOC = 25%

- Fig. A10 the maximum SOC gradient in 75 Ah cell during 3C discharge at 25°C for different tab configurations
- The simulation conditions were same to the results obtained in section 6.3
- It can be observed that the maximum current gradient and SOC gradient do not appear at the same time interval
- The CT and CWT configurations helps to reduce the SOC gradient as well as current gradient in the cell